

**A Thesis Submitted for the Degree of PhD at the University of Warwick**

**Permanent WRAP URL:**

<http://wrap.warwick.ac.uk/79967>

**Copyright and reuse:**

This thesis is made available online and is protected by original copyright.

Please scroll down to view the document itself.

Please refer to the repository record for this item for information to help you to cite it.

Our policy information is available from the repository home page.

For more information, please contact the WRAP Team at: [wrap@warwick.ac.uk](mailto:wrap@warwick.ac.uk)



# **Modelling and Simulation Study of IGCC Power Plant with Activated Carbon-based Carbon Capture Process**

by

**Yue Wang**

Thesis

Submitted to the University of Warwick

for the degree of

**Doctor of Philosophy**

School of Engineering

March 2016

# Table of Contents

<b>List of Figures</b>	<b>vii</b>
<b>List of Tables</b>	<b>xvi</b>
<b>List of Symbols and Abbreviations</b>	<b>xix</b>
Chapter 1    Introduction .....	1
1.1    Background .....	1
1.2    Study Aims and Methodology .....	2
1.3    Thesis Outlines .....	4
1.4    Publications.....	7
Chapter 2    Introduction of IGCC Power Plant and Overview of the Major Sub-Systems....	9
2.1    Overview of the IGCC Technology Development .....	9
2.2    Description of An IGCC Process.....	12
2.2.1    Introduction of the whole process .....	12
2.2.2    Introduction of Gasifier .....	14
2.2.3    Water Gas Shift Reactor .....	26
2.2.4    Acid Gas Removal (AGR).....	27
2.2.5    Gas Turbine and Combined Cycle .....	29
2.2.6    Air Separation Unit.....	30

2.3	Summary .....	31
Chapter 3	Zero-dimension Mathematical Model of Gasification Process Based on Texaco Gasifier	33
3.1	Description of Texaco Gasifier Process .....	33
3.2	Mathematical Model of Texaco Gasifier .....	35
3.2.1	Overview of the Texaco Gasifier Model Development .....	35
3.2.2	Texaco Gasification Syngas Prediction Model Development.....	36
3.3	Texaco Gasifier Syngas Prediction Results and Discussion.....	47
3.3.1	Steady State Prediction and Model Validation.....	47
3.3.2	Syngas contents change with water/coal ratio change .....	49
3.3.3	Syngas contents change with oxygen/coal ratio change.....	51
3.3.4	Syngas contents change with operation temperature change .....	52
3.3.5	Summary of the Texaco gasifier simulation.....	54
3.4	Model test for other type of gasifier .....	55
3.5	Summary .....	57
Chapter 4	One dimension model of Shell slagging gasifier.....	58
4.1	Introduction of Shell Slagging Gasifier .....	58
4.2	Shell Gasifier Model.....	60

4.2.1	“Three Zones” Assumption .....	60
4.2.2	Gasification Model Assumptions .....	61
4.2.3	Shell Gasifier Model Development .....	63
4.3	Model Parameterization and Simulation Procedure .....	77
4.3.1	Model Parameterization.....	77
4.3.2	Flow Chart for Simulation.....	79
4.4	Results and Discussion .....	82
4.4.1	Results of Oxygen input step change 1% and 5% .....	82
4.4.2	Results of steam input step change 20% .....	90
Chapter 5	Auxiliary Modules In Gasification Enabled Plant.....	98
5.1	Introduction of Thermolib Software .....	98
5.1.1	Gas Phase Calculation .....	99
5.1.2	Liquid Phase Calculation.....	102
5.1.3	Vapour-liquid Equilibrium Calculation.....	106
5.1.4	Mixture Calculation.....	108
5.1.5	Limitation of Thermolib Software.....	109
5.2	Gas Quench Process Model for Shell Gasifier .....	110
5.2.1	Gas Quench Model .....	110

5.2.2	Syngas Cooling Model .....	114
5.3	Total Water Quench Model for Texaco Gasifier .....	117
5.4	Simplified Water Gas Shift Reactor Model .....	120
5.5	Simplified Sulphur Removal Model .....	128
5.5.1	COS Hydrolysis Reactor .....	128
5.5.2	Simplified H <sub>2</sub> S Removal Unit .....	130
5.6	Summary .....	131
Chapter 6	Modelling of A Combined Cycle Power Plant .....	132
6.1	Gas Turbine Model .....	132
6.1.1	Introduction of Gas Power Cycle .....	132
6.1.2	Gas Turbine Model Developed with Thermolib .....	139
6.2	HRSG Model .....	143
6.2.1	Introduction of Steam Power Cycle .....	143
6.2.2	Single Stage HRSG Model .....	148
6.2.3	Dual Stage HRSG Model .....	150
6.3	Combined Cycle Power Plant Model .....	165
6.4	Summary .....	167
Chapter 7	Carbon Capture Process Model Based on PSA and Energy Penalty analysis. ....	168

7.1	Introduction of PSA Model Developed by UoB.....	169
7.1.1	Activated Carbon Sample Preparation .....	169
7.1.2	Adsorption Isotherms Model for Activated Carbons .....	170
7.2	PSA Model Development and Analysis .....	181
7.3	Penalty Analysis of IGCC with PSA Carbon Capture Process .....	186
7.4	Discussion of CO <sub>2</sub> /H <sub>2</sub> Based on Experiment Data from UoN.....	190
7.5	Summary .....	190
Chapter 8	Conclusion, Limitations and Future work .....	192
8.1	Conclusions.....	192
8.2	Limitations .....	195
8.3	Future work.....	196
	References .....	198
	Appendix CHP Model Based on UoW Campus Plant with Applied Controllers .....	203
A.1	Introduction of CHP Power Plant Model .....	203
A.2	Performance Analysis of CHP Power Plant Model .....	212
A.3	Discussion and summary .....	218

# List of Figures

Figure 2.1.Simplified Schematics diagram of an IGCC system.....	13
Figure 2.2 Simplified Schematics diagram and temerature filed in a moving bed gasifier ....	16
Figure 2.3 Schematics of Lurgi dry ash gasifier with temperature and gas composition files (Supp, 1990) .....	17
Figure 2.4 Simplified Schematics diagram and temperature profile of a fluid bed gasifier (Simbeck et al., 1993).....	18
Figure 2.5 Winkler process.....	19
Figure 2.6 HT Winkler gasifier (NETL, 2013) .....	20
Figure 2.7 KBR Transport.....	20
Figure 2.8 Lurgi CFB gasifier .....	21
Figure 2.9 A top-fired entrained-flow gasifier and its temperaure file(Breault, 2010).....	22
Figure 2.10 GE gasifier .....	23
Figure 2.11 Shell gasifier .....	24
Figure 2.12 MHI gasifier .....	25
Figure 2.13 Tsinghua staged oxygen process (NETL, 2013, Yang et al., 2011) .....	25
Figure 2.14 Three types of water gas shift reactions (LindeGroup.Ltd, 2015).....	27



Figure 2.15 AGR technologies classification (NETL, 2013) .....	28
Figure 2.16 a)Tail gas treatment dedicated for H <sub>2</sub> S removal b) Tail gas treatment integrated with upstream AGR process .....	29
Figure 2.17 Schematics of combined cycle in IGCC process (IEA, 2011).....	30
Figure 2.18 Schematics of typical air separation unit (Jones et al., 2011) .....	31
Figure 2.19 Schematics of IGCC process simulated in this thesis .....	32
Figure 3.1 Structure of Texaco gasifier (Wang et al., 2015).....	34
Figure 3.2 Energy balance for gasifier .....	43
Figure 3.3 Flow chart of Newton-Raphson method for syngas contents calculation.....	46
Figure 3.4 Syngas content change with H <sub>2</sub> O/coal ratio.....	50
Figure 3.5 Syngas content change with H <sub>2</sub> O/coal ratio.....	50
Figure 3.6 Syngas content change with oxygen/coal ratio unit.....	51
Figure 3.7 Syngas content change with oxygen/coal ratio unit.....	52
Figure 3.8 Syngas contents change with operation temperature .....	53
Figure 3.9 Syngas contents change with operation temperature .....	53
Figure 3.10 Syngas contents change with operation pressure .....	54
Figure 3.11 Syngas content change with operation pressure .....	54
Figure 4.1 Schematics of Shell gasifier (Sun et al., 2011) .....	60

Figure 4.2 The “three zones” inside gasifier (Sun et al., 2011).....	61
Figure 4.3 The Schematics of slag layer building process .....	69
Figure 4.4 Velocity field in x direction for film fluid with variable viscosity (Bird et al., 2001) .....	70
Figure 4.5 Flow chart of steady state model parameterization.....	80
Figure 4.6 Flow chart of the dynamic performance simulation .....	81
Figure 4.7 Whole process Schematics of Shell gasifier model .....	82
Figure 4.8 Dynamic change of raw syngas temperature with 1% and 5% oxygen input rise .	83
Figure 4.9 Dynamic change of liquid slag surface temperature with 1% and 5% oxygen input rise .....	83
Figure 4.10 Dynamic change of refractory wall temperature with 1% and 5% oxygen input rise .....	84
Figure 4.11 Dynamic change of liquid layer average temperature with 1% and 5% oxygen input rise .....	84
Figure 4.12 Dynamic change of solid layer average temperature with 1% and 5% oxygen input rise .....	85
Figure 4.13 Dynamic change of exit slag mass flow with 1% and 5% oxygen input rise .....	85
Figure 4.14 Dynamic change of liquid slag layer thickness with 1% and 5% oxygen input rise .....	86

Figure 4.15 Dynamic change of solid slag layer thickness with 1% and 5% oxygen input rise .....	86
Figure 4.16 Dynamic change of CO concentration with 1% and 5% oxygen input rise.....	88
Figure 4.17 Dynamic change of H <sub>2</sub> concentration with 1% and 5% oxygen input rise .....	88
Figure 4.18 Dynamic change of CGE 1% and 5% oxygen input rise .....	89
Figure 4.19 Dynamic change of CO <sub>2</sub> concentration with 1% and 5% oxygen input rise.....	89
Figure 4.20 Dynamic changes of gas temperature with 20% steam / 1% Oxygen input rises	90
Figure 4.21 Dynamic changes of liquid layer surface temperature with 20% steam / 1% Oxygen input rises .....	91
Figure 4.22 Dynamic changes of refractory wall temperature with 20% steam/1% Oxygen input step rises .....	91
Figure 4.23 Dynamic changes of liquid slag average temperature with 20% steam/1% Oxygen input step rises .....	92
Figure 4.24 Dynamic changes of solid slag average temperature with 20% steam/1% Oxygen input step rises .....	92
Figure 4.25 Dynamic change of exit slag mass flow rate with 20% steam/1% Oxygen input step rises .....	93
Figure 4.26 Dynamic change of liquid slag layer thickness with 20% steam/1% oxygen input step rises .....	93

Figure 4.27 Dynamic change of solid slag layer thickness with 20% with 20% steam/1%oxygen input step rises.....	94
Figure 4.28 Dynamic change of CO concentration with 20% steam/1%oxygen input step rises .....	94
Figure 4.29 Dynamic change of H2 concentration with 20% steam/1%oxygen input step rises .....	95
Figure 4.30 Dynamic change of CO2 concentration with 20% steam/1%oxygen input step rises.....	95
Figure 4.31 Dynamic change of CGE with 20% steam/1%oxygen input step rises .....	96
Figure 5.1 Schematics of Thermolib chemical database .....	101
Figure 5.2 Temperature range for each substance in chemical database .....	102
Figure 5.3 Coefficients for the calculation of liquid phase density.....	103
Figure 5.4 Coefficients for the calculation of liquid phase specific heat capacity.....	104
Figure 5.5 Schematic of coefficients and temperature ranges for evaporation enthalpy calculation.....	105
Figure 5.6 Flowchart of Shell gasifier with gas quench and syngas cooling system .....	111
Figure 5.7 Schematics of Shell gasifier with gas quench and syngas cooling system(Higman and van der Burgt, 2008d) .....	111
Figure 5.8 Schematics of heat transfer happen in NTU heat exchanger (Eutech, 2013) .....	115

Figure 5.9 Schematics for WGS with heat recovery block for Shell gasifier .....	122
Figure 5.10 Schematics for WGS with heat recovery block for Texaco gasifier.....	122
Figure 5.11 1st stage WGS shifted syngas temperature dynamic change .....	124
Figure 5.12 1st stage WGS shifted syngas CO <sub>2</sub> concentration dynamic change .....	124
Figure 5.13 1st stage WGS shifted syngas H <sub>2</sub> concentration dynamic change .....	125
Figure 5.14 2nd stage WGS shifted syngas temperature dynamic change.....	125
Figure 5.15 2nd stage WGS shifted syngas CO <sub>2</sub> concentration dynamic change .....	126
Figure 6.1 Schematics illustration of Brayton cycle .....	133
Figure 6.2 T-s and P-v diagrams of Brayton cycle (MAE115, 2012).....	134
Figure 6.3 Actual Brayton cycle in T-s diagram by considering the irreversibility (MAE115, 2012).....	137
Figure 6.4 Gas turbine model developed by Thermolib.....	141
Figure 6.5 Dynamic change of power in gas turbine.....	143
Figure 6.6 Schematics diagram of an ideal Rankine cycle.....	144
Figure 6.7 (a) Ideal Rankine cycle in T-s diagram (b) Actual Rankine cycle in T-s diagram (MAE115, 2012).....	145
Figure 6.8 Schematics of single stage HRSG model developed with Thermolib .....	149
Figure 6.9 Dynamic change of single stage HRSG net power generation .....	150

Figure 6.10 Flue gas pathway in HRSG .....	150
Figure 6.11 LP steam generation in HRSG .....	151
Figure 6.12 HP steam generation .....	151
Figure 6.13 Schematics of dual-stage HRSG developed with Thermolib.....	153
Figure 6.14 Dynamic change of steam cycle power generations .....	165
Figure 6.15 Combined cycle Schematics .....	166
Figure 6.16 Combined cycle in T-s diagram.(Çengel and Boles, 2006) .....	166
Figure 7.1 Modified AC sample .....	169
Figure 7.2 Test rig built by UoB (Caldwell, 2015) .....	170
Figure 7.3 Experiment isotherms for unmodified AC for CO <sub>2</sub> (black circles) and N <sub>2</sub> (white circles) at 30 °C (a) and 45 °C (b) and the simulation results of isotherm models: Langmuir model (dashed), LF model (solid) and DSL model (dotted) (Caldwell et al., 2015) .....	176
Figure 7.4 Experiment isotherms for unmodified AC for CO <sub>2</sub> (black circles) and N <sub>2</sub> (white circles) at 30 °C (a) and 45 °C (b) and the simulation results of isotherm models: Langmuir model (dashed), LF model (solid) and DSL model (dotted) (Caldwell et al., 2015) .....	176
Figure 7.5 The Schematics of four step cycle of PSA process (Caldwell, 2015).....	182
Figure 7.6 Process configuration for 8 beds 9 steps PSA process with two pressure equalisation and one recycled purge stream (Caldwell, 2015).....	185
Figure A.1 Layout of micro-CHP of UoW (Serth and Lestina, 2014) .....	204

Figure A.2 Shell-tube boiler of UoW (Serth and Lestina, 2014) .....	205
Figure A.3 Power production system Schematics of CHP in UoW .....	206
Figure A.4 Power production system Schematics of CHP in UoW .....	207
Figure A.5 Comparison of simulated electrical output without controller and operational data in a summer working day .....	212
Figure A.6 Comparison of simulated gas flow with feedback control and operational data in a summer working day .....	212
Figure A.7 Comparison of simulated electrical output without controller and operational data in a winter working day .....	213
Figure A.8 Comparison of simulated gas flow with feedback control and operational data in a winter working day .....	213
Figure A.9 Dynamic behaviour of electricity generation with/without feedback controller	213
Figure A.10 Comparison of simulated thermal output without control and operational data in a summer working day .....	214
Figure A.11 Comparison of simulated water flow rate with control and operational data in a summer working day .....	215
Figure A.12 Comparison of simulated water flow rate without control and operational data in a winter working day .....	215
Figure A.13 Comparison of simulated water flow rate with control and operational data in a winter working day .....	215

Figure A.14 Dynamic behaviour of heat exchanger thermal output .....	216
Figure A.15 Comparison of simulated boiler thermal power output without control and operational data in winter working day .....	216
Figure A.16 Comparison of simulated boiler thermal power output with control and operationa data in a spring working day.....	217
Figure A.17 Comparison of simulated boiler output water temperaturewith and without control in a winter working day.....	217
Figure A.18 Dynamic change of boiler themal power outputwith/without control .....	217
Figure A.19 Dynamic change of boiler water temperature output with/without control .....	217



# List of Tables

Table 2.1 Main Milestones of IGCC Technology Development .....	11
Table 2.2 Fluid bed gasification processes.....	19
Table 2.3 Entrained-flow gasification processes.....	23
Table 3.1 Model input with three types of coals .....	47
Table 3.2 Comparison of simulation results and Reference data .....	48
Table 3.3 Model input based on Lunan factory.....	49
Table 3.4 Dry Syngas Output Content Compare.....	49
Table 3.5 Shell gasifier Model Input.....	55
Table 3.6 Shell gasifier Model output with reference data .....	56
Table 4.1 Input parameters of dynamic Shell gasifier model.....	77
Table 4.2 Kick off data dynamic Shell gasifier model.....	78
Table 5.1 Parameters of raw syngas, recycled cold gas and quenched gas.....	113
Table 5.2 Model input using typical british coal.....	117
Table 5.3 Simulation results by using typical British coal.....	118
Table 5.4 Calculation for raw syngas and quenched syngas parameters .....	120
Table 5.5 Parameters of two stages WGS outlet syngas parameters of Shell and Texaco gasifier .....	127

Table 5.6 Parameters of two stages WGS outlet syngas parameters of Texaco gasifier.....	127
Table 5.7 Parameters COS free syngas parameters of Shell and Texaco gasifier.....	129
Table 5.8 Parameters of sweet syngas parameters of Texaco gasifier .....	130
Table 6.1 Gas turbine model input .....	142
Table 6.2 GE 6B Gas turbine operation data comparing with refrence data.....	142
Table 6.3 Parameters of flue gas, exhaust gas to atmosphere and generated main steam.....	149
Table 6.4 Parameters of HP secondary super heater .....	154
Table 6.5 Parameters of LP tertiary super heater .....	155
Table 6.6 Parameters of HP primary super heater.....	156
Table 6.7 Parameters of LP secondary super heater.....	157
Table 6.8 Parameters of HP evaporator.....	158
Table 6.9 Parameters of HP HT economizer.....	159
Table 6.10 Parameters of LP Primary super heater .....	160
Table 6.11 Parameters of LP Evaporator .....	161
Table 6.12 Parameters of HP LT Economizer.....	162
Table 6.13 Parameters of LP Economizer .....	163

Table 7.1 The breakthrough capacities of CO <sub>2</sub> /N <sub>2</sub> mixtures separated using unmodified activated carbon for each experimental run and the predicted capacity for pure components based on the LF and DSL models.....	177
Table 7.2 Breakthrough Predicted multicomponent adsorption capacities based on the multicomponent LF and DSL models and the corresponding IAST models for CO <sub>2</sub> /N <sub>2</sub> mixtures separated using unmodified activated carbon (Caldwell et al., 2015).....	178
Table 7.3 Predicted selectivities of CO <sub>2</sub> /N <sub>2</sub> mixture using unmodified AC based on multicomponent LF and DSL models and the corresponding IAST models (Caldwell, 2015) .....	179
Table 7.4 The breakthrough capacities of CO <sub>2</sub> /N <sub>2</sub> mixtures separated using modified activated carbon for each experimental run and the predicted capacity for pure components based on the LF and DSL models.....	179
Table 7.5 Breakthrough Predicted multicomponent adsorption capacities based on the multicomponent LF and DSL models and the corresponding IAST models for CO <sub>2</sub> /N <sub>2</sub> mixtures separated using modified activated carbon (Caldwell, 2015) .....	180
Table 7.6 Predicted selectivities of CO <sub>2</sub> /N <sub>2</sub> mixture using unmodified AC based on multicomponent LF and DSL models and the corresponding IAST models (Caldwell, 2015) .....	181
Table 7.7 Capture rate and purities for CO <sub>2</sub> and N <sub>2</sub> using 4-step Skarstrom PSA process(Caldwell, 2015).....	183
Table 7.8 CO <sub>2</sub> and N <sub>2</sub> capture rate and purity for 9 steps 8 beds cycle .....	185

Table 7.9 Parameters of Texaco-based IGCC power plant under different carbon capture rates .....	187
Table A.1 Cummins 1370 GQMA CHP unit specification .....	203
Table A.2 Design characteristics of gas engine controller .....	210
Table A.3 Design characteristics of heat recovery subsystem controller.....	210
Table A.4 Design characteristics of auxiliary boiler subsystem controller.....	211

# List of Symbols and Abbreviations

## List of symbols

$A$	Carbon conversion rate	-
$A^p$	Parameters for enthalpy calculation in NIST polynominals	-
$A^s$	Interface area between recirculation zone and wall	m <sup>2</sup>
$A_{isl}$	The surface area of liquid slag layer	m <sup>2</sup>
$B$	Parameters for enthalpy calculation in NIST polynominals	-
$C$	Parameters for enthalpy calculation in NIST polynominals	-
$D$	Parameters for enthalpy calculation in NIST polynominals	-
$E$	Parameters for enthalpy calculation in NIST polynominals	-
$F$	Parameters for enthalpy calculation in NIST polynominals	-

$G$	Parameters for enthalpy calculation in NIST polynomials	-
$H$	Parameters for enthalpy calculation in NIST polynomials	-
$A_0$	Parameters for specific enthalpy calculation in NASA polynomials	-
$B_0$	Parameters for specific enthalpy calculation in NASA polynomials	-
$C_0$	Parameters for specific enthalpy calculation in NASA polynomials	-
$D_0$	Parameters for specific enthalpy calculation in NASA polynomials	-
$E_0$	Parameters for specific enthalpy calculation in NASA polynomials	-
$F_0$	Parameters for specific enthalpy calculation in NASA polynomials	-
$G_0$	Parameters for specific enthalpy calculation in NASA polynomials	-
$H_0$	Parameters for specific enthalpy calculation in NASA polynomials	-

$A_1$	Parameters for liquid density calculation in NASA polynomials	-
$B_1$	Parameters for liquid density calculation in NASA polynomials	-
$C_1$	Parameters for liquid density calculation in NASA polynomials	-
$D_1$	Parameters for liquid density calculation in NASA polynomials	-
$A_2$	Parameters for liquid mole specific capacity in NASA polynomials	-
$B_2$	Parameters for liquid mole specific capacity in NASA polynomials	-
$C_2$	Parameters for liquid mole specific capacity in NASA polynomials	-
$D_2$	Parameters for liquid mole specific capacity in NASA polynomials	-
$A_3$	Parameters for liquid mole specific enthalpy in NASA polynomials	-
$B_3$	Parameters for liquid mole specific enthalpy in NASA polynomials	-

$A_4$	Parameters for saturation pressure calculation in NASA polynomials	-
$B_4$	Parameters for saturation pressure calculation in NASA polynomials	-
$D_{coal,moisture,O}$	mass flow of oxygen contained in the moisture content carried by coal on a dry ash-free basis	$\text{kJ s}^{-1}$
$D_{steamblast,O}$	mass flow of oxygen contained in the steam blast	$\text{kJ s}^{-1}$
$D_{oxygenblast,Ar}$	mass flow of Argon carried by the oxygen blast	$\text{kJ s}^{-1}$
$D_{oxygenblast,N}$	nitrogen mass flow carried by oxygen blast	$\text{kJ s}^{-1}$
$e$	base of the natural logarithm	-
$g$	Gravitational acceleration	$\text{m s}^{-2}$
$H_{in,coal}$	Enthalpy flow carried by coal	$\text{kJ s}^{-1}$
$H_{in,H_2O}$	Enthalpy flow carried by $H_2O$	$\text{kJ s}^{-1}$
$H_{in,Oxygenblast}$	Enthalpy flow carried by oxygen blast	$\text{kJ s}^{-1}$



$H_{out,rawsyngas}$	Enthalpy flow carried out by raw syngas	$\text{kJ s}^{-1}$
$H_{out,flyash}$	Enthalpy flow carried out by fly ash	$\text{kJ s}^{-1}$
$H_{loss}$	Heat loss rate	$\text{kJ s}^{-1}$
$H_{out,slag}$	Enthalpy flow carried out by slag	$\text{kJ s}^{-1}$
$H_{steam}$	Enthalpy flow carried out by steam in membrane wall	$\text{kJ s}^{-1}$
$H_T$	standard enthalpy of gas in temperature $T$	$\text{kJ/kmol}$
$H_{out,uncarbon}$	Enthalpy flow carried out by unreacted carbon	$\text{kJ s}^{-1}$
$H_{298.15}$	standard enthalpy of gas using standard temperature 298.15K and pressure $1.01\text{e}^5 \text{ Pa}$	$\text{kJ/kmol}$
$HHV_i$	Higher heating value of syngas content $i$	$\text{kJ}$
$HHV_{carbon}$	Higher heating value of carbon	$\text{kJ}$
$HHV_{coalfeed}$	Higher heating value of coal feed	$\text{kJ}$
$HHV_{raw,syngas}$	Higher heating value of	$\text{kJ}$

raw syngas

$h_l$	Enthalpy flow carried by liquid slag layer	$\text{kJ kg}^{-1} \text{ s}^{-1}$
$\overline{h_l}$	The average enthalpy carried by liquid phase slag	$\text{kJ kg}^{-1} \text{ s}^{-1}$
$h_m$	The mole enthalpy of ideal gas	$\text{kJ mol}^{-1}$
$h_{mixgas}$	<u>Mass</u> specific enthalpy of mixed gas	$\text{kJ kg}^{-1}$
$h_{raw}$	<u>Mass</u> specific enthalpy of <u>raw syngas</u>	$\text{kJ kg}^{-1}$
$h_{cold}$	<u>Mass</u> specific enthalpy of <u>raw syngas</u>	$\text{kJ kg}^{-1}$
$\overline{h_{ssl}}$	The average enthalpy carried by solid phase slag	$\text{kJ kg}^{-1} \text{ s}^{-1}$
$M$	Number of transfer unit	-
$M(A_r)$	Molecular mass of argon	-
$M(C)$	Molecular mass of carbon	-
$M(H_2)$	molecular mass of hydrogen	-
$M(N_2)$	molecular mass of nitrogen	-

$M(S)$	molecular mass of Sulphur	-
$M(O_2)$	molecular mass of oxygen	-
$m_{ash,in}$	Liquid ash droplet input mass flow rate	$kg\ s^{-1}$
$m_l$	Mass of liquid slag layer	kg
$m_{lsl,out}$	Exiting mass flow rate of liquid slag layer	$kg\ s^{-1}$
$\dot{m}_{mixgas}$	Mass flow rate of mixed syngas	$kg\ s^{-1}$
$\dot{m}_{raw}$	Mass flow rate of raw syngas	$kg\ s^{-1}$
$\dot{m}_{cold}$	Mass flow rate of <u>cold</u> <u>recirculated</u> syngas	$kg\ s^{-1}$
$m_{slag}$	Mass flow rate of exiting slag	$kg\ s^{-1}$
$m_{ssl,m}$	Melting flow rate from solid slag layer	$kg\ s^{-1}$
$m_{flyash}$	mass flow rate of fly ash	$kg\ s^{-1}$
$m_{uncarbon}$	mass flow rate of unreacted carbon	$kg\ s^{-1}$
$N_{C,0}$	equivalent input carbon content mole flow rate	$kmol\ s^{-1}$

$N_{H_2,0}$	equivalent input hydrogen mole flow	$\text{kmol s}^{-1}$
$N_g$	raw syngas mole flow rate	$\text{kmol s}^{-1}$
$N_{O_2,0}$	equivalent input nitrogen content mole flow rate	$\text{kmol s}^{-1}$
$N_{N_2,0}$	equivalent input nitrogen content mole flow rate	$\text{kmol s}^{-1}$
$N_{S,0}$	equivalent input sulphur mole flow	$\text{kmol s}^{-1}$
$n_i$	mole flow rate of syngas content $i$	$\text{kmol s}^{-1}$
$n_{in,Ar}$	input argon mole flow	$\text{kmol s}^{-1}$
$n_{in,N_2}$	input nitrogen mole flow	$\text{kmol s}^{-1}$
$n_{in,O_2}$	input oxygen mole flow	$\text{kmol s}^{-1}$
$P$	Gasification pressure	kPa
$P_{ref}$	Reference pressure	kPa
$\dot{Q}$	Actual heat transfer rate of two flows	kW
$\dot{Q}_{\max}$	Possible maximum heat flux between two flows	kW

$Q_{conv}$	Convective heat transfer	kW
$Q_{g,sl}$	Heat flux for gasification zone to liquid slag layer	kW
$Q_{rad}$	Radiant heat transfer	kW
$q_{g,sl}$	Heat flux from gas volume to liquid slag layer	kW
$q_{ssl,w}$	Heat flux from solid slag layer to refractory wall	kW
$q_{w,tube}$	Heat flux from refractory wall to metal tube	kW
$R$	Universal ideal gas constant	-
$s_m$	Mole entropy	J mol <sup>-1</sup> K <sup>-1</sup>
$s_{m,NASA}$	Mole entropy parameter calculated by NASA polynominals	
$T$	Temperature	K
$T_g$	gasification temperature	K
$T_{in,Oxygenblast}$	oxygen blast temperature	K
$T_{lst,0}$	Liquid phase slag surface temperature	K

$T_{lsl}$	Liquid slag layer surface temperature	K
$\bar{T}_{lsl}$	Average temperature of liquid slag	K
$\bar{T}_{ssl}$	Average temperature of solid slag layer	K
$T_m$	Ash melting temperature	K
$T_{tube}$	Temperature of metal tube	
$T_w$	Refractory wall temperature	K
$\bar{T}_w$	Average temperature of refractory wall	K
$U$	Overall heat transfer coefficient	$\text{W m}^{-2} \text{K}$
$V$	Gas total volume	$\text{m}^3$
$V_m$	Mole volume of gas properties	$\text{m}^3 \text{mol}^{-1}$
$V_z$	velocity of the liquid slag flow along $z$ axis	$\text{m s}^{-2}$
$\bar{V}_z$	Average velocity of the liquid layer	$\text{m s}^{-2}$
$v$	mean velocity of the gas in recirculation zone	$\text{m s}^{-1}$

$X_{CO}$	mol concentration of CO	-
$X_{CO_2}$	mol concentration of CO <sub>2</sub>	-
$X_{CH_4}$	mol concentration of CH <sub>4</sub>	-
$X_{COS}$	mol concentration of COS	-
$X_{H_2O}$	mol concentration of H <sub>2</sub> O	-
$X_{N_2}$	mol concentration of N <sub>2</sub>	
$X_{SO_2}$	mol concentration of SO <sub>2</sub>	-
$Y_C$	carbon mass concentration in the dry coal on a ash-free basis	-
$Y_H$	hydrogen mass content in the dry coal on a ash-free basis	-
$Y_N$	nitrogen mass content in the dry coal on a ash-free basis	-
$Y_S$	sulphur mass content in the dry coal on a ash-free basis	
$Y_o$	oxygen mass content in coal on a dry ash-free basis	-

$Z_{em}$	Empirical parameter for coal ash melting temperature calculation	-
----------	--	---

$Z_{O_2}$	oxygen purity	-
-----------	---------------	---

## Greek sympols

$\alpha$	parameter to describe how fast the viscosity increases as $x$ increase	-
----------	--	---

$\sigma$	Stefan-Boltzman constant	$\text{kW m}^{-2} \text{K}^{-4}$
----------	--------------------------	----------------------------------

$\delta$	Thickness of film layer	m
----------	-------------------------	---

$\delta_{lsl}$	Thickness the liquid slag layer	m
----------------	---------------------------------	---

$\delta_{ssl}$	Thickness the solid slag layer	m
----------------	--------------------------------	---

$\varepsilon$	Effectiveness of NTU heat exchanger	-
---------------	-------------------------------------	---

$\varepsilon_s$	Emissivity of slag layer	-
-----------------	--------------------------	---

$\gamma_g$	convective heat transfer coefficient	$\text{kW m}^{-2} \text{K}^{-1}$
------------	--------------------------------------	----------------------------------

$\rho_c$	Liquid density at critical temperature	$\text{kg m}^{-3}$
----------	--	--------------------

$\rho_{f,sat}$	Saturated liquid density	$\text{kg m}^{-3}$
----------------	--------------------------	--------------------



$\rho_g$	gas density	kg m <sup>-3</sup>
$\rho_{ssl}$	solid slag density	kg m <sup>-3</sup>
$\mu$	viscosity	kPas
$\mu_0$	viscosity in liquid slag layer surface	
$\varepsilon_s$	Emissivity	-
$\gamma_g$	convective heat transfer coefficient	kWm <sup>-2</sup> K <sup>-1</sup>
$\kappa$	thermal conductivity of raw syngas	kW m <sup>-1</sup> K <sup>-1</sup>
$\psi$	Parameter for evaporation calculation	-
$\tau$	Parameter used for liquid density calculation	-
$\tau_{xz}$	viscous momentum flux on flat xz	Pa
$\beta$	angle between $x$ axis and vertical direction	grad
$\phi_m$	Melting slag mass flow rate per unit square	kg s <sup>-1</sup> m <sup>-2</sup>
$\Delta h_m$	transition enthalpy	kW kg <sup>-1</sup>

$\Delta T_{\max}$	Maximum temperature difference of two flows	K
-------------------	--	---

### Dimensionless groups

$Re$	Renolds	-
$Nu$	Nusselt number	-
$Pr$	Prandtl number	-

## **List of Abbreviations**

ACs	Activated carbons
AGR	Acid Gas Removal unit
ASU	Air Separation Unit
BLT	Biggest Log Modulus tuning
CC	Carbon Capture
CGE	Cold Gas Efficiency
DSL	Dual site Langmuir-Freundlich
FAD	Fundamental angle difference
GEM	Gasification-Enabled Module
HP	High Pressure
HRSG	Heat Recovery Steam Generator
IASL	Ideal Adsorbed Solution Theory
LF	Langmuir-Freundlich
IGCC	Integrated Gasification Combined Cycle
LP	Low Pressure
MP	Medium Pressure
NTU	Number of Transfer Unit

MAE	Mean Absolute Error
PSA	Pressure Swing Adsorption
SISO	Single Input and Single Output
SSE	Sum of Squared relative Errors
SCGP	Shell Coal Gasification Process
UoB	University of Birmingham
UoN	University of Nottingham
UoW	University of Warwick
WGS	Water Gas Shift reactor

# Acknowledgements

First and foremost, I would like to express gratitude to my supervisor, Professor Jihong Wang. As a meticulous scholar, her persistence attitude and inspiring ideas continuously guide me in the research life. The project aims can't be achieved without her support and advices on the modelling equation derivation and documents revision. I will benefit with the knowledge and spirit learnt from her in my following career.

Secondly, I would also like to give thanks to my parents and my wife Lily. My families' support is the great drive during my Ph.D. study. They are always there when I need support thus I can dedicate myself to the work. My families' love and patience will always be the power sauce to crack any obstacle in my life.

Thirdly, I would like to thank colleagues and friends, Shen Guo, Hao Liu, Hao Sun, Xing Luo, Zhiwei Yang, Jacek Wojcik , Chirstopher Krupke, Mark Dooner and Simon Caldewell. I learnt a lot form them. I will always remember the time we spend together and cherish this period as the most beautiful memory.

In addition, I would also like to give my thanks to Dr. Zacharie Tamainot-Telto and Prof. Hao Liu for spending time to read my thesis. I would like to give special thanks to Prof. Hao Liu and Prof. Junfu Lv, the books and papers they provided help me learn the fundamental knowledge of gasification and carbon capture.

Finally, I would like to thank EPSRC and CSC council for providing the financial support to help me finish this project.

# Declaration

This thesis is submitted in partial fulfilment for the degree of Doctor of Philosophy under the regulations set out by the Graduate School at the University of Warwick. This thesis is solely composed of research completed by Yue Wang, except where stated, under the supervision of Professor Jihong Wang between the dates of June 2011 and September 2015. No part of this work has been previously submitted to any other institution for a higher degree.

Yue Wang

September 2015

# Abstract

Integrated Gasification Combined Cycle (IGCC) is considered as a viable option for low emission power generation and carbon-dioxide sequestration. Modelling development and simulation study is essential part for the process of IGCC design and development. This PhD project is aiming to conduct the modelling and simulation study of IGCC power plant by building sub-modules such as gasifier, water gas shift reactor, acid gas removal unit, gas turbine and HRSG, etc. and connecting these modules together for the whole process study. In addition, the impact for the integration of IGCC with activated carbons-based pressure swing adsorption carbon capture process is investigated by using a PSA model developed and validated by University of Birmingham.

A simplified zero dimension gasification model is developed based on Texaco gasifier and validated by reference and industry data. The model development is based on mass balance, chemical equilibrium and energy balance. The prediction results for syngas contents concentrations are proved to be reasonably acceptable and the syngas contents changes with key input parameters changes are studied. The model is then used to generate a variable syngas stream to study the dynamic performance of the other sub-modules.

A one dimension dynamic model based on Shell slagging gasifier is developed. The model can successfully show the characteristics of slag layers formation and the syngas stream change with response to input parameters change. By using step rise of oxygen input and steam blast input, the dynamic performance of syngas temperature, syngas contents, slag mass flow rate and slag layers thickness is analysed and compared. It is found that oxygen input show relative larger impact on gasifier operation than steam blast for the studied working conditions.

Auxiliary modules in a gasification enabled plant and combined cycle power plant are modelled with Thermolib Software. Basic principles of this software are introduced. Simplified quench process, WGS with heat recovery, acid gas removal unit, gas turbine, HRSG and electrical generator are modelled by using the blocks from Thermolib. The simulation results show the dynamic changes of key output variables such as power output, syngas temperature and contents concentrations.

PSA model developed by UoB based on ACs is introduced and a 9 step 8 beds cycle model is used for the integration with IGCC model. This PSA model can achieve 80.89% CO<sub>2</sub> capture rate with 87.33% of N<sub>2</sub> recovery rate without any additional equipment. N<sub>2</sub> is used to represent H<sub>2</sub> for the simulation. Four cases for IGCC integrated with carbon capture are studied for the energy penalty analysis. It is predicted that the efficiency loss for IGCC power plant with 80.89% carbon capture will be 10.96%. The limitations of using N<sub>2</sub> to represent H<sub>2</sub> for the PSA model are discussed and it is predicted the real efficiency loss will be lower than the simulation results.



## **Chapter 1 Introduction**

This chapter introduces the background of the research project first. It explains the motivations for the research work. Secondly, study aims and methodology to conduct the work is explained. Then the outlines of this thesis is given, which gives a brief introduction of each chapter. Finally, the publications during the study are listed.

### **1.1 Background**

In the next decades, fossil fuel will continue to be the main energy in power and industry sectors worldwide, the CO<sub>2</sub> emission caused by fossil fuel combustion now becomes a global issue. Carbon capture and storage (CCS) technology is an attractive greenhouse mitigation strategy, which can be integrated with conventional power generation stations. Although demonstration projects have shown the viability of CCS integration with small scale coal and gas fired power plants (Rubin et al., 2007), the reduction in power plant efficiency, capital cost of construction and system operation complexity are still the main barriers for the deployment of CCS.

Integrated gasification combined cycle (IGCC) offers the benefits over conventional coal fired power plants, especially with regard to the environment and feedstock flexibility (Yue et al., 2013). The gasification of solid fuels such as coal and biomass can not only generate much less hazardous gas and inhalable particles than traditional power plants, but also offer its advantages in the integration with carbon capture and storage units. Since the synthesis gas produced by coal gasification is primarily formed by hydrogen and carbon monoxide, the water shift reaction of synthesis gas with steam can easily convert the carbon monoxide to carbon dioxide and generate additional hydrogen, which offers ideal environment for pre-combustion capture of high concentration carbon dioxide in the shifted syngas. Pressure

swing adsorption (PSA), with easy operation procedure and low economic cost, is an attractive technology for the pre-combustion capture in IGCC power plant (Bell et al., 2010). Meanwhile, activated carbons (ACs) based adsorbents have gained interests and are proved to be suitable for pre-combustion carbon capture, some of these large microporous materials show high selectivity of CO<sub>2</sub> over other gases hence they are ideal for the utilisation in pressure swing adsorption process (Caldwell et al., 2015, Drage et al., 2009).

In order to investigate the operation of IGCC with PSA carbon capture based on activated carbon adsorbents, the University of Nottingham (UoN), the University of Warwick, the University of Birmingham (UoB), the University college of London (UCL), Tsinghua University (THU) and the Chinese Academy of Sciences (CAS) set up a collaborative research project with the funding support from the Engineering and Physical Sciences Research Council (project number: EP/I010955/1). The role of Warwick in the project is to conduct the modelling and simulation study of IGCC and explore the impact of its integration with ACs based PSA unit. The work presented in this thesis focuses on the development of IGCC model and the efficiency loss caused by PSA carbon capture process is discussed as well.

## **1.2 Study Aims and Methodology**

The work conducted by the University of Warwick is to develop the whole IGCC plant model and perform simulation study to IGCC power plant dynamic responses and the impact of integration with a carbon capture process. This work starts with the mathematical modelling of the essential sub-modules in an IGCC power plant, which is formed by the gasification - enabled module (GEM) and combined cycle power generation block. The performance of an IGCC power plant without carbon capture is studied to understand the operation of the sub modules; this will prepare a platform for the integration of IGCC with PSA carbon capture

process. The results of the PSA model developed by UoB are then used to investigate its impact to the IGCC power plant, especially the efficiency loss caused by the reduction of hydrogen in syngas, the subsequent performance of gas turbine and heat recovery steam generator blocks (HRSG) are studied.

The modelling work of the IGCC process starts from the GEM plant model development. The GEM module includes the gasifier with quench block, shift reactor with heat recovery block, COS hydrolysis block and H<sub>2</sub>S removal block. Two types of gasifiers (Texaco gasifier with water quench and Shell gasifier with gas quench) are modelled based on mass balance and energy balance equations. The lumped gasifier model can predict the syngas contents and other properties when given the parameters of feedstock inputs and oxidants. The syngas stream generated by the gasifier block will then pass the shift reactor with heat recovery and sulphur removal blocks developed with Simulink based toolbox-Thermolib. The equation based toolbox provides variable blocks which are viable for thermodynamic system modelling and simulation. Moreover, the syngas contents simulation benefits from the powerful chemical media database of Thermolib, which makes it possible to simulate the reactions and thermodynamic processes. The performance of each block are analysed, the property changes of syngas stream such as temperature, pressure, enthalpy and syngas contents concentrations are tracked and studied. The modules in gasification enabled module (GEM) plant are developed and validated based on published references and internal research report (M.Karmarkar, 2005).

The fuel gas stream is then transported to the power generation block which is formed by gas turbine, HRSG and electricity generators. The gas turbine (GT), heat recovery steam generator (HRSG) and electricity generators are modelled with Thermolib toolbox as well. The

configuration and parameterization of each module are based on published references and internal research report as well.

The final stage of this project work is to investigate the impact of PSA unit to IGCC power plant. After integrating the PSA unit model with the power plant model, it is viable to analyse the energy conversion efficiency of the IGCC power plant. In addition, the fuel gas changed caused by the PSA unit under different carbon capture rates will also influence the operation of power block, which leads to power efficiency changes.

### **1.3 Thesis Outlines**

There are eight chapters in this thesis. Chapter 1 introduces the background of project and outlines the study aims and methodology. Meanwhile, the publications during the period of the Ph.D. study are listed in the next section.

Chapter 2 provides a detailed description of an IGCC power plant. The history of gasification technologies and the widely used commercial gasification technologies are outlined and compared. The working principles of shift reactor, sulphur removal unit and combined cycle power plant are depicted in this chapter as well. This chapter is aiming to reveal the whole picture of the IGCC power plant and the blueprint of the IGCC model developed in this work.

Chapter 3 presents the development of a zero-dimension Texaco gasifier model. This model is capable of predicting the syngas composition with the given feed stock and oxidant parameters. The detailed derivation of mass balance and energy balance equations are outlined. The model is then validated by comparing the simulation results of different types of coal under pre-defined working conditions. The comparison of simulation results with data from published references and industry data provided by THU reveals that this model can

give accurate prediction of syngas stream. Meanwhile, the impact of the key parameter changes such as coal slurry concentration, oxygen/coal ratio and working pressure are studied. To show the model flexibility, it is also used for the steady state simulation of Shell gasifier in the end of this chapter.

Chapter 4 focuses on the development of a dynamic model of Shell-slugging gasifier. Shell gasifier is selected because its unique slagging characteristic offers conservation of energy and mass. The detailed derivation of mass balance and energy balance equations are mainly presented in this chapter, the dynamic performance of Shell gasifier (slag layers thickness, syngas output contents concentrations, temperature files of syngas, slag layers and refractory wall and cold gas efficiency) with step changes of oxygen and steam inputs are studied as well.

Chapter 5 presents the background knowledge of Thermolib toolbox first; the gas phase and liquid phase calculation equations are detailed. The theories used in Thermolib for stream state calculation are the main focus in this part. Since the auxiliary modules of the gasification enabled module plant (GEM) are developed based on Thermolib, it is necessary to introduce the theory to explain the basic working principles of Thermolib blocks. The second part of the chapter introduces the modules of water quench for Texaco gasifier, gas quench and heat recovery for Shell gasifier, shift reactor with heat recovery for both Texaco and Shell gasifiers. The heat exchanger which utilises heat released by the endothermic water gas shift reaction is modelled to study the process of generating low pressure (LP) and high pressure (HP) steam for the HRSG module in power generation section. The shifted syngas is then treated by COS hydrolysis reactor and a simplified H<sub>2</sub>S removal unit, the sulphur removal model is built to represent the process of removing the sulphides.

Chapter 6 starts from outline of the development of power generation plant, which is formed by gas turbine, HRSG and electricity generator. The gas turbine module is developed based on Brayton cycle while the single stage HRSG is developed based on Rankine cycle. In order to study the integration of shift reactor with power generation plant, a two stage HRSG is developed and validated based on an internal research report (M.Karmarkar, 2005). The dynamic performance of the combined cycle based on Texaco gasifier is studied.

In order to study the impact of ACs-based PSA unit to the IGCC power plant, the experiment and simulation work conducted by the University of Birmingham is introduced in Chapter 7. The work starts from the pure isotherm tests for two ACs samples (unmodified AC and modified AC).  $N_2$  is used to represent  $H_2$  in this part. Several isotherm models are built and compared for the adsorption capacity prediction, which aims to provide a viable model to predict the cyclic outputs of the PSA process. The multicomponent DSL model is found to give the best prediction results for  $CO_2/N_2$  mixture adsorption; it is then used as the basic unit for PSA cyclic model. Finally the 9 steps 8 beds PSA model simulation results provide relative high purity and capture rate for both of  $CO_2$  and  $N_2$ . The results are used to build a model which is then connected with the IGCC power plant model; the efficiency losses on different  $CO_2$  capture rate are then simulated. At the end of Chapter 7, the potential of using  $CO_2/H_2$  for the PSA process is discussed based on the experiment data provided by the University of Nottingham; it is concluded that the  $CO_2/N_2$  predicts a worse separation than  $CO_2/H_2$  separation, which indicates that the actual efficiency losses for  $CO_2/H_2$  separation should be lower.

Chapter 8 provides the main conclusions and limitations of the project work. The potential future work is discussed and suggested in the chapter.

Appendix A detailed a research project based on the combined cycle power (CHP) plant elaborated on the campus of the University of Warwick. The model is developed with Thermolib and Simulink and simplified controllers are applied. The CHP model simulation results for different seasons are compared with the operation data collected from the University of Warwick and the dynamic performance of the CHP power plant is analysed.

## **1.4 Publications**

Journal papers:

- Y. Wang, A. Bermukhambetova, J. Wang, M. Dooner, J. Lv, Q. Gao, Modelling of the Whole Process of a University Campus CHP Power Plant and Dynamic Performance Study, accepted by International Journal of Automation and Computing.

The contents of this paper are presented in chapter 6.

- Y. Wang, J. Wang, X. Luo., S. Guo., J. Lv, Q. Gao., Dynamic modelling and simulation of IGCC process with Texaco gasifier using different coal, System Science and Control Engineering, Vol.3, pp198-210, 2015.

Part of the contents of this paper is presented in chapter 3 and 5.

Conference papers:

- Y. Wang, J. Wang, A. Bermukhambetova, S. Guo, J. Lv, Q. Gao , Dynamic simulation of combined heat and power system in University of Warwick, International Conference on Automation & Computing, Cranfield UK, Sep 2014.
- Y. Wang, J. Wang, S. Guo, J. Lv, Q. Gao, Dynamic Modelling and Simulation Study

of Texaco Gasifier in an IGCC Process, International Conference on Automation & Computing, London UK, Sep 2013.

- Z. Sun, Y. Dai, H. Liu, Y. Wang, J. Wang, Dynamic performance of a dual-pressure waste heat recovery system under partial load operation, International Conference on Automation & Computing, Loughborough University, UK, Sep 2012.

#### Oral presentations:

- J. Wang, J. Wood, S. Caldwell and Y. Wang, 2011. Modelling of Pre-Combustion Carbon Dioxide Capture and Power Plant Cycle at IGCC Power Stations. Oral Presentation at the Mathematical Modelling and Simulation of Power Plants and CO<sub>2</sub> Capture Workshop, Warwick, UK, 20-21 March 2012.
- Y. Wang, S. Caldwell, J. Wang, J. Wood, S. Guo, Dynamic simulation study on IGCC process with novel activated carbon based pre-combustion carbon capture, presentation in 10th European Conference on Coal Research and its Applications, Hull, UK, Sep 2014.

#### Poster competitions:

- Y. Wang, J. Wang, Modelling and Simulation Study of an IGCC Power Plant with Carbon Capture Processes, poster competition in IET Engineering Prize Award Evening(in association with industry, Mar 2014).
- Y. Wang, J. Wang, IGCC+CCS: An Odyssey to Clean Coal and Low Carbon Power Generation, The Midlands Energy Graduate School Annual Conference, System Thinking in Energy, Sep 2012.



## **Chapter 2 Introduction of IGCC Power Plant and Overview of the Major Sub-Systems**

This chapter gives an introduction of IGCC process and an overview of IGCC technology development. A detailed description to the IGCC sub-systems is presented including: gasifier, water quench, air separation unit, water gas shift reactor, Sulphur removal, gas turbine and heat recovery generator. The potential benefits of IGCC process combined with pre-combustion carbon capture process is discussed, physical-adsorbents and activated carbon-based pressure swing adsorption process are described as the technologies can be incorporated with IGCC for CO<sub>2</sub> abatement.

### **2.1 Overview of the IGCC Technology Development**

The conversion from solid fuel such as coal, biomass to gas fuel has contributed to human civilization development from ancient time. Although the production and utilization of coal and biomass can trace back to Stone Age, gasification didn't achieve industrial operation until the foundation of the London Gas, Light and Coke Company in 1812 (Higman and van der Burgt, 2003). Gasification technology was only developed to generate town gas, blast furnace gas and producer gas in the early stage (1900s to 1920s) due to the limitation of oxidant production technology (Higman and van der Burgt, 2008a). In the late 1920s to 1940s, the commercialization of cryogenic air separation technology which is developed by Carl Linde (Higman and van der Burgt, 2008a) finally achieved continuous supply of oxygen as oxidant, this revolutionary progress makes it available for the production of synthesis gas rich in hydrogen and carbon monoxide. The well-known Lurgi moving bed pressurized gasification technology and Koppers-Totzek entrained-flow process emerged during this period. During the following 40 years, gasification technologies were mainly used in the ammonia industry for poly-synthesis. It was the oil crisis in early 1970s that promotes great interests in utilizing

coal gasification for power generation and offers an alternative to the shortage of petrol supply (Higman and van der Burgt, 2008a). Using syngas for power generation starts from the idea of injecting it to gas turbines during 1950s to 1960s (Zhang et al., 2013). The development of gas turbine technology, especially the largely rise of tolerance for the gas turbine inlet temperature, made this application into reality. Hence, the conceptual technology known as Integrated Gasification Combined Cycle (IGCC) was proposed, theoretically tested and verified in 1970s. It is considered as a promising process which can efficiently synthesis fuel gas from coal or biomass for power generation with low emission. The first generation of demonstration IGCC power plants includes Cool Water, Plaquemine (USA, 1987), Lünen (Germany, 1972). During 1990s, more commercial scale IGCC power plants with larger capacity were built and considerable experiences in construction, operation and commercialization were gained and researched at this stage, hence it is also known as “lessons learned” period. The main milestones in the IGCC development history are listed in Table 2.1. Since beginning of this millennium, global warming and extreme weather caused by greenhouse gases such as carbon dioxide and methane started to attract more and more interests on IGCC technology. As considered as a “capture ready” technology for CO<sub>2</sub> abatement, IGCC regained governments and researchers interests for its availability for CO<sub>2</sub> sequestration as well as low pollutants emission. A large number of IGCC projects were announced and constructed worldwide, especially in countries with rich coal reserves such as China, India and Malaysia (Higman and van der Burgt, 2008a). Although some uncertainty comes along with IGCC, the interests in this technology will continue and grow for some time.

Table 2.1 Main Milestones of IGCC Technology Development

Time	Milestones
1812	Foundation of London Gas, Light and Coke Company. Gasification firstly used as a commercial process to generate town gas for lighting and cooking. (Higman and van der Burgt, 2003)
1887	Lurgi GmbH of Germany was granted the first major patent in gasification process.(Miller, 2005)
1895	William Hampson and Carl von Linde independently filed for patent of the cryogenic cycle used in the air liquefaction process. Continuous oxidant supply for gasification became possible.(Higman and van der Burgt, 2008a)
1950	Gumz propose the idea of injecting synthesis gas to gas turbine as fuel to generate electricity.(Higman and van der Burgt, 2008a)
1970s	U.S government started to sponsor studies to test the idea of using syngas as fuel for gas turbines. The syngas was produced by coal gasification process. (Higman and van der Burgt, 2003)
1980s	Cool Water Project (96MW) was launched in 1984 as part of DOE's clean coal technology program. Texaco gasifier derived from Texaco heavy oil gasification technology was used for syngas synthesis while a GE-7E gas turbine was selected in the combined cycle. (NETL, 2013)
1994	The first commercialized IGCC power plant in the world, Netherlands Buggenum Power Plant (253MW) began service. A Single dry coal feed Shell gasifier SCGP unit was used in this project. (Miller, 2005)
1996	Polk Tampa Power station (250MW) achieved operation. This station firstly integrated ASU and gas turbine by injecting nitrogen generated from ASU to gas turbine for the aim of NOx control.(NETL, 2013)
1998	One of the largest commercial IGCC projects started operation in Puertollano, Spain with net capacity of 330MW. (Higman and van der Burgt, 2008a)
2012	Huaneng GreenGen started up successfully in Tianjin, China. With three phases of schedule, 650 MW of net power will make it the world's largest IGCC project and also the first plant explicitly built for carbon capture and storage. (NETL, 2013)

## **2.2 Description of An IGCC Process**

### **2.2.1 Introduction of the whole process**

IGCC is a complicated system consists of several sub-systems, which make its construction and operation more difficult than the traditional pulverized coal power plants. Figure 2.1 shows a Schematic of an IGCC power plant using coal slurry-feed Texaco gasifier with water quench. Pure oxygen generated by ASU is used as the oxidant for the gasification process. In this process, coal is pulverized into particles with diameter of less than 0.1mm (Siva Ariyapadi, 2008) by coal handling and preparation system. Then the pulverized coal is mixed with water to form coal water slurry and then injected into the gasifier and react with oxygen. The high temperature (1250~1600°C), and high pressure (over 40 bar) reaction environment can easily generate synthesis gas rich in hydrogen and carbon monoxide with high sensible heat, meanwhile the ash contents in the coal will form liquid phase slag of low viscosity and be removed from the gasifier (Higman and van der Burgt, 2008d).

The synthesis gas is firstly cooled in the quench water and releases part of the sensible heat. After cooling process, the raw syngas will pass the water gas shift reactor. The catalyst-supported water gas shift reaction will convert the carbon monoxide contents in the syngas into hydrogen and carbon dioxide, which enhances the syngas heat value and the partial pressure of carbon dioxide. The high carbon dioxide content condition is favoured by the pressure-swing adsorption of CO<sub>2</sub> in the carbon capture unit.

The other impurities in the syngas such as particles sulphur and mercury will be further removed in the syngas clean-up process. The sweet syngas will then be further compressed and heated and injected into the gas turbine, the combustion of syngas in the combustion chamber will release flue gas and drive the turbines for power generation. The nitrogen flow

generated by ASU will be used as diluents for the fuel gas combustion to control NO<sub>x</sub> emission (Wang et al., 2015) since the mixing of nitrogen and syngas can decrease the combustion chamber temperature. The degree of ASU and gas turbine integration is often discussed in this process. 100% of integration means that there is no independent compressor in the ASU and all of the air input to ASU is compressed by gas turbine compressors. The higher degree of integration will result in electrical efficiency and less construction cost. However, independent ASU will improve the maximum power output and improve the flexibility by shortening the start-up time and avoiding the shock combustion in the gas turbine. (Xu et al., 2012).

The flue gas exiting the gas turbine will be directed to heat recovery steam generator; the sensible heat in the flue gas will be recovered to generate steam to drive steam turbine and electrical generator for additional electricity generation. Hence the net efficiency is improved by the combined cycle, which makes IGCC economically competitive with traditional PC power plants. The submodules modelled in this thesis include gasifier with quench, shift reactor with heat recovery, sulphur removal unit, gas turbine, heat recovery steam generator, electrical generator and carbon capture unit.

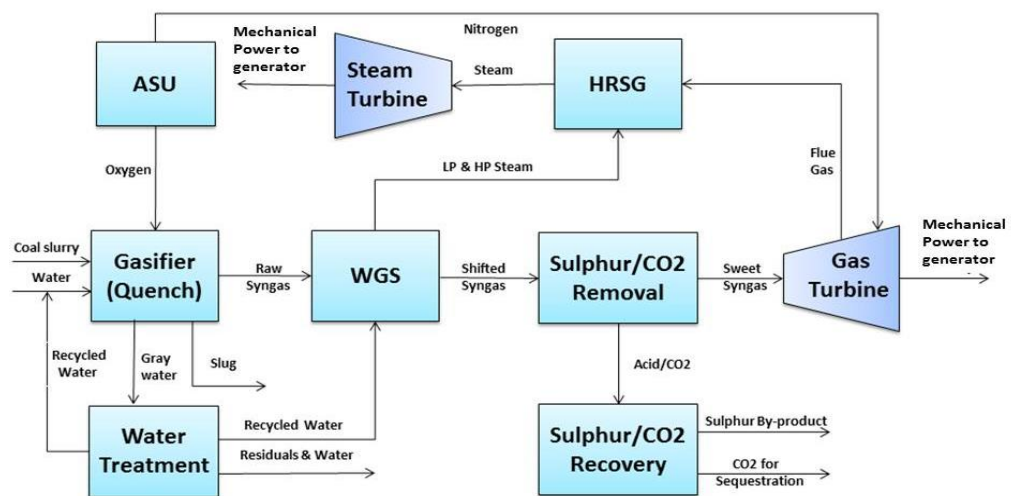


Figure 2.1.Simplified Schematics diagram of an IGCC system

### 2.2.2 Introduction of Gasifier

Among all the sub-systems of an IGCC process, the most important and complicated one is the gasifier, where complicated partial oxidation reactions will happen and convert coal to raw synthesis gas. Oxygen and steam are used as oxidant in this process. For example, the basic working process of a typical Texaco gasifier is: coal feed is injected into the gasifier through nozzles. The high temperature and high pressure within the furnace will make the moisture content evaporate rapidly and the pulverized coal particles will devolatilize and yield coal tar, gaseous hydrocarbons and oil. The gaseous components and volatiles will consume rapidly with steam and oxygen. The burning carbon char will react with oxygen, carbon dioxide, hydrogen while the reaction products will react with each other as well. The raw syngas generated by the gasifier is rich in  $H_2$  and CO and also includes  $CO_2$ ,  $CH_4$ ,  $N_2$ ,  $H_2O$ , particle and some sulphide such as COS,  $H_2S$  and  $SO_2$ . The wet syngas leaves the gasification zone with liquid slag and enters water quench zone where the slag will be cooled and deposited, then removed from the lock hopper (Higman and van der Burgt, 2003).

A number of different gasification technologies have been developed in the past 100 years (Higman and van der Burgt, 2003). Nowadays, over 90% (Higman and van der Burgt, 2003) of commercialised gasifiers running in the world are either directly provided or derived from four major commercial gasifier manufacture companies: Sasol-Lurgi Company, GE (originally developed by Texaco company), Shell Company and ConnocoPhillips E-gas (originally developed by Dow). The most widely accepted classification of gasifiers is based on the fluid regime of the coal feed inside. The classic gasification technologies include Moving-bed, Fluidized bed and Entrained-flow bed

(Rao and Rubin, 2002). Although all of the three types of gasifiers have their own pros and cons, they can all be utilized in IGCC power plants (Rao and Rubin, 2002). Currently, the most widely used technology in commercialized IGCC power plants is the entrained-flow gasifier. Some typical gasifier of these three technologies will be introduced and compared below:

#### **2.2.2.1 Moving Bed Gasifier**

Moving bed gasifier which is also known as fixed bed gasifier is the oldest gasification technology among the three types. Since 1882 the first Lurgi gasifier was launched in Germany (Higman and van der Burgt, 2003), this technology has been developed and improved continuously. A moving bed gasifier uses lump coal as raw material, which are located in a moving bed from the top of the refractory-lined vessel. The bed moves downward slowly and reacts with a blast of air or oxygen contents coming from the bottom of the gasifier vessel. This counter-flow arrangement leaves the coal continuously react with oxygen and the resident time for coal in the gasifier can be as long as 1 hour (Higman and van der Burgt, 2003). The gasification process in this type of gasifier is under moderate pressure (25~30bar) and temperature of 1250°C(Higman and van der Burgt, 2003). The synthesis gas temperature is generally low when the blast flow is wet air. This is caused by the high nitrogen content (over 50%) in the syngas. The Schematics of moving bed gasification process and temperature file from top to bottom are shown in Figure 2.2 below:

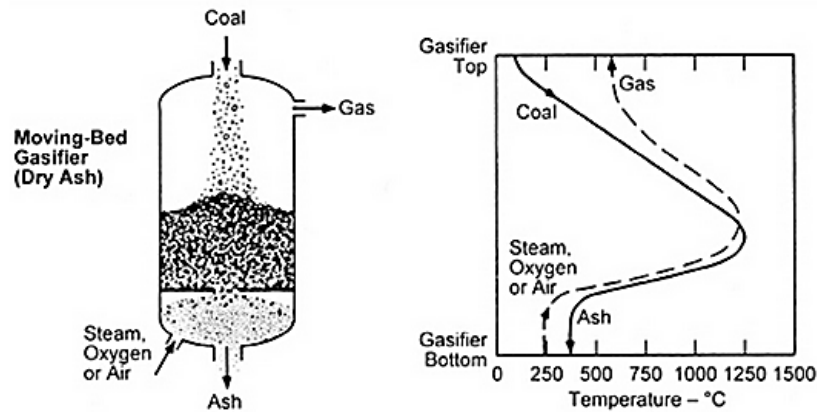


Figure 2.2 Simplified Schematics diagram and temperature profile in a moving bed gasifier (Higman and van der Burgt, 2008d)

One of the most widely used moving bed gasification technologies is the Sasol-Lurgi dry bottom process (Figure 2.3). The gasifier vessel is built with double refractory wall. The boiling water filling between these two walls can provide intensive cooling for the furnace while generating moderate pressure steam. From the top to the bottom, the gasifier can be geometrically divided into four zones: “dry zone”, “decarbonisation zone”, “gasification zone” and “combustion zone”. The coal feed from the top lock hopper will be distributed by the mechanic coal distributor; it will be heated and dried in the “drying zone” near the top area while cooling the upward moving syngas flow. Then the coal will be further heated and devitalized in the “decarbonisation zone” by the hot blast of syngas flow. In the “gasification zone”, the devitalized coal will react with upstream of oxygen,  $\text{CO}_2$  and steam and generate raw syngas. In the “combustion zone” where temperature reaches highest point, remaining char and residual oil will react with oxygen and burn. It needs to be emphasized that the “four zones” division is not strictly pure, the transition between these zones are gradual (Higman and van der Burgt, 2008d). A rotating grate is installed at the bottom of the gasifier to remove the ash from combustion zone. The high temperature ash can preheat the up-going blast of steam and



oxygen flow, and then it will be cooled down and removed through the ash lock. Since the temperature in the bottom area of the gasifier is lower than the ash fusion point, there won't be slagging occurring and the ash will be removed as dry ash (Rao and Rubin, 2002).

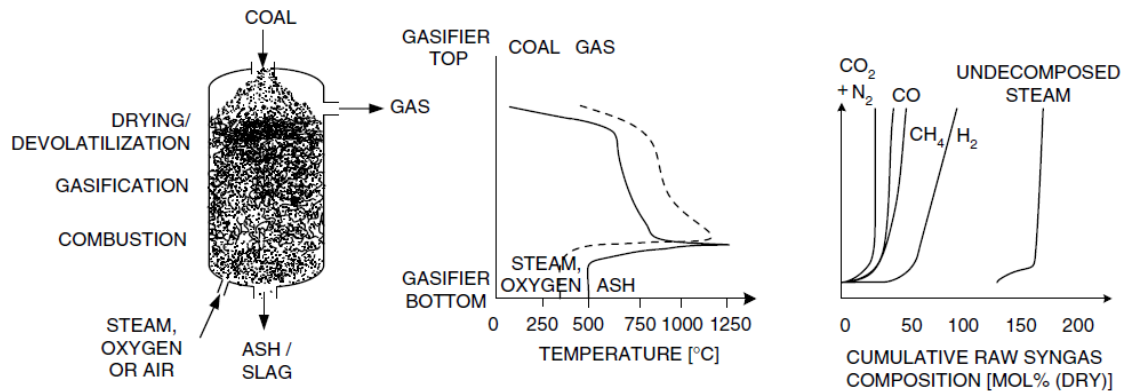


Figure 2.3 Schematics of Lurgi dry ash gasifier with temperature and gas composition files (Supp, 1990)

#### 2.2.2.2 Fluid Bed Gasifier

In a Fluid bed gasifier (Figure 2.4), the pulverized feedstock such as coal and biomass particles will be suspended in an oxygen-rich atmosphere, the solid particles act like fluid in this process. The fluidization and circulation of solid phase particles makes fluid bed gasifier a well-stirred reactor in which the old feedstock particle, partial-oxidized particles and complete-oxidized particles can be consistently mixed and react.

There are three regimes of fluid bed gasification process: bubbling fluid beds, circulating fluid beds (CFB) and transport reactors fluid bed (Higman and van der Burgt, 2008d). Feed stock particles will be introduced into the reactor and mixed with oxygen/steam mixed blast from the bottom of the gasifier, the synthesis gas usually exits from the top of the cyclone. Meanwhile, large particles will be captured by the cyclone and re-circulated to the reactor. The gasification reaction usually operated in moderately high temperature

which ensures the carbon conversion rate (90-95%) can satisfy the industrial command. It is important that the operation temperature of fluid bed gasifier should not exceed the ash fusion temperature, or the ash content of the feedstock will start to agglomerate and form large particles which might cause de-fluidization and other problems. On the other hand, the working temperature can't be too low since more tar will form if the coal particles are heated slowly. The typical working temperature for fluid bed gasifier is 950-1100°C for coal and 800-950°C for biomass (Higman and van der Burgt, 2003). A Schematics diagram and temperature profile for fluid bed gasifier is shown in Figure 2.4.

Fluid bed gasifier is favored for its capability of consuming low grade coal, even the coal gangue, waste and other materials which are hardly adoptable for moving bed and entrained-flow gasifiers can be cracked and consumed by fluid bed gasifier. The feedstock needs to be grounded to certain size, which should not exceed 10mm in case of defluidization. On the other hand, the lifting of too many fine particles in the hot syngas is not favoured since this may choke the whole system and shut down the gasifier.

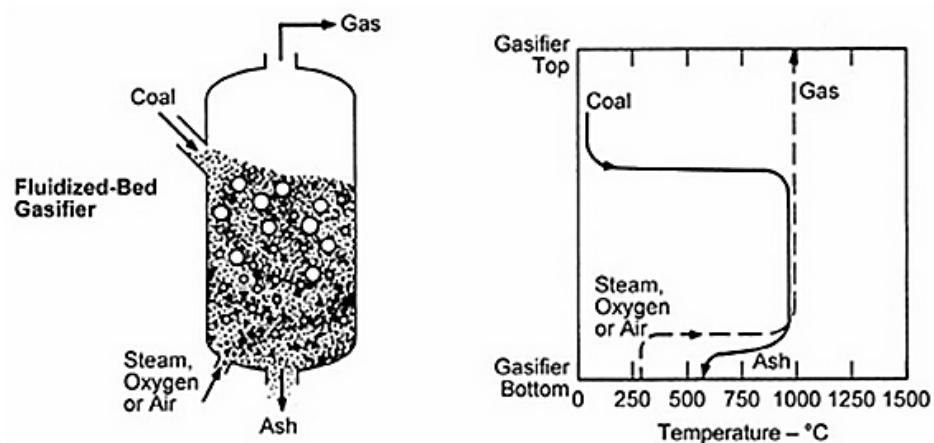
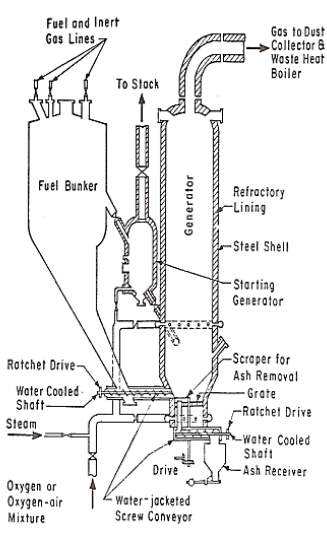
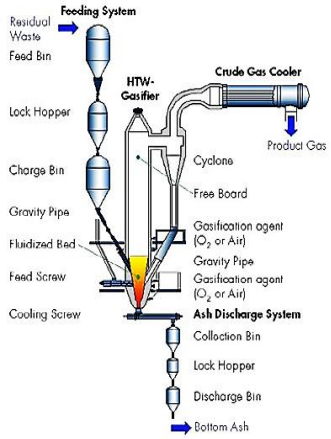
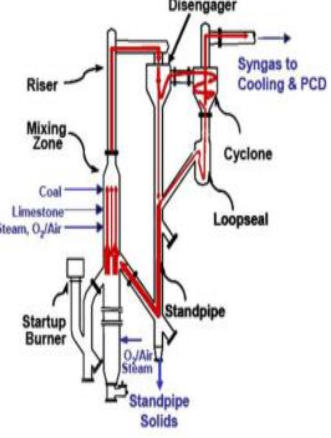


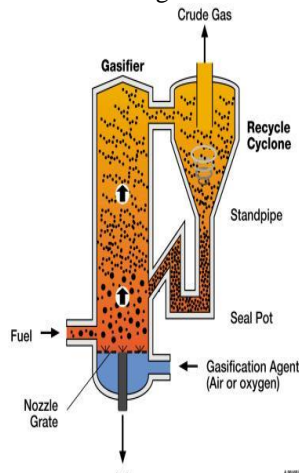
Figure 2.4 Simplified Schematics diagram and temperature profile of a fluid bed gasifier (Simbeck et al., 1993)

Some typical commercial fluid bed gasifiers are listed in Table 2.2 below. The historical evolution, working principles and main characteristics of these processes are shown and compared.

Table 2.2 Fluid bed gasification processes

PROCESSES	WORKING PRINCIPLES	CHARACTERISTICS
<p>Winkler process</p> <ul style="list-style-type: none"> <li>Patented in 1922, first plant built in 1925, 70 reactors have been built in history (Higman and van der Burgt, 2003)</li> <li>Schematics figure</li> </ul>  <p>Figure 2.5 Winkler process</p>	<ul style="list-style-type: none"> <li>Screw conveyor carries coal feedstock</li> <li>Oxygen/air blast enter gasifier via the conical gate at the bottom of gasifier.</li> <li>Refractory lined furnace.</li> <li>Incorporated with partly radiant waste heat recovery boiler and cyclone</li> <li>Unreacted carbon can be burned in the boiler and ash is removed by cyclone and water wash.</li> </ul>	<ul style="list-style-type: none"> <li>Commercial plants consume brown coal, coke, sub-bituminous and bituminous coal.</li> <li>Operation temperature: 950-1050 °C (Higman and van der Burgt, 2003)</li> <li>Operation at atmospheric pressure (Breault, 2010)</li> <li>Gasifier carbon conversion rate less than 80% since over 20% carbon remains in the ash is transported by the hot syngas</li> </ul>
<p>High Temperature Winkler (HTW)</p> <ul style="list-style-type: none"> <li>Developed in 1970s by Rheinbraun (RWE)</li> <li>Schematics figure</li> </ul>	<ul style="list-style-type: none"> <li>Fine grinded coal feed is first stored in feed bin then pressurized in a lockhopper. The pressurized coal is stored in charge bin and then fed to the reactor by a continuously screwing feeder. Alternatively, the coal feed can also be fed directly into the reactor via gravity pipe by air.</li> <li>Oxygen/air/steam blast is injected into the reactor</li> </ul>	<ul style="list-style-type: none"> <li>Originally developed for lignite gasification based on Winkler process, aiming to improve the carbon conversion rate.</li> <li>Capable of gasifying wide variety of coal feedstock and biomass.</li> <li>Operation temperature 840-</li> </ul>

 <p>Figure 1: HT Winkler gasifier system (source: Uhde)</p> <p>Figure 2.6 HT Winkler gasifier (NETL, 2013)</p>	<p>through the bottom of the gasifier. The fluidized coal, semi-coke and ash particles react with the blast in the gasification zone.</p> <ul style="list-style-type: none"> <li>Hot raw syngas exits the reactor from the top and cooled by syngas cooler. Fine ash particles and unreacted coal, coke and char are removed and returned to the reactor by cyclone, which can improve the carbon conversion rate.</li> <li>Ash is cooled in cyclone and returned to gasifier to maximize carbon conversion.</li> </ul>	<p>1100°C</p> <ul style="list-style-type: none"> <li>Operation pressure 25-30 bar.</li> </ul>
<p><b>KBR Transport</b></p> <ul style="list-style-type: none"> <li>Developed by KBR and Southern Company and U.S Department of Energy.</li> <li>Design is developed from the technology for gasoline refinery in 1940s.</li> <li>Schematics figure</li> </ul>  <p>Figure 2.7 KBR Transport (NETL, 2013)</p>	<ul style="list-style-type: none"> <li>Separate lock hopper convey the feedstock, sorbent (limestone for sulfur removal) to the mixing zone of gasifier</li> <li>Fuel, sorbent, oxidant, recycled particles from standpipe are mixed in the mixing zone for gasification. Gas is entrained to riser before entering the disengager.</li> <li>Large particles are removed in the disengager by gravity. Hot syngas exits the disengager to the cycle and will pass the syngas coolers. Remaining particles will be removed by the cyclone and recycled to the gasifier through looseal and standpipe.</li> </ul>	<ul style="list-style-type: none"> <li>Higher gas velocity over the traditional fluid bed gasifiers. Riser velocity reaches 11-18m/s (Smith, 2002).</li> <li>Gasifier internal operation temperature 815-1065 °C (Siva Ariyapadi, 2008).</li> <li>Pressure between 11 and 18 bar.</li> <li>Average carbon conversion rate 95%, up to 98% conversion rate is achieved. (Higman and van der Burgt, 2003)</li> <li>Oxidant blast can be oxygen or air.</li> </ul>
<p><b>CFB PROCESSES</b></p> <ul style="list-style-type: none"> <li>Two main manufacturers of CFB gasifiers: Envirotherm and Foster Wheeler.</li> </ul>	<ul style="list-style-type: none"> <li>Grinded fuel is transported through the inlet located in the low part of the reactor and entrained by the oxidant agent coming through the nozzle gate.</li> <li>Large particles will be</li> </ul>	<ul style="list-style-type: none"> <li>Large particles are recycled continuously until the size is small enough for gasification. The particle size is not important concern for gasification process.</li> </ul>

<ul style="list-style-type: none"> <li>• Envirotherm gasifier technology is derived by Lurgi company for alumina calcination</li> <li>• Schematics figure</li> </ul>  <p>Figure 2.8 Lurgi CFB gasifier (V.Krigmont, 1999)</p>	<p>recycled by the internal cyclone for further gasification even they are entrained along with the hot raw syngas.</p> <ul style="list-style-type: none"> <li>• A standpipe and seal pot is used for recirculate the particles removed by cyclone.</li> </ul>	<ul style="list-style-type: none"> <li>• High gas velocity of 5-8 m/s [(Higman and van der Burgt, 2003)]</li> <li>• CFB gasifier offers better material mixing which enhance the mass and heat transfer during the gasification process. Meanwhile, it offers wide flexibility for feedstock, especially for biomass and waste.</li> </ul>
--	--	--

The fluid bed gasifier utilize the fluidilization of solid particles for gasification, the fluidilization enhances the mass and heat transfer between particles and oxidants, the recirculation of unreacted particles can also improve the overall reaction. Adding adsorbent such as limestone in the feedstock can significantly reduce the acid gas emission which is enciroment-friendly and economicly efficient. Moreover, fluid bed is ideal for the gasification of special application such as biomass and waste. But the gasification process is limited by relatively low temperature and pressure, the carbon conversion rate of fluid bed is low compared with entrained flow gasifier. Thus fluid bed gasifier is not usually chosen for power generation process such as IGCC.

### 2.2.2.3 Entrained-flow Gasifier

The entrained-flow gasifier can practically utilize all grades of coal as feedstock. The feedstock is transported to gasifier either as liquid phase coal slurry which mixed by fine coal particles and water or high-density fluidilized dry coal particles. The coal feed ususally enters

the furnace with oxidant stream co-currently. Although air and oxygen blast can both satisfy the oxidant supply for gasification process, oxygen flow is more favoured to achieve better carbon conversion rate and higher syngas quality. With the high temperature and pressure working condition, the entrained-flow gasifier can produce high quality tar-free syngas in the existing three gasification processes with the high carbon conversion rate of over 99%. The operation temperature of entrain-flow gasifier is above the ash melting temperature, which causes the slag agglomeration. Moreover, the sensible heat in the raw syngas is high due to the high operation temperature, which leaves the gasifier with relatively low cold gas efficiency (CGE). To utilize the sensible heat, radiant syngas cooling systems are usually adopted to heat feed water or generate saturated steam.

The commercialisation of entrained-flow gasifier started from 1950s. Being one of the most successful coal gasification processes, entrained-flow gasifiers are favoured for large scale power generation and poly-generation industries. The first IGCC demonstration power plant in the world (coolwater) adopted GE (originally Texaco) gasifier for syngas production. A typical top-fired slagging entrained-flow gasifier and its temperature file is shown in Figure 2.9 :

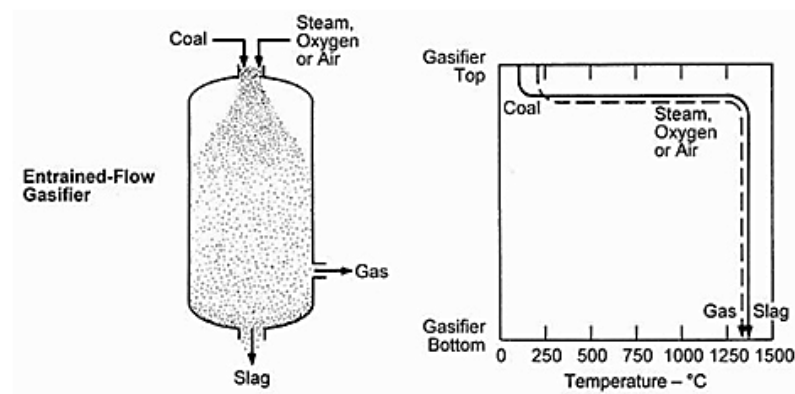
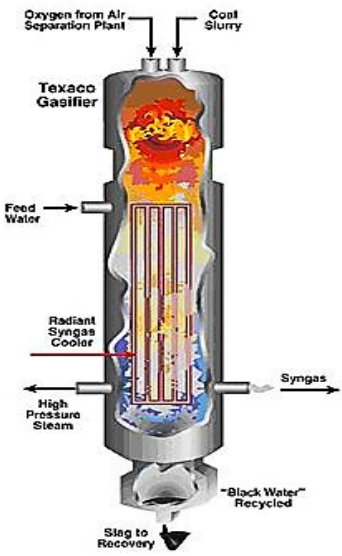


Figure 2.9 A top-fired entrained-flow gasifier and its temperature profile (Breault, 2010).

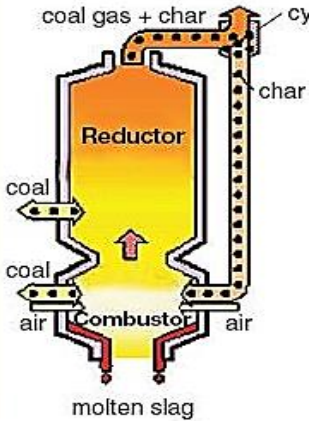
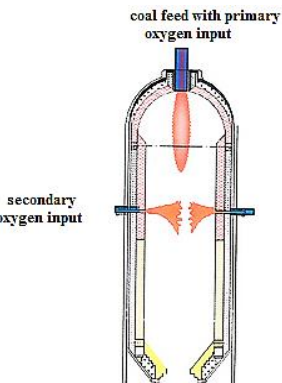
As one of the best commercialized coal gasification processes, entrained-flow gasifier has a big family. The historical evolution, working principle and characteristics of typical entrained-flow gasifiers are listed in Table 2.3

Table 2.3 Entrained-flow gasification processes

PROCESSES	WORKING PRINCIPLES	CHARACTERISTICS
<p>GE Energy process</p> <ul style="list-style-type: none"> <li>Originally is known as Texaco gasifier which was developed by Texaco company for heavy oil gasification.</li> <li>One of the most widely used gasification technology in the world.</li> <li>Schematics figure of a GEE gasifier with syngas cooler configuration.</li> </ul>  <p>Figure 2.10 GE gasifier (NETL, 2013)</p>	<ul style="list-style-type: none"> <li>Pulverized coal particles are mixed with water to form coal slurry. Slurry is pumped into the burner along with oxygen through the burner located on the top of the gasifier.</li> <li>Raw syngas (mainly formed of hydrogen and carbon monoxide) leaves the gasifier through the water quench while the slag is quenched in the water pool and removed by the lock hopper.</li> <li>The raw syngas can also be cooled by radiant and convection cooler and generate high pressure steam for heat recovery steam generator.</li> <li>The black water is processed in flash tanks and form gray water for coal slurry preparation.</li> </ul>	<ul style="list-style-type: none"> <li>Coal slurry is used as coal feed and oxygen (purity&gt;95%) blast as oxidant.</li> <li>Operation pressure &gt; 30bar (vary in power generation and chemical applications), temperature 1200~1480°C.</li> <li>Refractory bricks is used for inner lining but needs regular maintenance.</li> <li>GEE gasifier usually uses total water quench for syngas cooling. Quench syngas temperature is between 200 ~300°C.</li> <li>Waterfall syngas cooler configuration can be used for heat recovery. In this design the radiant cooler and convection cooler can utilize the syngas sensible heat to heat HP steam(up to 115bar)(Higman and van der Burgt, 2003)</li> </ul>
<p>Shell SCGP process</p> <ul style="list-style-type: none"> <li>Derived from the residual oil gasification process of Shell in 1950s.</li> <li>Shell coal gasification process</li> </ul>	<ul style="list-style-type: none"> <li>The transport gas (syngas, CO<sub>2</sub> or nitrogen) carries the fine pulverized dry coal into the gasifier through the burners located at the bottom of the furnace.</li> </ul>	<ul style="list-style-type: none"> <li>Coal is pulverized to particles with diameter less than 90 μm.</li> <li>Fast reaction speed, the residence time of coal particles in the vessel is</li> </ul>

<p>(SCGP) was developed in 1970s from demonstration and was adopted in the Buggenum IGCC power plant at Netherland in 1987.</p> <ul style="list-style-type: none"> <li>• Schematics figure of SCGP.</li> </ul> <div data-bbox="343 421 667 846" data-label="Image"> </div> <p>Figure 2.11 Shell gasifier (Sun et al., 2011, Breault, 2010)</p>	<ul style="list-style-type: none"> <li>• Pure oxygen (purity&gt;95%) and steam are mixed and injected into the furnace as oxidant.</li> <li>• The extreemly exothermal gasification reaction can release huge amount of sensible heat. There are water wall formed by tube bundle located in the refractory-lined vessel. The water wall circulates water to the reactor and generate high pressure superheated steam by utilizing the sensible heat.</li> <li>• Liquid slag flows along the water tube and is cooled to form solid slag layer, which can protect the tube and refractory wall from being burned and corroded. The liquid slag leaving the reactor is solidied by water bath and removed by the lock hopper.</li> <li>• Filter and cylone removes the particles contained in the raw hot syngas.</li> <li>• The hot syngas passes the water bath and enters the syngas cooler to generate further superheated steam.</li> </ul>	<p>only 0.5~4 s.</p> <ul style="list-style-type: none"> <li>• Typical operation temperature 1500°C and pressure between 30 and 40 bar.</li> <li>• High carbon conversion rate can be up to 99%.</li> <li>• Hot syngas leaves the water bath at the temperature of 900 °C.</li> </ul>
<p>MHI process</p> <ul style="list-style-type: none"> <li>• Developed by Mitsubishi Heavy Industries (MHI) in 1980s.</li> <li>• Achived commecial running in the 1700 tpd, 250MW IGCC power plant at Nakoso in 2004.</li> <li>• Unique two-stage reactor design for efficiency maximization</li> <li>• Schematics figure</li> </ul>	<ul style="list-style-type: none"> <li>• Reactor has been divided into two sections, high temperature combustor located in lower part and low temperature reductor located in higher part.</li> <li>• Pulverized dry coal is fed into both sections separately. The portion fed into the combustor section is injected along with air supply and generate carbon dioxide, carbon monoxide and water vapor. Operation temperature in this section is higher than ash soften point and the slag will be quenched in the water bath and removed by the lock hopper located in the bottom.</li> <li>• Gas produced in combustor section rises to the reductor section where the other portion of coal feed is added with out air blast. Further endothermic gasificaiton reactions will happen in this section.</li> </ul>	<ul style="list-style-type: none"> <li>• Wide flexibility for coal.</li> <li>• High temperature in combustor section, up to 1800°C.</li> <li>• Operation temperature decrease from combusotor to recutor section. The hot syngas leaves the gasifier at temperature of 1100°C.</li> </ul>



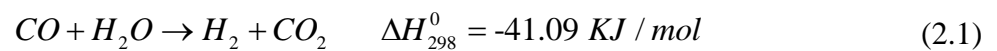
 <p>Figure 2.12 MHI gasifier (NETL, 2013)</p>	<ul style="list-style-type: none"> <li>• The reductor temperature is lower than ash soften temperature thus the molten ash can be solidified.</li> <li>• Hot syngas leaves from the top of gasifier.</li> <li>• Filter and cyclone remove the char and unburned coal back to the gasifier.</li> </ul>	
<p>Tsinghua Process</p> <ul style="list-style-type: none"> <li>• Developed by Tsinghua Univeristy from 1990s.</li> <li>• First two-stage, entrained flow gasifier achieved commercial running in 2003.</li> <li>• Second generation with coal slurry feed and water wall cooling technologies was put in operation in 2011.</li> <li>• Schematics figure</li> </ul>  <p>Figure 2.13 Tsinghua staged oxygen process (NETL, 2013, Yang et al., 2011)</p>	<ul style="list-style-type: none"> <li>• Five stages of coal gasification processes with staged oxygen supply.</li> <li>• First stage: coal slurry feed injection from the top of gasifier, moisture removal and volatile matter release.</li> <li>• Second stage: combustion</li> <li>• Third stage: gasification</li> <li>• Fourth stage: re-burning</li> <li>• Fifth stage: re-gasification.</li> <li>• Staged oxygen supply decrease the top burner temperature wich extend the burner lifetime.</li> </ul>	<ul style="list-style-type: none"> <li>• Wide flexibility for coal feed stock, even coal with high ash content, high ash soften point.</li> <li>• Operation temperature up to 1500°C.</li> <li>• Operation pressure range from 35 bar to 65 bar.</li> </ul>

Entrained-flow gasifier is the primary choice for IGCC power plants, no matter it is in the demo stage or commercialized stage. The modelling of entrained-flow gasifier is the main focus in this thesis, which will be described in Chapter 3.

### 2.2.3 Water Gas Shift Reactor

After quench and further cooling and further cleaning up, the main contents in the raw syngas generated by the gasifier include carbon monoxide, hydrogen, carbon dioxide, methane and some other impurities. In IGCC process with carbon capture unit, it is necessary to eliminate the carbon monoxide and increase hydrogen content in the syngas, which can be achieved by using water gas shift reactor.

Water gas shift (WGS) reaction is exothermic and limited by chemical equilibrium. The reversible reaction is shown as follow:



In an industry process, the performance of the shift reactor relies on efficient catalyst and precisely controlled working conditions. The industrialization of shift reaction came with the development of ammonia synthesis. The iron and chromium based catalyst developed by Bosch and Wilde in 1912 (Smith et al., 2010) works efficiently in the temperature range of 400 to 500 °C and capable of reducing the carbon monoxide content to 2% (Smith et al., 2010).

There are three types of shift reactions which are classified by reaction temperature range:

- High temperature (HT) shift reaction with the temperature range of 300~450°C, carbon monoxide content can drop down to approximate 2.5% in the dry shifted syngas outlet.
- Medium temperature (MT) shift reaction with the temperature range of 220~270°C, carbon monoxide content can drop down to approximate 0.5% in the dry shifted syngas outlet.

- Low temperature (LT) shift reaction with the temperature range of 180 to 250°C, carbon monoxide content can drop to approximate 0.2% in the dry shifted syngas output.

The three types of shift reactions temperature ranges and capability of eliminating the carbon monoxide content in syngas are shown in Figure 2.14 .

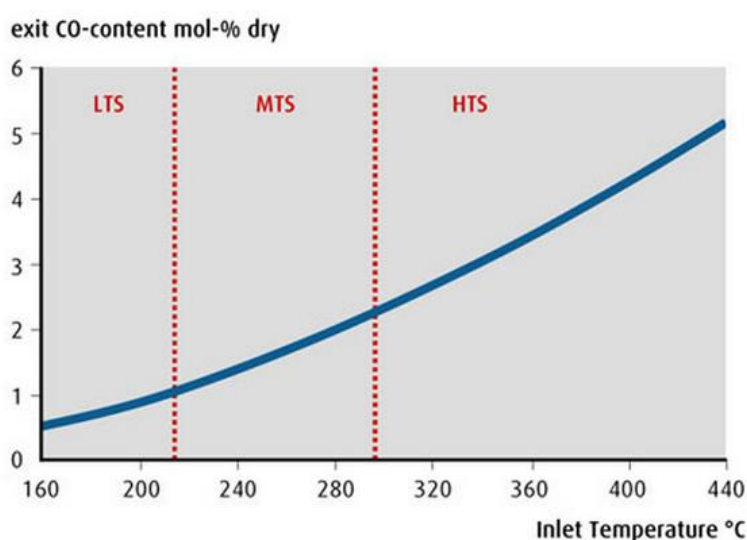


Figure 2.14 Three types of water gas shift reactions (LindeGroup.Ltd, 2015)

In this thesis, the LT and HT shift reactors are both adopted. The shift reactor model built in this project will be used to analyze the content change in the syngas as well as the energy conversion caused by this process. The WGS unit is also used to generate HP and LP steam for the heat recovery steam generator.

#### 2.2.4 Acid Gas Removal (AGR)

The acid gas contents in shifted syngas include hydrogen sulfide ( $H_2S$ ), carbonyl sulfide (COS) and carbon dioxide ( $CO_2$ ). In this project, carbon dioxide will be removed by activated carbon via pressure swing adsorption (PSA) process, thus the acid gas removal unit mainly focuses on the removal of hydrogen sulfide and carbonyl sulfide.

Many technologies have been developed for acid gas removal in the industrial process. The conventional process such as Rectisol and Selexol normally consist of absorber cloumn with regenerative solvent, sulfur reveory unit and tail gas treating tower. Different solvents can be used for AGR, chemical solvents such as amine-based ethanolamine (MEA) and Methyl diethanolamine (MDEA), physical solvents such as dimethyl ethers of polyetheylene glycol for Selexol process, methanol for Rectisol process and sulfinol used in the hybrid or composiute process. Some examples are shown in the Figure 2.15 below:

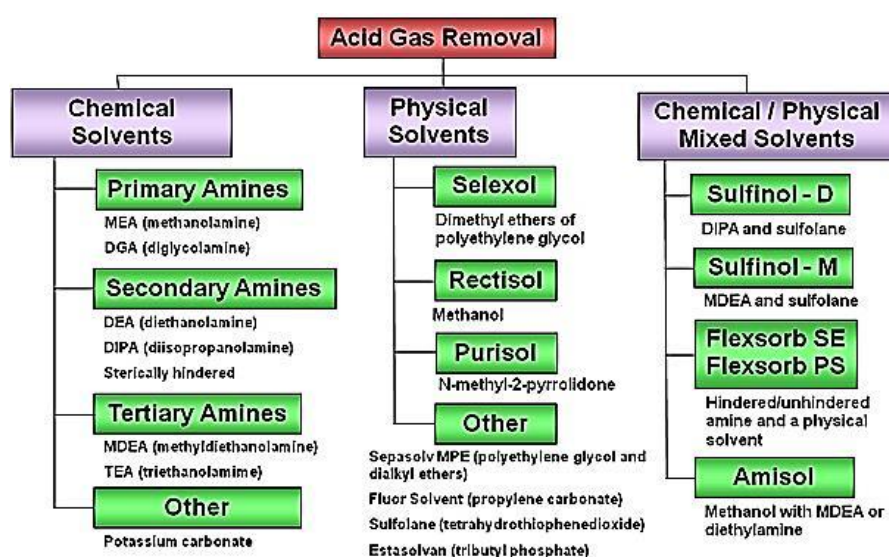


Figure 2.15 AGR technologies classification (NETL, 2013)

The captured sulfide is usually recovered as the form of solid sulfur. One of the well known sulfur recovery technology is the Claus Process. Elemental sulfur will be recovered from H<sub>2</sub>S by combustion with air or oxygen. The tailgas of Claus process usually contain H<sub>2</sub>S and SO<sub>2</sub>, small amount of COS may also exist. The tail gas treatment can remove the remaining sulfide from the syngas via hydrogenation and hydrolysis process. There are many alternatives have been commercialized for sulfur removal and recovery process, Figure 2.16 shows two typical tail gas treatment process Schematics (Gasification, 2005):

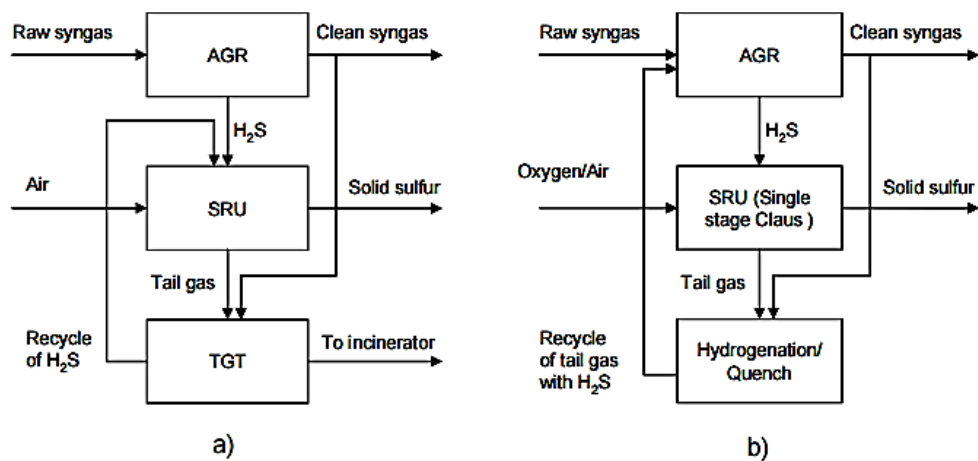


Figure 2.16 a) Tail gas treatment dedicated for H<sub>2</sub>S removal b) Tail gas treatment integrated with upstream AGR process

### 2.2.5 Gas Turbine and Combined Cycle

In IGCC process, sweet syngas will be compressed and injected into gas turbine with air/oxygen and diluent then burn in the combustion chamber to generate electricity. Due to the high hydrogen content in the sweet syngas, modification need to be made for the conventional gas turbine. The remaining heat in the exhaust gas will be utilized by heat recovery steam generator for further electricity generation. The combined cycle used in IGCC process is derived from the proven natural gas combined cycle power generation technology.

The integration of HRSG with upstream systems needs careful tuning and precise control. The hot flue gas of the gas turbine will transfer heat to HRSG to generate superheated HP steam as well as reheat IP steam and LP steam. The HRSG will also generate HP and LP steam from syngas cooling system and WGS unit. Combined cycle is an advanced commercialized technology for power generation. A simplified Schematics of the combined cycle is shown in Figure 2.17:

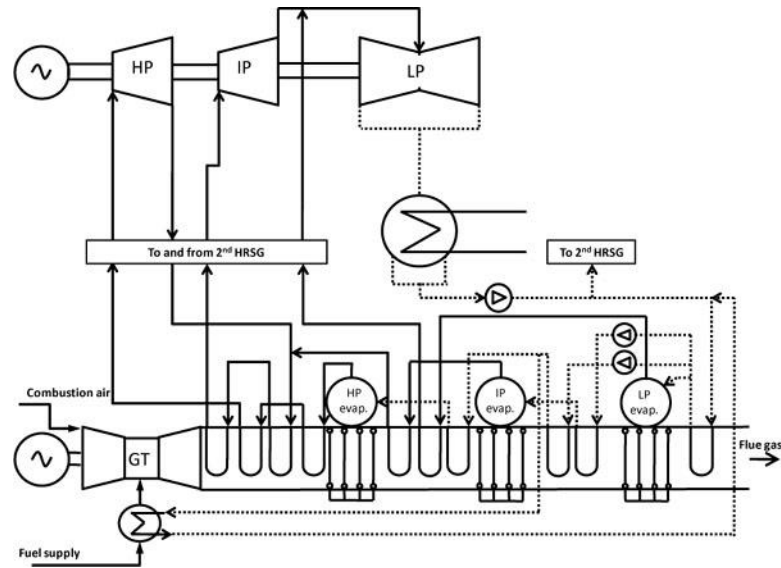


Figure 2.17 Schematics of combined cycle in IGCC process (IEA, 2011)

### 2.2.6 Air Separation Unit

Air separation unit is only used in the IGCC process which adopted oxygen blast entrained flow gasifier. The oxygen generated by ASU is injected into the gasifier for gasification process as oxidant. Meanwhile, the nitrogen can be used as diluent in the gas turbine for low NO<sub>x</sub> emission.

The commercial air separation technology is based on Linde cycle for cryogenic air liquefaction and distillation at low temperature (approximate  $-184^{\circ}\text{C}$ ) (Yue Wang, 2013). Compressed air is cooled to a cryogenic temperature by heat exchange with product gases. The liquefied air is fed to the distillation column which is composed of many stages. The air liquid is heated and distilled to produce oxygen and nitrogen.

Air separation process is highly energy consuming, especially for air compression work. Normally the air is compressed to approximate 5 bar and fed into the ASU unit. The product oxygen and nitrogen are available at approximate 1 bar (Yue Wang, 2013). A typical air separation unit is shown in Figure 2.18:

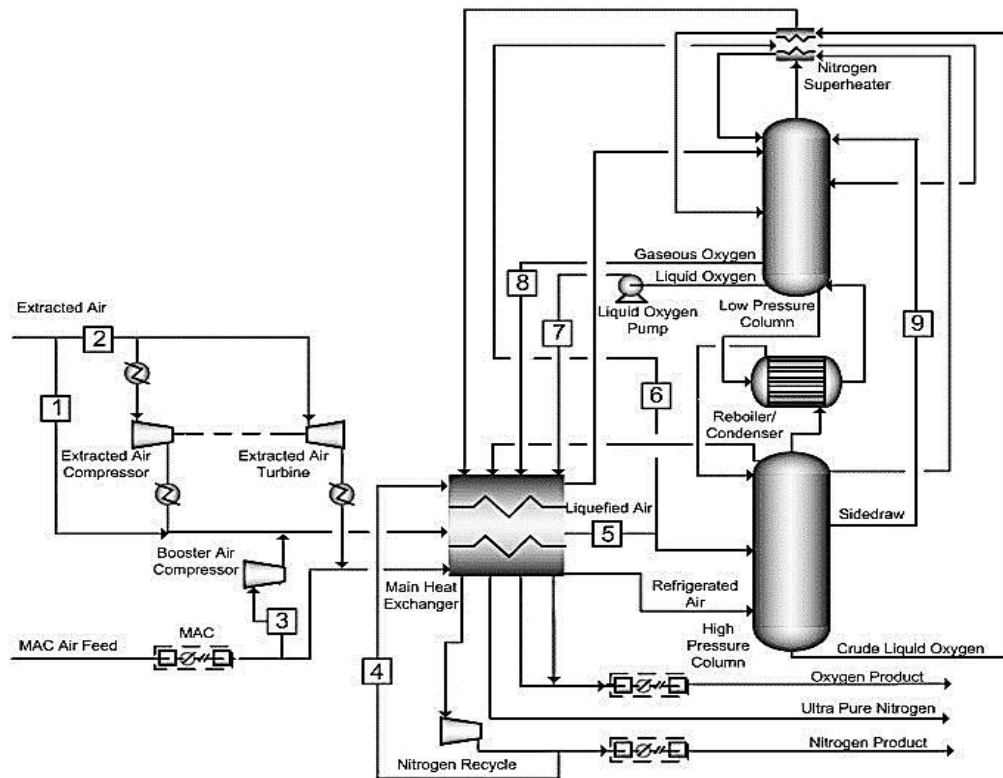


Figure 2.18 Schematics of typical air separation unit (Jones et al., 2011)

## 2.3 Summary

In this chapter, the development history of IGCC process is reviewed. IGCC process is a complex system composed of different subsystems. The three different types of gasification technologies are listed and compared, including some examples of commercial gasifiers of each regime. The auxiliary subsystems for syngas cooling and cleaning, acid gas removal, power generation and air separation unit are briefly introduced as well. This chapter is aiming to show the whole picture of IGCC process by introducing the main subsystems. The whole process model is established by the integration of well developed and validated sub-modules: Gasifier with quench, shift reactor with heat recovery, acid gas removal unit, gas turbine, heat recovery steam generator, electrical generator and carbon capture unit, the simulated IGCC block diagram is shown in Figure 2.19.

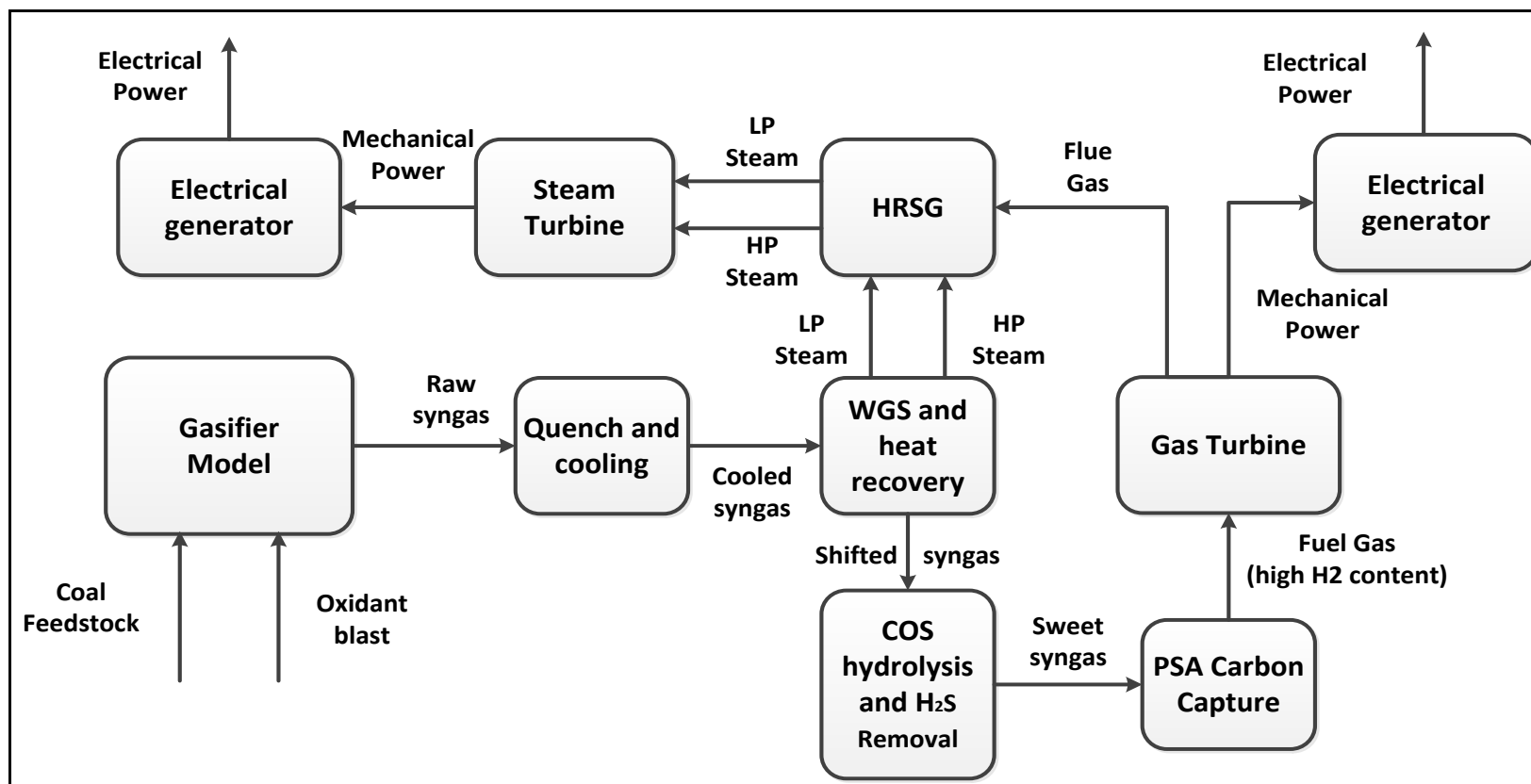


Figure 2.19 Schematics of IGCC process simulated in this thesis



## **Chapter 3 Zero-dimension Mathematical Model of Gasification Process Based on Texaco Gasifier**

This chapter focuses on the mathematic modelling of a gasification process. It starts with the fundamental theory of thermodynamics and kinetics of coal gasification. Then the development of zero dimension syngas prediction model based on the structure of Texaco gasifier is described in detail, this model is built on the principle of achieving mass balance, chemical equilibriums and energy balance. This syngas prediction model can calculate the mole concentration of the contents  $H_2$ ,  $CO$ ,  $CO_2$ ,  $CH_4$ ,  $COS$ ,  $H_2S$ ,  $N_2$ ,  $H_2O$  and  $Ar$ . With the model, for the working condition with pre-defined input and operation pressure and temperature, the raw syngas amount, heating value, sensible enthalpy can be calculated as well. Four different types of coal are chosen for model simulation. The simulation results are compared with the reference data (Azuhata et al., 1986). The changes in the key parameters of gasifier operation such as oxygen/coal ratio, water/coal ratio, operation temperature, operation pressure are modelled for different working conditions of Texaco gasifier. The changes of syngas contents are shown and analyzed. With the parameters analysis, the working principle of Texaco gasifier is clearly understood, and valuable information is gained for achieving the best operation for Texaco gasifier. To learn the applicability of this model for other commercial gasifiers, the model is used to simulate a Shell gasifier using EI Cerrejon coal and the results are compared with the data from industry.

### **3.1 Description of Texaco Gasifier Process**

Texaco gasification technology, also known as coal slurry gasification technology, is developed by Texaco Company, initially aiming for heavy oil gasification. Texaco gasifier

structure is shown in Figure 3.1. It uses coal slurry, which is mixed by pulverized coal particles and water, as raw material, and uses oxygen as gasification agent. The cylinder tube is a steel pressure vessel lined with inner refractory bricks wall inside. The gasifier can be divided into two sections: gasification and syngas cooling sections. The working principle and main operation characteristics of Texaco gasifier were introduced in Chapter 2.

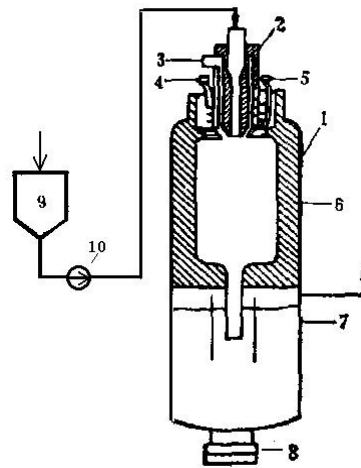


Figure 3.1 Structure of Texaco gasifier (Wang et al., 2015)

- 1-Gasifier 2-Nozzle 3-Oxygen input 4-Cooling water input 5- Cooling water output 6-Refractory bricks liner  
7-Quenching water input 8-Slag output 9-Coal slurry tank 10- Coal slurry pump

The working process is described below. Coal slurry is injected into the gasifier furnace through nozzles, the moisture content of coal slurry droplets will evaporate rapidly and the pulverized coal particles will devolatilize and yield char, tar and gaseous hydrocarbons. The gaseous components and volatiles will be consumed rapidly with steam and oxygen. The combustion of char will react with oxygen, carbon dioxide, hydrogen while the reaction products react with each other as well. The whole gasification process involves complex physical and chemical reactions (Slycke et al., 2015). The gasifier generates wet syngas composed by CO, CO<sub>2</sub>, H<sub>2</sub> and steam. Syngas leaves the gasification zone with slag and enters the water quench zone where the slag is deposited in the slag tank and removed by lock hopper. Raw syngas will be cooled and cleaned after quenching process. During the

whole pyrolysis and gasification process, the residence time of coal particle is less than 4 seconds (Schoen, 1993). Comparing with the large running time scale of gasifier which is usually set as  $10^3$ s (Schoen, 1993), it is reasonable to assume that the evaporation, pyrolysis and gasification reactions will finish as soon as the slurry is injected into the gasifier.

## **3.2 Mathematical Model of Texaco Gasifier**

### **3.2.1 Overview of the Texaco Gasifier Model Development**

The challenge of modelling the gasification process is to deal with the complexity of chemical reactions involved in it. Researchers in chemical engineering field have studied coal gasification processes and developed models based on the principle of mass and energy balances. Many experimental-based researches were reported to validate the models and study the methods for gasification optimization.(Vamvuka et al., 1995a, Ni and Williams, 1995, Watkinson et al., 1991, Azuhata et al., 1986, Buskies, 1996). The earliest report on modelling this process can be found in 1970s (Ubhayakar et al., 1977), in which one-dimensional model considered fluid mix in axial direction, coal pyrolytic cracking and devolatilization. Smoot and Brown (Brown et al., 1986) provided an approach to evaluate different chemical kinetics data and to estimate the input parameters, and this method has laid the foundation of many subsequent works. Wen and Chaung (Wen and Chaung, 1979) built a model of Texaco gasifier which divided the furnace into three zones to describe the processes from pyrolytic cracking to gasification. Mass balance and energy balance equations are built for each zone. Govind and Shah (Govind and Shah, 1984) introduced momentum conservation to the former work and calculate the temperature, concentration and fluid field in the axial direction. Brown and Smoot's (Brown et al., 1986) experiments reveal four different coal's characteristic in gasification process. Their study focuses on the influence of water/coal ratio, oxygen/coal ratio and coal particle dimension to carbon conversion rate. Ni

and William (Ni and Williams, 1995) reported a multi-variable model for Shell gasifier, in which 16 reactions are simulated using chemical kinetics data, and the gasifier was divided into the pyrolytic cracking zone and the volatile combustion zone.

Most of the models reported in the literatures are based on experimental data using a data driven approach, which limits the suitability of model as its working conditions are varying in a wide range. The model using CFD (Yang et al., 2011) software can well describe the temperature and fluid field inside the gasifier by giving boundary conditions. But for IGCC process, syngas contents and its state parameters are important for the overall process simulation and analysis. Thus a generic gasifier model is favoured in this project to give accurate prediction of the syngas contents based on specific working conditions. In this chapter, the development and validation of a zero dimension gasifier model is introduced.

### **3.2.2 Texaco Gasification Syngas Prediction Model Development**

A zero-dimension model developed is based on the principle of mass balance of the elements C, H, O, N, S and Ar; chemical equilibrium and energy balance. The model can calculate the mole concentration of syngas contents when 1kg of raw coal feed is injected into the gasifier with slurry water and oxygen blast under pre-defined working conditions. For the Texaco gasifier, the slurry water plays the role of steam blast as the slurry droplet will evaporate when it is injected into the gasifier, thus the slurry water flow is equalized to steam blast in the following simulation. The building of this model is rooted from the work of Watkinson and Lucas (Watkinson et al., 1991). The main assumptions are listed below:

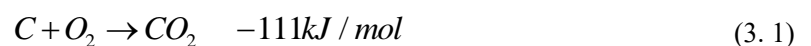
- 1) The flow in the gasifier furnace is simplified as uniformed laminar flow, and the differences of temperature, concentration, pressure and material exchanges in radial direction are not taken into consideration. Actually, laminar flow only exists in the

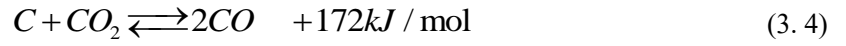
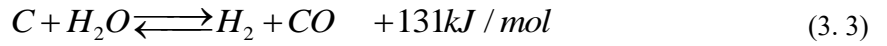
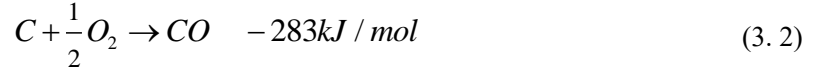
lower part of the gasifier, the flow between nozzles and lower part should be jet flow surrounded by a strong back flow zone. The eddy turbulent is not considered in the modelling process as the syngas content will not be affected by this flow type. Thus, it is acceptable for the global laminar assumption.

- 2) The preheating of slurry droplet, moisture evaporation and coal devolatilization will finish as soon as the coal slurry is injected into the gasifier. The nozzles are surrounded by high pressure high temperature gas flow.
- 3) The released volatile combustion and carbon pyrolytic and char combustion reactions reach chemical equilibrium as soon as the slurry enters the furnace. The chemical equilibrium constants of homogeneous reactions inside the gasifier are used to describe the reactions. This assumption is reasonable due to the high heating rate in entrained-flow gasifier.
- 4) Nitrogen and Argon are assumed to be steady and will not participate in any chemical reaction. It is assumed that all oxygen is consumed, and the carbon conversion is 99.5% in the entire gasifier (J.Eurlings, 1999a, Sun et al., 2011).
- 5) Generated raw syngas contains CO, CO<sub>2</sub>, H<sub>2</sub>, CH<sub>4</sub>, SO<sub>2</sub>, COS, H<sub>2</sub>S, Ar, N<sub>2</sub> and steam, the residue tar and fly ash are not considered in this syngas model.
- 6) The working condition is stable when the coal slurry and oxygen is injected into the gasifier, which means working temperature and pressure are stable in this syngas model.

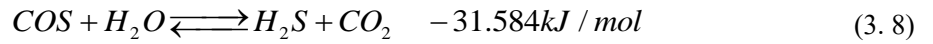
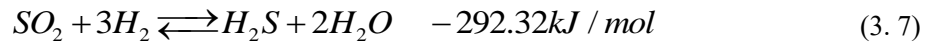
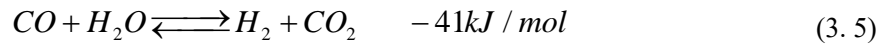
The chemical reactions involved in the simulation are listed and described as follows:

Char coal combustions (heterogeneous reactions)





Volatile combustions (homogeneous reactions)



Positive sign represents endothermic reactions and negative sign exothermic reaction.

Thus mass balance equations can be established based on the considered chemical reactions and assumptions. The equations based on elements balance are shown as follows; the parameters on the right side of equations can be calculated by coal feed input data, the parameters on the left side are syngas mole flow and syngas contents mole concentrations:

Carbon mass conservation equation:

$$N_g (X_{CO} + X_{CO_2} + X_{CH_4} + X_{COS}) = N_{C,0} A \quad (3.9)$$

where  $N_{C,0}$  stands for the known input carbon content mole flow rate in the coal feedstock.

Its value can be obtained by ultimate analysis and calculated by the equation below.  $A$  is the

pre-defined carbon conversion rate as 99.5% in assumption (4).  $N_g$  denotes the raw syngas mole flow rate while  $X$  is the mole concentration of syngas contents.

$$N_{C,0} = \frac{D_{drycoal} \cdot Y_C}{M(C)} \quad (3.10)$$

where  $D_{drycoal}$  is the mass flow of dry ash-free basis of coal feed,  $Y_C$  is the carbon mass concentration in the dry ash-free basis,  $M(C)$  is the molecular mass of carbon.

Oxygen mass conservations equation:

$$N_g (0.5X_{CO} + X_{CO_2} + X_{SO_2} + 0.5X_{COS} + 0.5X_{H_2O}) = N_{O_2,0} \quad (3.11)$$

where  $N_{O_2,0}$  is the equivalent input oxygen content mole flow rate. Its value can be obtained by combining the input oxygen blast multiplies pre-defined purity, oxygen content in slurry water, dry coal on a ash-free basis and moisture content carried by dry coal on a ash-free basis, which can be obtained by ultimate analysis. The value of  $N_{O_2,0}$  can be calculated by equation below:

$$N_{O_2,0} = \frac{D_{O_2} \cdot Z_{O_2} + D_{drycoal} \cdot Y_o + D_{coal,moisture,O} + D_{steamblast,O}}{M(O_2)} \quad (3.12)$$

where  $D_{O_2}$  denotes the input oxygen blast mass flow rate while  $Z_{O_2}$  is the pre-defined oxygen purity (94% mass),  $D_{drycoal}$  denotes the mass flow rate of dry ash-free basis of coal,  $Y_o$  is oxygen mass content in coal on a dry ash-free basis,  $D_{coal,moisture,O}$  is the mass flow of oxygen contained in the moisture content carried by coal on a dry ash-free basis,  $D_{steamblast,O}$  is the mass flow of oxygen contained in the steam blast.  $M(O_2)$  is the molecular mass of oxygen

Hydrogen mass conservation:

$$N_g (2X_{CH_4} + X_{H_2S} + X_{H_2} + X_{H_2O}) = N_{H_2,0} \quad (3.13)$$

where  $N_{H_2,0}$  denotes the equivalent input hydrogen mole flow. Its value can be obtained by summing the hydrogen contents in dry ash-free coal, coal feed moisture and steam blast. The value of  $N_{H_2,0}$  can be calculated by the equation below:

$$N_{H_2,0} = \frac{D_{drycoal} \cdot Y_H + D_{coal,moisture,H} + D_{steamblast,H}}{M(H_2)} \quad (3.14)$$

where  $Y_H$  is the hydrogen mass content in the dry ash-free basis of coal,  $D_{coal,moisture,H}$  is the mass flow of hydrogen contained in the moisture carried by coal on a dry ash-free basis.  $D_{steamblast,H}$  is the mass flow of hydrogen contained in the steam blast.  $M(H_2)$  is the molecular mass of hydrogen.

Nitrogen mass conservation equation:

$$N_g (X_{N_2}) = N_{N_2,0} \quad (3.15)$$

Nitrogen is assumed to be inert during the gasification process thus the nitrogen mass flow comes from the nitrogen carried by oxygen blast (the impurity of oxygen blast) and the nitrogen contained in dry ash-free basis of coal. In some dry coal feed gasifier such as Shell and GSP, the coal feed is carried by transport nitrogen, this part of nitrogen needs to be considered for such type of gasifier. The value of  $N_{N_2,0}$  is calculated by equation below:

$$N_{N_2,0} = \frac{D_{drycoal} \cdot Y_N + D_{oxygenblast,N}}{M(N_2)} \quad (3.16)$$

where  $Y_N$  denotes the nitrogen mass content in the dry ash-free basis of coal,  $D_{oxygenblast,N}$  denotes the nitrogen mass flow carried by oxygen blast.  $M(N_2)$  is the molecular mass of Nitrogen.



Sulphur mass conservation equation:

$$N_g (X_{SO_2} + X_{H_2S} + X_{COS}) = N_{S,0} \quad (3.17)$$

Sulphur only exists in the dry ash-free basis of coal, the sulphur content will influence the acid stream in the raw syngas, the value of  $N_{S,0}$  is calculated by equation below:

$$N_{S,0} = \frac{D_{drycoal} \cdot Y_S}{M(S)} \quad (3.18)$$

where  $Y_S$  denotes the sulphur mass content in the coal dry ash-free basis. Its value can be obtained from the coal ultimate analysis data.  $M(S)$  is the molecular mass of Sulphur.

Argon mass conservation equation:

$$N_g (X_{Ar}) = N_{Ar,0} \quad (3.19)$$

Argon is inert gas carried by the input oxygen blast (argon impurity in oxygen stream) and will not involve in any chemical reaction,  $N_{Ar,0}$  is calculated by equation (3. 20) below:

$$N_{Ar,0} = \frac{D_{oxygenblast,Ar}}{M(Ar)} \quad (3.20)$$

where  $D_{oxygenblast,Ar}$  is the mass flow of Argon carried by the oxygen blast, an argon/oxygen ratio will be defined and its value will be assigned based on reference data (J.Eurlings, 1999a) in the input parameters.  $M(Ar)$  is the molecular mass of Argon.

Based on Dalton's law (Watkinson et al., 1991), the sum of all the syngas contents mole concentration will equal to 1, thus we can have Equation (3. 21) below;

$$X_{CO} + X_{CO_2} + X_{CH_4} + X_{H_2} + X_{H_2O} + X_{H_2S} + X_{SO_2} + X_{COS} + X_{N_2} + X_{Ar} = 1 \quad (3.21)$$

Based on chemical equilibrium (Higman and van der Burgt, 2008c) of heterogeneous reactions (3. 5) to (3. 8) , four Equations (3. 22 ) to (3. 25) (Watkinson et al., 1991) can be derived respectively as below:

$$\frac{X_{H_2} X_{CO_2}}{X_{CO} X_{H_2O}} = 0.0265 e^{3956/T_g} \quad (3.22)$$

$$\frac{X_{CH_4} X_{H_2O}}{X_{CO} X_{H_2}^3 P^2} = 6.7125 \times 10^{-14} e^{27020/T_g} \quad (3.23)$$

$$\frac{X_{H_2S} X_{H_2O}^2}{X_{SO_2} X_{H_2}^3 P} = 4.3554 \times 10^{-4} e^{26281/T_g} \quad (3.24)$$

$$\frac{X_{H_2S} X_{CO_2}}{X_{COS} X_{H_2O}} = 0.75314 e^{4083/T_g} \quad (3.25)$$

where  $T_g$  is the gasification temperature and  $P$  is the gasification pressure.

### Energy balance:

Figure 3.2 below shows the general energy balance for a gasifier. The input energy is carried by coal feed (high calorific value and sensible heat), water/steam blast (sensible heat) and oxygen blast (sensible heat). The output energy streams include the raw syngas (heating value and sensible heat), sensible heat in slag and fly ash, heating value and sensible heat of unburned carbon and heat loss. In some gasifier with water fall built on the refractory wall, output heat will also include the saturated steam enthalpy (In this model, the heat used to

generate saturated steam is not considered). Gasification process involved recycled syngas is not consider in this model either.

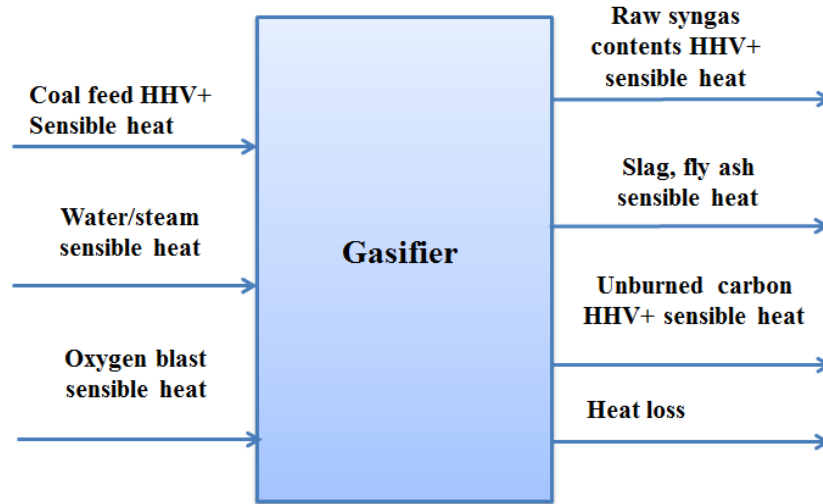


Figure 3.2 Energy balance for gasifier

The syngas contents considered in this model includes CO, CO<sub>2</sub>, H<sub>2</sub>, CH<sub>4</sub>, N<sub>2</sub> COS, H<sub>2</sub>S, Argon and H<sub>2</sub>O. Based on the description of energy balance and Hess's law (Brescia et al., 1975), the following Equation (3.26) is built as below.

$$\begin{aligned}
 H_{in,coal} + H_{in,oxygenblast} + H_{in,H_2O} = H_{out,rawsyngas} \\
 + H_{out,slag} + H_{out,flyash} + H_{out,uncarbon} + H_{loss}
 \end{aligned}
 \quad (3.26)$$

where  $H_{in,coal}$  includes the HHV for coal feedstock and its sensible heat, the value can be obtained by published literatures (J.Eurlings, 1999a, Schoen, 1993). For gas phase contents, the enthalpy of them with given temperature can be calculated by combining HHV and sensible enthalpy changes. The reference state for the calculation is standard condition (103.1KPa and 298.15K)(Glassman et al., 2015).  $H_{in,Oxygenblast}$  is the energy flow carried by oxygen blast which includes the oxygen, transported nitrogen and minimum amount of Argon. Its value can be calculated by Equation (3.27) below.

$$H_{in,Oxygenblast} = n_{in,O_2} \int_{298.15}^{T_{in,Oxygenblast}} c_{p,O_2} dT + n_{in,N_2} \int_{298.15}^{T_{in,Oxygenblast}} c_{p,N_2} dT + n_{in,Ar} \int_{298.15}^{T_{in,Oxygenblast}} c_{p,Ar} dT \quad (3.27)$$

where  $n_{in,O_2}$ ,  $n_{in,N_2}$  and  $n_{in,Ar}$  denote the mole flow rate of oxygen blast, nitrogen contained in oxygen blast and Argon contained in oxygen blast respectively.  $c_p$  denotes the specific heat in constant pressure.  $T_{in,Oxygenblast}$  denotes the oxygen blast temperature.

The enthalpy carried by  $H_2O$  depends on the state of input and will differ by liquid phase and superheated steam phase, its value  $H_{in,H_2O}$  is calculated by Equation (3.29).

$$H_{in,H_2O} = n_{in,H_2O} \int_{298.15}^{T_{in,H_2O}} c_{p,H_2O} dT \quad (3.28)$$

where  $n_{in,H_2O}$  denotes the mole flow rate of  $H_2O$  input,  $c_{p,H_2O}$  denotes the specific heat in constant pressure of  $H_2O$  input and  $T_{in,H_2O}$  denotes the  $H_2O$  input temperature. The energy flow carried out by raw syngas includes HHV and sensible heat of each syngas contents, its value  $H_{out,rawsyngas}$  can be calculated by Equation (3.29).

$$H_{out,rawsyngas} = \sum_i n_i HHV_i + \sum_i n_i \int_{298.15}^{T_g} c_{p,i} dT \quad (3.29)$$

where  $n_i$  denotes the mole flow rate of syngas content  $i$ ,  $HHV_i$  denotes the HHV of syngas content  $i$ .  $c_{p,i}$  denotes the specific heat of content  $i$  in constant pressure.  $T_g$  denotes the syngas temperature. The ash content in coal feedstock exists in fly ash and exiting slag. The energy carried by fly ash is the sensible heat of fly ash, its value  $H_{out,flyash}$  can be calculated by Equation (3.30).

$$H_{out, flyash} = m_{flyash} \int_{298.15}^{T_g} c_{p, flyash} dT \quad (3.30)$$

where  $m_{flyash}$  denotes the mass flow rate of fly ash,  $c_{p, flyash}$  denotes the specific heat of fly ash in constant pressure. Similarly, the energy carried out by exiting slag is its sensible heat as well, the value  $H_{out, slag}$  can be calculated by Equation (3.31).

$$H_{out, slag} = m_{slag} \cdot \int_{298.15}^{T_g} c_{p, slag} dT \quad (3.31)$$

where  $m_{slag}$  denotes the mass flow rate of exiting slag,  $c_{p, slag}$  denotes its specific heat in constant pressure. The energy carried by unreacted carbon includes its HHV and sensible heat, the value  $H_{out, uncarbon}$  can be calculated by Equation (3.32).

$$H_{out, uncarbon} = m_{uncarbon} \cdot HHV_{carbon} + m_{uncarbon} \int_{298.15}^{T_g} c_{p, uncarbon} dT \quad (3.32)$$

where  $m_{uncarbon}$  denotes the mass flow rate of unreacted carbon and  $HHV_{carbon}$  denotes the higher heating value of carbon,  $c_{p, uncarbon}$  denotes the carbon's specific heat in constant pressure.

The syngas prediction model with the energy balance can predict the heating value and sensible heat of raw syngas as well as the total heat loss (Glassman et al., 2015). With these results the cold gas efficiency (CGE) (Higman and van der Burgt, 2008b) can be calculated by the following Equation (3.33):

$$CGE = \frac{HHV_{raw, syngas}}{HHV_{coalfeed}} \quad (3.33)$$

Based on assumption (6), the working temperature and pressure is stable in this syngas prediction model, which means  $P$  and  $T_g$  will be used as input in this simulation process.

There are 11 unknown variables in equations (3. 9) ,(3. 11),(3. 13),(3. 15),(3. 17 ),(3. 19),(3. 21) (3. 22 ),(3. 23) and (3. 24); this non-linear equation set can be solved with Newton-Raphson method. The solver is coded in Matlab, the basic idea is using iteration calculation by giving reasonable initial value. The flow chart of Matlab code is shown in Figure 3.3. The results of this equation set will be the syngas contents concentration under the pre-defined working condition.

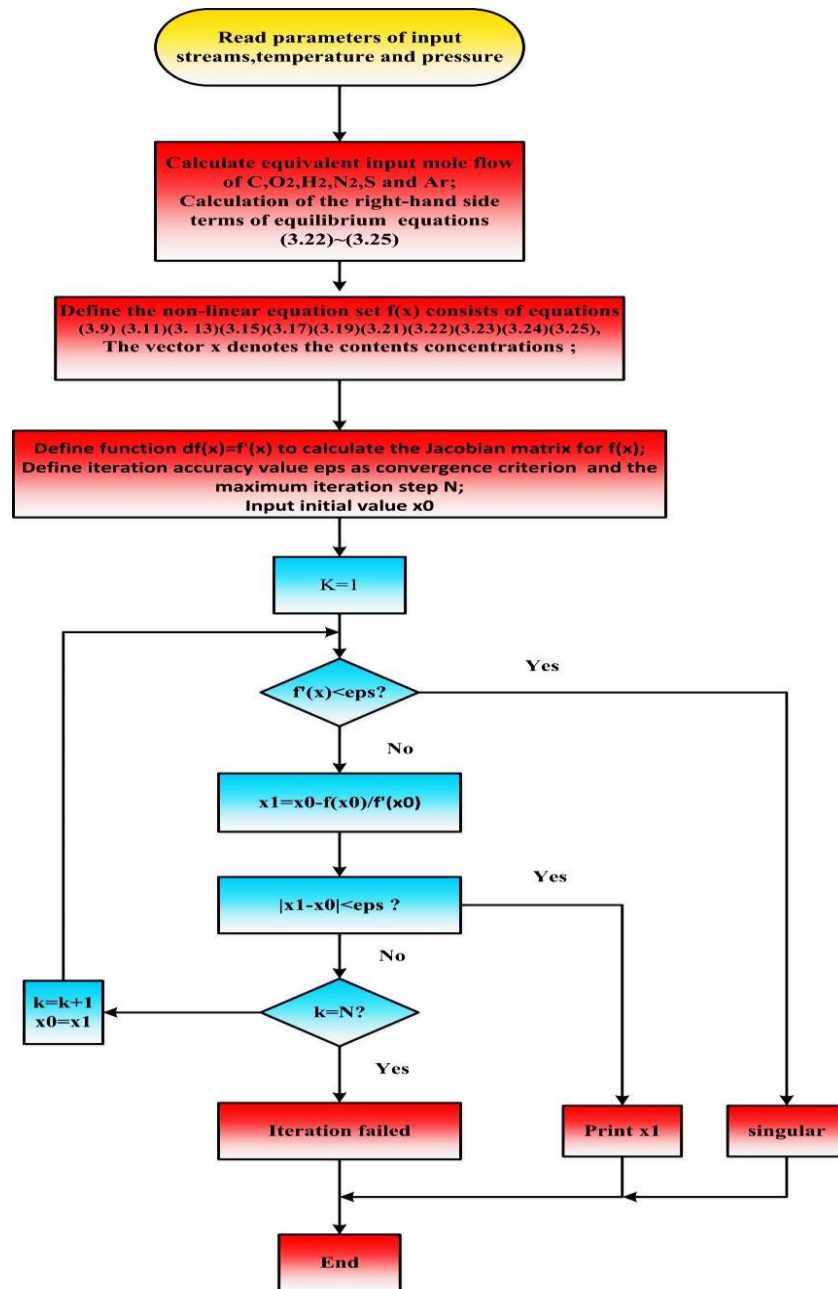


Figure 3.3 Flow chart of Newton-Raphson method for syngas contents calculation

### 3.3 Texaco Gasifier Syngas Prediction Results and Discussion

#### 3.3.1 Steady State Prediction and Model Validation

Three different types of coal (Illinois 6<sup>#</sup>, Australia and Fluid coke) (Watkinson et al., 1991) are used in the model test. The model input variables include oxygen/coal ratio, water/coal ratio, ultimate analysis of coal, oxygen purity, pressure and temperature, etc. The values of input data are listed in Table 2.1. The simulation results of the final steady state and their associated testing reference data (Watkinson et al., 1991) are shown in Table 3.2. And for error analysis, the mean absolute error (MAE) between simulation results and reference data is calculated as well and listed in the end of Table 3.2.

Table 3.1 Model input with three types of coals

Input	Unit	Illinois 6 <sup>#</sup>	Australia	Fluid coke
Slurry flowrate	kg/s	1	1	1
Slurry concentration	kg coal/ kg slurry	0.665	0.621	0.606
O <sub>2</sub> purity	Vol. %	98	99.6	100
O <sub>2</sub> /coal	kg O <sub>2</sub> / kg dry coal (no ash)	0.86	0.87	1.03
Ar/O <sub>2</sub>	kg Ar/kg O <sub>2</sub>	0	0	0
Gasifier pressure	MPa	4.083	4.083	4.083
Temp.	°C	1141	1044	1060
Heat loss	H.H.V. %	2	2	2
Ultimate analysis(dry ash-free)	Mass %			
C	%	69.6	66.8	86
H	%	5.3	5.0	2.0
O	%	10	7.3	2.3
N	%	1.3	1.7	1.0
S	%	3.9	4.2	8.3
Ash	%	10	15	0.5

Table 3.2 Comparison of simulation results and Reference data

	Illinois 6 <sup>#</sup>		Australia		Fluid coke	
	R(mol%)	S(mol%)	R(mol%)	S(mol%)	R(mol%)	S(mol%)
CO	41.0	41.0	35.2	35.4	47.1	47.2
H <sub>2</sub>	29.80	30.1	29.9	29.6	24.3	23.7
CO <sub>2</sub>	10.2	10.0	12.8	12.8	13.2	13.3
H <sub>2</sub> O	17.1	16.8	20.3	20.0	12.7	13.0
CH <sub>4</sub>	0.3	0.15	0.02	0.22	0.09	0.33
N <sub>2</sub>	0.80	0.9	0.63	0.63	0.4	0.3
H <sub>2</sub> S	1.1	1.01	1.14	1.10	2.2	2.07
COS		0.04		0.25		0.10
MAE		0.26		0.14		0.21

The comparison in Table 3.2 shows that the simulation results (column S) match well with the reference data (column R) for the three types of coal feed. The gasifier simulation results are then compared with reference data from the Lu-nan fertilizer factory located in Shandong province, China.

Model input data are shown in Table 3.3. The prediction of the output dry syngas content results and industry data are shown in Table 3.4. It needs to be aware that the syngas contents CH<sub>4</sub>, COS, SO<sub>2</sub>, N<sub>2</sub> and Argon are treated as one stream since there is no detailed data available from reference. Table 3.4 data show the simulation result of CO is higher than industry data while H<sub>2</sub> result is lower, this is possibly caused by the error of equilibrium Equation (3. 22 ) for the water gas shift reaction, which means the reaction in real condition moves left. Relative large error for CH<sub>4</sub>+Sulfide+N<sub>2</sub>+Ar is possibly caused by the difference between theoretical parameters of Equations (3. 24),(3. 25), (3. 26) and real conditions as well. (Yue et al., 2013).



Table 3.3 Model input based on Lunan factory

Input	Unit	Data
Slurry Rate	t/d	650
Slurry Concentration	kg coal/kg slurry	0.66
Oxygen Purity	Vol. %	98
Oxygen/coal	kg O <sub>2</sub> /kg drycoal (no ash)	0.96
Pressure	MPa	4.0
Temperature	°C	1350
Heat Loss	H.H.V. %	2
Ultimate analysis	%	
C	%	71.5
H	%	4.97
O	%	11.15
N	%	1.07
S	%	2.16
Ash	%	9.15

Table 3.4 Dry Syngas Output Content Compare

	CO	H <sub>2</sub>	CO <sub>2</sub>	CH <sub>4</sub> +Sulfide+N <sub>2</sub> +Ar
Industry	48.82	36.58	14.41	0.19
Simulation	49.54	35.69	12.79	1.98
Relative error (%)	1.5	2.4	11.24	not specified

### 3.3.2 Syngas contents change with water/coal ratio change

To further test the model under Lunan condition, the change of oxygen/coal ratio and oxygen/coal ratio's effects to the syngas content are studied. Figure 3.4 and Figure 3.5 show the slurry concentration's effect onto syngas contents. The results of main syngas contents such as CO, H<sub>2</sub>, CO<sub>2</sub>, and H<sub>2</sub>O need more attention since they will cause the main influence to gasifier CGE and the downstream units.

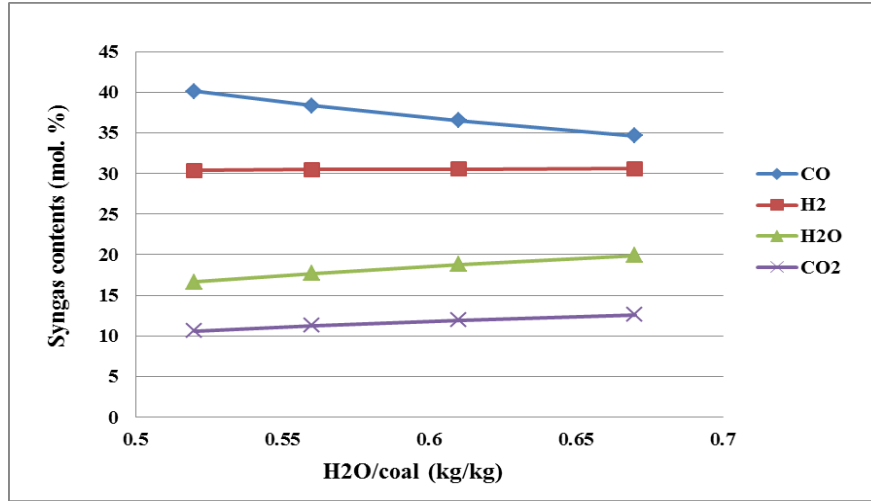


Figure 3.4 Syngas content change with H<sub>2</sub>O/coal ratio

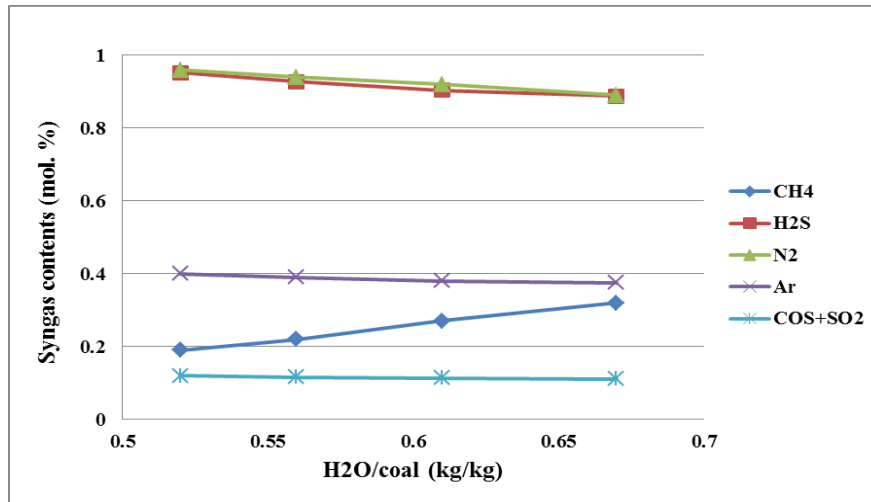


Figure 3.5 Syngas content change with H<sub>2</sub>O/coal ratio

As shown in Figure 3.4 and Figure 3.5, when the H<sub>2</sub>O/coal ratio increases from 0.52 to 0.67, CO content decreases while H<sub>2</sub> almost keeps steady (slightly rise), CO<sub>2</sub> and CH<sub>4</sub> decrease. When H<sub>2</sub>O/coal increases, which mean the slurry concentration reduce, less coal feed enters the gasifier, but the oxygen/coal ratio remains, that means oxygen input will decrease as well, thus the gasification process is weakened and the content change will happen. Actually the raw syngas production will decrease, the slightly rise of H<sub>2</sub> is the result of this. The production of hydrogen has been weakened as well. Thus the H<sub>2</sub>O/coal ratio needs to be carefully tuned in operation. Similar conclusion is proposed by Azuhata's work (Azuhata et al., 1986, Yue et al., 2013).

### 3.3.3 Syngas contents change with oxygen/coal ratio change

Figure 3.6 and Figure 3.7 show the syngas content change with oxygen/coal ratio. The rise of this ratio means the increase of oxygen supply, which will definitely enhance the combustion and raise gasifier temperature, thus enhance the gasification process (raw syngas sensible heat rises). But it will also consume more CO and H<sub>2</sub> released from the volatile, which causes the decrease of CO and H<sub>2</sub> content and the increase of CO<sub>2</sub> content. This may cause negative effect to the CGE, thus the oxygen/coal ratio needs to be carefully tuned as well to maintain the best working condition. Similar conclusion is proposed by Azuhata's research work (Azuhata et al., 1986, Vamvuka et al., 1995a) and Vamvuka's simulation results (Vamvuka et al., 1995a) as well.

Govind (Govind and Shah, 1984) proposed a conclusion: the effect caused by H<sub>2</sub>O/coal ratio changes is stronger than that caused by oxygen/coal ratio changes. The comparison of Figure 3.4~Figure 3.7 shows the similar trend. From the results it can be concluded that the best oxygen/coal ratio and H<sub>2</sub>O/coal can be highlighted through the simulation study for different types of coal. Due to the higher sensitivity of gasifier operation to H<sub>2</sub>O/coal, the water/steam blast needs to be well controlled in the real operation.

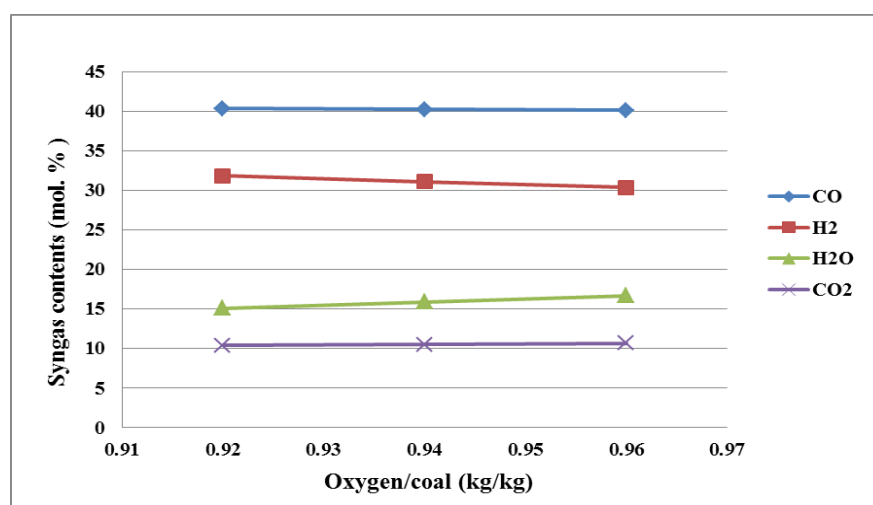


Figure 3.6 Syngas content change with oxygen/coal ratio unit

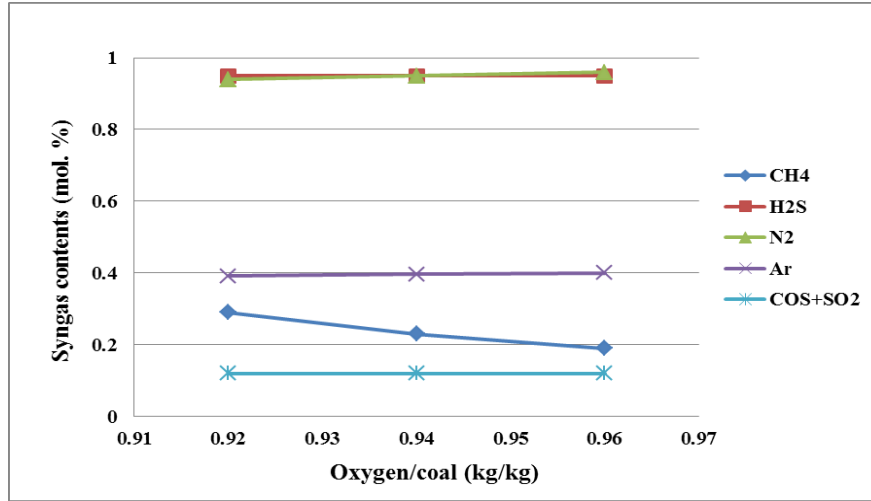


Figure 3.7 Syngas content change with oxygen/coal ratio unit

### 3.3.4 Syngas contents change with operation temperature change

Figure 3.8 and Figure 3.9 show the syngas concentration changes with operation temperature. The simulation is conducted by adjusting the heat loss factor while keeping the other input data stable, and then calculating the working temperature by solving energy balance equations.

When the operation temperature rises, CO concentration rises and H<sub>2</sub> concentration slightly drops. The effective raw syngas contents of CO+ H<sub>2</sub> is kept steady. CO<sub>2</sub> production also drops, which can be explained by the chemical equilibrium change of water-gas shift reaction. Methane production drops due to the equilibrium change of methane formation reaction. In real industry, the heat loss is caused by radiant and convective heat transfer from gas phase zone to the refractory wall, and it is usually treated as a function of higher heating value of the coal feed (Brown et al., 1986).

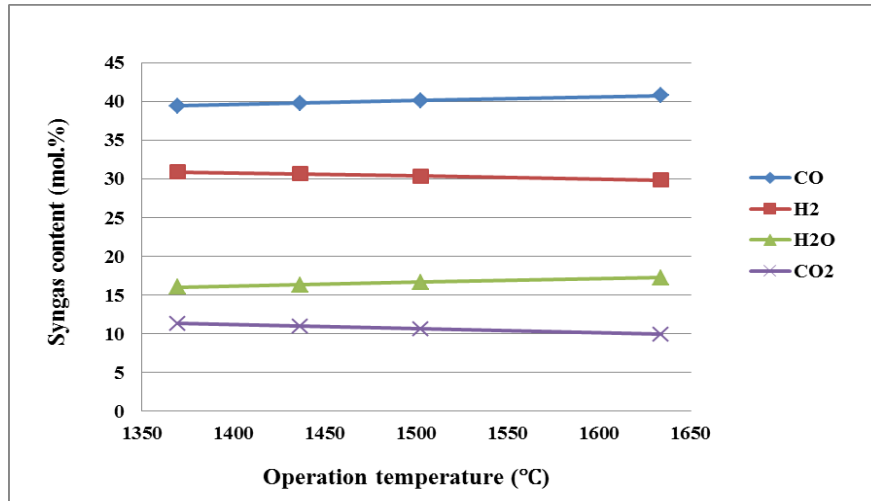


Figure 3.8 Syngas contents change with operation temperature

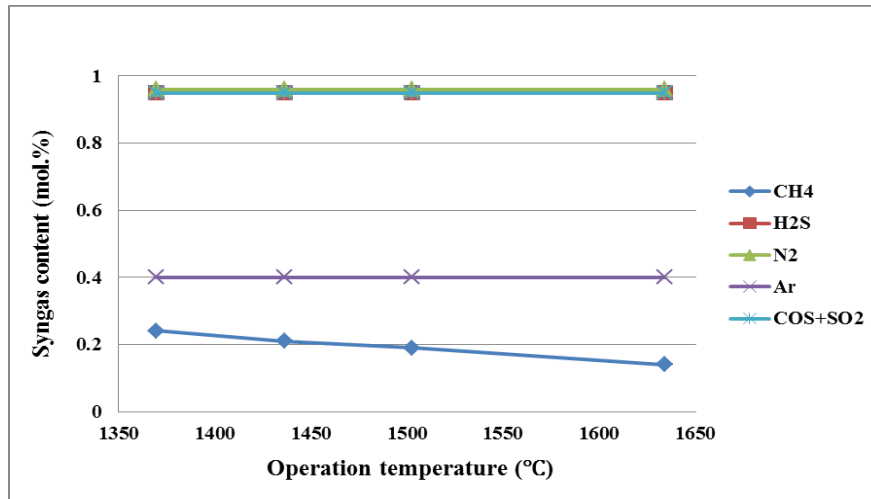


Figure 3.9 Syngas contents change with operation temperature

Figure 3.10 and Figure 3.11 show the syngas concentration change with the operation pressure. The effect of pressure change is achieved by the influence to chemical equilibrium. During the model adjustment, it can be found that as the pressure value rises, the initial guess for the temperature needs to be set to a lower value.

The CO concentration has a slightly drop due to the equilibrium change of the water gas shift reaction, CH<sub>4</sub> concentration rises since the rise of the pressure and the drop of the temperature will enhance the methane formation reaction by moving the equilibrium.

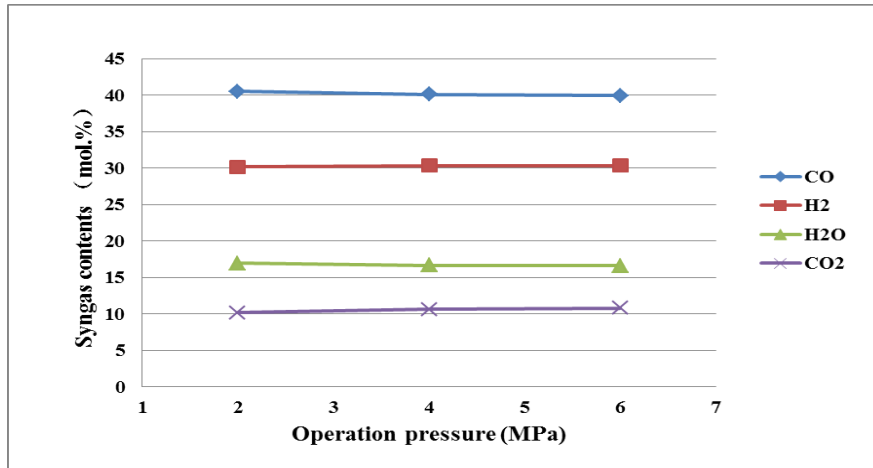


Figure 3.10 Syngas contents change with operation pressure

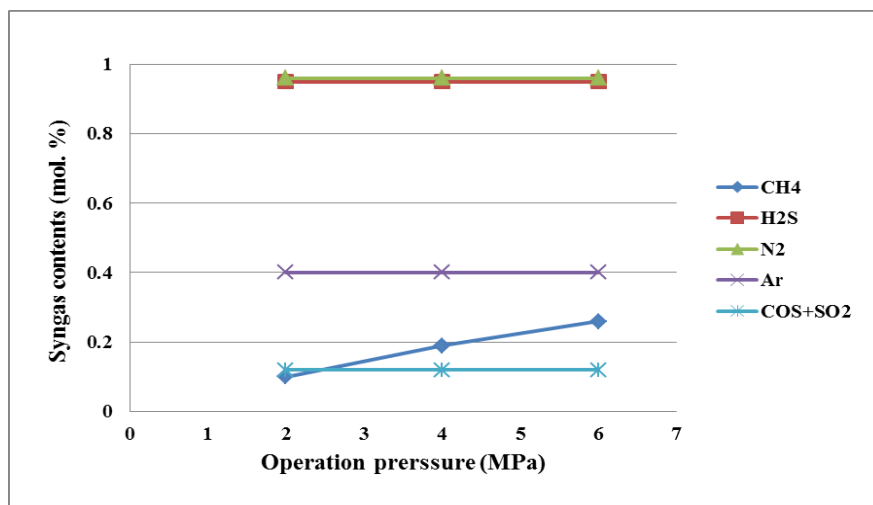


Figure 3.11 Syngas content change with operation pressure

### 3.3.5 Summary of the Texaco gasifier simulation

The gasifier model can provide relatively accurate syngas contents prediction from the validation of four different types of coal. The change of key input parameters shows some inspiration for gasifier operation.

The initial value of syngas contents concentration data need to be carefully chosen to ensure the equations will converge in the defined steps N. The choice for initial value is usually based on experiences and relative technical references. The simulation results can reveal the real operation of Texaco gasifier and show the syngas contents change under different

working conditions. Thus this model provides a potential tool for working condition optimization with a wide range of coal types and gasifiers.

### 3.4 Model test for other type of gasifier

The mass balance, energy balance and chemical equilibriums equations are deducted based on general working principles of coal gasification, this model can be used for study of other types of entrained-flow gasifiers such as Shell, U-gas and Lurgi, etc. A Shell gasifier using EL Cerrejon coal is used for the study. The input variables for the model is listed in Table 3.5 (J.Eurlings, 1999a).

Table 3.5 Shell gasifier Model Input

Input	Unit	Data
Oxygen Purity	Vol. %	95
Nitrogen in oxygen blast/oxygen	kg /kg	0.00653
Argon in oxygen blast/oxygen	kg /kg	0.05252
Oxygen/ dry coal ash-free basis	kg /kg	0.932
Steam/ dry coal ash-free basis	kg /kg	0.1454
Transport nitrogen/dry coal ash-free basis	kg /kg	0.061
Moisture content in coal feed	Mass%	2
Carbon conversion rate	%	99.5
Gasifier operation pressure	MPa	3.1
Gasifier operation temperature	°C	1450
Oxygen blast temperature	°C	265
Transport nitrogen pressure	MPa	3.5
Transport nitrogen temperature	°C	352
Coal feed temperature	°C	200
Coal feed specific heat	kJ/(kg°C)	0.92
Steam blast temperature	°C	380
Steam blast pressure	MPa	3.5
Heat Loss factor	H.H.V. %	0.5
Element analysis	Mass %	
C	%	75.7

H	%	4.97
O	%	9.12
N	%	1.43
S	%	0.87
Ash	%	7.91
Ultimate analysis	Mass %	
Ash	%	7.91
Volatiles	%	38.2
Carbon	%	53.9
HHV of input coal	kJ/kg	29994.56
Input coal mass	kg	1
Input coal sensible heat	kJ	182.5990
Oxygen(with Nitrogen and Argon)	kJ	194.5224
Transport nitrogen sensible heat	kJ	1.9500
Steam sensible heat	kJ	402.5003

With the input variable values listed above, the model is used to predict the syngas contents and establish the energy balance of Shell gasifier using EI Cerrejon coal. With 1 kg of raw coal with ash and moisture input to the model, the output of raw syngas data and CGE of the Shell gasifier can be calculated. The syngas contents mole concentrations are compared with reference data. Output data are shown in Table 3.6:

Table 3.6 Shell gasifier Model output with reference data

Parameter	Unit	Reference data	Simulation Data
Oxygen/dry coal ash-free basis	kg/kg	0.895	0.932
Steam/Oxygen	kg/kg	0.139	0.156
CO	%	62.1	62.1357
H <sub>2</sub>	%	31	31.5787
N <sub>2</sub>	%	3.1	2.7252
CO <sub>2</sub>	%	1.0	0.71
H <sub>2</sub> S+COS	%	0.23	0.27
CH <sub>4</sub>	%	0.05	0.06
Ar	%	0.8	1.13
H <sub>2</sub> O	%	1.7	1.38
SO <sub>2</sub>	%	none	0.0003
CGE	%	87.2	87.2
Raw syngas HHV	kJ	26155.3	26167.5



Unburned coal mass	kg	N/A	0.0037
Ash and slag mass	kg	N/A	0.0775
Raw syngas sensible heat	kJ	N/A	4522.0680
Unburned carbon heating value	kJ	N/A	121.7244
Heat loss	kJ	N/A	153.7780

Based on the simulation results, the model prediction results for CO, H<sub>2</sub> concentrations matches well with reference data (total mean absolute error for CO and H<sub>2</sub> is 1.9% ).The HHV results match well with the reference (MAE is 0.05%) shows that the energy balance equation is reasonably acceptable. Relative large error happens for the syngas contents CO<sub>2</sub> (29%) and Ar (41.2%), this may cause by the assumptions made for the calculation of chemical equilibrium.

### 3.5 Summary

In this chapter, a zero dimension model is developed to predict the syngas contents produced from Texaco gasifier and Shell gasifier, the model is derived by applying the mass balance, chemical equilibrium and energy balance. The simulation results of dry syngas match well with industry data. Also, H<sub>2</sub>O/coal ratio, oxygen/coal ratio, temperature and pressure's influence to syngas contents are studied. As the fuel gas contents CO, and H<sub>2</sub> can reveal the syngas quality while CO<sub>2</sub> is the main green gas emission content, these three contents are more important in the simulation. In order to maintain the stable operation of gasifier and generate raw syngas of high quality, lower H<sub>2</sub>O/coal ratio is favoured; oxygen/coal ratio needs to be well controlled to maintain the raw syngas quality. Usually, the change of operation temperature and pressure can't be modified directly, but the simulation results could provide a reasonable guide for the operator (such as change the coal feed rate, oxygen or steam blast rate to adjust pressure and temperature). The simulation results of raw syngas contents will be used as the input for downstream modules.

## **Chapter 4 One dimension model of Shell slagging gasifier**

The zero-dimension model introduced in Chapter 3 can be used to predict the syngas contents of different commercial gasifier. But this model is not able to show the dynamic characteristics of the gasifier working process. A more detailed model needs to be developed to prepare a time-driven gasifier model for the whole IGCC process. A dry-coal feed entrained-flow Shell gasifier is adopted for this target. Shell gasifier is dry coal feed entrained-flow gasifier, a slag layer will form during its working process when the unburned fly ash melt and agglutinate on the refractory wall. The slag layer provides an ideal module for mass and energy storage hence Shell gasifier is chosen for dynamic simulation study.

In this chapter, a one-dimension dynamic model of Shell gasifier with slagging is built. A chemical equilibrium-based syngas prediction sub-model is used to predict the main syngas contents ( $\text{CO}$ ,  $\text{CO}_2$ ,  $\text{H}_2$ ,  $\text{H}_2\text{O}$ ,  $\text{COS}$ ,  $\text{H}_2\text{S}$ ). Meanwhile, a slagging sub-model is developed and coupled with syngas model by analysing the energy balance inside the gasifier. The slag model is developed based on mass balance, energy balance and momentum balance and can predict the thickness of liquid phase layer and solid phase layer.

Different types of coal are used to test the model. The dynamic change of key parameters such as raw syngas temperature, liquid and solid slag layer thickness, hydrogen concentration and carbon monoxide concentration with response to steam/coal ratio and oxygen/coal ratio are analysed as well.

### **4.1 Introduction of Shell Slagging Gasifier**

As one of the most widely used dry coal feed entrained-flow gasifier, Shell Coal Gasification Process (SCGP) is also a good choice for IGCC power plant and has driven a lot of

researcher's interests (Schoen, 1993, Vamvuka et al., 1995b, Seggiani, 1998, Sun et al., 2011, Yang et al., 2011, Casella and Colonna, 2012, Zhang et al., 2013, Lee et al., 2014). The main difference between Shell and Texaco gasifiers is that Shell gasifier uses pressurized dry coal feed. The Shell gasifier can use pure oxygen or air as oxidant blast and steam as moderator. Since the heat inside the Shell gasifier doesn't need to evaporate the water content in slurry input used by the Texaco gasifier, the sensible heat in raw syngas can be higher hence usually Shell gasifier can have higher cold gas efficiency (CGE). Moreover, the syngas cooling system in Shell gasifier which is formed by radiant heat exchanger and convective heat exchanger can achieve better heat recovery from the raw syngas than water quench-applied Texaco gasifier. As a result, the investment of the Shell gasifier equipment will be higher.

The schematic diagram of the Shell gasifier is shown in Figure 4.1, apart from the inner lined refractory wall, a water wall system formed by tube sets is built between the refractory bricks and outer steel vessel body. The water fluid in the tube can recover the heat inside the furnace and moderate the working temperature.

The dry pulverized coal is driven by transport stream and injected into the gasifier with oxygen and steam blast through the bottom part diametrically located burners. The coal devolatilizes rapidly in the zone near the nozzles, and the combustion of volatiles and remaining chars will deplete the oxygen very fast. The intense heat released in the nozzle zone will sustain the gasification reactions of char, steam and gas products of volatile combustion. The up flow of the generated hot syngas will be mixed with the recycled cool syngas to solidify the fly ash in case the melted ash will agglomerate in the downstream units.

As shown in Figure 4.1, the inside part of the Shell gasifier is lined with membrane wall, between the membrane wall and refractory material there is a steam circuit formed by steel tubes, this circuit can absorb the heat to generate MP (medium pressure) saturate steam for

the heat recovery steam generator in combined cycle plants while avoiding overheat of the membrane wall. Due to the high working temperature and pressure (typically 1600°C and 3MPa), the ash content in coal feed will melt and form liquid slag droplets. The liquid phase slag will flow down along the wall, accumulate in a slag tap and be removed by the lock hopper at the bottom of the gasifier. During the flow of slag, part of the slag droplets will be solidified on the cold membrane wall and form a solid slag layer, which will increase the heat resistance between the gas volume and steam circuit.

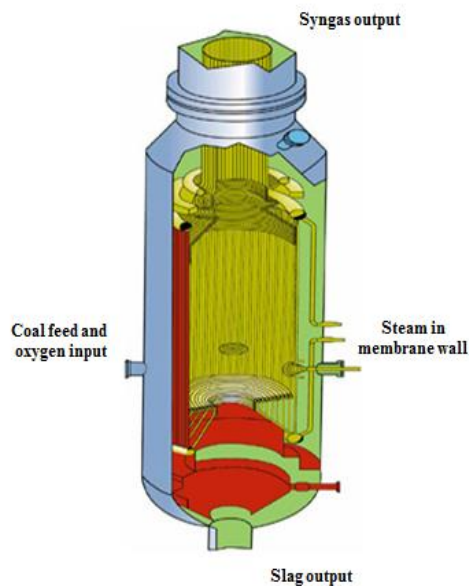


Figure 4.1 Schematics of Shell gasifier (Sun et al., 2011)

## 4.2 Shell Gasifier Model

### 4.2.1 “Three Zones” Assumption

The development of Shell gasifier model is inspired by the works of Schoen (Schoen, 1993) and Bo Sun (Sun et al., 2011). A “three zone” model for the gasifier inside the control volume is proposed and shown in Figure 4.2. It is assumed that the burner jets will impinge diametrically and create two vertically jets. The up flow jets will move to the exit and part of it will leave the gasifier while the rest part will move downward and form a large

recirculation jet along the wall. The down flow of the burner jets only occupies a small part of the gasifier volume. Based on this assumption, the gasifier volume can be divided into three zones: combustion zone (C) which is close to the burners with high temperature flame, the coal devolatilizes rapidly and will consume all the free oxygen in this zone; gasification zone (G)-the gasification reactions include homogeneous and heterogeneous reactions and form the raw syngas; recirculation zone (R) - the radiant and convective heat transfer from gas volume to the wall happens in this zone. This assumption is important for the heat transfer model establishment which is described in Section 4.2.3.1

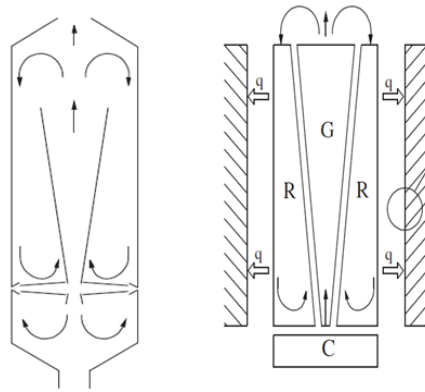


Figure 4.2 The “three zones” inside gasifier (Sun et al., 2011)

#### 4.2.2 Gasification Model Assumptions

In Chapter 3, the syngas model with whole contents was built and studied. The prediction results reveal that the major components CO, CO<sub>2</sub>, H<sub>2</sub> and H<sub>2</sub>S occupy over 99% of the total syngas contents. Hence the syngas prediction model can be simplified to make calculation faster. Assumptions are made for the Shell gasifier model, which is different from the zero-dimension model.

- 1) The devolatilization and gasification proceed in an infinite speed, all the gas phase reactions reaches chemical equilibrium as soon as the coal feed and oxygen, steam

blast are injected into the gasifier. The equilibrium assumption is throughout the whole gasifier.

- 2) Coal conversion rate is set to be constant as 99.5%, it is reasonable for Shell gasifier operation based on the published data for commercialized units (J.Eurlings, 1999a, Sun et al., 2011)
- 3) Nitrogen is assumed to be inert gas while argon is assumed to be present as  $N_2$  (Schoen, 1993). 90% of the Sulphur content in the coal will be converted into  $H_2S$  while the other 10% is changed to COS.  $SO_2$  is not considered in the simulation. The assumption is reasonable based on the published data of Nichols (Nichols et al., 1989).
- 4) Only the chemical equilibrium of water/gas shift reaction is considered in the model. Based on the simulation results in Chapter 3, it can be concluded that the water gas shift reaction will have very unique influence to the gasification and final syngas major contents. This assumption can be proved to be reasonable based on the published works (Schoen, 1993, Sun et al., 2011, Ruprecht et al., 1988).
- 5) The heat loss factor is set as 0.5% in this model; the heat generation of gasification process is used to increase the enthalpy of raw syngas and create heat flux to the slag layer.
- 6) It is assumed that 70% of the ash in coal feed reaches the liquid slag layer from the top of gasifier and flow along the wall to the slag tap located in the bottom, the rest 30% of ash turns to be fly ash and is treated as composition of the syngas (Schoen, 1993) .
- 7) Syngas contents prediction is steady by considering the syngas residence time scale comparing with IGCC dynamic behavior time scale ( $10^2$  to  $10^3$  s) (Yang et al., 2011, Sun et al., 2011, Schoen, 1993). Thus the dynamic behavior of gasifier occurs in the

slag layer is only caused by thermal effects rather than variations of crystallized components in the slag.

- 8) Flow in the liquid slag layer is assumed to be laminar flow. The liquid slag is assumed to be Newtonian fluid and the friction between the liquid layer and solid layer can be neglected, which means the sheer stress for on the liquid slag layer is caused by gravity. The slag model is assumed to be one dimension and independent with height. The melting of solid slag layer is transient and the melting enthalpy is assumed to be zero. Although there is research publication (Johnson, 1984) which reveal that the melting slag is Bingham plastic fluid, in this thesis, the melting part is assumed to be transient (Seggiani, 1998).
- 9) The densities, thermal conductivity, specific heat for both the liquid and solid layer are constant (these parameters are treated as single).
- 10) The temperature file of the slag layer is linear; viscosity of the liquid layer slag model is defined as the function of temperature according to reference (Bird et al., 2001, Seggiani, 1998).

#### **4.2.3 Shell Gasifier Model Development**

The Shell gasifier model is divided into two parts: the steady state syngas prediction model based on mass balance, chemical equilibrium and energy balance; dynamic model of slag layer based on mass balance and energy balance.

The syngas model is developed based on mass balance similar to Chapter 3 thus it will not be explained in details. Based on the Assumptions 3) and 4), the syngas model in Chapter 3 is simplified to Equations (4.1) to (4.6).

The mass balance equations are listed as follows:

$$N_g(X_{N_2}) = N_{N_2,0} \quad (4.1)$$

$$N_g(X_{H_2S}) = 0.9N_{S,0} \quad (4.2)$$

$$N_g(X_{COS}) = 0.1N_{S,0} \quad (4.3)$$

$$N_g(X_{CO} + X_{CO_2}) = 0.995N_{C,0} - N_g X_{COS} \quad (4.4)$$

$$N_g(0.5X_{CO} + X_{CO_2} + 0.5X_{H_2O}) = N_{O_2,0} - N_g(0.5X_{COS}) \quad (4.5)$$

$$N_g(X_{H_2} + X_{H_2O}) = N_{H_2,0} - N_g X_{H_2S} \quad (4.6)$$

The chemical equilibrium of water-gas shift reaction (4.7)

$$\frac{X_{H_2} X_{CO_2}}{X_{CO} X_{H_2O}} = 0.0265e^{3956/T_g} \quad (4.7)$$

$X$  denotes the mole concentration (%) and  $N$  denotes the mole quantity (kmol/s) of different contents.

The calculation of equivalent  $N_{C,0}$ ,  $N_{N_2,0}$ ,  $N_{O_2,0}$ ,  $N_{H_2,0}$ ,  $N_{S,0}$  is the same as the process described in Section 3.2.2.

The energy balance Equation (4.8) is the similar to Equation (3. 25) which has been proposed and explained in Section 3.2.2, the difference between the Texaco and Shell gasifier energy balance equation is that part of the energy of Shell gasifier is used to generate steam in the water fall circuit:



$$\begin{aligned}
H_{in,coal} + H_{in,oxygenblast} + H_{in,H_2O} = H_{out,rawsyngas} \\
+ H_{out,flyash} + H_{out,carbon} + H_{out,slag} + H_{loss} + H_{steam}
\end{aligned}
\tag{4.8}$$

Based on Assumption 5), the energy generated by the gasification process are used to increase the enthalpy of the raw syngas and create heat flux to slag layer, thus an important input factor for the following slag model, the slag input heat flux  $Q_{g,sl}$ , can be defined and calculated by solving the energy balance equation. The calculation of  $Q_{g,sl}$  is important since this factor couples the syngas prediction model and slag model.

The energy leaves the gasifier with hot syngas includes the chemical energy and sensible heat. For the syngas contents  $H_2S$ ,  $COS$ ,  $N_2$ ,  $Argon$ ,  $CO$ ,  $CO_2$ ,  $H_2$  and  $H_2O$ , the polynomials Equation (4.9) from NIST webbook (NIST, 2011) are used for enthalpy calculation based on the typical operation temperature of Shell gasifier (over 1600K (Schoen, 1993)). The polynomials for stand enthalpy at temperature  $T$  (K) calculation are shown as follows:

$$H_T - H_{298.15} = A^p \cdot T + B \cdot \frac{T^2}{2} + C \cdot \frac{T^3}{3} + D \cdot \frac{T^4}{4} - \frac{E}{T} + F - H
\tag{4.9}$$

where  $H_T$  is the standard enthalpy of gas in temperature  $T$  using standard temperature 298.15K and pressure  $1.01e^5$  Pa as a base point. The parameters A~H can be found for each gas in the database of NIST webbook and their value for the syngas contents can be referred to (NIST, 2011).

#### 4.2.3.1 Heat Transfer Model

The heat transfer between gas volume in recirculation zone and the slag layer includes radiative heat transfer and convective heat transfer. The radiant heat transfer is relatively

dominant in the process (Schoen, 1993). In this model, the radiant heat is transferred from gas to wall, the process can be described by Equation (4.10) as follows:

$$Q_{rad} = A^s \sigma \varepsilon_s (T_g^4 - T_{sl}^4) \quad (4.10)$$

where  $A^s$  is the interface area between recirculation zone and wall,  $\sigma$  is the Stefan-Boltzman constant (Schoen, 1993),  $\varepsilon_s$  is the emissivity of slag layer, which is set as 0.83 (Schoen, 1993).  $T_g$  denotes the gas volume temperature in recirculation zone, which is approximated as syngas temperature.  $T_{sl}$  is the liquid slag layer surface temperature. The convective heat transfer can be calculated by Equation (4.11) below:

$$Q_{conv} = A \gamma_g (T_g - T_{sl}) \quad (4.11)$$

where  $\gamma_g$  is the convective heat transfer coefficient, the fluid state of the gas flow in recirculation zone need to be judged by calculating the Renolds number  $Re$  using the equation below:

$$Re = \frac{\rho_g v L}{\mu} \quad (4.12)$$

where  $\rho_g$  is the gas density, the value can be determined by the raw syngas contents and thermodynamic state parameters.  $v$  is the mean velocity of the gas in recirculation zone, its value is approximately set as 10m/s (Schoen, 1993). As the flow of syngas inside the gasifier is approximately as jet flow in the tube, thus the characteristic length  $L$  is the inner diameter of gasifier.  $\mu$  is the dynamic viscosity of syngas, which can be calculated based on the contents and state data as well. The calculation result of  $Re$  reveals that the gas flow inside the gasifier is turbulent flow hence the Nusselt number  $Nu$  can be calculated by using Equation (4.13) below:

$$Nu = 0.023Re^{0.8}Pr^{0.4} \quad (4.13)$$

where  $Pr$  is the Prandtl number of the syngas under the defined working conditions. With the value of  $Nu$ , the convective heat transfer coefficient can hence be calculated by the following equation:

$$\gamma_g = \frac{Nu \cdot \kappa}{L} \quad (4.14)$$

Where  $\kappa$  is the thermal conductivity of raw syngas, which needs to be fit by using optional polynomials with the given syngas contents and state data. In this model, it is assumed that the thermal conductivity of syngas will not change with the syngas contents concentration (Schoen, 1993).

The total heat transfer between recirculation zone can hence be calculated by the following Equation (4.15), where the heat transfer area is approximated as the slag layer surface area  $A_{lsl}$ .

$$Q_{g,lsl} = A_{lsl} \sigma \varepsilon_s (T_g^4 - T_{lsl}^4) + A_{lsl} \gamma_g (T_g - T_{lsl}) \quad (4.15)$$

The heat flux  $Q_{g,lsl}$  is important during the simulation since it is a “bridge” which couple the syngas model and slag layer model, the calculated heat flux will be used in the energy balance sub-model.

#### 4.2.3.2 Slag Layer Building Model

Firstly slag properties used in the simulation are introduced. The dynamic behavior of slag is an issue involves the theory of heat transfer, fluid dynamics, chemical kinetics and thermodynamics. Hence the physical properties of slag layer are required during the slag

layer model building. The key parameters needed for the calculation include thermal conductivity, viscosity, melting temperature and specific heat etc. They can be obtained either from published literature (Yang et al., 2011, Schoen, 1993) or empirical equations .

The result obtained from empirical Equation (4.16) proposed by Seggiani (Seggiani, 1998) has been used to calculate the melting temperature  $T_m$  and viscosity  $\mu$  . This equation is derived from the relationship of basic constitutes and acid constitutes in the coal ash by using a parameter  $Z_{em}$ . The basic constitutes in coal ash include iron, calcium, magnesium and alkaline oxides while the acid constitutes are silica, alumina and titanium (Seggiani, 1998).

$$Z_{em} = \frac{Al_2O_3 + SiO_2 + TiO_2}{CaO + MgO + Fe_2O_3 + Na_2O + K_2O} \quad (4.16)$$

The melting temperature  $T_m$  can be calculated by using  $Z_{em}$  and the following Equation (4.17) :

$$T_m = 1385.44 + 74.1 \cdot Z_{em} \quad (4.17)$$

Based on the reference (Schoen, 1993), the result value for the EL Cerrejon coal used in this model will be 1642K and won't change during the simulation.

Based on the Assumption 8), the liquid slag layer temperature will be higher than  $T_m$  , , the viscosity of liquid slag  $\mu$  varied with temperature, its value which depends on the temperature file of the slag layer can be calculated by empirical Equation (4.18) proposed by Mills (Mills and Rhine, 1989) :

$$\mu = 5.12 \times 10^{-6} \exp\left(\frac{23180}{T}\right) \quad (4.18)$$

where  $\mu$  is the liquid slag viscosity in Poise (Schoen, 1993) ,  $T$  is the temperature profile of liquid slag layer. Since the temperature within the liquid slag layer varies, the viscosity within the slag layer varies as well.

The slag density for liquid slag layer is set as  $2500 \text{ kg/m}^3$  while the value of solid layer is  $2700 \text{ kg/m}^3$  (Schoen, 1993). The thermal conductivity and specific heat has been set from the literature of Schoen (Schoen, 1993) and Mills (Mills and Rhine, 1989) for typical slag deposits. The key parameters for slag properties can be found in Table 4.1 of Section 4.3.1(Page 77).

Subsequently, the formation of slag layer is modelled. The process of slag layers formation has been introduced in Section 4.2. The Schematics diagram of slag layer formation is shown in Figure 4.3:

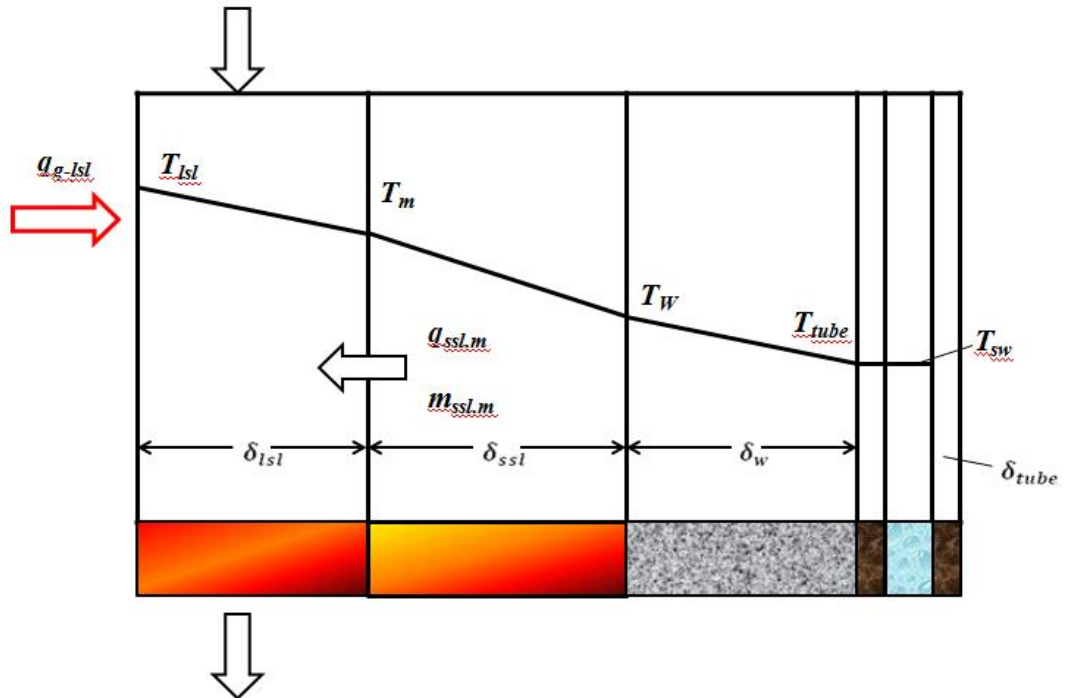


Figure 4.3 The Schematics of slag layer building process

The target of the slag model is to predict the dynamic change of the slag layer thickness and temperature with response to the step change of the key input parameters of the gasifier. The equations are deduced based on the momentum balance, mass balance and energy balance of the slag layers. Firstly, the velocity field of liquid slag layer along the wall is deduced. The flow of this liquid layer is treated as a liquid film flows along a plate (Bird et al., 2001):

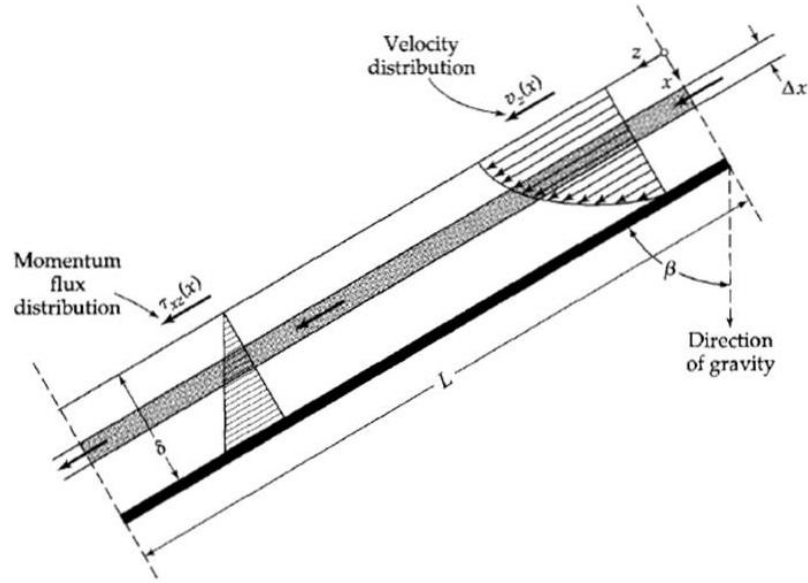


Figure 4.4 Velocity field in x direction for film fluid with variable viscosity (Bird et al., 2001)

The momentum flux conservation can be established by analyzing the convective momentum-flux tensor, viscous momentum-flux tensor and molecular momentum-flux tensor (Bird et al., 2001). With Assumption 8), the momentum flux of the liquid film along Z axis (Figure 4.4) is only contributed by the viscous momentum-flux, hence by eliminating the friction between liquid layer and solid layer, the momentum-flux conservation equation can be deduced as:

$$\frac{d\tau_{xz}}{dx} = \rho g \cos \beta \quad (4.19)$$

with boundary condition of

$$x = 0, \tau_{xz} = 0 \quad (4.20)$$

where  $\tau_{xz}$  denotes the viscous momentum flux,  $\beta$  is the angle between  $x$  axis and vertical direction (as shown in Fig. 4.4). This equation means the change of liquid film momentum is caused by the effect of gravity. The flux value is only depends on  $x$  (Figure 4.4), hence integration can be performed to Equation (4.19) by using the boundary condition shown in (4.20) and yield the momentum-flux distribution Equation (4.21).

$$\tau_{xz} = x \cdot \rho g \cos \beta \quad (4.21)$$

where  $x$  stands for the layer thickness, it is obvious that the momentum of liquid film increases along  $x$  axis, which is illustrated in Figure 4.4.

From Newton's law of viscosity (Asfaw et al., 2010) and with Assumption 8), the momentum flux tensor of newton fluid can be derived as Equation (4.22):

$$\tau_{xz} = -\mu \frac{dV_z}{dx} \quad (4.22)$$

where  $\mu$  is the viscosity of liquid slag flow,  $V_z$  is the velocity of the liquid slag flow along  $z$  axis. Hence the Equation (4.23) can be deducted by submitting Equation (4.22) to Equation (4.19):

$$\frac{d}{dx} \left( -\mu \frac{dV_z}{dx} \right) = \rho g \cos \beta \quad (4.23)$$

The viscosity of liquid is variable since the liquid slag layer is non-isothermal (Assumption 10)). But the viscosity can be well approximated by Equation (4.24) (Bird et al., 2001).

$$\mu = \mu_0 e^{-\alpha x / \delta} \quad (4.24)$$

where  $\mu_0$  is the viscosity in liquid slag layer surface and  $\alpha$  is a parameter to describe how fast the viscosity increases as  $x$  increase.  $\delta$  is the thickness of film layer.

$$\alpha = -\ln \frac{\mu(\delta_{lsl})}{\mu_0} \quad (4.25)$$

where  $\delta_{lsl}$  is the liquid slag layer,  $\mu(\delta_{lsl})$  is the function of  $\mu$  to  $\delta_{lsl}$  which is described by Equation (4.24). By using the Equation (4.18), the value of  $\alpha$  can be determined by the equation below:

$$\alpha = \frac{23180}{T_{lsl,0}} - \frac{23180}{T_m} \quad (4.26)$$

where  $T_{lsl,0}$  is the liquid phase slag surface temperature. By substituting Equations (4.24), (4.25) and (4.26) to Equation (4.23) and performing integration, the Equation (4.27) can be derived to calculate the liquid phase slag flow velocity  $V_z$ :

$$V_z = \frac{\rho_{lsl} g \delta_{lsl}^2 \cos \beta}{\mu_0} \left[ e^{\alpha} \left( \frac{1}{\alpha} - \frac{1}{\alpha^2} \right) - e^{\alpha x / \delta_{lsl}} \left( \frac{x}{\alpha \delta_{lsl}} - \frac{1}{\alpha^2} \right) \right] \quad (4.27)$$

Then the mass flow rate of liquid phase slag layer can be obtained by deriving the average velocity of this layer. The average velocity  $\bar{V}_z$  of the layer is calculated by Equation (4.28) below:

$$\bar{V}_z = \frac{\rho_{lsl} g \delta_{lsl}^2 \cos \beta}{\mu_0} \left[ e^{\alpha} \left( \frac{1}{\alpha} - \frac{1}{\alpha^2} + \frac{2}{\alpha^3} \right) - \frac{2}{\alpha^3} \right] \quad (4.28)$$

With the average velocity of liquid slag layer, the mass flow rate Equation (4.29) can be further derived as follows:



$$m_{lsl,out} = \int_0^{\delta_{lsl}} \pi \rho_{lsl} V_z D dx = \frac{\pi D \rho_{lsl}^2 g \delta_{lsl}^3 \cos \beta}{\mu_0} \left[ e^\alpha \left( \frac{1}{\alpha} - \frac{2}{\alpha^2} + \frac{2}{\alpha^3} \right) - \frac{2}{\alpha^3} \right] \quad (4.29)$$

With the exiting mass flow rate of  $m_{lsl,out}$ , the mass balance equation of liquid phase slag layer can be built and hereby the equation for the dynamic change of liquid slag layer thickness  $\delta_{lsl}$  can be derived as follow:

$$\frac{d\delta_{lsl}}{dt} = \frac{m_{ash,in} + m_{ssl,m} - m_{lsl,out}}{\rho_{lsl} A_{lsl}} \quad (4.30)$$

where  $m_{ash,in}$  is the liquid ash droplet input mass flow rate,  $m_{ssl,m}$  is the melting flow rate from solid slag layer,  $A_{lsl}$  is the surface area of liquid slag layer which can be equivalent to gasifier furnace inner area. The geometric data of gasifier can be found in Table 4.1 as well.

The energy balance for liquid slag layer can be deducted as follow:

$$\frac{d}{dt}(m_l \cdot h_l) = \sum q_{in} - \sum q_{out} + \sum m_{in} h_{in} - \sum m_{out} h_{out} \quad (4.31)$$

It can be further deducted as

$$\rho_{lsl} \delta_{lsl} c_{p,lsl} \frac{d\bar{T}_{lsl}}{dt} + \rho_{lsl} \bar{h}_{lsl} \frac{d\delta_{lsl}}{dt} = q_{g,lsl} - q_{lsl,ssl} + \frac{m_{lsl,in} h_{ash,in} - m_{lsl,out} h_{lsl,out}}{A_{lsl}} + m_{ssl,m} h_m \quad (4.32)$$

where  $\bar{h}_l$  is the average enthalpy carried by liquid phase slag,  $\bar{T}_{lsl}$  is the average temperature of liquid slag and approximated as the exiting slag temperature since the sensible heat of slag droplet is minor in energy balance,  $q_{g,lsl}$  is the heat flux from gas volume to liquid slag layer, which has been introduced in the beginning of Section 4.2.3.2,

$$\bar{h}_l = c_{p,l} \cdot \bar{T}_l \quad (4.33)$$

$$\bar{T}_{lsl} = \frac{T_{lsl,0} + T_m}{2} \quad (4.34)$$

$$q_{lsl,ssl} = \lambda_{lsl} \frac{T_{lsl,0} - T_m}{\delta_{lsl}} \quad (4.35)$$

With the Equations (4.33) ~ (4.35) above, the differential equation of the liquid slag layer surface temperature change can be derived as follow:

$$\frac{dT_{lsl,0}}{dt} = 2 \cdot \frac{q_{g,lsl} - \lambda_{lsl} \frac{T_{lsl,0} - T_m}{\delta_{lsl}} + c_{p,lsl} \left[ \frac{m_{lsl,in}}{A_{lsl}} (T_g - \bar{T}_{lsl}) + \phi_m (T_m - \bar{T}_{lsl}) \right]}{\rho_{lsl} c_{p,lsl} \delta_{lsl}} \quad (4.36)$$

From this equation it is obvious that the temperature change of liquid layer is mainly caused by the unbalance of heat fluxes. Once the gasification temperature change, the energy balance within the slag layer will be broken hence mass and temperature will both change with time. Meanwhile, the energy stored by slag layer will influence the gas volume temperature as well. Hence, the dynamic behavior can be studied since there are conservation of energy and mass in both liquid and solid slag layers.

Finally the solid slag layer is modelled. The only mass transfer of solid slag layer is the melting flow to liquid layer, thus the mass balance of the solid slag layer can be deducted as below:

$$\frac{d\delta_{ssl}}{dt} = - \frac{\phi_m}{\rho_{ssl}} \quad (4.37)$$

where  $\phi_m$  is the melting slag mass flow rate per unit square,  $\delta_{ssl}$  is the thickness of solid slag layer and  $\rho_{ssl}$  is the solid slag density. The energy balance Equation (4.38) of the solid slag

layer below is deduced by analysing the heat flux inputs and outputs, the input is the heat flux transferred from liquid slag layer and the outputs include the heat flux transferred from solid layer to refractory wall and the enthalpy carried out by melting solid slag flow:

$$c_{p,ssl} \rho_{ssl} \delta_{ssl} \frac{d\bar{T}_{ssl}}{dt} + \rho_{ssl} \bar{h}_{ssl} \frac{d\delta_{ssl}}{dt} = q_{lsl,ssl} - q_{ssl,w} - \phi_m h_m \quad (4.38)$$

where  $\bar{T}_{ssl}$  is the average temperature of solid slag layer, since the temperature file in slag layer is assumed to be linear. It can be calculated from the average value of melting temperature and refractory wall temperature (4.34)

$$\bar{T}_{ssl} = \frac{T_w + T_m}{2} \quad (4.39)$$

The heat flux from solid slag layer to refractory wall can be calculated by Equation (4.40) below:

$$q_{ssl,w} = \lambda_{ssl} \frac{T_m - T_w}{\delta_{ssl}} \quad (4.40)$$

where  $\lambda_{ssl}$  is the thermal conductivity of solid slag layer and  $\delta_{ssl}$  is the solid layer thickness.

The energy carried by melting slag flow contains its sensible enthalpy and the transition enthalpy, which is shown in Equation (4.41) below, since the transition enthalpy  $\Delta h_m$  can be approximated as 0, the total enthalpy can be considered as the sensible heat carried by melting slag flow.

$$h_m = c_{p,lsl} T_m + \Delta h_m \quad (4.41)$$

Hence derive the Equation (4.38) can be derived as Equation (4.42)

The energy balance of solid layer

$$\frac{d\delta_{ssl}}{dt} = \frac{\lambda_{lsl} \frac{T_{lsl,0} - T_m}{\delta_{lsl}} - \lambda_{ssl} \frac{T_m - T_w}{\delta_{ssl}} - \frac{1}{2} \rho_{ssl} \delta_{ssl} c_{p,ssl} \frac{dT_w}{dt}}{\rho_{ssl} [c_{p,ssl} (\frac{T_m - T_w}{2})]} \quad (4.42)$$

Based on the energy balance of refractory wall, Equation (4.43) can be derived, the input energy is the heat flux transferred from solid slag layer, the output is the heat flux transferred from refractory wall to metal tube of the steam circuit. Based on the linear temperature profile Assumption 10), the average temperature of refractory wall is derived as Equation (4.44),

$$\rho_w \delta_w c_{p,w} \frac{d\bar{T}_w}{dt} = q_{ssl,w} - q_{w,tube} \quad (4.43)$$

$$\bar{T}_w = \frac{T_w + T_{tube}}{2} \quad (4.44)$$

where  $q_{ssl,w}$  is the heat flux from refractory wall to water fall metal tube.  $\bar{T}_w$  is the average temperature of refractory wall. The water fall tubes are filled with medium pressure saturated steam. Based on the calculation, the metal tube temperature difference with the saturated water is within 1K due to the very small dimension of the tube wall (6mm) and relative large thermal conductivity of metal tube thermal conductivity (40W/m K), hence  $T_{tube}$  can be approximately considered as saturated water temperature in 4 MPa, which is 523K (Yang et al., 2011). Thus the differential equation for refractory wall temperature change can be derived as (4.47):

$$\bar{T}_w = \frac{T_w + T_{sw}}{2} \quad (4.45)$$

$$q_{w,tube} = \lambda_w \frac{T_w - T_{tube}}{\delta_w} \quad (4.46)$$

$$\frac{dT_w}{dt} = 2 \cdot \frac{q_{ssl,w} - q_{w,tube}}{\rho_w \delta_w c_{p,w}} \quad (4.47)$$

Hence the differential Equation (4.48) can be further derived for the change of solid slag thickness by substituting Equations (4.43) to (4.47) to Equation (4.42):

$$\frac{d\delta_{ssl}}{dt} = \frac{\lambda_{lsl} \frac{T_{lsl,0} - T_m}{\delta_{lsl}} - \lambda_{ssl} \frac{T_m - T_w}{\delta_{ssl}} - \frac{\rho_{ssl} \delta_{ssl} c_{p,ssl}}{\rho_w \delta_w c_{p,w}} (\lambda_{ssl} \frac{T_m - T_w}{\delta_{ssl}} - \lambda_w \frac{T_w - T_{tube}}{\delta_w})}{\rho_{ssl} [c_{p,ssl} (\frac{T_m - T_w}{2})]} \quad (4.48)$$

### 4.3 Model Parameterization and Simulation Procedure

#### 4.3.1 Model Parameterization

The EL Cerrejon coal (Sun et al., 2011) is selected as the input feedstock for the model validation. In Chapter 3, the proximate analysis and element analysis data are used for the steady state model validation. The parameters are used here as the model inputs. Based on the input data in Table 4.1, the kick-off data of dynamic model can be calculated: the values are listed in Table 4.2.

Table 4.1 Input parameters of dynamic Shell gasifier model

Parameter	Unit	Data
Coal flow rate	kg/s	22.2
Oxygen flow rate	kg/s	18.648
Steam flow rate	kg/s	1.528
Transport nitrogen flow rate	kg/s	1.578
Operation pressure	bar	27

Raw syngas HHV	kJ	29009
Thermal conductivity of solid slag layer	kW/m K	1.6e-3
Thermal conductivity of liquid slag layer	kW/m K	1.4e-3
Thermal conductivity of refractory bricks	kW/m K	4.0e-3
Thermal conductivity of metal tube	kW/m K	0.04
Thickness of refractory wall	m	0.02
Thickness of metal tube	m	0.006
Syngas velocity	m/s	10
Liquid slag viscosity	Pois	$5.12e^{-6} \exp(23180/T)$
Melting temperature	K	1642
Saturated water temperature	K	523
Density of solid layer	kg/m <sup>3</sup>	2700
Density of liquid layer	kg/m <sup>3</sup>	2500
Gasifier height	m	16.8
Gasifier diameter	m	4.63
Bo	kW/m <sup>2</sup> K <sup>4</sup>	5.67e-11
$\gamma_g$	kW/ m <sup>2</sup> K	0.2
Emissivity	none	0.83

Table 4.2 Kick off data dynamic Shell gasifier model

Parameter	Unit	Data
Gas volume temperature	K	1886.4
Slag surface temperature	K	1812.0
Refractory wall temperature	K	1045.4
Heat flux from gas volume to wall area	kW	26257.46
Liquid slag layer thickness	mm	2.6
Solid slag layer thickness	mm	8.0
Exit slag mass flow	kg/s	1.056
Argon mole concentration	%	1.21
COS mole concentration	%	0.015
H <sub>2</sub> S mole concentration	%	0.13
N <sub>2</sub> mole concentration	%	3.53
CO mole concentration	%	61.98
H <sub>2</sub> mole concentration	%	27.07
CO <sub>2</sub> mole concentration	%	1.97
H <sub>2</sub> O mole concentration	%	4.09
CGE	%	80.07

### 4.3.2 Flow Chart for Simulation

Steady state parameterization is necessary for the model setting up before it is used for dynamic simulation with respond to step change of inputs. The input data of coal feed and blasts can be used in the syngas prediction model and the energy balance model to predict the steady state raw syngas contents mole concentration and temperature profile from syngas to slag layer by Newton-Raphson method, which is similar to the model introduced in Chapter 3. Then based on the energy balance of syngas, the heat flux transferred from gas volume to wall area can be calculated; in this step, the remaining fly ash and unreacted carbon are considered as parts of the syngas.

In the steady state, the exiting mass flow rate of slag layer equals to zero and the heat flux from gas volume to liquid slag layer surface, liquid layer to solid layer, solid layer to refractory wall surface, and refractory wall to metal tube are all the same. The steady state parameterization flowchart is shown below as Figure 4.5.

Based on the mass balance of slag slayer model and the pre-defined slag properties, the thickness of liquid slag layer equation can be calculated. It is possible to subsequently build equation of the refractory wall surface temperature with the predefined refractory bricks parameters and the metal tube temperature. Finally, the solid slag layer thickness can be calculated with the heat flux, melting temperature and the refractory wall temperature. Hence the steady state parameterization can be finished and the results can be used as kick-off parameters for the dynamic simulation.

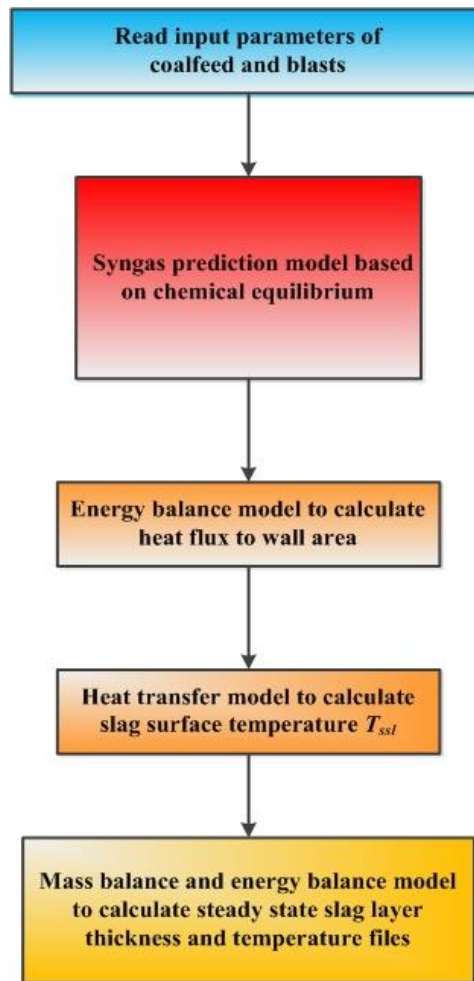


Figure 4.5 Flow chart of steady state model parameterization

The dynamic performance of Shell gasifier model is responded to the step change of input parameters. The most commonly used input parameters include oxygen/coal ratio and steam/coal ratio since the blasts are easier to be controlled than the dry coal feed. It is assumed that the step change of the oxygen input or steam input occurs at the 100th second during the operation process. The flow chart of calculation with the model is shown in Figure 4.6.



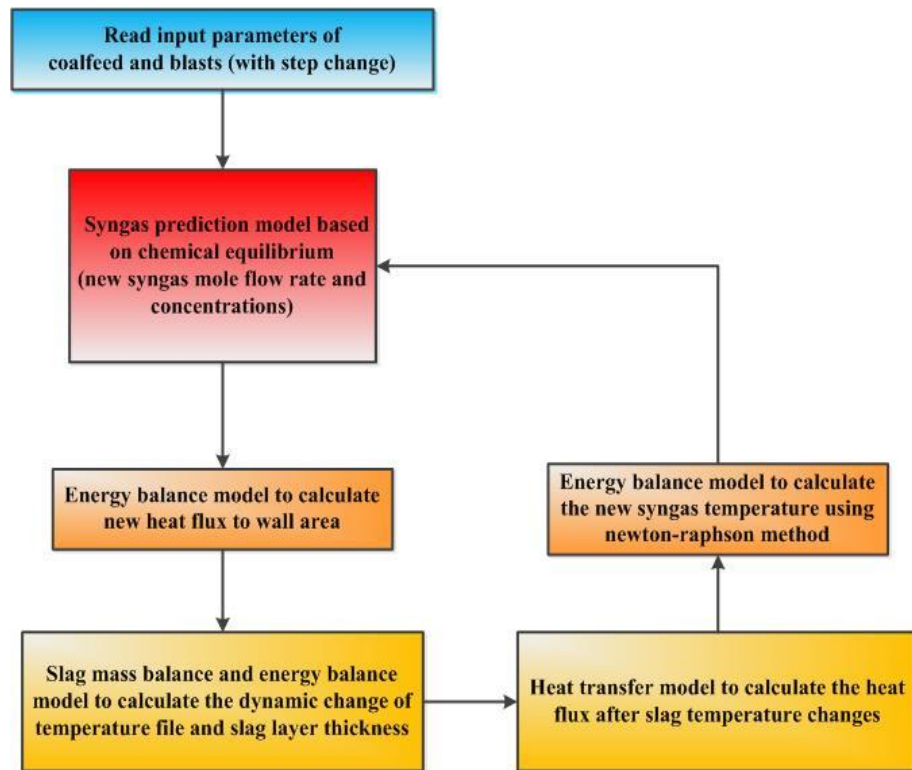


Figure 4.6 Flow chart of the dynamic performance simulation

During the dynamic simulation, when there is a step change in the inputs such as 1% increase of oxygen/coal ratio, the syngas prediction model and energy balance model will firstly calculate the syngas contents and gas temperature under the new condition by using Newton-Raphson method. Then the result of the changed heat flux transferred to slag surface will be used as input to the slag layer model. As the heat flux change, the original energy balance will be broken and cause the change of slag layer thickness and temperature file across the slag layers and refractory wall. Hence the new output from the slag layer model can be generated and the result of changed slag surface temperature will be used to recalculate heat flux in the heat transfer model with the changed gas temperature. The heat flux result generated by heat transfer model will subsequently be used as for syngas input prediction, and then the calculation of the following time step will start. The parameters involved in the calculation are shown in Figure 4.7, and the collected results of gas temperature, slag layer

thickness and temperature files across the slag layer will be shown and analyzed in the next section.

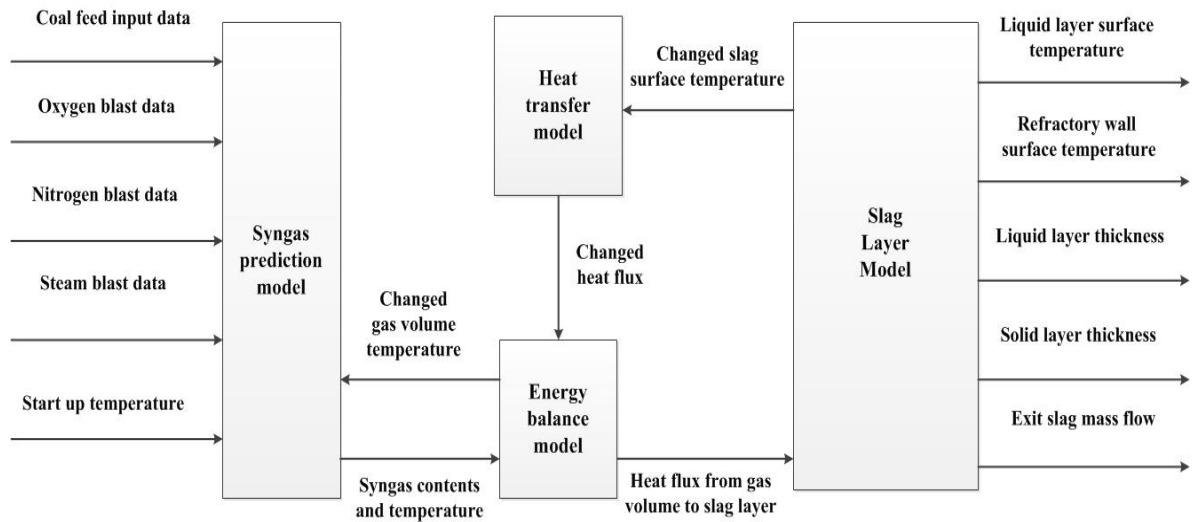


Figure 4.7 Whole process Schematics of Shell gasifier model

## 4.4 Results and Discussion

### 4.4.1 Results of Oxygen input step change 1% and 5%

The model is used to test the dynamic behavior of different working conditions. The first tested change is the 1% and 5% step change of oxygen/coal ratio and Figure 4.8 – Figure 4.19 reveal the subsequent dynamic performance of the gas volume, liquid slag layer surface temperature, refractory wall temperature, liquid slag layer thickness and average temperature, solid slag layer thickness and average temperature, etc. The Syngas contents concentration and CGE change with response to 1% and 5% input oxygen rise are analyzed as well.

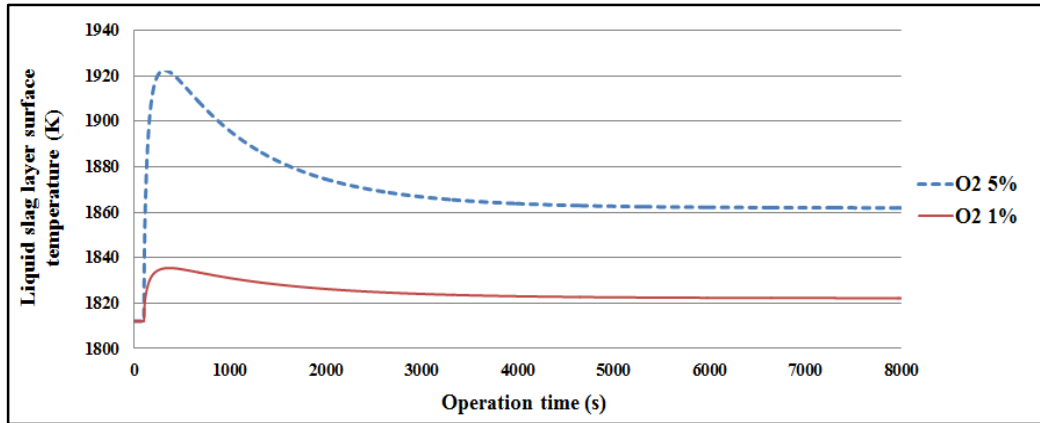


Figure 4.8 Dynamic change of raw syngas temperature with 1% and 5% oxygen input rise

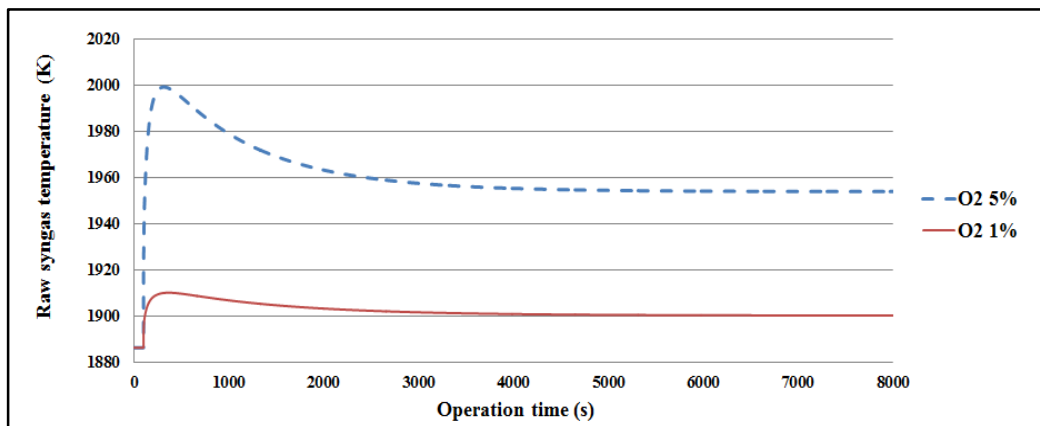


Figure 4.9 Dynamic change of liquid slag surface temperature with 1% and 5% oxygen input rise

As shown in Figure 4.8: when oxygen input rises, the gasification temperature will quickly raise (almost a step change) and enhance the combustion of fuel gas in the first stage, and then it will drop slightly until reaches the new equilibrium state. With 1% oxygen input rise, the gas temperature will go through a rise of around 25K, but the change with 5% oxygen input, the gas temperature rise is as high as 120K. A similar change of the liquid layer surface temperature is shown in Figure 4.9. As the gas volume temperature changes, more heat flux will be transferred to slag layer. Hence the liquid slag layer surface temperature changes by following the gas volume temperature. The heat flux to refractory wall will increase as well in this stage until a new stable state is established. The energy conservation of slag layer actually causes the relative slower change than the gas temperature itself. The dynamic

performance of refractory wall temperature shown in Figure 4.10 has revealed this point, which is similar to the trend demonstrated in reference (Yang et al., 2011). The dynamic change of liquid and solid slag layer average temperature are shown in and Figure 4.11 and Figure 4.12:

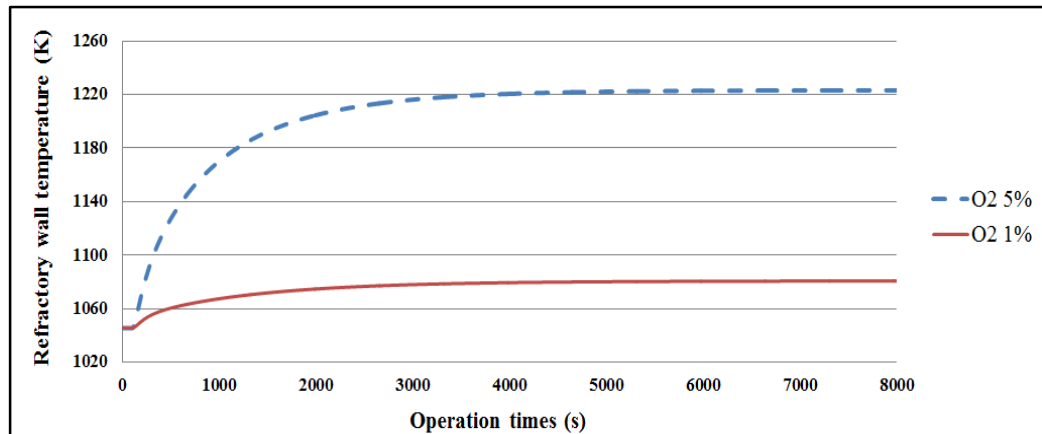


Figure 4.10 Dynamic change of refractory wall temperature with 1% and 5% oxygen input rise

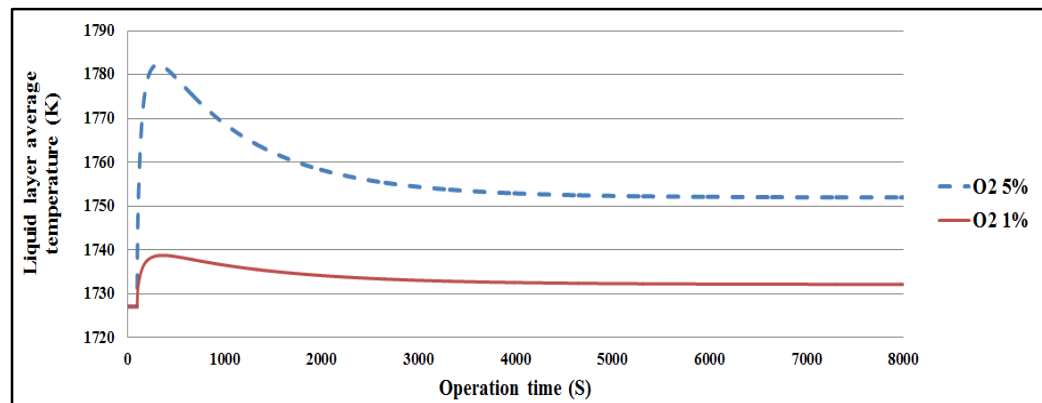


Figure 4.11 Dynamic change of liquid layer average temperature with 1% and 5% oxygen input rise

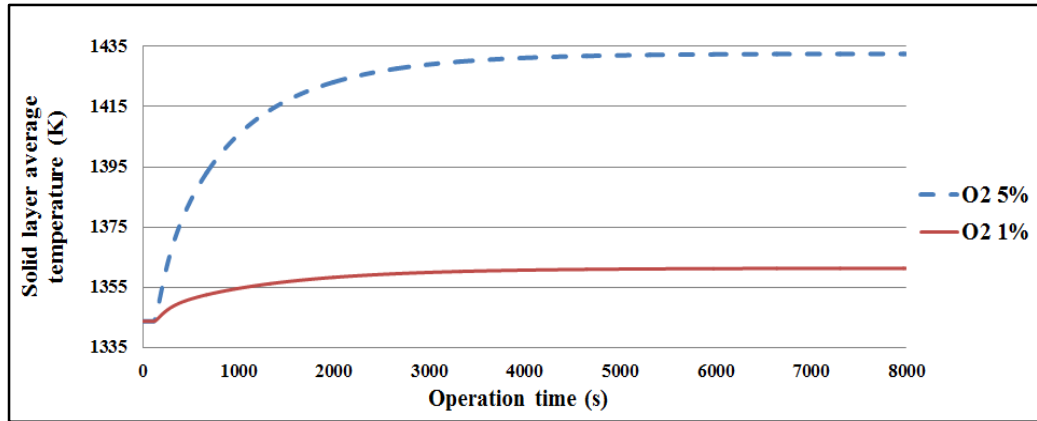


Figure 4.12 Dynamic change of solid layer average temperature with 1% and 5% oxygen input rise

With the temperature increases in the first stage, there will be more heat transferred from the gas volume through the slag layer to the refractory wall. Hence the solid slag layer starts to melt and the thickness of solid slag layer will decrease. The exiting slag mass flow rate, liquid slag layer thickness and solid slag layer thickness will change as well. The trends are shown in Figure 4.13 to Figure 4.15.

In the first stage, the viscosity of liquid slag layer is a function of temperature, when temperature rises, the viscosity of liquid slag layer will reduce and the flow speed of liquid slag will rise hence the exit slag flow rate will increase as well. In the second stage when temperature drops to reach a new state, the viscosity will subsequently reduce as well; the exit slag flow will reduce until reaches the original value and establish new balance state.

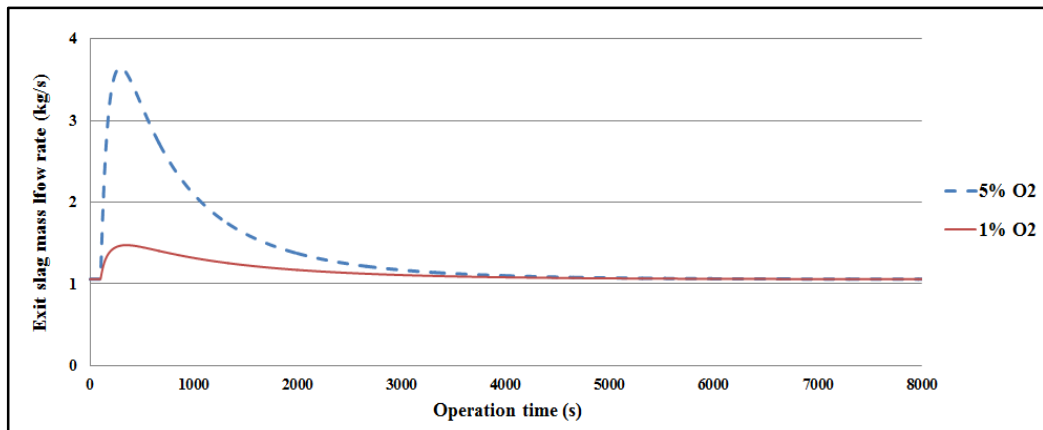


Figure 4.13 Dynamic change of exit slag mass flow with 1% and 5% oxygen input rise

Figure 4.13 shows that the exiting slag mass flow rate increases and exceeds the input slag flow rate which equals to its original value of steady state. In the second stage when gas temperature drops, the exiting mass flow rate will decrease as well until reach the same value as input mass flow rate. Similar trend of exit slag mass flow rate has been reported in references (Yang et al., 2011, Sun et al., 2011, Schoen, 1993).

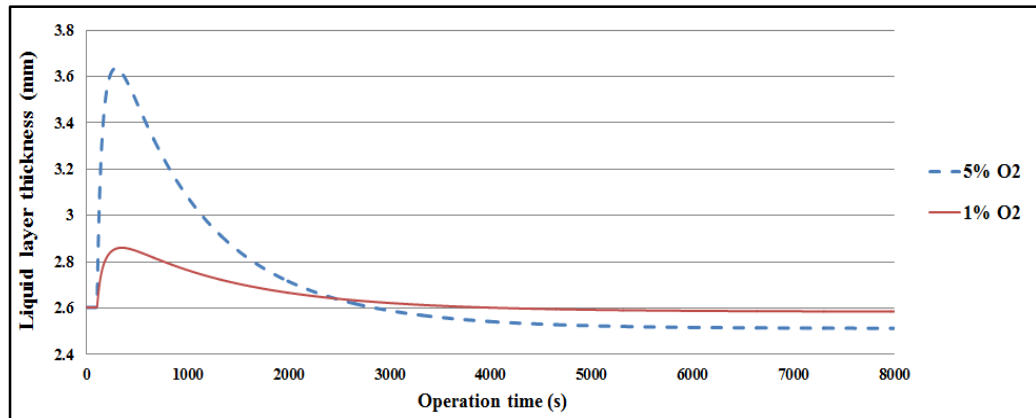


Figure 4.14 Dynamic change of liquid slag layer thickness with 1% and 5% oxygen input rise

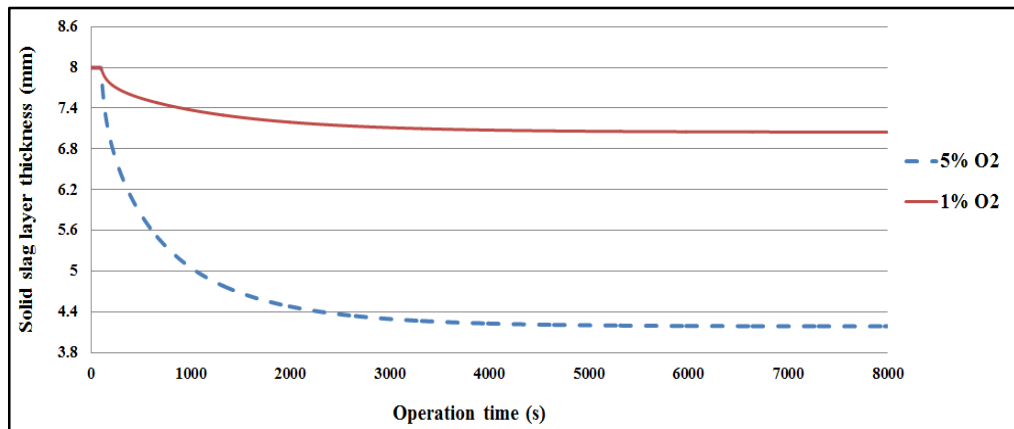


Figure 4.15 Dynamic change of solid slag layer thickness with 1% and 5% oxygen input rise

Figure 4.14 and Figure 4.15 show the dynamic change of liquid slag layer and solid slag layer thickness, the trends are similar with the results of Schoen (Schoen, 1993) and Seggiani (Seggiani, 1998). For the liquid slag layer, slag temperature rise causes the melting flow from solid slag to liquid slag rise, which is larger than the exit mass flow increase; hence the liquid slag layer thickness increases. In the second stage, the slag temperature drops, the exit slag

mass flow and melting slag mass flow both drop; hence the liquid slag layer thickness will drop as well. At the new stable state, the liquid slag layer thickness will be lower than the original state, since the steady temperature in this state is higher than the kick-off temperature.

Figure 4.15 reveals the dynamic change of solid slag layer, which is purely caused by the melting slag mass flow. The melting of solid slag layer delays the influence of the large temperature rise to refractory wall, which protects the wall from being burned by extremely hot gas volume. This effect is more obvious with the 5% oxygen input rises as the solid slag layer has dropped around 50%, if the solid slag layer disappears, the refractory bricks will be further damaged and may cause unexpected shut down accidents. The membrane wall behind refractory wall will be under the threat of hot gas volume once the bricks are burned, it is costly to repair. Hence in industry, the existence of slag is a very effective way to protect the inner lining of gasifier, new technology has been developed by Tsinghua University (Yang et al., 2011), which can extend gasifier refractory bricks and nozzles life by tuning the slagging process within the gasifier.

In terms of the syngas contents, with more oxygen inputs to the gasifier and the subsequent temperature rise in the first stage, the fuel gas CO and H<sub>2</sub> will be consumed due to the enhanced combustion and the CO<sub>2</sub> concentration will rise due to the combustion production (shown in Figure 4.16 to Figure 4.18).

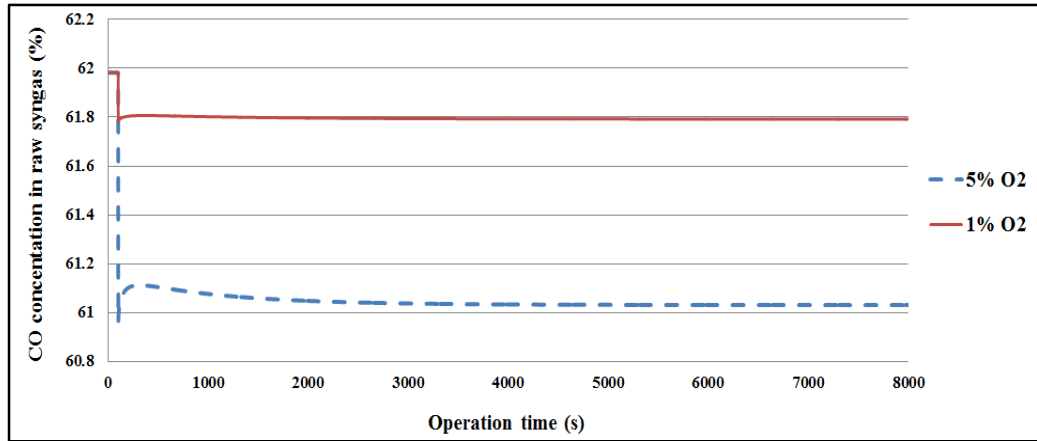


Figure 4.16 Dynamic change of CO concentration with 1% and 5% oxygen input rise

Figure 4.16 shows the dynamic change of CO concentration. In the first stage, with the oxygen input step rise and the subsequent temperature step rise, the combustion of CO is enhanced. In the second stage, the water gas shift reaction equilibrium moves left due to the temperature rise, which will slightly cause the increase of CO concentration, but this doesn't change the fact that the CO concentration is lower than the original kickoff state when it reaches the new steady state. The consumption of fuel gas CO in gasifier is not expected for IGCC process, since this will make the CGE drop hence causes the net efficiency drop.

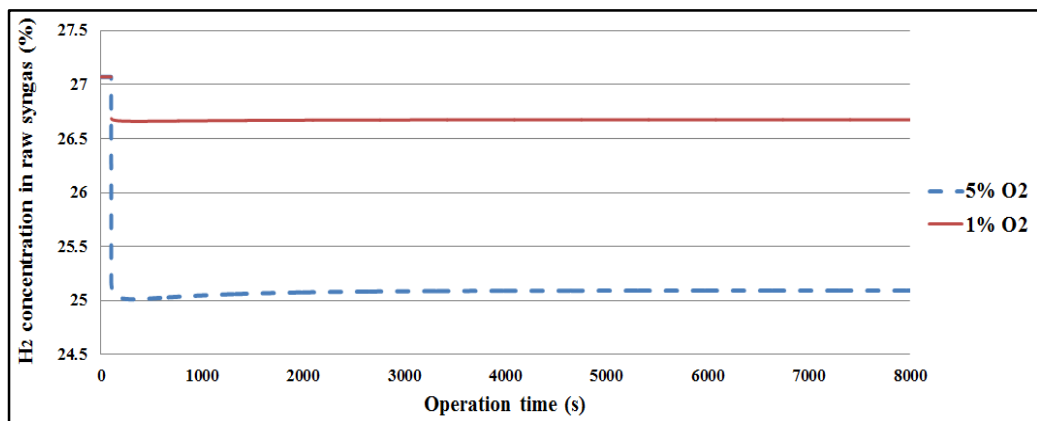


Figure 4.17 Dynamic change of H<sub>2</sub> concentration with 1% and 5% oxygen input rise



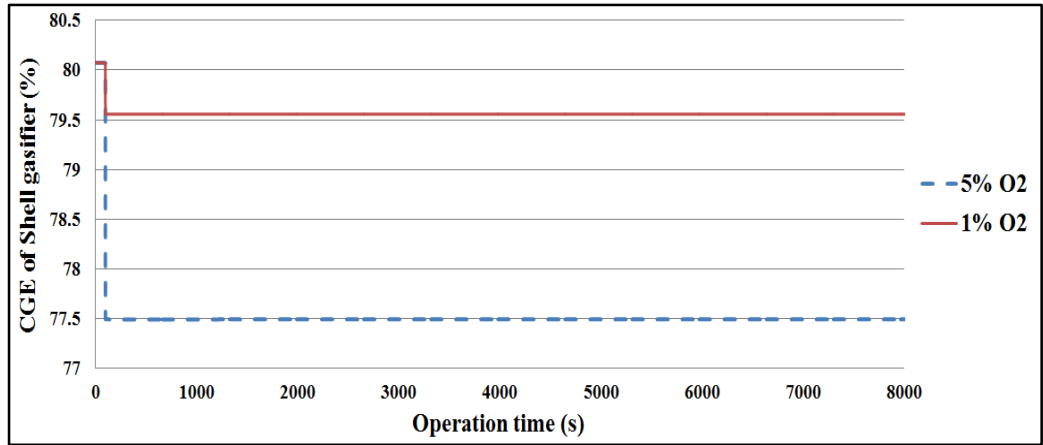


Figure 4.18 Dynamic change of CGE 1% and 5% oxygen input rise

Figure 4.17 shows the dynamic change of  $H_2$  concentration. Similar to  $CO$ , the consumption caused by  $H_2$  combustion is enhanced in the first stage. The equilibrium right-forward move of shift reaction causes a rise of  $H_2$  in the second stage. But the overall generation of  $H_2$  will decrease comparing with the kickoff state. Govind's (Govind and Shah, 1984) study of entrained gas flow gasifier and Vamvuka's (Vamvuka et al., 1995b) experiments results have proposed the similar conclusion. The dynamic trend of these fuel gases are similar to the results of Schoen and Sun's models (Schoen, 1993, Sun et al., 2011). The CGE of shell gasifier will decrease from 80.07% to 79.7% and 77.5% respectively for 1% and 5% oxygen input rises.

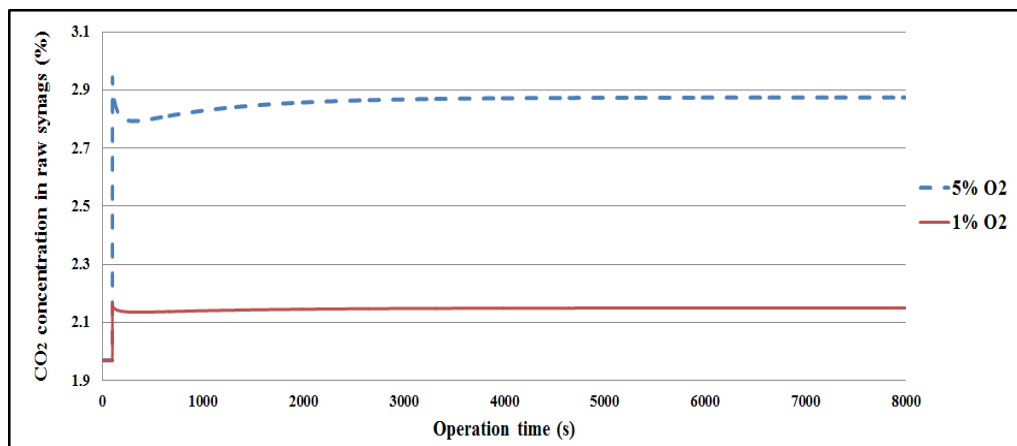


Figure 4.19 Dynamic change of  $CO_2$  concentration with 1% and 5% oxygen input rise

Figure 4.19 shows the dynamic change of CO<sub>2</sub> concentration with respond to 1% and 5% oxygen input rises. Unlike CO and H<sub>2</sub>, CO<sub>2</sub> rises in the first stage since the combustion of CO yields more CO<sub>2</sub>, the slight drop in the second stage is caused by equilibrium move as well. The final concentration of CO<sub>2</sub> is higher than kickoff state.

For the current model, the oxygen/coal ratio changes between 0.84 and 0.88, in this value range, the increase of oxygen input will cause CGE drop. The similar conclusion has been drawn in references (Hao Xie, 2013). The range of CGE value matches with the reference as well (J.Eurlings, 1999b).

#### 4.4.2 Results of steam input step change 20%

Besides oxygen/coal ratio, steam/coal ratio is another essential parameter to control the gasifier operation; normally the steam/coal ratio needs to be changed simultaneously when the oxygen input changes. To evaluate the influence purely caused by steam/coal ratio step change, the oxygen/coal ratio has been maintained as the original value in this part. The results of 1% oxygen input rise are shown together with 20% steam input rise together to evaluate which parameter will cause bigger influence to the gasifier operation.

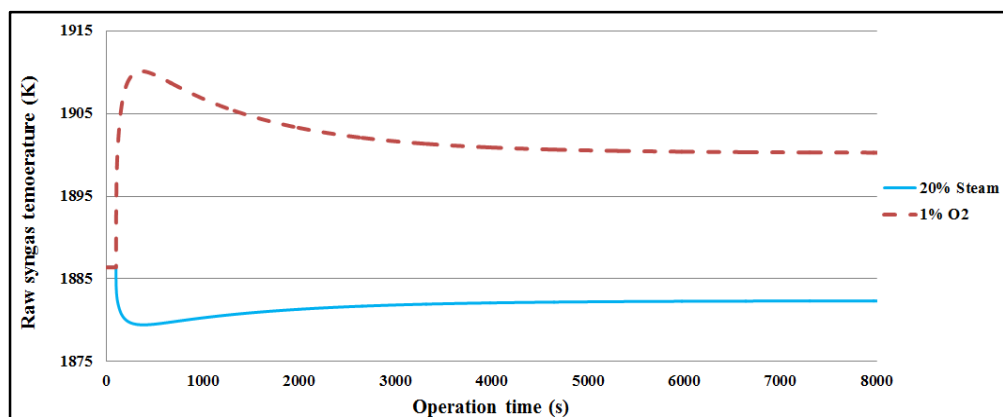


Figure 4.20 Dynamic changes of gas temperature with 20% steam / 1% Oxygen input rises

As shown in Figure 4.20 the increase of steam input will enhance the endothermic gasification reactions and cause the temperature drop in the first stage. Then temperature will slightly increase until it reaches the steady state. Comparing with the margin of temperature change of 1% oxygen input rise, the effect caused by 20% rise of steam input is weaker.

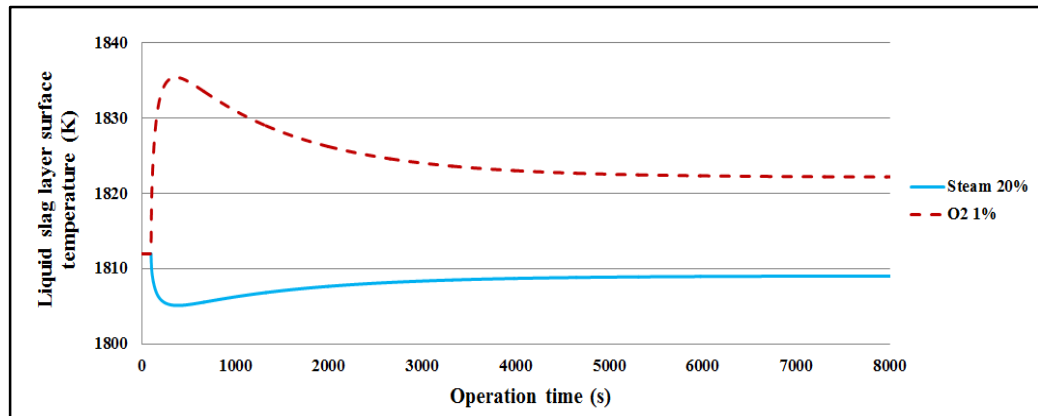


Figure 4.21 Dynamic changes of liquid layer surface temperature with 20% steam / 1% Oxygen input rises

As shown in Figure 4.21, in the first stage, the immediate drop of temperature will cause the heat flux transferred to slag layer decrease, hence the temperature of liquid layer surface temperature drops. It will reach new steady state; the temperature in this state is lower than the kickoff state. Similarly as gas temperature, 20% steam input rise's effect is weaker than 1% oxygen input rise.

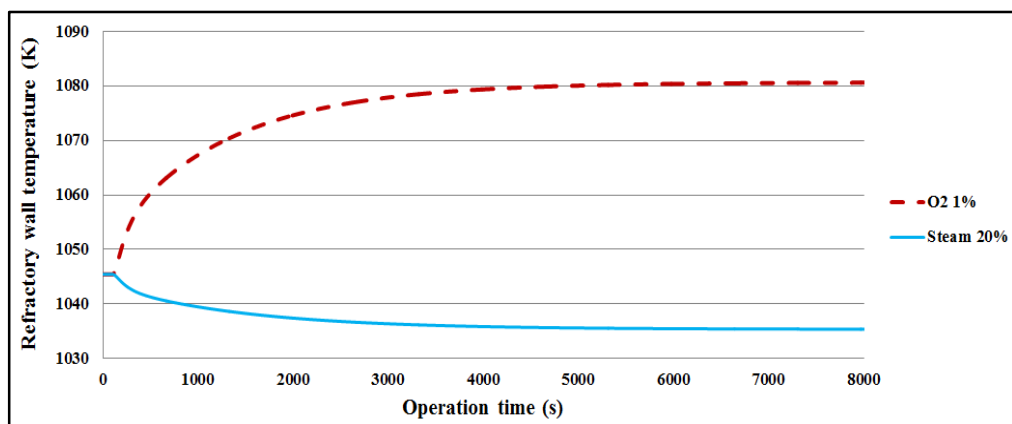


Figure 4.22 Dynamic changes of refractory wall temperature with 20% steam/1% Oxygen input step rises

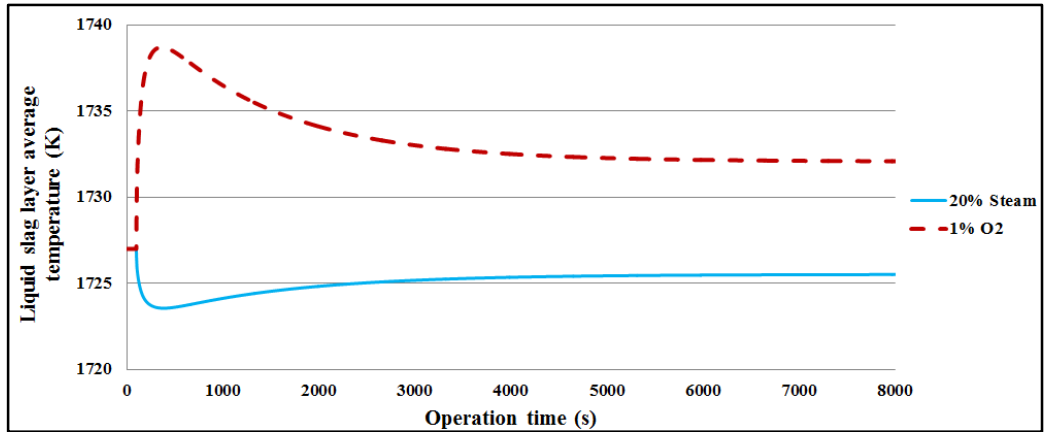


Figure 4.23 Dynamic changes of liquid slag average temperature with 20% steam/1% Oxygen input step rises

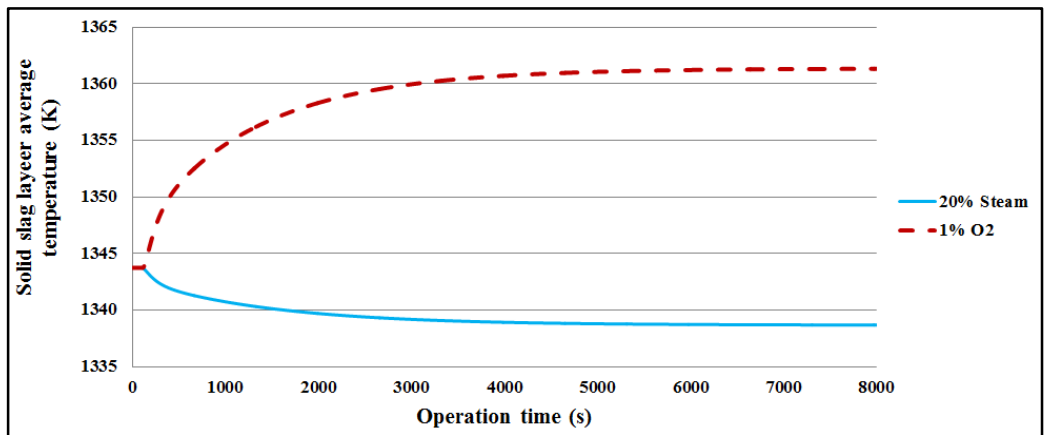


Figure 4.24 Dynamic changes of solid slag average temperature with 20% steam/1% Oxygen input step rises

As shown in Figure 4.22 to Figure 4.23 since the heat flux from gas volume to slag layer decrease with the 20% steam input, the temperature profiles within the slag layer will all decrease until new steady state is reached. The energy conservation in slag layer makes the change of these parameters much slower than the change of gas and slag surface temperatures.

Similar with gas volume temperature change, the effect caused by 20% steam step rise is weaker than that caused by 1% oxygen step rise. From Figure 4.25 to Figure 4.27, the dynamic change of exit slag mass flow rate and the slag layers thicknesses are shown.

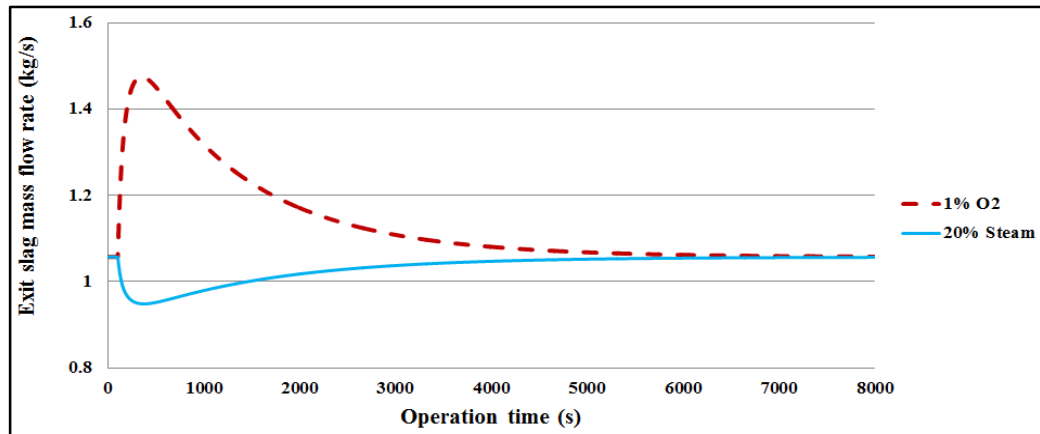


Figure 4.25 Dynamic change of exit slag mass flow rate with 20% steam/1% Oxygen input step rises

As shown in Figure 4.25, the exit slag mass flow rate will decrease; this is caused by the temperature drop of gas volume. In this stage, more liquid slag droplets will solidify and become solid slag, which causes the drop of exit mass flow rate. The mass flow rate will gradually rise in the second stage until it reaches the new steady state when the slag layers don't change, hence the value of exit mass flow rate equals to the kickoff state value. The effect of steam input change is weaker than that of oxygen input change.

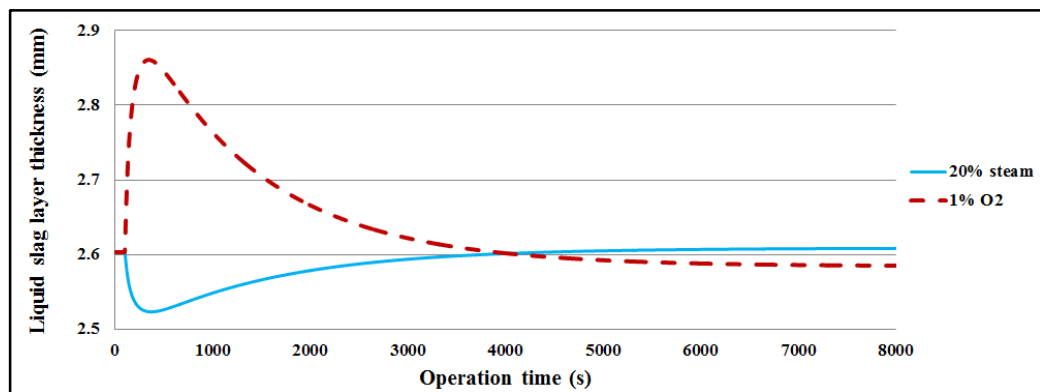


Figure 4.26 Dynamic change of liquid slag layer thickness with 20% steam/1% oxygen input step rises

As shown in Figure 4.26, the liquid slag layer decreases since more liquid slag droplets solidify to solid layer. In this stage, the melting flow of solid slag layer becomes 'negative'. The thickness change margin is less than that of oxygen input change as well.

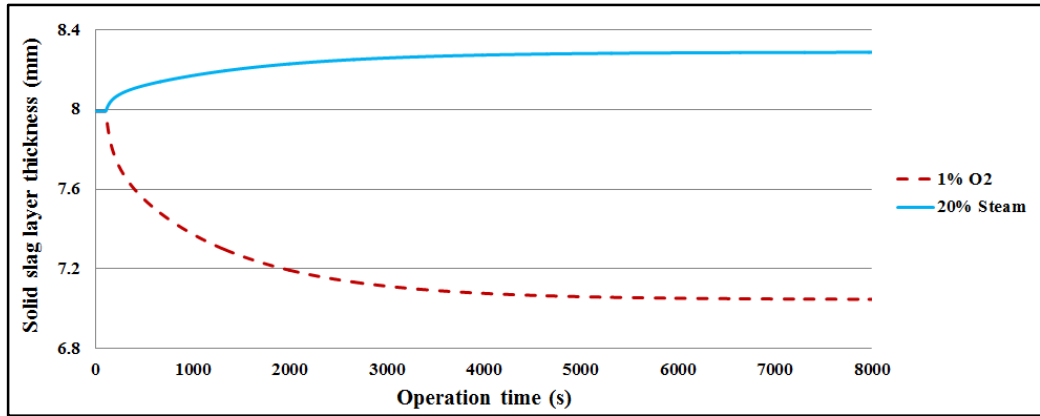


Figure 4.27 Dynamic change of solid slag layer thickness with 20% with 20% steam/1% oxygen input step rises

Figure 4.27 shows the dynamic change of solid slag layer with response to 20% steam input change. As the temperature file changes, the solidification and agglomerating of liquid slag layer cause the rise of solid slag layer thickness. Similar trends are found in references (Yang et al., 2011, Sun et al., 2011).

The syngas concentration dynamic changes which are caused by steam input change are shown in Figure 4.28 to Figure 4.30 below. Apparently, the impact of steam input change to syngas concentration is different from that caused by oxygen input step change.

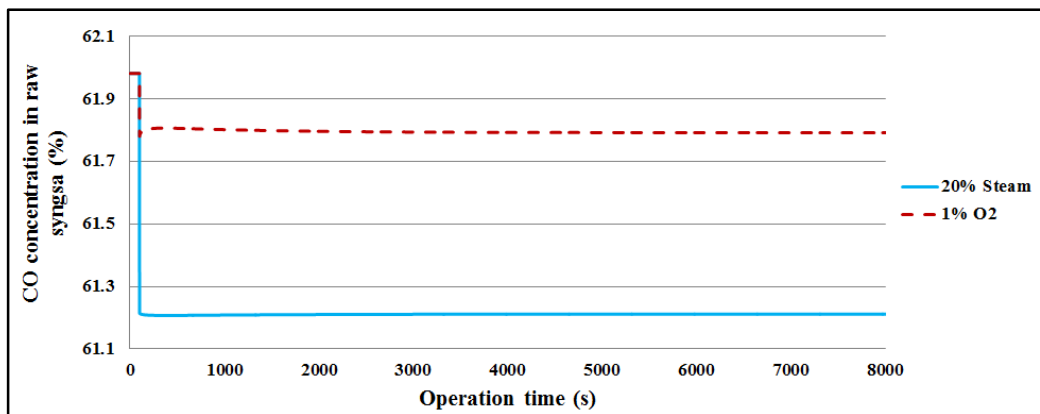


Figure 4.28 Dynamic change of CO concentration with 20% steam/1% oxygen input step rises

In the first stage, temperature drop and increase of steam input enhance the gasification process and weaken the combustion process. Apparently, the gasification process takes

advantage in this stage, the shift reaction moves to right and causes more CO is converted with steam to  $H_2$  and  $CO_2$ , the change margin is higher than that caused by oxygen input change.

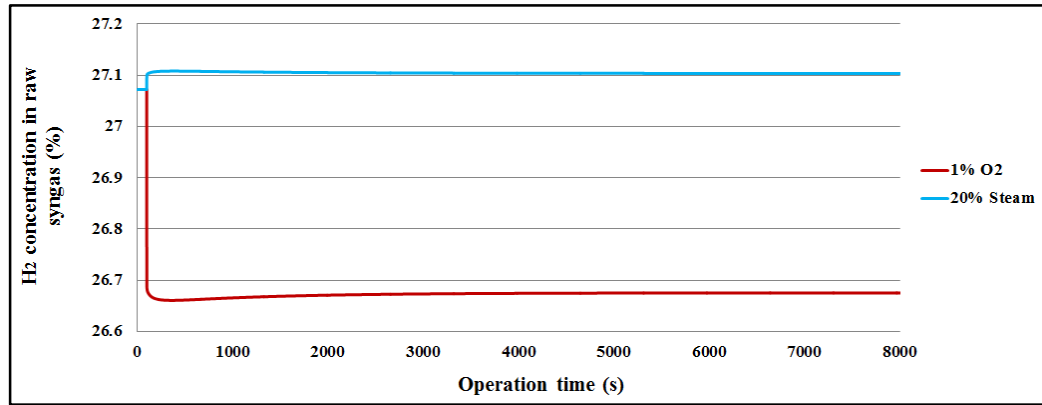


Figure 4.29 Dynamic change of  $H_2$  concentration with 20% steam/1% oxygen input step rises

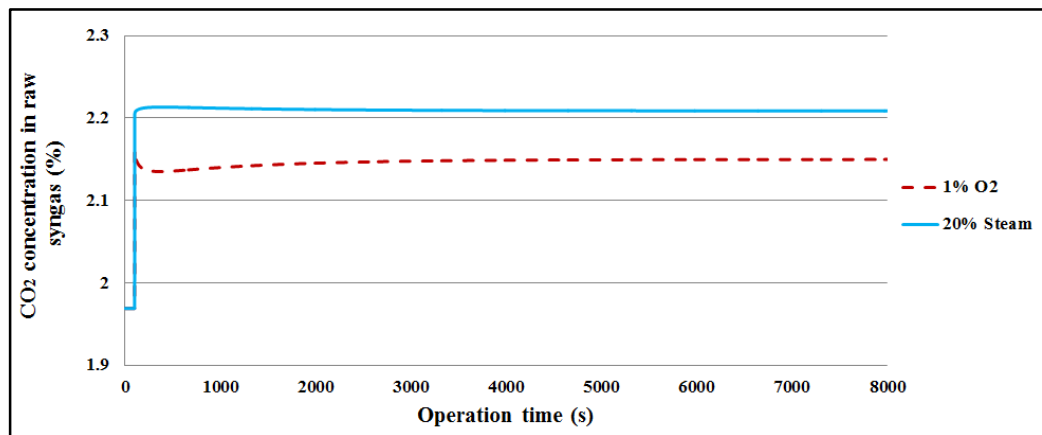


Figure 4.30 Dynamic change of  $CO_2$  concentration with 20% steam/1% oxygen input step rises

As shown in Figure 4.29, the enhanced gasification process and weakened combustion process will both cause the increase of hydrogen concentration. But the change margin is very small comparing with that caused by oxygen input rise. Figure 4.30 shows that the  $CO_2$  concentration rises in the first stage as enhanced shift reaction generation increase. The trends of the main syngas concentration agree with the results of Sun's model (Sun et al., 2011).

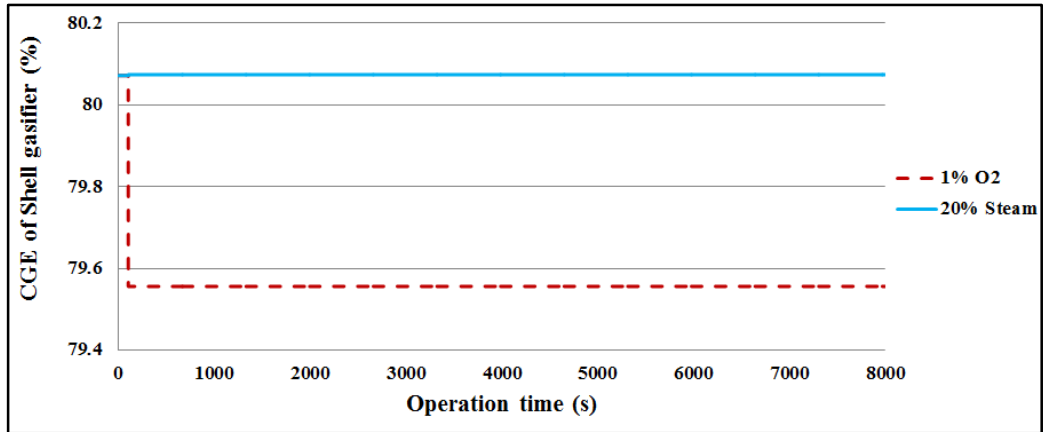


Figure 4.31 Dynamic change of CGE with 20% steam/1% oxygen input step rises

As shown in Figure 4.31, the CGE for steam increase condition almost maintain as the original value, which means the 20% increase of steam is much moderate comparing with oxygen input rise condition.

This model of Shell gasifier is used to analyze the dynamic response of key parameters to the step change of oxygen/coal ratio and steam/coal ratio. The result shows similar trends of gas and slag layers temperature profile with reference (Sun et al., 2011, Yang et al., 2011, Schoen, 1993). The dynamic simulation of Shell gasifier with slagging process reveals the following conclusions:

1. The oxygen input causes more rigorous effect to the gasifier operation than steam input. Hence it needs to be controlled very carefully. As the results of 5% output, the gas temperature undertook a step temperature jump of about 120 K, and the solid slag layer drops by almost 50%, which is extremely dangerous in real operation as the slag layer plays a role to protect the refractory wall when its thickness is a suitable value. Hence a limit for the current gasifier can be given, coal type and input data, once the oxygen input exceeds 7% rise, the solid slag layer will completely melt and cause damage to the refractory wall and membrane wall behind it.



2. The CGE drops in the working condition when oxygen input rises. The oxygen input must be well controlled to maintain ideal working condition and high net efficiency.
3. Steam input shows much weaker influence in the temperature profiles and slag thickness change, but cause relative stronger influence to the syngas contents concentration than the oxygen input does. The steam input flow rate in Shell gasifier is much smaller than oxygen flow rate, but it doesn't mean the effect caused by steam input can be ignored from the dynamic simulation study and further control strategy application may be necessary.
4. Both input values need to be carefully tuned to maintain the ideal operation of the gasifier. As the similar conclusion proposed in Chapter 3, the input oxygen and steam need to be controlled in a range by considering the coal feed types and working conditions.
5. Although the slag layer can protect the refractory wall from being burned by extremely hot syngas, its thickness can't increase without limit since it can also cause the thermal resistance for heat flux transfer from gas volume to the membrane wall. The steam generated in this water circuit will be used in the combined cycle power plant for electricity generation.
6. The dynamic simulation of gasifier can successfully reveal the operation of gasifier and predict the results of key parameters change. The dynamic trends of key parameters can perfectly match with references (Schoen, 1993, Yang et al., 2011, Sun et al., 2011). This dynamic model can provide raw syngas to the auxiliary modules downstream and available for future controller application to the IGCC model.

## **Chapter 5 Auxiliary Modules In Gasification Enabled Plant**

The raw syngas generated by gasifier will need further treatment before entering the power generation sector. The treatment of syngas includes quench cooling, further cooling for heat recovery, sulphur removal, and water gas shift reaction for non-carbon capture process. The model developed in this thesis is supposed to be connected with a Pressure Swing Adsorption (PSA) carbon capture model which is developed by the project co-operator and will be described in Chapter 7. Hence the shift reactor is compulsory in the project either for non-capture process or capture ready process.

Chapter 5 introduces the main auxiliary modules in a gasification enabled plant, the syngas clean up includes syngas quench, syngas cooling, sulphur removal and shift reaction process. The quench model is developed based on a pre-defined “fixation temperature” to predict the quenched syngas contents with respond to the temperature drop. The following modules are developed based on a Simulink toolbox-Thermolib, which provides either pre-built or customised blocks for the modelling of basic thermodynamic processes. The governing equations for the mostly used blocks such as heat exchanger, chemical reactor and mixer are introduced in this chapter as well

### **5.1 Introduction of Thermolib Software**

The auxiliary modules of IGCC power plants are developed by using a Simulink-based toolbox, Thermolib. Before starting to give detailed introduction of auxiliary modules, it is necessary to show the basic functions of Thermolib, especially the main thermodynamic laws this software is based on. Thermolib provides graphical blocks library for simulation of thermodynamic process, such as state change, chemical reactions, heat transfer, etc. The main

advantage of Thermolib includes a reliable database for different properties, which provides valid support for the thermodynamic state parameters calculation.

### 5.1.1 Gas Phase Calculation

There are two options for the modelling of gas phase properties in Thermolib, ideal gas mode and real gas mode. The model developed in this project is based on ideal gas model. The calculation of gas thermodynamic properties is based on the ideal gas law:

$$PV = nRT \quad (5.1)$$

where  $P$  denotes the gas pressure,  $V$  denotes the gas total volume,  $n$  denotes the mole amount of gas and  $T$  is the gas temperature. These parameters are the main state parameters in the thermodynamic calculation.  $R$  is the universal ideal gas constant, with the value of 8.3145 J/mol K. Thermolib uses the modified ideal gas law equation during the modelling process:

$$\begin{aligned} PV_m &= RT, \\ V_m &= \frac{V}{n} \end{aligned} \quad (5.2)$$

where  $V_m$  denotes the mole volume of gas properties, its definition Equation (5.2) is shown as above. For the ideal gas mode, the calculation of specific heat at constant pressure, enthalpy, entropy are based on the equations (5.3) to (5.6) as described below:

The mole specific heat at constant pressure  $C_{p,m}$  is calculated based on NASA polynomials (Eutech, 2013) :

$$c_{p,m} = R \cdot (A_0 + B_0 \cdot T + C_0 \cdot T^2 + D_0 \cdot T^3 + E_0 \cdot T^4) \quad (5.3)$$

where  $A_0$ ,  $B_0$ ,  $C_0$ ,  $D_0$ ,  $E_0$  are specific constants for different gas,  $T$  is the gas temperature.

Hence the mole enthalpy of ideal gas can be calculated by:

$$h_m - h_{298.15}^0 = R \cdot (A_0 \cdot T + B_0 \cdot \frac{T^2}{2} + C_0 \cdot \frac{T^3}{3} + D_0 \cdot \frac{T^4}{4} - \frac{E_0}{T} + F_0 - H_0) \quad (5.4)$$

When standard  $h_{298.15}^0$  is the mole standard formation enthalpy for ideal gas at standard reference state 298K,  $1.01 \times 10^5$  Pa.  $F_0$  and  $H_0$  are specific constants for different gas. The mole entropy can be calculated by Equation (5.5):

$$s_m = s_{m,NASA} - R \ln\left(\frac{P}{P_{ref}}\right) \quad (5.5)$$

where  $P_{ref}$  is the reference pressure,  $s_{m,NASA}$  is calculated based on NASA polynomials below:

$$s_{m,NASA} = R \cdot (A_0 \cdot \ln(T) + B_0 \cdot T + C_0 \cdot \frac{T^2}{2} + D_0 \cdot \frac{T^3}{3} - E_0 \cdot (\frac{2}{T^2}) + G_0) \quad (5.6)$$

The constants A-G of specific gas can be collected from the public chemical database NIST webbook and put into the chemical database of Thermolib. The chemical database structure is shown in Figure 5.1:

		Chemical Media Data	
	Species	CH4	H2O
	comment		
	formula		
	full_name	methane	water
	species_type		Steamtable
NASA-Polynomes			
A-element (high temp. range) [-]	NASA_A1_g	1.6355264300E+00	2.6770378700E+00
B-element (high temp. range) [1/K]	NASA_B1_g	1.0084279500E-02	2.9731832900E-03
C-element (high temp. range) [1/K^2]	NASA_C1_g	-3.3691625400E-06	-7.7376969000E-07
D-element (high temp. range) [1/K^3]	NASA_D1_g	5.3495866700E-10	9.4433668900E-11
E-element (high temp. range) [1/K^4]	NASA_E1_g	-3.1551883300E-14	-4.2690095900E-15
F-element (high temp. range) [K]	NASA_F1_g	-1.0005645500E+04	-2.9885893800E+04
G-element (high temp. range) [-]	NASA_G1_g	9.9931332600E+00	6.8825557100E+00
A-element (low temp range) [-]	NASA_A2_g	5.149876130E+00	4.198640560E+00
B1-element (low temp range) [1/K]	NASA_B2_g	-1.367097880E-02	-2.036434100E-03
C1-element (low temp range) [1/K^2]	NASA_C2_g	4.918005990E-05	6.520402110E-06
D1-element (low temp range) [1/K^3]	NASA_D2_g	-4.847430260E-08	-5.487970620E-09
E1-element (low temp range) [1/K^4]	NASA_E2_g	1.666939560E-11	1.771978170E-12
F1-element (low temp range) [K]	NASA_F2_g	-1.024664760E+04	-3.029372670E+04
G1-element (low temp range) [-]	NASA_G2_g	-4.641303760E+00	-8.490322080E-01
ture for low temperature NASA polynomials [K]	NASA T_min	2.000000000E+02	2.000000000E+02

Figure 5.1 Schematics of Thermolib chemical database

Normally, the constant values vary with different temperature ranges. The valid ranges of temperature are configured to have two sets: from T\_min to T\_mid, from T\_mid to T\_max. For the temperature which is lower than T\_min and higher than T\_max, constant mole specific heat value is adopted for numerical purpose. For the model developed in this project, all processes simulated are within the valid temperature range of NASA polynomials. An overview of the highlighted temperature range definition in chemical databased is shown in Figure 5.2 (For example, the valid temperature range for CH<sub>4</sub> is 200-6000K):

		Chemical Media Data					
		Species	CH4	H2O	H2O-IF97	CO	CO2
		comment			Usage for pure only. In mixtures please use H2O.		
		formula					
		full_name	methane	water	water IAPWS-IF97		
		species_type		Steamtable	IF97		
B-element (high temp. range) [1/K]	NASA_B1_g	1.0084279500E-02	2.9731832900E-03	2.9731832900E-03	1.3517281800E-03	2.7413199100E-03	
C-element (high temp. range) [1/K^2]	NASA_C1_g	-3.3691625400E-06	-7.7376969000E-07	-7.7376969000E-07	-4.8579407500E-07	-9.9582853100E-07	
D-element (high temp. range) [1/K^3]	NASA_D1_g	5.3495866700E-10	9.4433668900E-11	9.4433668900E-11	7.8853648600E-11	1.6037301100E-10	
E-element (high temp. range) [1/K^4]	NASA_E1_g	-3.1551883300E-14	-4.2690095900E-15	-4.2690095900E-15	-4.6980748900E-15	-9.1610346800E-15	
F-element (high temp. range) [K]	NASA_F1_g	-1.0005645500E+04	-2.9885893800E+04	-2.9885893800E+04	-1.4266117100E+04	-4.9024934100E+04	
G-element (high temp. range) [-]	NASA_G1_g	9.9931332600E+00	6.8825557100E+00	6.8825557100E+00	6.0170979000E+00	-1.9353485500E+00	
A-element (low temp. range) [-]	NASA_A2_g	5.149876130E+00	4.198640560E+00	4.198640560E+00	3.579533470E+00	2.356773520E+00	
B1-element (low temp. range) [1/K]	NASA_B2_g	-1.367097880E-02	-2.036434100E-03	-2.036434100E-03	-6.103536800E-04	8.984596770E-03	
C1-element (low temp. range) [1/K^2]	NASA_C2_g	4.918005990E-05	6.520402110E-06	6.520402110E-06	1.016814330E-06	-7.123562690E-06	
D1-element (low temp. range) [1/K^3]	NASA_D2_g	-4.847430260E-08	-5.487970620E-09	-5.487970620E-09	9.070058840E-10	2.459190220E-09	
E1-element (low temp. range) [1/K^4]	NASA_E2_g	1.666939560E-11	1.771978170E-12	1.771978170E-12	-9.044244990E-13	-1.436995480E-13	
F1-element (low temp. range) [K]	NASA_F2_g	-1.024664760E+04	-3.029372670E+04	-3.029372670E+04	-1.434408600E+04	-4.837196970E+04	
G1-element (low temp. range) [-]	NASA_G2_g	-4.641303760E+00	-8.490322080E-01	-8.490322080E-01	3.508409280E+00	9.901052220E+00	
Temperature for low temperature NASA polynomials [K]	NASA_T_min	2.000000000E+02	2.000000000E+02	2.731600000E+02	2.000000000E+02	2.000000000E+02	
Temperature between NASA high and low ranges [K]	NASA_T_mid	1.000000000E+03	1.000000000E+03	1.000000000E+03	1.000000000E+03	1.000000000E+03	
Maximum temperature for high-temp. Range [K]	NASA_T_max	6.000000000E+03	6.000000000E+03	1.073150000E+03	6.000000000E+03	6.000000000E+03	

Figure 5.2 Temperature range for each substance in chemical database

### 5.1.2 Liquid Phase Calculation

For saturated liquid phase substances involved in the simulation, Thermolib can provide accurate calculation of density, mole specific heat capacity, mole specific enthalpy, mole specific entropy and mole specific Gibbs function, etc (Eutech, 2013).

Equation (5.7) is used to calculate the temperature dependent saturated liquid density:

$$\rho_{f,sat}(T) = \rho_c \cdot (1 + A_1 \cdot \tau^1 + B_1 \cdot \tau^2 + C_1 \cdot \tau + D_1 \cdot \tau^4) \quad (5.7)$$

where  $\rho_c$  is the liquid density at critical temperature,  $A_1, B_1, C_1, D_1$  are coefficients of polynomials.  $\tau$  is calculated by Equation (5.8):

$$\tau = (1 - \frac{T}{T_c})^{1/3} \quad (5.8)$$

where  $T_c$  is the critical temperature of each species. Hence the general equation to calculate the compressible liquid density can be derived below with a pre-defined bulk module  $E$  :

$$\rho_f = \frac{\rho_{f,sat}}{1 - \frac{P - P_{sat}(T)}{E}} \quad (5.9a)$$

where  $\rho_{f,sat}$  is the fluid density at saturated temperature which can be calculated by Equations (5.7) and (5.8),  $P$  is the liquid pressure,  $P_{sat}(T)$  is the saturation pressure of liquid in temperature  $T$ ,  $E$  is the pre-defined bulk module which is derived as Equation (5.9b):

$$E = \frac{\rho_f \cdot dP}{d\rho_f} \quad (5.9b)$$

With the coefficients introduced above, we can have the liquid phase species density at different temperature and pressure, a schematic Figure5.3 shows the highlighted coefficients in Thermolib database which are used for the calculation of liquid density:

Chemical Media		Data				
Species		CH4	H2O	H2O-IF97	CO	CO2
comment				Usage for pure only. In mixtures please use H2O.		
formula						
full_name		methane	water	water IAPWS-IF97		
species_type			Steamtable	IF97		
Number of F atoms [-]	F_atoms	0	0	0	0	0
Number of Cl atoms [-]	Cl_atoms	0	0	0	0	0
Number of S atoms [-]	S_atoms	0	0	0	0	0
Number of Ar atoms [-]	Ar_atoms	0	0	0	0	0
Triple-point temperature [K]	T_triple	90.6941	273.16	273.16	68.16	216.592
Saturated liquid: $\rho_{sat} / \rho_c = (1 + A\tau + B\tau^2 + C\tau^3)$						
Liquid density [g/m <sup>3</sup> ]	rho_liq	422620.0	1.00E+06	1.00E+06	7.89E+05	1.03E+06
A-element	rho_liq_A	1.4707	2.485800E+00	2.485800E+00	1.7367	1.6082
B-element	rho_liq_B	1.220	-2.200800E+00	-2.200800E+00	0.142	1.291
C-element	rho_liq_C	-0.848	7.146700E+00	7.146700E+00	0.971	-0.858
D-element	rho_liq_D	0.595	-5.270500E+00	-5.270500E+00	-0.273	0.729
liquid bulk modul= $(\rho \cdot dP) / d(\rho)$ [N/m <sup>2</sup> ]	E_liq	1.09E+08	2.12E+09	2.12E+09	9.91E+07	2.86E+08

Figure 5.3 Coefficients for the calculation of liquid phase density

The liquid phase substances mole specific capacity at constant pressure is calculated with polynomials (Eutech, 2013) as shown below:

$$c_{p,m} = A_2 + B_2 \cdot T + C_2 \cdot T^2 + D_2 \cdot T^3 \quad (5.10)$$

The coefficients  $A_2, B_2, C_2, D_2$  are given in the chemical database of Thermolib. Similar with the calculation for gas phase substances mole specific heat at constant pressure, Equation (5.10) is valid within the defined temperature range. Density at states which exceed the temperature range is assumed to be constant; the highlighted coefficients and valid temperature ranges used in Equation (5.10) are shown in Figure 5.4:

Chemical Media Data						
	Species	CH4	H2O	H2O-IF97	CO	CO2
	comment			Usage for pure only. In mixtures please use H2O.		
	formula					
	full_name	methane	water	water (APWS-IF97)		
	species_type		Steamtable	IF97		
B-element	rho_liq_B	1.220	-2.200800E+00	-2.200800E+00	0.142	1.291
C-element	rho_liq_C	-0.848	7.146700E+00	7.146700E+00	0.971	-0.858
D-element	rho_liq_D	0.595	-5.270500E+00	-5.270500E+00	-0.273	0.729
liquid bulk modul=(rho*dp)/d(rho) [N/m^2]	E_liq	1.09E+08	2.12E+09	2.12E+09	9.91E+07	2.86E+08
Heat capacity of liquid (Cp = A + B*T + C*T^2 + D*T^3)						
A-element [J/mol*K]	Cp_liq_A	60	5.081069E+01	5.081069E+01	60	120
B-element [J/mol*K^2]	Cp_liq_B	0.000	2.129361E-01	2.129361E-01	0.000	0.000
C-element [J/mol*K^3]	Cp_liq_C	0.000	-6.309691E-04	-6.309691E-04	0.000	0.000
D-element [J/mol*K^4]	Cp_liq_D	0.000	6.483055E-07	6.483055E-07	0.000	0.000
temperature range minimum for polynomial [K]	Cp_liq_T_min	200.000	200.000	273.160	200.000	200.000
temperature range maximum for polynomial [K]	Cp_liq_T_max	6000.000	6000.000	1073.150	6000.000	6000.000

Figure 5.4 Coefficients for the calculation of liquid phase specific heat capacity

The enthalpy calculation for liquid substances is derived by taking account of the transition from liquid phase to gas phase, hence the consistency with gas phase calculation can be ensured (Eutech, 2013). The mole specific enthalpy of saturated liquid phase substance can be calculated by Equation (5.11):

$$h_{m,f,sat}(T) = h_{m,g}(T) - h_{f-g}(T) \quad (5.11)$$



where  $h_{m,g}(T)$  denotes the mole specific enthalpy of the substance is in gas phase at temperature  $T$ ,  $h_{f-g}(T)$  is the evaporation enthalpy of the substance at temperature  $T$ , which is calculated by the explicit given function as shown below:

$$h_{f-g}(T) = A_3 \cdot \exp(-B_3 \cdot \psi) \cdot (1 - \psi)^{C_3} \quad (5.12)$$

Where  $A_3, B_3, C_3$  are the unique coefficients for evaporation calculation,  $\psi$  can be calculated below:

$$\psi = 1 - \frac{T}{T_c} \quad (5.13)$$

where  $T_c$  is the substance's critical temperature. The highlighted coefficients and temperature ranges included in chemical database are shown in Figure 5.5 :

Chemical Media Data						
	Species	CH4	H2O	H2O-IF97	CO	CO2
	comment			Usage for pure only. In mixtures please use H2O.		
	formula					
	full_name	methane	water	water IAPWS-IF97		
	species_type		Steamtable	IF97		
	cond_liq_T_max	1.830000E+02	6.230000E+02	6.230000E+02	1.280000E+02	2.990000E+02
Thermal Conductivity of gas ( $k = A + B \cdot T + C \cdot T^2 + D \cdot T^3$ )						
A-element [W/m*K]	cond_gas_A	-1.869000E-03	7.341000E-03	7.341000E-03	5.067000E-04	-7.215000E-03
B-element [W/m*K^2]	cond_gas_B	8.727000E-05	-1.013000E-05	-1.013000E-05	9.125000E-05	8.015000E-05
C-element [W/m*K^3]	cond_gas_C	1.179000E-07	1.801000E-07	1.801000E-07	-3.524000E-08	5.477000E-09
D-element [W/m*K^4]	cond_gas_D	-3.614000E-11	-9.100000E-11	-9.100000E-11	8.199001E-12	-1.053000E-11
temperature range minimum for polynomial [K]	cond_gas_T_min	2.730000E+02	2.730000E+02	2.730000E+02	1.150000E+02	1.850000E+02
temperature range maximum for polynomial [K]	cond_gas_T_max	1.270000E+03	1.070000E+03	1073.150	1.670000E+03	1.670000E+03
evaporation Enthalpy ( $k = A \cdot \exp(-B \cdot \tau) \cdot (1 - \tau)^C$ )						
A-element [J/mol]	evap_enth_A	1.007663E+04	5.125268E+04	5.125268E+04	8098.183089	2.541137E+04
B-element	evap_enth_B	-2.547753E-01	-2.221000E-01	-2.221000E-01	-0.128814261	-5.675000E-03
C-element	evap_enth_C	4.033796E-01	4.165000E-01	4.165000E-01	0.394498605	4.037000E-01
temperature range minimum for polynomial [K]	evap_enth_T_min	9.160100E+01	2.800000E+02	2.800000E+02	68.8416	2.200000E+02
temperature range maximum for polynomial [K]	evap_enth_T_max	1.886584E+02	6.400000E+02	6.400000E+02	131.5314	3.000000E+02

Figure 5.5 Schematic of coefficients and temperature ranges for evaporation enthalpy calculation

For the calculation in dense state and supercritical regions, the pressure dependent liquid enthalpy is determined by linear interpolation which is shown in Equation (5.14):

$$h_{m,f}(T, P) = h_{m,f,sat}(T) + \frac{P - P_{sat}}{P_c - P_{sat}} \cdot (h_{m,g}(T, P_c) - h_{m,f,sat}(T)) \quad (5.14)$$

Where  $h_{m,g}(T, P_c)$  is the mole specific heat of gas phase substance at temperature  $T$  and critical pressure  $P_c$ ,  $h_{m,f,sat}(T)$  is the mole specific heat of saturated liquid phase substance at temperature  $T$ .

### 5.1.3 Vapour-liquid Equilibrium Calculation

Both of liquid and gas phases are assumed to be in thermodynamic equilibrium in Thermolib model. Hence for one substance, when the liquid and gas phase coexist during the simulation, the pressure, temperature of both phases are the same. The Antonie equation (5.15) (Eutech, 2013) is used for the saturation pressure calculation, the saturation pressure  $P_{sat}$  is handled as a function of the saturation temperature:

$$\lg(P_{sat}) = A_4 - \left( \frac{B_4}{T_{sat} + C_4} \right) \quad (5.15)$$

where  $P_{sat}$  denotes the saturation pressure with unit bar while  $T_{sat}$  denotes saturation temperature with unit Kelvin.  $A_4, B_4, C_4$  are component-specific coefficients. Raolt's rule is used in Thermolib for the calculation of vapour liquid equilibrium of mixture. Two main assumptions are made for liquid phase (Eutech, 2013) :

- 1) For pure liquid substance  $i$ , the fugacity  $f_i^f$  at temperature  $T$  and pressure  $P$  equal to its saturated liquid or vapour fugacity  $f_i^{sat}$  at the same temperature, the relationship is shown as Equation (5.16) :

$$f_i^f = f_i^{sat} \quad (5.16)$$

2) Pure saturated vapour follow the ideal gas law, the saturated vapour fugacity  $f_i^{sat}$  equals to its saturated pressure :

$$f_i^{sat} = P_i^{sat} \quad (5.17)$$

Hence we can have equation (5.18) as follow to calculate the fluid fugacity:

$$f_i^f = P_i^{sat} \quad (5.18)$$

For substance  $i$  of vapour phase, assumption is made that pure gas behaves the same as ideal gas at temperature  $T$  and pressure  $P$ , hence the fugacity of vapour phase  $f_i^g$  equals to its pressure:

$$f_i^g = P \quad (5.19)$$

Ideal solution assumption is applied in Thermolib model, which means for component  $i$  in mixture, the product of its gas phase mole concentration  $x_i$  and fugacity  $f_i^g$  equals to the product of its liquid phase mole concentration  $y_i$  and fugacity  $f_i^f$  (Eutech, 2013). Hence Equation (5.20) is derived below:

$$x_i \cdot f_i^g = y_i \cdot f_i^f \quad (5.20)$$

By substituting Equations (5.16) ~ (5.19) to Equation (5.20), we can have Equation (5.21):

$$x_i \cdot P = y_i \cdot P_i^{sat} \quad (5.21)$$

Based on Dalton's law, the sum of all components concentration equals to 1 for both liquid and gas phases, hence we can have the following equations:

$$\sum x_i = 1 \quad (5.22)$$

$$\sum y_i = 1 \quad (5.23)$$

For component  $i$ , its total mole value  $Z_i$  contain both liquid phase and gas phase, hence we can have Equation (5.24) as below:

$$Z_i = x_i \cdot M + y_i \cdot N \quad (5.24)$$

where  $M$  and  $N$  are the total moles of gas flow and liquid flow contained in mixture, respectively. During the calculation for mixture with  $n$  kinds of components, we can establish  $2+2n$  equations with  $2+2n$  unknown numbers, when  $n$  is larger than two, the nonlinear equations will be solved by the TPVaporFraction block in Thermolib (Eutech, 2013), this block is used in many modules built with Thermolib.

#### 5.1.4 Mixture Calculation

From analysis of the system, there is hardly any process with only one pure substance; the raw syngas, shifted syngas, sweet syngas, fuel gas and flue gas are all mixture, hence the calculation of mixture properties is essential for the modelling work. In Thermolib, the properties of a mixture are based on the weighted average of the pure substances that build up the mixture. Hence we can have Equation (5.25) to calculate the mixture enthalpy  $H_{mix}$ :

$$H_{mix} = \sum_i (n_{i,g} \cdot h_{m,i,g} + n_{i,f} \cdot h_{m,i,f}) \quad (5.25)$$

where  $n_{i,g}$  denotes the mole of component  $i$  in gas phase,  $h_{m,i,g}$  denotes the mole specific enthalpy of component  $i$  in gas phase,  $n_{i,f}$  denotes the mole of component  $i$  in liquid phase,

and  $h_{m,i,f}$  denotes the mole specific enthalpy of component  $i$  in liquid phase. Similarly to enthalpy, the entropy of mixture  $S_{mix}$  can be calculated as Equation (5.26) (Eutech, 2013):

$$S_{mix} = \sum_i (n_{i,g} \cdot s_{m,i,g} + n_{i,f} \cdot s_{m,i,f}) - R \cdot \sum_i (n_{i,g} \cdot \ln x_i) \quad (5.26)$$

where  $s_{m,i,g}$  is the mole specific entropy of component  $i$  in gas phase while  $s_{m,i,f}$  denotes the mole specific entropy of component  $i$  in liquid phase.  $x_i$  is the mole fraction of component  $i$  in gas phase. For the process happens in supercritical state, it is assumed only vapour phase substance exists, the saturated pressure is handled as a extrapolation of Antonie equation. The auxiliary modules which will be introduced below will calculate the properties of working medias in IGCC gasification enabled plant are all based on the laws and equations described in this section.

### 5.1.5 Limitation of Thermolib Software

Thermolib is developed aiming to provide dynamic simulation of thermodynamic systems with limitations. As a simplified toolbox based on Simulink, Thermolib have limitations below (Eutech, 2013):

- 1) There are no detailed geometries modelled;
- 2) There are no potential or kinetic energy modelled;
- 3) There are no solid state substance modelled;
- 4) There are no supersonic flows or pressure/shock waves modelled ;
- 5) The interactions of substances such as solute and solution, zoetrope are not modelled.

Comparing with sophisticated commercial process simulation software such as Aspen Plus or Aspen Dynamics, Thermolib can't provide detailed chemical reactions mechanism simulation, nor the chemical industry process package simulation. But Thermolib can provide compiled blocks developed based on explicit thermodynamic laws and differential equations, and the powerful database introduced from public databased such as NIST webbook can also save a lot of efforts on the mass and energy balance calculations which frequently happen in Chapter 3 and Chapter 4. Moreover, modification on the blocks can be made to do customized parameterization and develop new block for unique working condition simulation.

This project focuses on the dynamic simulation of IGCC systems aiming to understand how the equations based system operates and how will the PSA carbon capture influence the operation of IGCC, especially on the energy penalty and efficiency lost. Hence, Thermolib is a reliable and flexible platform to handle and we can do further programming based on its library.

## **5.2 Gas Quench Process Model for Shell Gasifier**

### **5.2.1 Gas Quench Model**

The syngas generated by the gasifier will first go through a quench process to cool down, which can solidify the fly ash contents by cooling them down below the ash melting point hence prevent the downstream module from being damaged by the ash particles. For Shell gasifier, the raw syngas will be quenched by 250 °C recycled ash-free clean gas before entering the syngas coolers located downstream. The flow diagram for the gasifier with quench and syngas cooling system model is shown in Figure 5.6 :

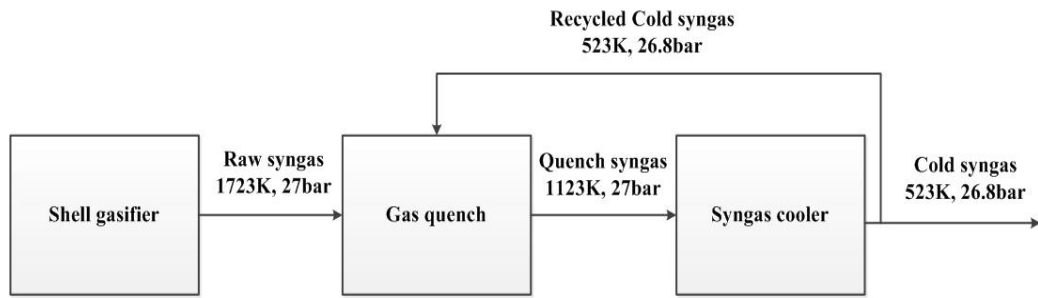


Figure 5.6 Flowchart of Shell gasifier with gas quench and syngas cooling system

As shown in Figure 5.5, the raw syngas will go through gas quench and further syngas cooling process and its temperature drops to 523K and can be used in the downstream shift reactions and sulphur removal.

Part of cold gas is taken at the syngas cooler output and recycled to quench the hot raw syngas. A more detailed Schematics diagram is shown in Figure 5.7 to show the industry running of Shell gasifier with gas quench and syngas cooling .

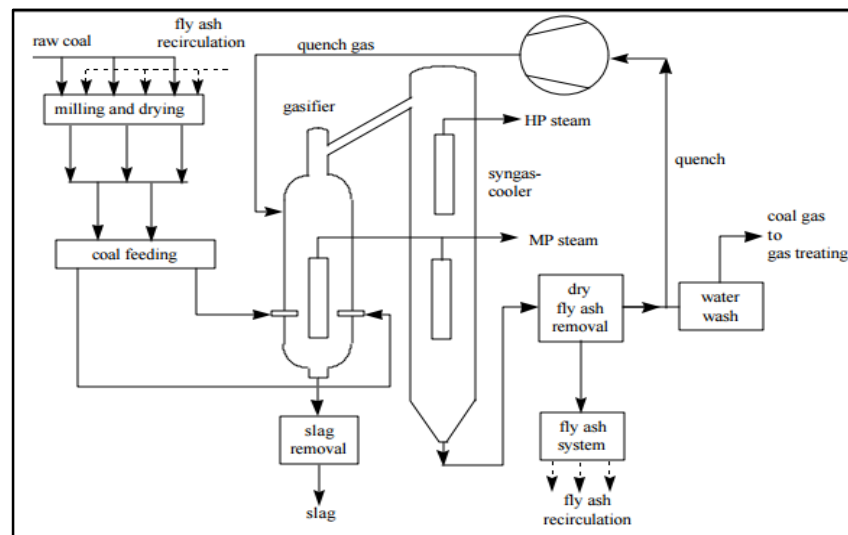


Figure 5.7 Schematics of Shell gasifier with gas quench and syngas cooling system(Higman and van der Burgt, 2008d)

The main issue caused by cold gas quench is the raw syngas temperature drop, the chemical equilibrium of water gas shift reaction will move to right, which will cause the syngas

contents concentration change, also cause Equation (4.7) losing its validity (Schoen, 1993). Hence a fixation temperature (Schoen, 1993, Casella and Colonna, 2012) needs to be introduced here to re-calculate the syngas contents. A quench gas model is built to simulate this process, the main assumptions for this model are shown below:

- 1) The syngas equilibrium fixation temperature is assumed to be 1450 K (Schoen, 1993), below which Equation (4.7) is not valid and the syngas contents will not change. Hence the final raw syngas concentration is calculated based on the chemical equilibrium at 1450 K.
- 2) The effect caused by syngas contents change from gasification temperature to the fixation temperature is considered to be negligible; its effect in the quench process is secondary comparing with the temperature drop. Hence during the quench process, the syngas contents concentrations are considered as constants, which are the values in fixation temperature.
- 3) The syngas is considered as ideal gas, the mixing of raw syngas and recycled cool gas is assumed to be finished instantaneously. The quenched syngas temperature is 1123 K (Schoen, 1993)
- 4) The mole flow rate of recycled cold syngas versus mole flow rate of raw syngas is set as 0.99 and this ratio is calculated based on the energy balance for gas streams before quench and after quench which will be introduced in the following Equation (5.27) although there is not many academic publication talking about the value for recycle cold gas ratio, the similar process is used in real industry and recorded in Higman's second edition "gasification" (Higman and van der Burgt, 2008d).



A simplified mixer model is built to simulate the gas quench process for Shell gasifier, commercial Simulink-based toolbox Thermolib is adopted to build the auxiliary modules in gasification enabled plant. The mixer block can simulate the gas quench mixing process based on the assumptions that have been made. The inputs include raw syngas at 1773 K and recirculated syngas at 523 K, the quenched gas temperature will drop to 1173 K. The mass balance equation for the gas quench process is shown below:

$$\dot{m}_{mixgas} = \dot{m}_{raw} + \dot{m}_{cold} \quad (5.27)$$

where  $\dot{m}_{mixgas}$  denotes the mass flow rate of mixed syngas,  $\dot{m}_{raw}$  and  $\dot{m}_{cold}$  are the mass flow rate of raw syngas and recirculated cold gas respectively. The energy balance equation of gas quench process is described below:

$$\dot{m}_{mixgas} \cdot h_{mixgas} = \dot{m}_{raw} \cdot h_{raw} + \dot{m}_{cold} \cdot h_{cold} \quad (5.28)$$

where  $h_{mixgas}$ ,  $h_{raw}$  and  $h_{cold}$  denote the mass specific enthalpy of mixed gas, raw syngas and recirculated syngas respectively. The mixer model used for gas quench process simulation adopts ideal gas mode and the calculation for thermodynamic properties will follow the equations described in Section 5.1. The parameters of raw syngas, recycled cold gas and calculation results of quenched gas are listed in Table 5.1:

Table 5.1 Parameters of raw syngas, recycled cold gas and quenched gas

Parameter	Raw syngas	Recycled cold gas	Quenched gas to syngas cooler
Gas temperature (K)	1773	523	1173
Pressure (bar)	27	27	27
Mass flow rate $\dot{m}$ (kg/s)	41.29	40.78	82.07
Mole flow rate $\dot{n}$ (mol/s)	2031	2016	2031

Heat capacity rate Cpdot (W/K)	60337.6	70695.7	134537
H <sub>2</sub> S mole concentration (%)	0.13	0.13	0.13
COS mole concentration (%)	1.46e-2	1.46e-2	1.46e-2
N <sub>2</sub> mole concentration (%)	3.43	3.43	3.43
CO mole concentration (%)	60.72	60.72	60.72
H <sub>2</sub> mole concentration (%)	29.83	29.83	29.83
CO <sub>2</sub> mole concentration (%)	1.57	1.57	1.57
H <sub>2</sub> O mole concentration	3.21	3.21	3.21

### 5.2.2 Syngas Cooling Model

The 1123 K quenched gas will pass the syngas cooler and the heat recovery during this process will be used to generate HP steam which will be used in HRSG for electricity generation. The heat transfer process is simulated with block from Thermolib.

The heat exchanger block is built with Thermolib based on NTU (number of transfer unit) method (Eutech, 2013). The flows of the media involved in the heat exchanger are handled as thermal mass (Eutech, 2013). The heat transfer between the thermal masses is driven by the temperature difference of two flows. Meanwhile, the heat exchange from flow to environment is considered. A Schematics of heat transfer happen within the NTU heat exchanger is shown in Figure 5.8.

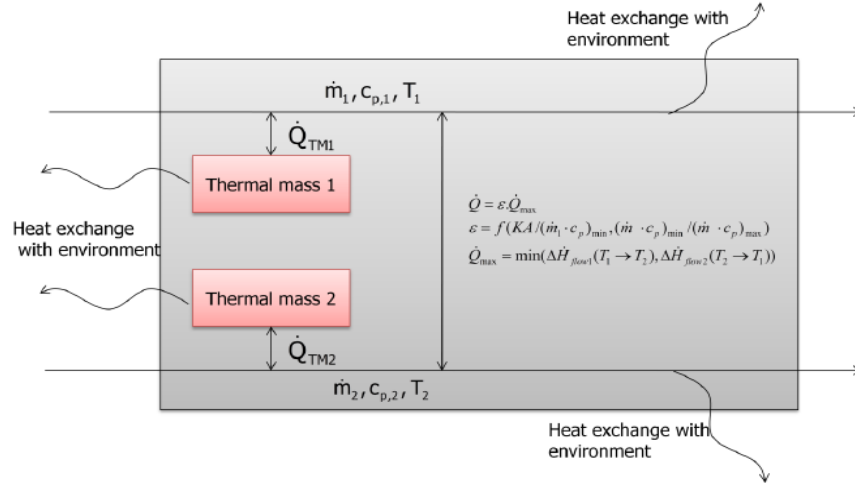


Figure 5.8 Schematics of heat transfer happen in NTU heat exchanger (Eutech, 2013)

For the NTU method, the effectiveness of heat exchanger  $\varepsilon$  is introduced. As shown in Equation (5.29), the numerator  $\dot{Q}$  is the actual heat transfer rate of two flows while the denominator  $\dot{Q}_{\max}$  is the possible maximum heat flux rate between two flows which is caused by the possible maximum temperature difference during the heat transfer process.

$$\varepsilon = \left( \frac{\dot{Q}}{\dot{Q}_{\max}} \right) \quad (5.29)$$

The heat flux  $\dot{Q}$  between two flows is calculated by Equation (5.30):

$$\dot{Q} = \dot{C}_{\min} \cdot \Delta T_{\max} \quad (5.30)$$

$$\dot{C}_{\min} = \min(\dot{m}_1 c_{p1}, \dot{m}_2 c_{p2}) \quad (5.31)$$

$$\dot{C}_{\max} = \max(\dot{m}_1 c_{p1}, \dot{m}_2 c_{p2}) \quad (5.32)$$

Where  $\Delta T_{\max}$  is the maximum temperature difference of these two flows.  $\dot{C}$  is the product of media's mass flow rate (kg/s)  $\dot{m}$  and specific heat in constant pressure  $c_p$ . Footnotes min and

max denote the minimum and maximum  $\dot{C}$  in these two flows. A non-dimensional number  $C$  is introduced to evaluate the ratio between minimum and maximum  $\dot{C}$ , which is described as the equation shown below:

$$C = \frac{\dot{C}_{\min}}{\dot{C}_{\max}} \quad (5.33)$$

By substituting equation (5.29) to (5.30), we can have Equation (5.34) to calculate the heat flux between two flows:

$$\dot{Q} = \varepsilon \cdot \dot{C}_{\min} \cdot (T_{gas,in} - T_{steam,in}) \quad (5.34)$$

where  $T_{gas,in}$  (K) is the temperature of hot gas input and  $T_{steam,in}$  (K) is the temperature of cold steam input. Since the syngas flow and steam flow are defined as counter flow in the heat exchanger, hence the effectiveness  $\varepsilon$  can be calculated by Equation (5.35) (Eutech, 2013)

$$\varepsilon = \frac{1 - \exp(-M \cdot (1 - C))}{1 - C \cdot \exp(-M \cdot (1 - C))} \quad (5.35)$$

where

$$M = \frac{UA}{\dot{C}_{\min}} \quad (5.36)$$

$M$  is the NTU (Number of Transfer Unit), which is a non-dimensional number.  $U$  is the overall heat transfer coefficient,  $A$  is the surface area available for the heat transfer, and thus  $UA$  will be the overall heat transfer rate in the heat exchanger, it is defined in the block mask and can be calculated with the parameters of syngas and steam. With the NTU heat

exchanger block, the heat transfer process between hot flow and cold flow can be calculated; the syngas can be cooled to 1123K by transferring heat to HP steam.

### 5.3 Total Water Quench Model for Texaco Gasifier

Unlike Shell gasifier using gas quench, the slurry feed to the Texaco gasifier uses total water quench. Comparing with partial quench or gas quench, total quench is effective and much less expensive than using the complex syngas cooling system in Shell gasification process. But the total quench process will cause energy losses. The overall efficiency of the Texaco gasifier with total quench is lower than Shell gasifier with syngas cooling (Higman and van der Burgt, 2008d).

The input parameters for the Texaco gasifier based on internal research report (M.Karmarkar, 2005) are shown in Table 5.2:

Table 5.2 Model input using typical british coal

Input	Unit	Data
MF coal input	t/h	128
Slurry Concentration	kg coal/kg slurry	0.65
Oxygen Purity	Vol. %	95
Nitrogen/oxygen	kg/kg	0.0184
Argon/oxygen	kg/kg	0.0395
Oxygen/coal	kg O <sub>2</sub> /kg dry coal	1.02
Pressure	MPa	6.0
Temperature	°C	1300
Heat Loss	H.H.V. %	2
Ultimate analysis	%	
C	%	74.95
H	%	5.45
O	%	6.74
N	%	1.59

S	%	2.3
Ash	%	8.46
Fixed carbon	%	57.94
Volatile matter	%	33.6
HHV	kJ/kg	30182

Table 5.3 Simulation results by using typical British coal

syngas contents	H <sub>2</sub>	N <sub>2</sub>	H <sub>2</sub> O	CO	CO <sub>2</sub>	Ar	COS	H <sub>2</sub> S
Concentration (%)	27.76	1.02	18.69	40.27	10.83	0.83	0.06	0.53
Mole flow rate (mol/s)	1.1991	0.0441	0.8074	1.7393	0.4680	0.0359	0.0026	0.0230

Since the data of raw syngas contents in reference (M.Karmarkar, 2005) are treated as confidential, only the shifted syngas contents concentration data are provided in the report. Hence, the simulation will be carried out with the guessed conditions and the simulation results will be compared with the reference data after the shift reaction happen. The results will be used to adjust the simulation conditions afterwards. The COS and H<sub>2</sub>S contents only account for around 0.5% of the total mole flow in syngas, so the removal of such minimum amount of sulphides will not cause major changes in the state parameters of the syngas stream, the detailed investigation of COS and H<sub>2</sub>S removal process is out of the scope of this work hence the following sulphur removal simulation will be simplified.

The raw syngas stream generated by the Texaco gasifier will flow down from the reaction zone and enter the water quench zone at the bottom of the vessel through a down comer under the water level, then the quenched gas will gradually bubble up and leave the gasifier (M.Karmarkar, 2005). The slag fly ash carried in the syngas will be solidified fast and settled down, finally is removed from the lock hopper at the bottom of the quench chamber. During

the quench process, the water is quickly heated by the radiant heat of the syngas. This process involves heat transfer among solid, gas and liquid phase mass, which is an extremely fast and complicated issue.

The evaporation of water during the quench process will cool the syngas and its temperature will drop from around 1300°C to around 247°C (M.Karmarkar, 2005). The temperature drop and direct contact of raw syngas and water will cause water gas shift reaction equilibrium to change as well, based on the fixation temperature assumption as 1450 K, the quenched gas contents concentration will be further revised and won't change when temperature drops below 1450 K, with this quench gas contents revision, CO<sub>2</sub> content and H<sub>2</sub>/CO ratio will raise.

The total quench is proved to be advantageous when the final product is hydrogen (Higman and van der Burgt, 2008d). Since introduction of water which drives the shift reaction move mentioned above, the saturated steam contents in syngas (more than 60% mole) requires no more steam added in the following water gas shift reactor. Although the total quench is not exoegetically elegant, it is an ideal choice for IGCC with capture ready design aiming to use hydrogen as fuel gas (M.Karmarkar, 2005). Moreover, comparing with the complex and expensive syngas cooling system, the water quench Texaco gasifier is simpler and benefits from its lower cost.

The detailed dynamics of quench process is not modelled due to the limitation of the software tool and the limited data in references. It is simplified and simulated by using a mixer block in Thermolib. This mixer module can simulate the direct mix of syngas and water then predict the physical parameter of quenched syngas. The simulation results are shown in Table 5.4 below:

Table 5.4 Calculation for raw syngas and quenched syngas parameters

Parameter	Raw syngas	Quenched gas
Gas temperature (K)	1573	511
Pressure (bar)	60	59.8
Mole flow rate $\dot{n}$ (mol/s)	4319.5	8619
H <sub>2</sub> S mole concentration (%)	0.53	0.265
COS mole concentration (%)	0.06	0.03
N <sub>2</sub> mole concentration (%)	1.02	0.511
CO mole concentration (%)	40.27	20.18
H <sub>2</sub> mole concentration (%)	27.76	13.91
CO <sub>2</sub> mole concentration (%)	10.83	5.43
Argon mole concentration (%)	0.83	0.42
H <sub>2</sub> O mole concentration (%)	18.69	59.96

The quenched syngas contains large amount of water (60%), which is sufficient for the water gas shift reaction. Hence there is no extra steam added in the shift reactor for Texaco total quench gasifier. It is necessary to mention that the water carried by syngas contains both liquid and gas phase.

#### 5.4 Simplified Water Gas Shift Reactor Model

For both Shell and Texaco gasifiers, the cool syngas from quench module will subsequently enter the WGS (water gas shift reactor) for the following reasons:

- 1) WGS is important for the preparation of CO<sub>2</sub> sequestration because the CO<sub>2</sub> concentration rises, which is ideal for PSA adsorption capture which is necessary for the PSA carbon capture process;
- 2) CO<sub>2</sub> can be used as diluent in gas turbine and reduce the NO<sub>x</sub> emission;
- 3) Conversion of gaseous impurities such as COS, HCN;
- 4) The shift reaction is exothermic, the heat release by shift reaction can be used to heat HP and LP steam which will be used in HRSG to produce mechanical power. This



can improve the efficiency of IGCC power plant.

The water gas shift reaction is shown below:



In industry, shift reactor adopts variable catalyst for the different working conditons. The most widely used catalysts for high temperature WGS are  $Fe_2O_3$ ,  $Cr_2O_3$  and  $MgO$  (Newsome, 1980). For low temperature WGS,  $CuO$ ,  $ZnO$  and  $Al_2O_3$  are reported as the typical choice (Smith et al.). Shift reactor can be located either prior to AGR (Acid gas removal) or after AGR since the catalyst poisoning issue caused by sulphide has been solved (M.Karmarkar, 2005). In this study, the shift reactor is located prior to AGR.

The primary aim to build shift reactor model in this study is to prepare high  $H_2$  and  $CO_2$  content shifted syngas stream for the combined cycle power plant, then investigate the performance of IGCC power plant. The detailed chemical reaction process with catalysts is out of the scope of this work, thus a reaction rate-controlled reactor block developed in Thermolib toolbox is adopted to simulate the WGS reaction process. The block can predict the syngas contents and temperature changes. Two shift reactors blocks are connected in series in this model and their reaction rates are defined respectively as 0.9 and 0.8 (Wang et al., 2015), respectively.

Heat exchanger modules are used for raising HP and LP steam by recovering the heat from the both stages of shift reactor model. The syngas temperature from the first stage reactor is normally over 683K (M.Karmarkar, 2005); this syngas stream is used to generate HP steam. Its temperature drops to around 523K and then it will enter the second stage reactor. The heat release from the second reactor is much less than the first stage due to a much lower CO

concentration in the current syngas. The syngas temperature is around 550K, and then it will be cooled to 303K for the following sulphur removal process. The Schematics of WGS with heat recovery configurations are shown below in Figure 5.9 and Figure 5.10, respectively.

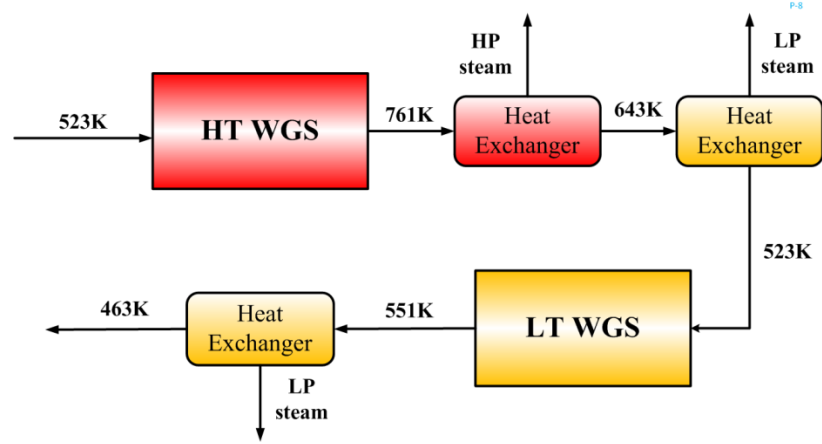


Figure 5.9 Schematics for WGS with heat recovery block for Shell gasifier

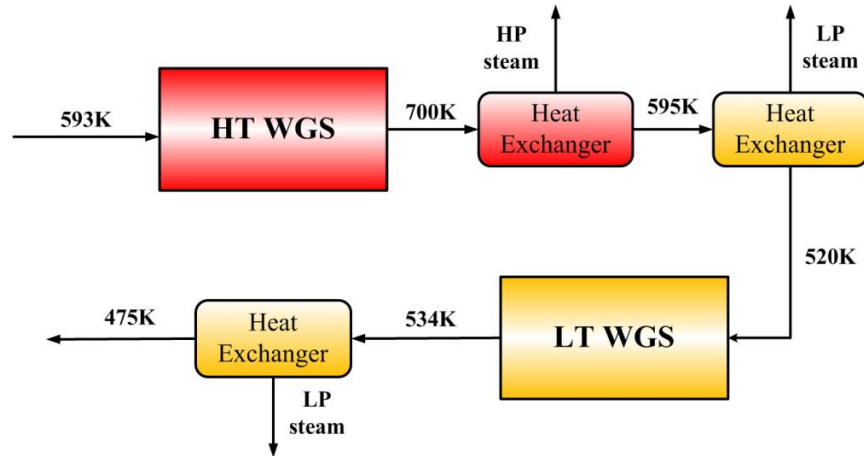


Figure 5.10 Schematics for WGS with heat recovery block for Texaco gasifier

The shift reactor model is developed based on mass balance and energy balance. The mass balance equation for gas contents  $i$  is shown below:

$$\frac{dM_i}{dt} = \sum x_{i,in} \cdot \dot{M}_{in} - \sum x_{i,out} \cdot \dot{M}_{out} + \sum R_i \quad (5.38)$$

where  $M_i$  (kg) denotes the mass of content  $i$ ,  $x_{i,in}$  and  $x_{i,out}$  denote the mole concentration of content  $i$  in the input and output streams respectively.  $\dot{M}_{in}$  and  $\dot{M}_{out}$  denote the mass flow rate (kg/s) of input and output streams respectively while  $R_i$  (kg/s) denotes the net mass production rate of content  $i$  by chemical reactions. There is no mass accumulation considered in this reactor model. The energy balance equation derived based on first law (Eutech, 2013) of the reactor is shown below:

$$\frac{dU}{dt} = \sum_i \dot{H}_{i,in} - \sum_j \dot{H}_{j,out} + \sum_k \dot{Q}_k + \sum P_m \quad (5.39)$$

where  $U$  denotes the internal energy (kJ) within the reactor,  $\dot{H}_{i,in}$  (kW) denotes the enthalpy flow rate of content  $i$  in the input stream,  $\dot{H}_{j,out}$  (kW) denotes the enthalpy flow rate of content  $j$  in the output stream,  $\dot{Q}_k$  (kW) denotes the heat flow rate caused by heat transfer and  $P_m$  (kW) denotes the mechanical power, which equals to zero for the reactor.

In terms of dynamic simulation, the results of shift reactor model in Shell-based GEM plant is presented. It is assumed that the mole flow rate of syngas stream generated by Shell gasifier is assumed to reach the full load value in 100s (Wang et al., 2015), the dynamic change of first and second stage reactor temperature and the contents concentrations are shown in the Figure 5.11:

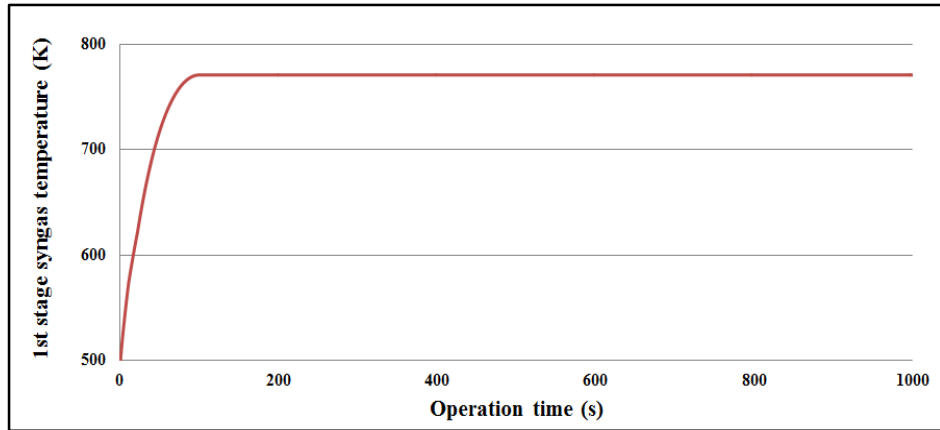


Figure 5.11 1st stage WGS shifted syngas temperature dynamic change

As shown in Figure 5.11, the syngas temperature rises to 761 K when it passes through the 1<sup>st</sup> stage WGS reactor, which is caused by the heat released from the exothermic shift reaction. The steam used for the first stage WGS is the exhaust steam from the steam turbine (Kreutz et al., 2010), which is preheated and compressed before it is mixed with the syngas to meet the reaction demand. The mixing process is simulated with a mixer block in Thermolib with a pressure loss factor of  $1e-5$  considered.

The CO<sub>2</sub> and H<sub>2</sub> concentration dynamic changes of the first stage WGS are shown in Figure 5.12 and Figure 5.13:

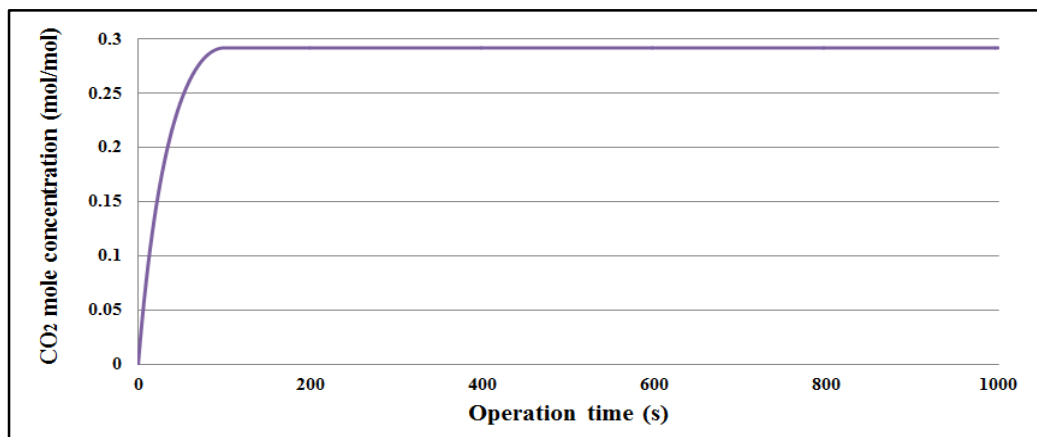


Figure 5.12 1st stage WGS shifted syngas CO<sub>2</sub> concentration dynamic change

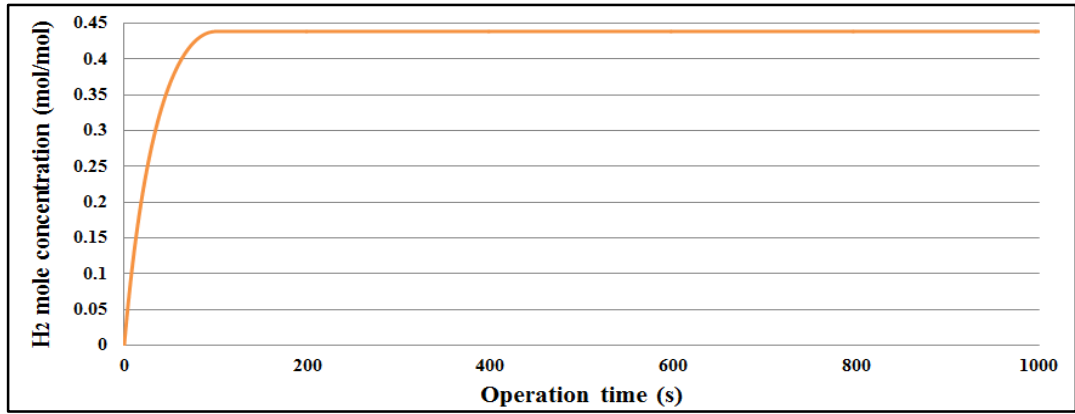


Figure 5.13 1st stage WGS shifted syngas H<sub>2</sub> concentration dynamic change

As shown in Figure 5.12 and Figure 5.13, the CO<sub>2</sub> and H<sub>2</sub> concentration in the wet syngas rises, which are caused by water gas shift reaction. The reaction rate of the first stage is set to be 0.9, hence it will convert most of CO to CO<sub>2</sub> and generate extra H<sub>2</sub>. The high hydrogen and CO<sub>2</sub> concentration is favoured by the pressure swing adsorption process since CO<sub>2</sub> has a high partial pressure in the shifted syngas.

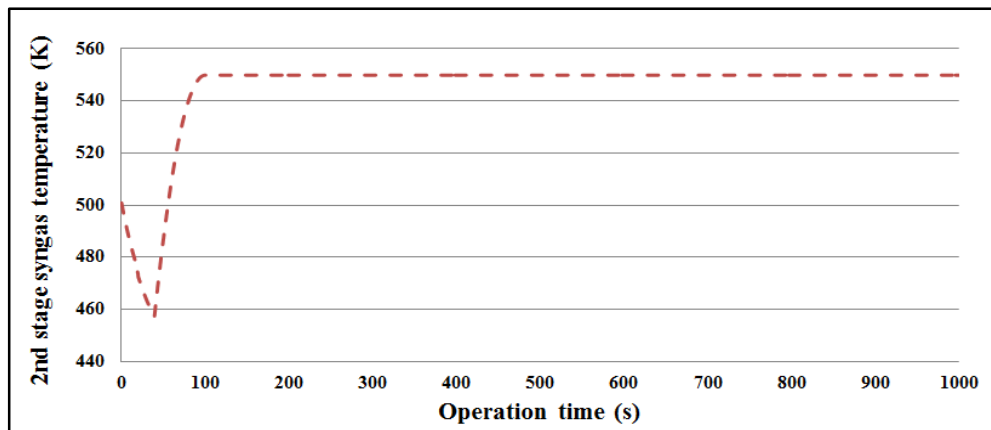


Figure 5.14 2nd stage WGS shifted syngas temperature dynamic change

As shown in Figure 5.14, the temperature of outlet syngas of the second stage low temperature WGS has experienced a drop first and then rises to the final temperature around 550K. The first temperature drop is caused by heat transfer from syngas to HP steam in the heat exchanger. As the syngas input gradually rises in the following time until it reaches maximum value after 100 seconds, the syngas temperature will rise to around 550K.

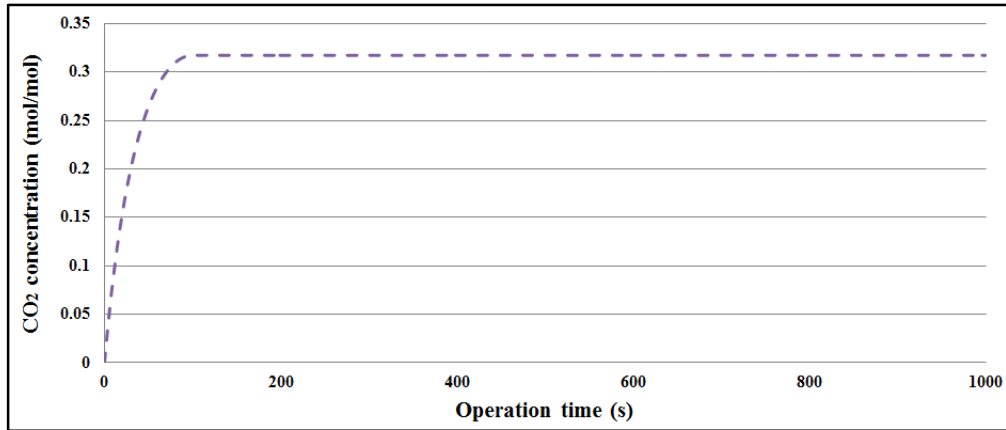


Figure 5.15 2nd stage WGS shifted syngas CO<sub>2</sub> concentration dynamic change

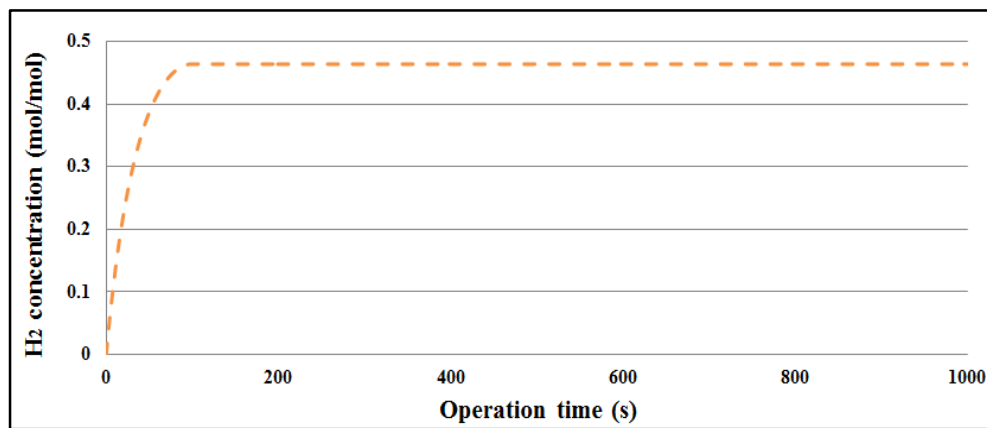


Fig. 5. 16 2<sup>nd</sup> stage WGS shifted syngas H<sub>2</sub> concentration dynamic change

The concentration of CO<sub>2</sub> and H<sub>2</sub> rises in the LT WGS as well, the final H<sub>2</sub> mole concentration is 46.4%, and CO<sub>2</sub> mole concentration is 31.7%. In terms of mole concentration in the dry stream, the ratios for these two contents are 57.1% and 39.1% respectively.

For the Texaco gasifier, there is no additional steam added for WGS, since there is enough saturated steam is carried by the syngas from quench chamber. Hence the changes of syngas contents concentration in WGS are transient. The detailed syngas parameters from HL and LT WGS outlets of Shell and Texaco gasifier are listed in Table 5.5:

Table 5.5 Parameters of two stages WGS outlet syngas parameters of Shell and Texaco gasifier

Parameter	HT WGS Shell	LT WGS Shell	HT WGS Texaco	LT WGS Texaco
Gas temperature (K)	770.685	549.753	698.698	556.379
Pressure (bar)	26.943	26.943	59.8	59.8
Mole flow rate $\dot{n}$ (mol/s)	3911	3911	8619	8619
Heat capacity rate $\dot{C}_p$ (W/K)	147334	140072	321479	310702
H <sub>2</sub> S mole concentration (%)	0.067	0.067	0.263	0.263
COS mole concentration (%)	0.008	0.008	0.030	0.030
N <sub>2</sub> mole concentration (%)	1.782	1.782	0.507	0.507
CO mole concentration (%)	3.154	0.631	4.008	1.463
H <sub>2</sub> mole concentration (%)	43.874	46.397	29.843	32.388
CO <sub>2</sub> mole concentration (%)	29.204	31.727	21.423	23.968
H <sub>2</sub> O mole concentration	21.344	18.821	43.509	40.964

Internal research report (M.Karmarkar, 2005) provides the data of shifted syngas for Texaco-based GEM plant. The comparison of Texaco gasifier simulation and reference data are shown below:

Table 5.6 Parameters of two stages WGS outlet syngas parameters of Texaco gasifier

Parameter	Shifted syngas R	Shifted syngas S
Gas temperature (K)	-	556.379
Pressure (bar)	59.78	59.8
H <sub>2</sub> S mole concentration (dry %)	0.51	0.445
H <sub>2</sub> S mole flow rate (kmol/h)	94.06	81.60
COS mole concentration (dry %)	0.00	0.05
COS mole flow rate (kmol/h)	0.2	9.07
N <sub>2</sub> mole concentration (dry %)	0.77	0.507
N <sub>2</sub> mole flow rate (kmol/h)	143.14	157.44
CO mole concentration (dry %)	2.47	2.48
CO mole flow rate (kmol/h)	456.36	453.90
H <sub>2</sub> mole concentration (dry %)	55.5	54.7
H <sub>2</sub> mole flow rate (kmol/h)	10259.69	10121.2
CO <sub>2</sub> mole concentration (dry %)	39.87	40.60
CO <sub>2</sub> mole flow rate (kmol/h)	7371.3	7436.89

As shown in Table 5.6, the simulation results show high accuracy for the major parameters of shifted syngas stream including the gas flow rate and syngas contents concentration such as CO, CO<sub>2</sub> and H<sub>2</sub>, etc. Relative large error exist for the COS and H<sub>2</sub>S simulation results. This is caused by the 9:1 assignment of sulphur assumption in syngas prediction model, which is introduced in Chapter 4. Since the total mole concentration of COS and H<sub>2</sub>S in the syngas stream is less than 0.5% in dry stream and 0.25% in wet steam, the error in sulphides is ignored and the simulation results will be used in the following COS and H<sub>2</sub>S removal process.

## **5.5 Simplified Sulphur Removal Model**

### **5.5.1 COS Hydrolysis Reactor**

The sulphide impurities contained in the shift syngas include COS and H<sub>2</sub>S. COS content in the syngas is not easy to be removed by most acid gas removal processes (Gasification, 2005), hence it is necessary to convert it to H<sub>2</sub>S which can be removed either by chemical reaction or physical adsorption in the AGR unit.

Based on the design information in internal research report (M.Karmarkar, 2005), the catalysts used in shift reactor can not only convert CO to CO<sub>2</sub> and H<sub>2</sub>, but also to H<sub>2</sub>S. A chemical reactor block is used to work as the COS hydrolysis reactor to convert 90% of COS to H<sub>2</sub>S and calculate the parameters of syngas. In this reactor, the minimum quality of COS will react with the steam and convert to CO<sub>2</sub> and H<sub>2</sub>S. The hydrolysis reaction is shown below:





The COS hydrolysis reaction is slightly exothermic. Considering the minimum amount of COS and heat generation, the simulation results shows the temperature of syngas almost remains the same. The simulation results of the syngas contents mole concentrations (%) from the hydrolysis reactor are shown in Table 5.7:

Table 5.7 Parameters COS free syngas parameters of Shell and Texaco gasifier

Parameters	Shell	Texaco
$\dot{n}$ (mol/s)	3911	8619
P (bar)	26.98	59.8
T (K)	549.753	556.603
CO (%)	0.63	1.46
CO <sub>2</sub> (%)	31.73	24.00
H <sub>2</sub> O (%)	18.81	40.94
H <sub>2</sub> (%)	46.40	32.39
N <sub>2</sub> (%)	1.78	0.51
H <sub>2</sub> S (%)	0.0743876	0.29
COS (%)	7.587e-4	2.97899e-3
Argon (%)	0.566361	0.417059

The syngas leaving the COS hydrolysis reactor will be first cooled by feed water to around 473K and pass the condenser where the syngas is further cooled to around 303K (M.Karmarkar, 2005). Then the condensed water will be removed. A gas dryer module of

Thermolib is adopted to simulate this process. The syngas leaving the gas dryer contains a small amount of water and will be transported to H<sub>2</sub>S removal unit.

### 5.5.2 Simplified H<sub>2</sub>S Removal Unit

The H<sub>2</sub>S removal processes include chemical reaction removal and physical sorbents adsorption. The H<sub>2</sub>S absorber is supposed to remove nearly all the H<sub>2</sub>S and small amount of CO<sub>2</sub> by lean solvent. Due to the limitation of Thermolib functions on solid phase physical solvent involved application, the H<sub>2</sub>S removal is assumed to work as a “filtering” process with a simplified model. The temperature and pressure during this process are assumed to be constant. With 99% of H<sub>2</sub>S removal, the parameters of syngas will be calculated. Considering the minimum amount (0.07% for Shell and 0.2% for Texaco) of H<sub>2</sub>S concentration in syngas, the error in syngas contents concentrations and enthalpy can be ignored. The energy penalty of AGR and sulphur regeneration will be considered as auxiliary power consumption in the whole process energy analysis in Chapter 7.

The simulation results of sweet syngas contents mole concentrations (%) are shown in Table 5.8:

Table 5.8 Parameters of sweet syngas parameters of Texaco gasifier

	Shell	Texaco
Ndot (mol/s)	3911	8691
P (bar)	26.9435	59.8
T (K)	304.8056	303.882
H <sub>2</sub> O (%)	18.81	40.94
CO (%)	0.63	1.46
CO <sub>2</sub> (%)	31.73	24.00
H <sub>2</sub> (%)	46.40	32.39

N <sub>2</sub> (%)	1.78	0.51
H <sub>2</sub> S (%)	0.07	0.29
COS (%)	7.76e-4	2.98e-3
Argon (%)	0.57	0.42

## 5.6 Summary

Chapter 5 introduced the basic principles and equations used in Thermolib, especially the polynomials used for the calculation of enthalpy, specific enthalpy, phase equilibrium and other key thermodynamic parameters in the simulation. The main auxiliary modules such as syngas quench and syngas cooler for Shell gasifier, water quench for Texaco gasifier, shift reactors and internal heat exchangers, COS hydrolysis reactor and simplified H<sub>2</sub>S removal unit in GEM are introduced. The modular methodology in Chapter 5 is different from the derived equation based on the method shown in Chapter 3 and Chapter 4, since the thermodynamic and chemical process calculation in the auxiliary modules need a database for the calculation of key parameters change during the process. Hence Thermolib is an ideal choice for the modelling work in this part.

The simulation results reveal that the shift reactor can increase the H<sub>2</sub> and CO<sub>2</sub> contents, the heat released by shift reactor is adopted to raise HP and LP steam for HRSG. Due to the limitation of Thermolib function on solid state involved process, the acid gas removal process is simplified.

## **Chapter 6 Modelling of A Combined Cycle Power Plant**

The syngas generated by GEM will be used as fuel to power the turbine machinery and generate electricity. The equipment which can convert the chemical energy and enthalpy to power are called heat engines. Heat engines have been studied for long time in history. The heat engines usually undertake thermodynamic cycles which can be divided as gas power cycle and vapour cycles (Çengel and Boles, 2006). In this study, the most widely used unit-gas turbine based on Braydon Cycle(Çengel and Boles, 2006) is chosen and modelled using the simulation tool - Thermolib and it burns the syngas to produce mechanical power. The mechanical power will subsequently be transferred to drive the synchronized generator through the connection shaft to produce electricity.

Meanwhile, to recover the enthalpy carried by the hot exhaust flue gas of the gas turbine, a heat recovery steam generator (HRSG) is added and modelled based on Rankine Cycle, which uses gas turbine exhausts to generate steam, and in turn to drive the steam turbine and the generator to produce electricity. The combination of gas turbine and HRSG is called combined cycle, which is used in IGCC power plants for electrical power generation.

During the project period, a model for the combined heat and power plant at University of Warwick is also studied and reported in this chapter.

### **6.1 Gas Turbine Model**

#### **6.1.1 Introduction of Gas Power Cycle**

Gas power cycles are thermodynamic cycles using gas as working fluid. The basic gas power cycles include internal combustion engine using reciprocating pistons (Otto cycle), gas turbine using rotor blades (Brayton cycle) and external combustion engine (Sterling cycle).

The reciprocating engines are usually small, compacted and with high efficiency, but the power capacity is normally not high. Hence they are often used as power in automobiles, merchant ships and small scale distributed power generation plants. Turbomachines such as gas turbines are with larger power capacity, high start-up speed and good flexibility; hence gas turbines are widely used in distributed power generation, military ships and aircrafts (jet engines).

Gas turbine cycle (Brayton cycle) was firstly proposed by George Brayton in around 1870 (Çengel and Boles, 2006), the cycle was used in a reciprocating oil-burning engine. Nowadays, gas turbine cycle usually uses compressor and turbine simultaneously. The schematic figure of Brayton cycle is shown in Figure 6.1:

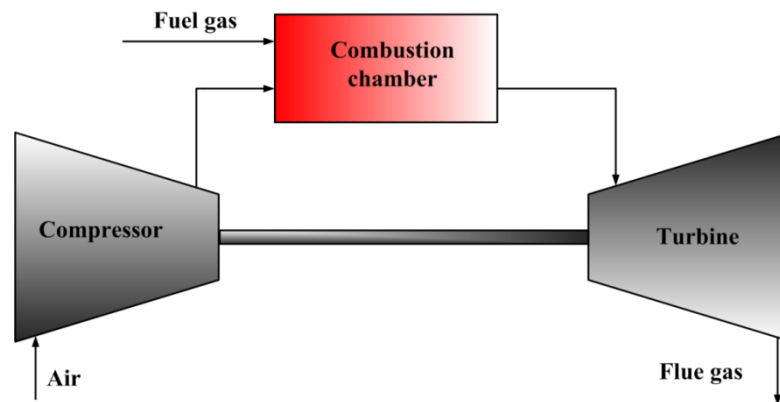


Figure 6.1 Schematics illustration of Brayton cycle

As the Figure 6.1 shown above, Brayton cycle is an open cycle with four processes: air compression in compressor where its temperature and pressure both rise, combustion of mixed fuel gas and air inside combustion chamber, expansion of gas in turbine block which drives rotor blades and generates mechanical power, exhaust flue gas ejection to the atmosphere. For simplification in theoretical study, we usually handle Brayton cycle as a closed cycle while studying the ideal Brayton cycle (Çengel and Boles, 2006), which is shown in Figure 6.2:

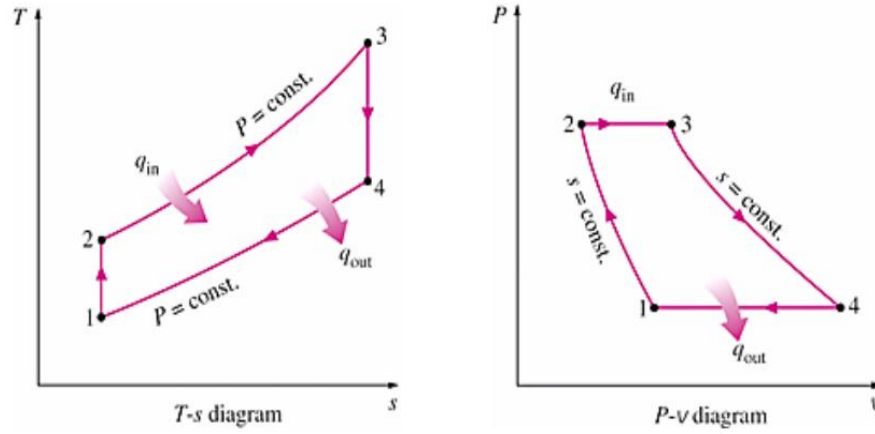


Figure 6.2 T-s and P-v diagrams of Brayton cycle (MAE115, 2012)

The ideal Brayton cycle includes four internal reversible processes (Çengel and Boles, 2006): 1-2 is isentropic compression of air in compressor; 2-3 is the combustion of mixed fuel gas and air in combustion chamber, which is considered as a isobaric heat addition; 3-4 is isentropic expansion process of flue gas in turbine block; 4-1 is the isobaric heat rejection process, working fluid return to original state of 1. For simplification, fuel gases are approximated as cold air in the derivation of Brayton cycle thermal efficiency equation(Çengel and Boles, 2006).

For the isobaric heat addition and rejection processes

$$q_{in} = c_p \cdot (T_3 - T_2) \quad (6.1)$$

$$q_{out} = c_p \cdot (T_4 - T_1) \quad (6.2)$$

$q_{in}$  denotes the input enthalpy flow (kJ/kg) while  $q_{out}$  denotes the output enthalpy flow (kJ/kg).  $c_p$  (kJ kg<sup>-1</sup> K<sup>-1</sup>) is the specific heat at constant pressure.  $T_1$  (K) to  $T_4$  (K) are the temperature at state point 1 to 4.

The thermal efficiency of ideal Brayton cycle  $\eta_{ideal, Brayton}$  can be derived as:

$$\eta_{ideal,Brayton} = 1 - \frac{q_{out}}{q_{in}} = 1 - \frac{c_p \cdot (T_4 - T_1)}{c_p \cdot (T_3 - T_2)} = 1 - \frac{T_4 - T_1}{T_3 - T_2} \quad (6.3)$$

Process 1-2 and 3-4 are isentropic compression and isentropic expansion respectively, hence we can have Equations (6.4) and (6.5) below:

$$\frac{T_4}{T_3} = \left(\frac{p_4}{p_3}\right)^{\frac{k-1}{k}} \quad (6.4)$$

$$\frac{T_1}{T_2} = \left(\frac{p_1}{p_2}\right)^{\frac{k-1}{k}} \quad (6.5)$$

where  $p$  is the pressure (Pa) at each state point and  $k$  is the specific heat ratio (constant volume specific heat divided by constant pressure specific heat with unit of  $\text{kJ m}^{-3} \text{K}^{-1}$ ):

$$k = \frac{c_v}{c_p} \quad (6.6)$$

Meanwhile, the processes 2-3 and 4-1 are isobaric, with Equations (6.4) and (6.5), hence we can have:

$$\frac{T_4}{T_3} = \frac{T_1}{T_2} \quad (6.7)$$

By substituting (6.7) to (6.3), the efficiency of ideal Brayton cycle  $\eta_{ideal,Brayton}$  can be derived as:

$$\eta_{ideal,Brayton} = 1 - \frac{T_1}{T_2} = 1 - \left(\frac{p_1}{p_2}\right)^{\frac{k-1}{k}} = 1 - \frac{1}{\gamma_c^{\frac{k-1}{k}}} \quad (6.8)$$

where  $\gamma_c$  is the compression ratio and can be calculated by Equation (6.9):

$$\gamma_c = \frac{p_2}{p_1} \quad (6.9)$$

Based on the equations above, we can conclude that the thermal efficiency of ideal Brayton cycle will increase when the pressure ratio increases. This conclusion is also applied to the analysis of real Brayton cycle (Çengel and Boles, 2006). But it is necessary to emphasize that the pressure ratio cannot be raised without any limitation, the current technology for compressor is the first limitation for pressure ratio increases, meanwhile, the maximum temperature at the end of combustion process (state point 3)  $T_3$  is also limited by the materials used for gas turbine manufacture.

In order to investigate the optimized Brayton cycle working condition, another parameter  $\tau_B$  as the temperature rise ratio is introduced:

$$\tau_B = \frac{T_3}{T_1} \quad (6.10)$$

Then the net work of ideal Brayton cycle  $w_{net}$  can be calculated by Equation (6.11):

$$w_{net} = (h_3 - h_4) - (h_2 - h_1) = c_p \cdot T_1 \cdot (\tau_B - \tau_B \cdot \gamma_c^{\frac{1-k}{k}} - \gamma_c^{\frac{k-1}{k}} + 1) \quad (6.11)$$

when the values of  $T_1$  (atmosphere temperature at state point 1,K) and  $T_3$  (maximum combustion temperature at state point 3,K) are confirmed, the maximum network  $w_{net,max}$  (kJ/kg) can be calculated as:

$$w_{net,max} = c_p \cdot T_1 (\sqrt{\tau_B} - 1)^2 \quad (6.12)$$



where the optimized pressure ratios  $\gamma_{c,opt}$  is:

$$\gamma_{c,opt} = \tau^{\frac{k}{2(k-1)}} \quad (6.13)$$

The optimized pressure ratio can give us guide for gas turbine working condition optimization.

With the derivation for the ideal Brayton cycle, we can subsequently derive the thermal efficiency for real Brayton cycle. The derivation for real Brayton cycle needs to consider the irreversibility in the compression and expansion processes. As shown in Fig. 6.3 (a), the compressed working fluid in real cycle will reach state 2a, not 2s as the ideal cycle does; the end state of expansion will be 4a in real cycle not 4s as the ideal cycle. In addition, pressure drop during the heat addition and rejection will cause further irreversibility and influence the calculation results. During the derivation of ideal cycle, only the irreversibility in compression and expansion are considered, the process is shown in Figure 6.3 (b).

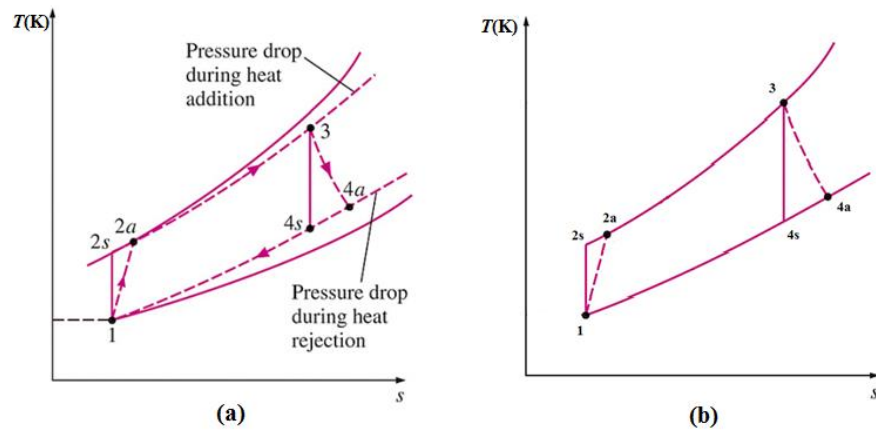


Figure 6.3 Actual Brayton cycle in T-s diagram by considering the irreversibility (MAE115, 2012)

The isentropic efficiency (Çengel and Boles, 2006) is introduced to describe the effects caused by irreversibility in compressor and turbine. The equation of isentropic efficiencies of compressor  $\eta_{s,compressor}$  and turbine  $\eta_{s,turbine}$  are shown as follows:

$$\eta_{s,compressor} = \frac{h_{2s} - h_1}{h_{2a} - h_1} \quad (6.14)$$

$$\eta_{s,turbine} = \frac{h_3 - h_{4a}}{h_3 - h_{4s}} \quad (6.15)$$

When the specific heat capacity is assumed to be constant, the thermal efficiency of actual Brayton cycle can be subsequently derived as Equation (6.16) (Çengel and Boles, 2006):

$$\eta_{actual} = \frac{\eta_{s,turbine} \cdot (T_3 - T_{4s}) - \frac{T_{2s} - T_1}{\eta_{s,compressor}}}{T_3 - T_1 - \frac{T_{2s} - T_1}{\eta_{s,compressor}}} \quad (6.16)$$

Equation (6.16) can also be transformed to the function of compressor ratio  $\gamma_c$  and temperature rise ratio  $\tau_B$ , which is Equation (6.17) below:

$$\eta_{actual} = \frac{\eta_t \cdot \frac{\tau_B^{\frac{k-1}{k}}}{\gamma_c^{\frac{k-1}{k}}} - \frac{1}{\eta_c}}{\frac{\tau_B^{\frac{k-1}{k}}}{\gamma_c^{\frac{k-1}{k}}} - 1 - \frac{1}{\eta_c}} \quad (6.17)$$

For the parameters involved in the calculation, the higher the isentropic efficiencies  $\eta_{s,compressor}$  and  $\eta_{s,turbine}$  are, the higher the thermal efficiency will be. The higher the temperature rise ratio  $\tau_B$  is, the higher the thermal efficiency will be. With the rise of compressor ratio, the thermal

efficiency will firstly rise and reach the maximum value then start to drop (Çengel and Boles, 2006).

The definition of these parameters' value is important during the simulation of gas turbine. For example, the isentropic efficiencies of compressor and turbine are influenced by the design of flow channels between rotor blades, the precision of design and manufacture. The maximum temperature  $T_3$  is limited by materials of nozzles and combustion chamber and hot-end blades. The  $\text{NO}_x$  emission control is also needed to be considered in the parameterization work (M.Karmarkar, 2005).

### 6.1.2 Gas Turbine Model Developed with Thermolib

An isentropic compressor module developed in Thermolib (Figure 6.4) is adopted to model the compression process; this module can compress the incoming flow to a given outlet pressure. In order to get accurate simulation results, the value of compressor isentropic efficiency  $\eta_{s,compressor}$  is set to be 0.8, which can decrease the error between simulation results and practical working conditions (Wang et al., 2015). The mechanical power during the compression  $P_{compressor}$  (kW) is calculated as:

$$P_{compressor} = \dot{m}_{air} \cdot (h_{2a} - h_1) = \frac{\dot{m}_{air} \cdot (h_{2s} - h_1)}{\eta_c} \quad (6.18)$$

A mixer module which has been introduced in Chapter 5 is adopted to simulate the mixing process of compressed air and fuel gas generated by GEM. The pressure loss during the mixing process is considered and the mixed gas and air will subsequently burn in the combustion chamber.

The combustion chamber is modelled with a reactor block in Thermolib block library, which is introduced in Chapter 5. The chemical reactions considered in the combustion process include:



The hot gas will pass through the turbine block where the gas pressure drops to the demanded value and the mechanical power generation is calculated based on the input and output enthalpy difference. A turbine block in Thermolib is adopted to model this process. Similar with the compressor block, the isentropic efficiency of the turbine block  $\eta_{s,turbine}$ , which is described by Equation (6.15), is introduced to improve the calculation accuracy. The mechanical power generation  $P_{turbine}$  can be calculated by:

$$P_{turbine} = \dot{m}_{flue} \cdot (h_3 - h_{4a}) = \dot{m}_{flue} \cdot (h_3 - h_{4s}) \cdot \eta_t \quad (6.22)$$

where  $\dot{m}_{flue}$  denotes the mass flow rate of hot flue gas. The net power generation by the whole gas turbine will be the difference between  $P_{turbine}$  and  $P_{compressor}$ . The Schematics diagram of gas turbine model developed in Thermolib is shown in Figure 6.4:

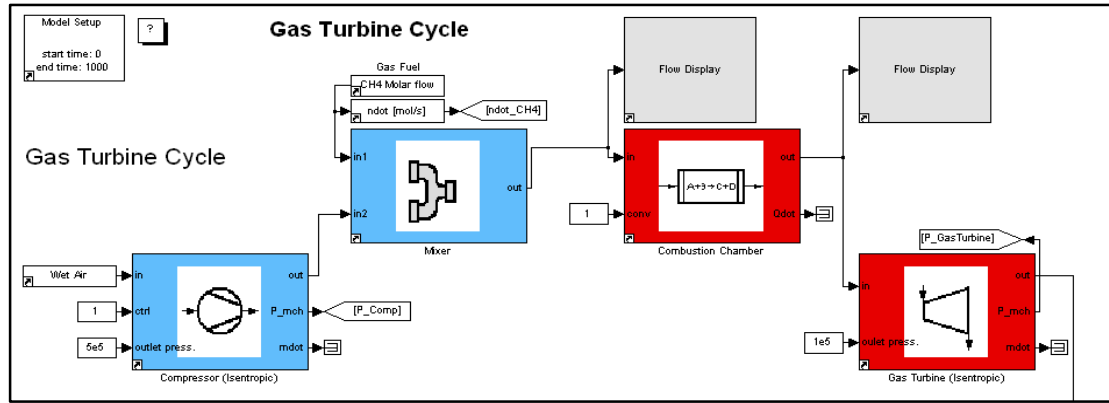


Figure 6.4 Gas turbine model developed by Thermolib

The syngas generated via the Texaco gasifier case introduced in Chapter 5 is used for steady and dynamic simulation study. The results from internal research report (M.Karmarkar, 2005) are used as the reference for the modelling and steady state validation for both of gas turbine module and HRSG module. In this case, only 17% of the total syngas generation is injected to the gas turbine.

The 25 bar fuel gas will mix with the wet air and undertake combustion in the combustion chamber. The compression ratio is set as 13.14 by giving consideration of optimization Equation (6.13) and limitation of the gas turbine design for syngas burning. The gas temperature after combustion  $T_3$  is 1367.8K, the actual outlet flue gas temperature is 836.4 K, which can satisfy the demand for HRSG module (M.Karmarkar, 2005). It is necessary to mention that in real industry, the gas turbine which is designed to burn methane or heavy oil needs modification to burn hydrogen; the combustion nozzle area needs to be increased and combustor outlet temperature needs to be controlled as well (M.Karmarkar, 2005). For syngas with a high hydrogen concentration, diluent gas such as nitrogen needs to be added to control combustion temperature for  $\text{NO}_x$  emission control. In the current case,  $\text{CO}_2$  can play this role as diluent gas, hence no nitrogen is added.

The model input data including syngas and wet air are shown in Table 6.1:

Table 6.1 Gas turbine model input

Parameters	Design data	Contents data
Syngas	Mass flow (kg/s):19.55	H <sub>2</sub> (mol%): 52
		CO <sub>2</sub> (mol%): 37.26
	P (bar): 25.85	N <sub>2</sub> (mol%): 7.6
		CO (mol%):2.5
	T (°C): 300	Ar (mol%):0.6
		H <sub>2</sub> O (mol%):0.04
Wet air	Mass flow (kg/s): 125.85	N <sub>2</sub> (mol%): 77.6
	P (bar): 1.013	O <sub>2</sub> (mol%): 20.8
	T (°C): 15	Ar (mol%): 0.8
		H <sub>2</sub> O (mol%):0.8

Gas turbine operation parameters and the steady state simulation results are shown in Table 6.2.

Table 6.2 GE 6B Gas turbine operation data comparing with reference data

Parameters	Reference data	Simulation results
Flue gas mass flow rate (kg/s)	145.4	145.4
Flue gas T (°C)	562	563
Flue gas P (bar)	1.013	1.013
CO <sub>2</sub> (mol%)	7.49	7.49
N <sub>2</sub> (mol%)	68.33	68.34
O <sub>2</sub> (mol%)	12.81	12.82
Ar (mol%)	0.82	0.82
H <sub>2</sub> O(mol%)	10.55	10.53

The simulation results show high accuracy with the design data (in terms of the steady state), which can well prove the model configuration and parameterization are reasonably acceptable. In terms of dynamic response study, the simulation results of net power generation, compressor power, gas turbine power output are shown in Figure 6.5.

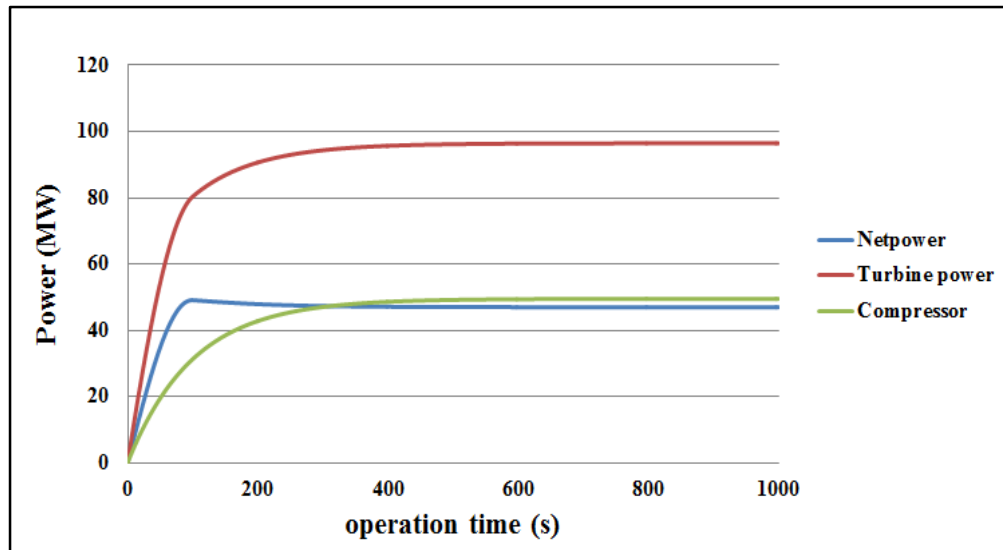


Figure 6.5 Dynamic change of power in gas turbine

As shown in Figure 6.5, when the syngas input rises to the steady state in 100 second, the total power generation by gas turbine is 96.45 MW. Since the turbine and compressor are having a co-shaft, the power of the compressor will come from the turbine. The compressor power in this case is 49.49 MW; hence the net power output of gas turbine module is 46.96 MW. The steady state of the gas turbine thermal efficiency is 31.67%.

## 6.2 HRSG Model

### 6.2.1 Introduction of Steam Power Cycle

The gas turbine exhaust temperature is usually higher than 500 °C, hence the thermal efficiency of gas turbine cycle is normally around 33% (Wang et al., 2015). To recover the heat in exhaust gas, a heat recovery steam generator (HRSG) is usually adopted to work with

gas turbine together to compose the combined cycle, which can utilize the exhaust heat of gas turbine to generate steam and drive the steam turbine to produce electricity. The HRSG working cycle is the well-known Rankine cycle (Çengel and Boles, 2006), which is widely used in steam cycle-based power generation industry.

The Rankine cycle was firstly proposed and named by Prof. William Rankine (Rankine, 1853). The equipment used in this cycle includes feed water pump, boiler, steam turbine and condenser (as shown in Figure 6.6). The feed water pressure will be raised by feed water pump first and transported to boiler, where the saturated water will be heated to superheat vapour, the vapour will expand in the steam turbine and generate mechanical power, then condensed in condenser hence form a closed cycle.

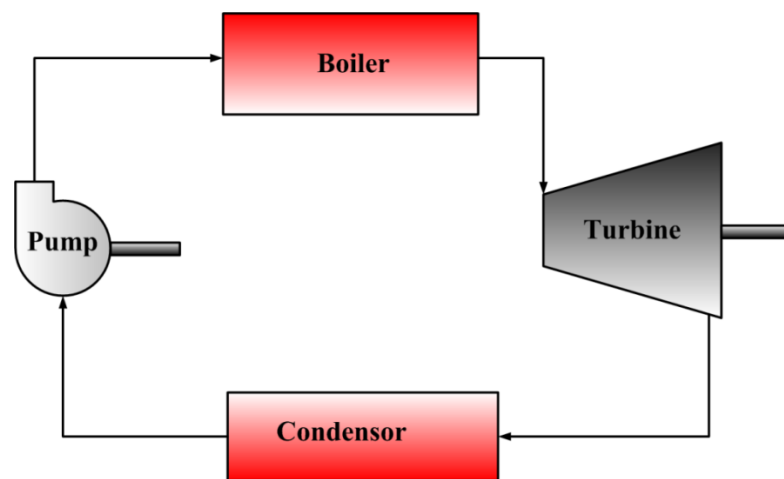


Figure 6.6 Schematics diagram of an ideal Rankine cycle

Unlike the Brayton cycle, Rankine cycle is a truly closed cycle and the working fluid will return to its original state after undertaking the four working steps. The ideal Rankine cycle by eliminating all internal irreversibility is shown in the T-s diagram below (Figure 6.7 (a)), which includes four working processes:

- 1-2, isentropic compression in feed water pump;



- 2-3, isobaric heat addition in the boiler;
- 3-4, isentropic expansion in steam turbine;
- 4-1, isobaric heat rejection in condenser .

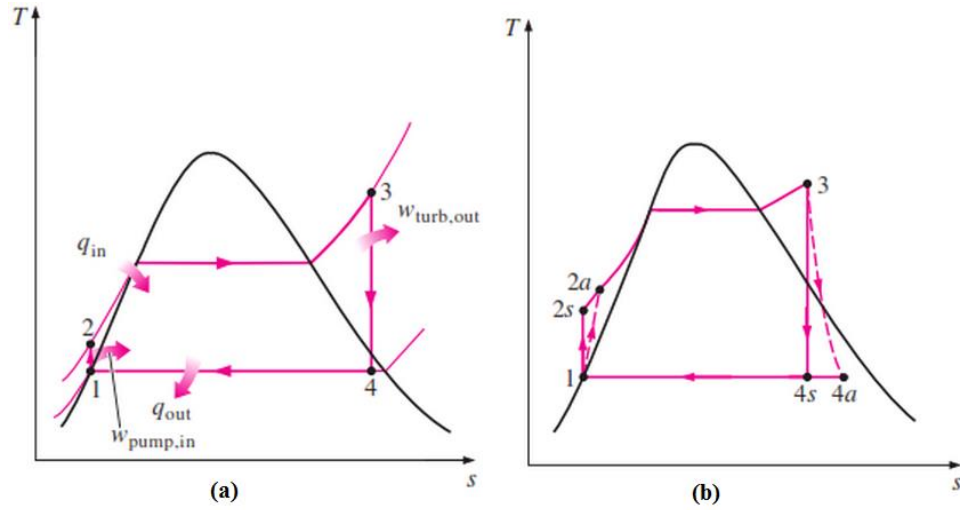


Figure 6.7 (a) Ideal Rankine cycle in T-s diagram (b) Actual Rankine cycle in T-s diagram (MAE115, 2012)

The saturated feed water at State 1 is compressed to the working pressure of the boiler and reaches State 2. The compressed water will subsequently enter into the boiler, which is actually working as a heat exchanger, can transfer the heat to water to reach to superheated steam. The heat transfer is driven by the large temperature difference of flames and flue gas inside the furnace and working fluid in the water wall; hence there will be irreversibility exist in this process that cause pressure drop. In the ideal Rankine cycle, this loss is ignored by assuming the heat transfer process is reversible. The derivation of ideal Rankine cycle thermal efficiency is shown as follows (Çengel and Boles, 2006):

The pump specific energy consumption  $W_{pump,in}$  (kJ/kg) can be calculated by Equation (6.23):

$$W_{pump,in} = h_{2,R} - h_{1,R} \quad (6.23)$$

where  $h_{1,R}$  and  $h_{2,R}$  are the specific enthalpy for working fluid in the state 1, 2 of Rankine cycle shown in Figure 6.7 (a). Since water can be approximately considered as incompressible fluid, the specific volume in States 1 and 2 can be considered as constant. Hence the pump specific energy consumption Equation (6.24) can be simplified as the product of specific volume  $v$  ( $\text{m}^3/\text{kg}$ ) and pressure rise  $\Delta p$  (kPa):

$$W_{\text{pump},in} = v \cdot \Delta p \quad (6.24)$$

The heat addition in boiler can be calculated by Equation (6.25):

$$q_{in} = h_{3,R} - h_{2,R} \quad (6.25)$$

where  $h_{3,R}$  (kJ/kg) denotes the specific enthalpy per unit mass in State 3 for Rankine cycle.

The power generation by the steam turbine  $w_{\text{turb},out}$  is calculated by Equation (6.26):

$$W_{\text{turb},out} = h_{3,R} - h_{4,R} \quad (6.26)$$

where  $h_{4,R}$  (kJ/kg) is the specific enthalpy in State 4 for Rankine cycle. Finally, the heat rejection in the condenser  $q_{out}$  (kJ/kg) can be calculated by Equation (6.27):

$$q_{out} = h_{4,R} - h_{1,R} \quad (6.27)$$

The thermal efficiency of ideal Rankine cycle  $\eta_{\text{ideal},R}$  can be calculated by:

$$\eta_{\text{ideal},R} = \frac{w_{\text{net}}}{q_1} = \frac{(h_{3,R} - h_{4,R}) - (h_{2,R} - h_{1,R})}{(h_{3,R} - h_{2,R})} = \frac{(h_{3,R} - h_{4,R}) - v \cdot \Delta p}{(h_{3,R} - h_{2,R})} \quad (6.28)$$

For actual Rankine cycle (shown in Figure 6.7(b)), we only consider the irreversibility during compression and expansion, the actual state of feed water to the boiler will be 2a, not 2s. Meanwhile, the actual state of steam turbine output will be 4a, not 4s. The derivation of actual Rankine cycle thermal efficiency and power output are presented in this section. Similar to the gas turbine process, the isentropic efficiency of the pump  $\eta_p$  and steam turbine  $\eta_{st}$  will be introduced to improve the accuracy of simulation.

$$\eta_p = \frac{h_{2s,R} - h_{1,R}}{h_{2a,R} - h_{1,R}} \quad (6.29)$$

$$\eta_{st} = \frac{h_{3,R} - h_{4a,R}}{h_{3,R} - h_{4s,R}} \quad (6.30)$$

where  $h_{2s,R}$ ,  $h_{2a,R}$ ,  $h_{4a,R}$  and  $h_{4s,R}$  (kJ/kg) are specific enthalpy flow per unit mass at state 2s and 2a, 4a and 4s, respectively for Rankine cycle. The actual pump energy consumption  $W_{pump}$  (kJ/kg) and steam turbine work output  $W_{st}$  (kJ/kg) can be represented by Equations (6.31) and (6.32):

$$W_{pump} = h_{2a,R} - h_{1,R} = \frac{v \cdot \Delta p}{\eta_p} \quad (6.31)$$

$$W_{st} = h_{3,R} - h_{4a,R} = (h_{3,R} - h_{4s,R}) \cdot \eta_{st} \quad (6.32)$$

Hence the thermal efficiency of actual Rankine cycle  $\eta_{actual,R}$  is:

$$\eta_{actual,R} = \frac{w_{net}}{q_1} = \frac{(h_3 - h_{4a}) - (h_{2a} - h_1)}{(h_3 - h_{2a})} = \frac{(h_3 - h_{4s}) \cdot \eta_{st} - \frac{v \cdot \Delta p}{\eta_p}}{(h_3 - h_{2a})} \quad (6.33)$$

### 6.2.2 Single Stage HRSG Model

A single stage HRSG model is developed using Thermolib, which includes five blocks: pump, boiler, steam turbine, condenser and a water tank for water supply.

For the pump model, it is similar to the compressor block model introduced in Section 6.1.1. The difference from compressor block is that pump is specially used for compressing liquid phase working fluid (Eutech, 2013). The power  $P_{mch}$  (kW) for raising water pressure in this process can be calculated as well.

$$P_{mch} = \dot{m}_{water} \cdot (h_{2a} - h_1) = \frac{\dot{m}_{water} \cdot v \cdot \Delta p}{\eta_p} \quad (6.34)$$

where  $\dot{m}_{water}$  (kg/s) denotes the mass flow rate of feed water, the isentropic efficiency is  $\eta_p$  can be specified as the model input. In this model, its value is set as 0.8.

The boiler and condenser blocks modelled with a heat exchanger block were introduced in Chapter 5. In the boiler block, heat is transferred from gas turbine exhaust to the feed water; water will be heated to superheated steam and drives the steam turbine to produce mechanical power. In the condenser block, the exhaust steam will be cooled to subcooled water by cold water. The steam turbine block is the same as the module adopted in the gas turbine model. The exhaust steam state is limited by steam dryness fraction (usually higher than 0.88 (M.Karmarkar, 2005)) since the moisture contents in steam will cause erosion to the turbomachine and unexpected power loss and operation depravation. A Schematics diagram of the single stage HRSG model developed with Thermolib is shown in Figure 6.8:

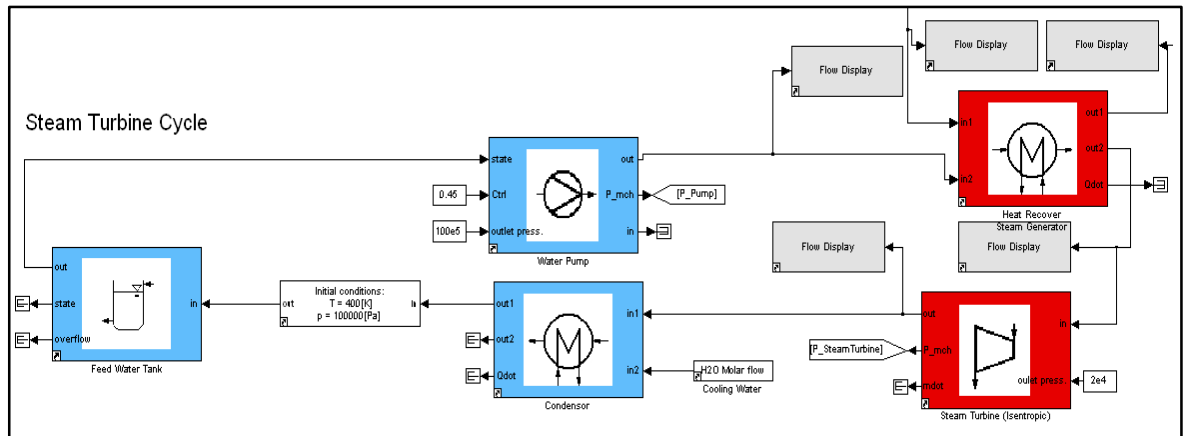


Figure 6.8 Schematics of single stage HRSG model developed with Thermolib

The parameters of single stage HRSG performance are shown in Table 6.3 and the parameters of main steam are from typical working condition for single stage HRSG (Duan, 2010):

Table 6.3 Parameters of flue gas, exhaust gas to atmosphere and generated main steam

Parameters	Flue gas	Exhaust gas	Main steam
Mass flow rate (kg/s)	145.4	145.4	23
T (°C)	563	150.5	358
P(bar)	1.04	1.04	63

The net power generation by single stage HRSG in steady state is 17.8 MW, which means power recovery from gas turbine cycle is 17.8 MW. In this case, the combined cycle efficiency will increase from 31.67% to 43.7%. The dynamic change of steam cycle net power generation is shown in Figure 6.9 .

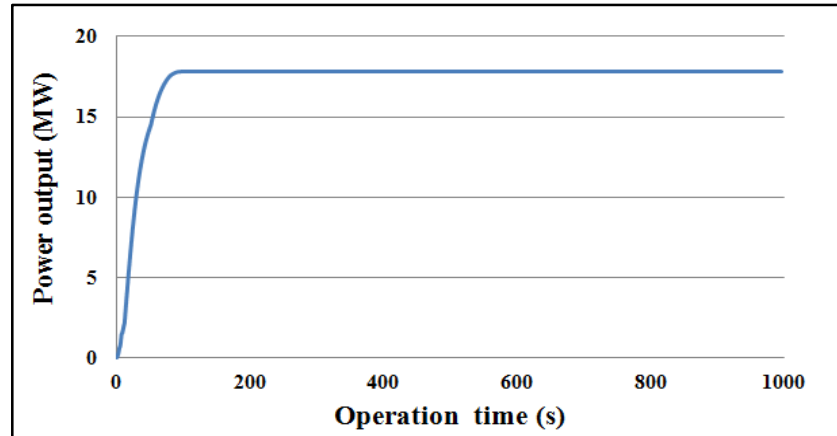


Figure 6.9 Dynamic change of single stage HRSG net power generation

### 6.2.3 Dual Stage HRSG Model

In order to improve the overall thermal efficiency of HRSG to achieve working condition optimization, a dual pressure HRSG Model is developed based on the configuration and design data proposed in reference (M.Karmarkar, 2005). Single stage HRSG can only produce steam of one pressure level. Dual stage HRSG produce HP and LP steam hence two steam circles are applied in this configuration and more heat can be recovered from the gas turbine flue gas. There are 10 banks of tube that form the heat exchanger located in this HRSG, 5 for LP cycle and 5 for HP cycle. The heat exchangers in LP cycle include: LP economiser, LP evaporator, LP primary super heater, LP secondary super heater and LP tertiary super heater. The flue gas pathway in these 10 stages of heat exchangers is shown in Figure 6.10.

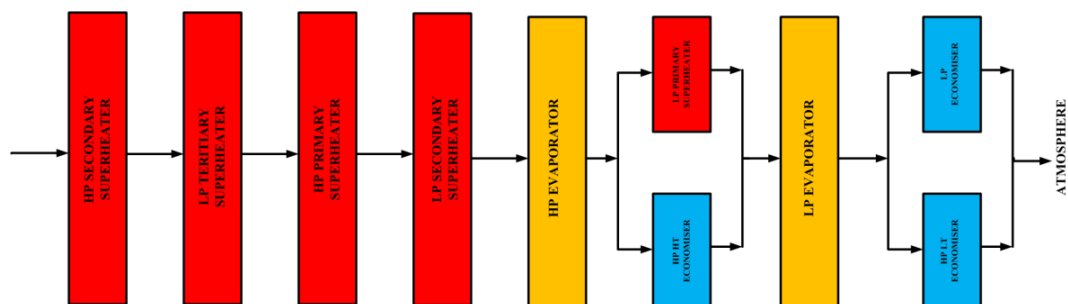


Figure 6.10 Flue gas pathway in HRSG

The Schematics diagram of the steam generation in LP cycle is shown in Figure 6.11. The LP feed water will be evaporated in the LP evaporator and mixed with LP saturated steam generated by GEM (introduced in Chapter 5), then became superheated steam in the following stages of heat exchangers and be transported to LP steam turbine to generate mechanical power.

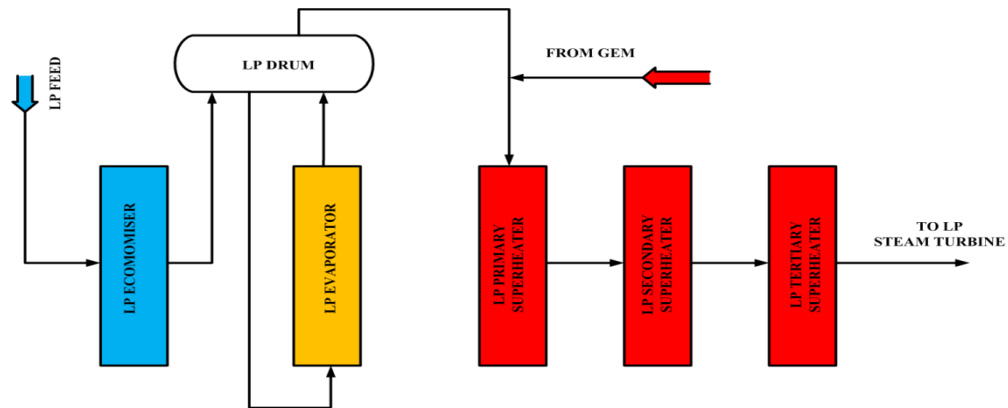


Figure 6.11 LP steam generation in HRSG

For the HP steam generation (Figure 6.12), the HP feed water will be heated in HP LT and HT economizer and evaporated in HP evaporator. After mixing with HP saturated steam generated by GEM, the steam will be further superheated in the following HP primary super heater an HP secondary super heater. The superheated steam will be transported to HP steam turbine to generated mechanical power.

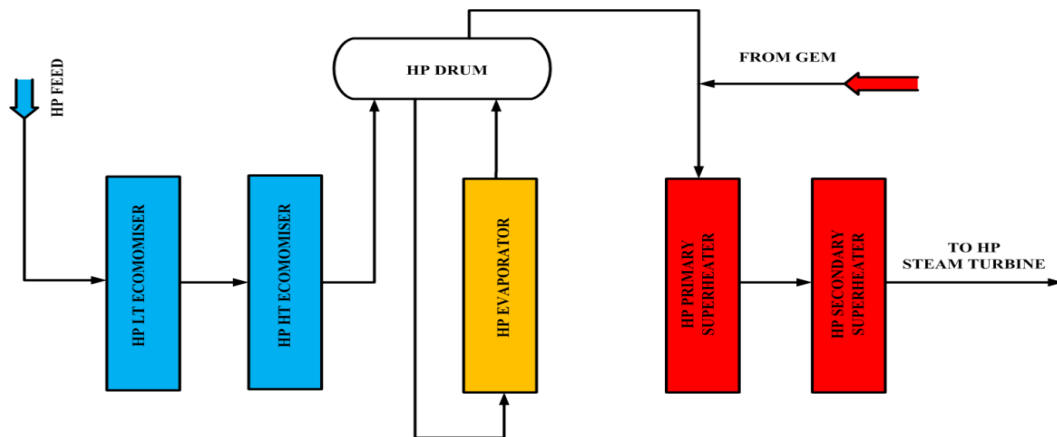


Figure 6.12 HP steam generation

The dual pressure HRSG model developed with Thermolib is shown in Figure 6.10. The heat transfer coefficients of ten stages of heat exchangers are calculated based on flue gas temperature data proposed in internal research report (M.Karmarkar, 2005), the steam generation of all the heat exchangers have been carefully tuned and validated based on the design data as well.

All the heat exchangers are modelled by using the heat exchanger block which has been introduced in Chapter 5. The overall heat transfer coefficients are calculated based on the syngas state parameters change. In some stages such as evaporators, there will be phase change of cold fluid occur, this process is approximated by setting the average enthalpy change of water, evaporation latent heat and steam. The simulation methodology is introduced in Chapter 5 as well. The dual pressure HRSG model is shown in Figure 6.13:



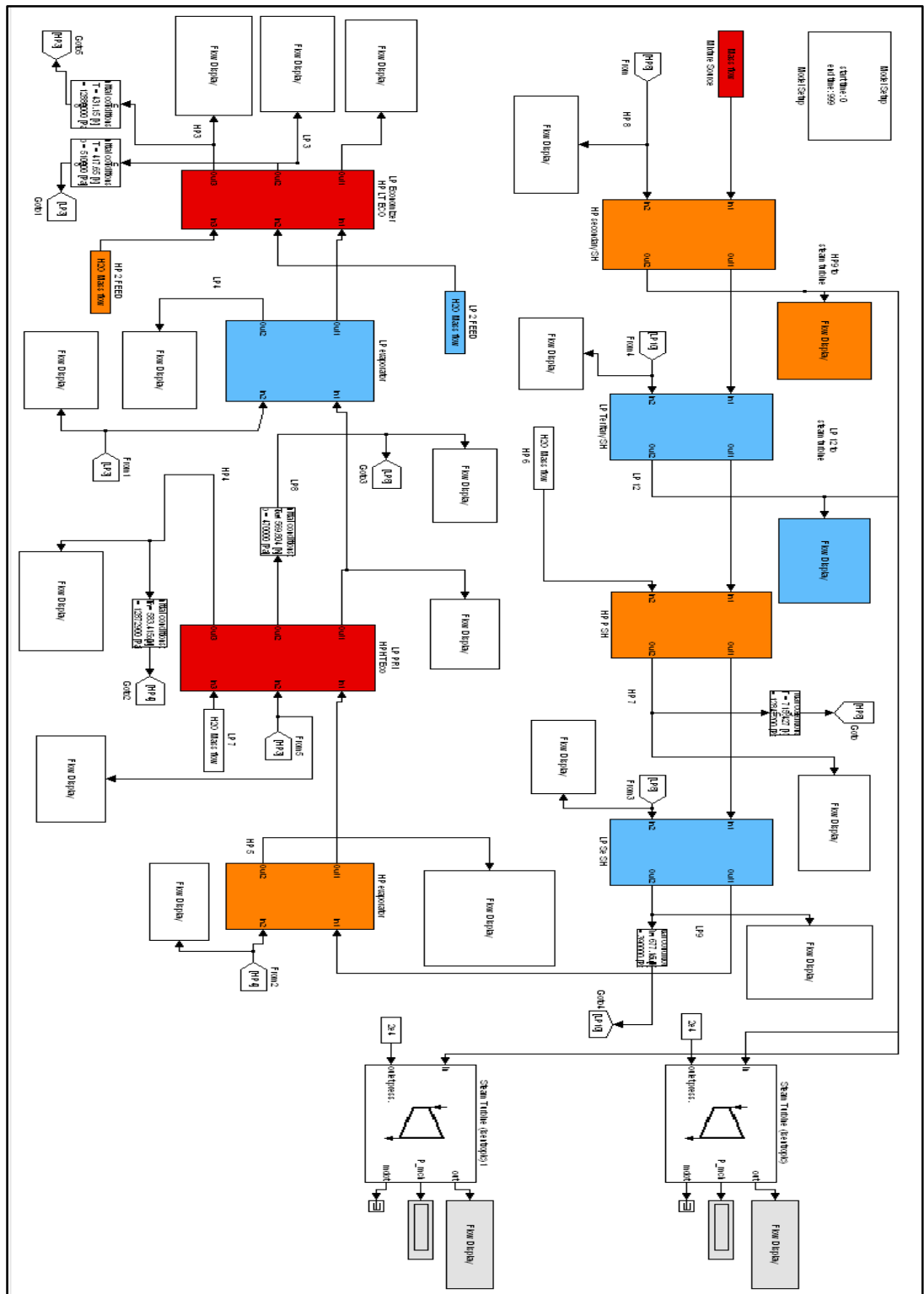


Figure 6.13 Schematics of dual-stage HRSG developed with Thermolih

The steady state simulation results of flue gas, LP steam and HP steam at different stages of heat exchangers are shown in Tables 6.4-6.13 and compared with the data in references.

Mean absolute error (MAE) of each stage flue gas and steam temperature and pressure simulation result are analysed.

Table 6.4 Parameters of HP secondary super heater

Parameters	Reference	Simulation
Flue gas input	Mass flow rate (kg/s):145.4	Mass flow rate (kg/s):145.4
	Temperature (°C) : 561	Temperature (°C) : 562
	Pressure (bar): 1.04	Pressure (bar): 1.04
Flue gas output	Mass flow rate (kg/s):145.4	Mass flow rate (kg/s):145.4
	Temperature (°C) : 530	Temperature (°C) : 530.15
	Pressure (bar): 1.04	Pressure (bar): 1.04
HP steam input	Mass flow rate (kg/s):19.494	Mass flow rate (kg/s):19.494
	Temperature (°C) : 442	Temperature (°C) : 442
	Pressure (bar): 128.4	Pressure (bar): 128.5
HP steam output	Mass flow rate (kg/s):19.494	Mass flow rate (kg/s):19.494
	Temperature (°C) : 541	Temperature (°C) : 541.2
	Pressure (bar): 125	Pressure (bar): 125

In the HP secondary super heater, HP steam will be superheated and then injected into the HP steam turbine. The MAE of this stage is 0.01%.

Table 6.5 Parameters of LP tertiary super heater

Parameters	Reference	Simulation
Flue gas input	Mass flow rate (kg/s):145.4	Mass flow rate (kg/s):145.4
	Temperature (°C) : 530	Temperature (°C) : 530.1
	Pressure (bar): 1.039	Pressure (bar): 1.04
Flue gas output	Mass flow rate (kg/s):145.4	Mass flow rate (kg/s):145.4
	Temperature (°C) : 463	Temperature (°C) : 463.6
	Pressure (bar): 1.034	Pressure (bar): 1.034
LP steam input	Mass flow rate (kg/s):55.747	Mass flow rate (kg/s):55.747
	Temperature (°C) : 404	Temperature (°C) : 404
	Pressure (bar): 3.9	Pressure (bar): 3.9
LP steam output	Mass flow rate (kg/s):55.747	Mass flow rate (kg/s): 55.747
	Temperature (°C) : 499	Temperature (°C) : 499.3
	Pressure (bar): 2.8	Pressure (bar): 2.8

In the LP tertiary super heater, LP steam will be superheated and then injected into the LP steam turbine. The MAE of this stage is 0.03%.

Table 6.6 Parameters of HP primary super heater

Parameters	Reference	Simulation
Flue gas input	Mass flow rate (kg/s):145.4	Mass flow rate (kg/s):145.4
	Temperature (°C) : 463	Temperature (°C) : 463.6
	Pressure (bar): 1.034	Pressure (bar): 1.034
Flue gas output	Mass flow rate (kg/s):145.4	Mass flow rate (kg/s):145.4
	Temperature (°C) : 436	Temperature (°C) : 431.3
	Pressure (bar): 1.033	Pressure (bar): 1.033
HP steam input	Mass flow rate (kg/s):19.494	Mass flow rate (kg/s):19.494
	Temperature (°C) : 377	Temperature (°C) : 377
	Pressure (bar): 128.7	Pressure (bar): 128.7
HP steam output	Mass flow rate (kg/s):19.494	Mass flow rate (kg/s): 19.494
	Temperature (°C) : 442	Temperature (°C) : 442.3
	Pressure (bar): 128.4	Pressure (bar): 128.4

In the HP secondary super heater, HP steam will be superheated to around 442°C. The MAE of this stage is 0.2%.

Table 6.7 Parameters of LP secondary super heater

Parameters	Reference	Simulation
Flue gas input	Mass flow rate (kg/s):145.4	Mass flow rate (kg/s):145.4
	Temperature (°C) : 436	Temperature (°C) : 434.5
	Pressure (bar): 1.033	Pressure (bar): 1.033
Flue gas output	Mass flow rate (kg/s):145.4	Mass flow rate (kg/s):145.4
	Temperature (°C) : 362	Temperature (°C) : 360.1
	Pressure (bar): 1.032	Pressure (bar): 1.032
LP steam input	Mass flow rate (kg/s):55.747	Mass flow rate (kg/s): 55.747
	Temperature (°C) : 298	Temperature (°C) : 298
	Pressure (bar): 4.7	Pressure (bar): 4.7
LP steam output	Mass flow rate (kg/s):19.494	Mass flow rate (kg/s): 19.494
	Temperature (°C) : 404	Temperature (°C) : 404.1
	Pressure (bar): 3.9	Pressure (bar): 3.9

In the LP secondary super heater, LP steam will be superheated to around 404°C. The MAE of this stage is 0.09%.

Table 6.8 Parameters of HP evaporator

Parameters	Reference	Simulation
Flue gas input	Mass flow rate (kg/s):145.4	Mass flow rate (kg/s):145.4
	Temperature (°C) : 362	Temperature (°C) : 354
	Pressure (bar): 1.032	Pressure (bar): 1.032
Flue gas output	Mass flow rate (kg/s):145.4	Mass flow rate (kg/s):145.4
	Temperature (°C) : 335	Temperature (°C) : 335.5
	Pressure (bar): 1.031	Pressure (bar): 1.031
HP steam input	Mass flow rate (kg/s):3.444	Mass flow rate (kg/s):3.444
	Temperature (°C) : 312	Temperature (°C) : 312
	Pressure (bar): 128.8	Pressure (bar): 128.7
HP steam output	Mass flow rate (kg/s):3.444	Mass flow rate (kg/s): 3.444
	Temperature (°C) : 331	Temperature (°C) : 331.07
	Pressure (bar): 128.8	Pressure (bar): 128.7

The HP evaporator will convert the saturated water to HP saturated steam. The HP steam temperature will rise to 331°C. The MAE of this stage is 0.04%.

Table 6.9 Parameters of HP HT economizer

Parameters	Reference	Simulation
Flue gas input	Mass flow rate (kg/s):145.4	Mass flow rate (kg/s):145.4
	Temperature (°C) : 335	Temperature (°C) : 335
	Pressure (bar): 1.031	Pressure (bar): 1.031
Flue gas output	Mass flow rate (kg/s): To be confirmed (TBC)	Mass flow rate (kg/s):145.4
	Temperature (°C) : TBC	Temperature (°C) : 319.7
	Pressure (bar): TBC	Pressure (bar): 1.027
HP steam input	Mass flow rate (kg/s):3.444	Mass flow rate (kg/s):3.444
	Temperature (°C) : 158	Temperature (°C) : 158
	Pressure (bar): 128.8	Pressure (bar): 128.8
HP steam output	Mass flow rate (kg/s):3.444	Mass flow rate (kg/s): 3.444
	Temperature (°C) : 312	Temperature (°C) : 310.4
	Pressure (bar): 128.8	Pressure (bar): 128.73

The HP HT economizer will heat the HP water from 158 °C to around 310 °C. The MAE of this stage is 0.19%.

Table 6.10 Parameters of LP Primary super heater

Parameters	Reference	Simulation
Flue gas input	Mass flow rate (kg/s):TBC	Mass flow rate (kg/s):145.4
	Temperature (°C) : TBC	Temperature (°C) : 319.7
	Pressure (bar): TBC	Pressure (bar): 1.027
Flue gas output	Mass flow rate (kg/s): 145.4	Mass flow rate (kg/s):145.4
	Temperature (°C) : 270	Temperature (°C) : 271.0
	Pressure (bar): 1.027	Pressure (bar): 1.027
LP steam input	Mass flow rate (kg/s):55.747	Mass flow rate (kg/s): 55.747
	Temperature (°C) : 231	Temperature (°C) : 231
	Pressure (bar): 5	Pressure (bar): 5
LP steam output	Mass flow rate (kg/s): 55.747	Mass flow rate (kg/s): 55.747
	Temperature (°C) : 298	Temperature (°C) : 298.6
	Pressure (bar): 4.7	Pressure (bar): 4.7

The LP Primary super heater will generate LP superheated steam with temperature of around 298 °C. The MAE of this stage is 0.2%.



Table 6.11 Parameters of LP Evaporator

Parameters	Reference	Simulation
Flue gas input	Mass flow rate (kg/s): 145.4	Mass flow rate (kg/s):145.4
	Temperature (°C) : 270	Temperature (°C) : 270
	Pressure (bar): 1.027	Pressure (bar): 1.027
Flue gas output	Mass flow rate (kg/s): 145.4	Mass flow rate (kg/s):145.4
	Temperature (°C) : 165	Temperature (°C) : 164.8
	Pressure (bar): 1.027	Pressure (bar): 1.027
LP input	Mass flow rate (kg/s):7.817	Mass flow rate (kg/s): 7.817
	Temperature (°C) : 144	Temperature (°C) : 144
	Pressure (bar): 5.1	Pressure (bar): 5.1
LP output	Mass flow rate (kg/s): TBC	Mass flow rate (kg/s): 7.817
	Temperature (°C) : 152	Temperature (°C) : 152.7
	Pressure (bar): 5.1	Pressure (bar): 5.1

The LP evaporator will generate LP steam of around 152°C. The MAE of this stage is 0.1%.

Table 6.12 Parameters of HP LT Economizer

Parameters	Reference	Simulation
Flue gas input	Mass flow rate (kg/s): 145.4	Mass flow rate (kg/s): 145.4
	Temperature (°C) : 165	Temperature (°C) : 165
	Pressure (bar): 1.027	Pressure (bar): 1.027
Flue gas output	Mass flow rate (kg/s): TBC	Mass flow rate (kg/s):145.4
	Temperature (°C) : TBC	Temperature (°C) : 159.9
	Pressure (bar): TBC	Pressure (bar): 1.027
HP input	Mass flow rate (kg/s):3.444	Mass flow rate (kg/s):3.444
	Temperature (°C) : 105	Temperature (°C) : 105
	Pressure (bar): 128.8	Pressure (bar): 128.8
HP output	Mass flow rate (kg/s): 3.444	Mass flow rate (kg/s): 3.444
	Temperature (°C) : 158	Temperature (°C) : 158.2
	Pressure (bar): 128.8	Pressure (bar): 128.7

The HP LT economizer will generate HP saturated water of around 158 °C. The MAE of this stage is 0.07%.

Table 6.13 Parameters of LP Economizer

Parameters	Reference	Simulation
Flue gas input	Mass flow rate (kg/s): TBC	Mass flow rate (kg/s):145.4
	Temperature (°C) : TBC	Temperature (°C) : 159.9
	Pressure (bar): TBC	Pressure (bar): 1.027
Flue gas output	Mass flow rate (kg/s): 145.4	Mass flow rate (kg/s):145.4
	Temperature (°C) : 151	Temperature (°C) : 151.35
	Pressure (bar): 1.026	Pressure (bar): 1.026
LP input	Mass flow rate (kg/s):7.817	Mass flow rate (kg/s): 7.817
	Temperature (°C) : 105	Temperature (°C) : 105
	Pressure (bar): 5.1	Pressure (bar): 5.1
LP output	Mass flow rate (kg/s): 3.444	Mass flow rate (kg/s): 3.444
	Temperature (°C) : 144	Temperature (°C) : 144.7
	Pressure (bar): 5.1	Pressure (bar): 5.1

The LP economizer can heat the LP saturated water to around 144°C. The MAE of this stage is 0.12%.

The steady state simulation results show high accuracy with the reference data (MAEs of flue gas and steam output simulation results range from 0.01% to 0.2%), which means the HRSG

model developed with Thermolib can successfully simulate the heat recovery steam generation process.

In this case, the evaporator bank pinch point is 8°C, super heater bank pinch point is 20°C, economizer pinch point is 8°C and the economizer approach point is 7°C (M.Karmarkar, 2005). Meanwhile, the economizer inlet water temperature is also set to be higher than the acid gas dew point to avoid the possible corrosion; the final exhaust gas temperature is set as 151°C, which is higher than acid gas dew point as well to avoid possible corrosion caused by acid condensation.

In terms of dynamic changes of power generation, the dynamic change of LP and HP cycle power output are studied. The net power output by subtracting the power required by LP and HP feed water pumps and pre-heating is shown as well. The net power generation of dual-stage power generation is 50.3 MW; the LP cycle contributes 33.4 MW while HP cycle contributes 20.6 MW (exclude feed water pump power), the back pressure of steam turbine is 20000 Pa. The current efficiency of the combined cycle is increased to 65.6% (with GEM steam). Unlike the gas power cycle, the steam cycle utilized the HP and LP steam generated by GEM (shift reactors), hence the start state of steam cycle is the power generation of this two steam cycles.

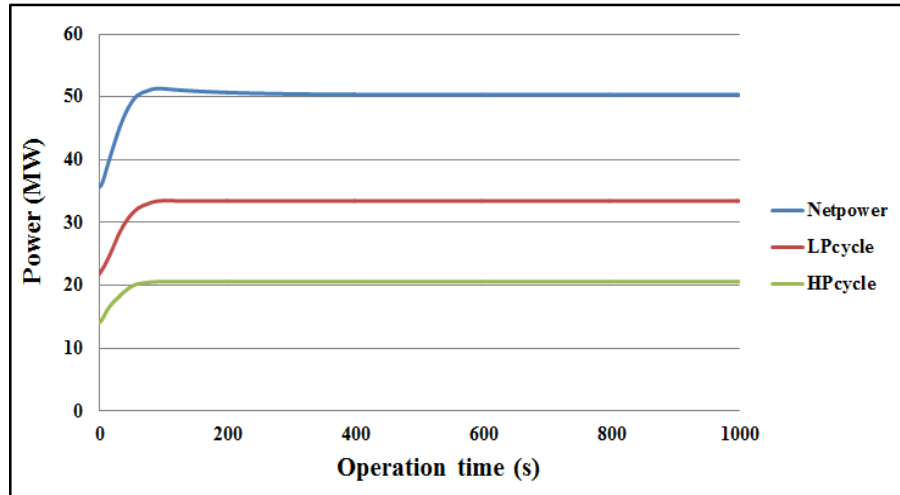


Figure 6.14 Dynamic change of steam cycle power generations

### 6.3 Combined Cycle Power Plant Model

A Schematics diagram of combined cycle power plant is shown in Figure 6.15, which is a combination of Brayton cycle and Rankine cycle. The combined cycle in T-s diagram is shown in Fig. 6.16.

The advantage combined cycle is its ability to recover the exergy of both cycles: the gas turbine cycle which has high average temperature during heat addition process can absorb heat from fuel combustion with lower temperature difference, while the steam cycle which has low average temperature during heat rejection process can release heat to atmosphere with relative lower temperature difference (Duan, 2010). Hence the overall efficiency can be improved. The integration of combined cycle with GEM (gasification enabled module) plant can improve the overall efficiency of IGCC as well.

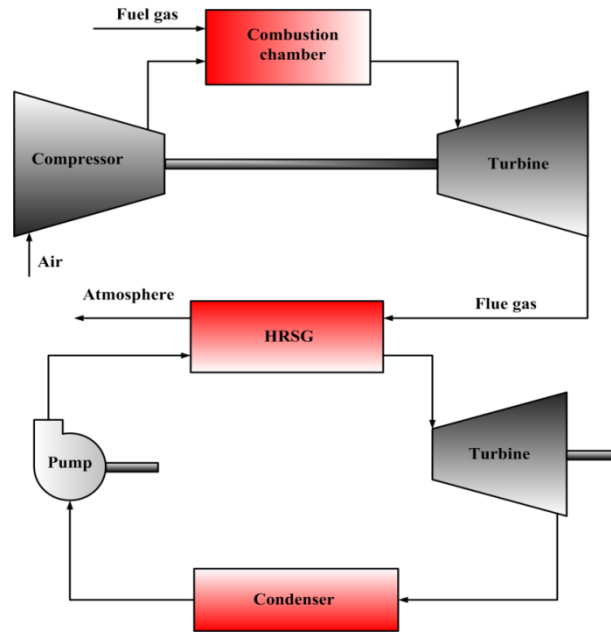


Figure 6.15 Combined cycle Schematics

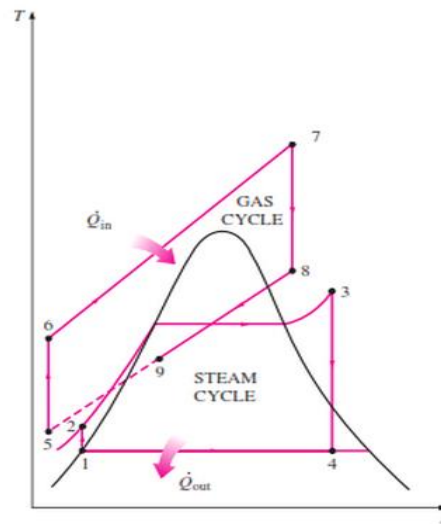


Figure 6.16 Combined cycle in T-s diagram.(Çengel and Boles, 2006)

In Sections 6.1, 6.2, 6.3, the model of combined cycle is introduced and analysed. The results analysed in Section 6.3 is the results of combined cycle formed with gas turbine and dual pressure HRSG. The dynamic performance of gas turbine and HRSG power generation is under the working condition of GEM module syngas generation detailed in Chapter 5.

## 6.4 Summary

Results Gas turbine model and two HRSG models are developed and analysed in this chapter. The models developed with Thermolib show relative high accuracy in terms of the steady state simulation. The single gas turbine thermal efficiency turns to be 31.67%, the combined cycle of gas turbine with single stage HRSG presents 43.7% of thermal efficiency.

The dual stage HRSG integrated with GEM plant generate around 50MW power which improve the combined cycle efficiency to 65.6%. Hence the integration with GEM can definitely produce more electricity than the independent combined cycle plant.

## **Chapter 7 Carbon Capture Process Model Based on PSA and Energy Penalty analysis**

Chapter 7 focuses on the carbon capture process based on PSA using ACs (activated carbons). The basic idea of PSA is to utilize the AC's different selectivity of CO<sub>2</sub> over H<sub>2</sub> under different pressure conditions to separate CO<sub>2</sub> and H<sub>2</sub> contents in the syngas stream, the captured CO<sub>2</sub> is compressed for sequestration and H<sub>2</sub> is used as the fuel gas for the gas turbine. The ACs samples used for experiments and simulation are developed by UoN (University of Nottingham), the experiments and simulation works are conducted by UoB (University of Birmingham), the results are provided by UoB for the application with IGCC model. Chapter 7 provides a brief introduction of the samples characteristics and the governing equations used in the PSA process simulation work conducted by UoB. The simulation results of PSA process based on the activated carbon samples are then used in the penalty analysis for IGCC.

Due to the limitation of direct connection of PSA model and IGCC model, the dynamic process of PSA is not modelled in this work; it is handled as a black box model by using the simulation results from UoB and integrated with IGCC model. The main energy penalty of PSA is caused by the recovery rate of hydrogen. The loss of hydrogen during PSA process will reduce the fuel gas input to the gas turbine and subsequently influence the power generation of the combined cycle. The energy losses for different capture rates are shown at the end of this chapter.

It is necessary to emphasize that the simulation conducted by UoB is based on the mixture of carbon dioxide and nitrogen, nitrogen is used to replace hydrogen in this case to show the working principle (Caldwell et al., 2015).



## **7.1 Introduction of PSA Model Developed by UoB**

### **7.1.1 Activated Carbon Sample Preparation**

The unmodified and modified activated carbon materials are produced by University of Nottingham with the techniques described by Sun (Sun et al., 2013). The samples are both prepared from phenolic resin by using hydrothermal process. The activation of carbon beads are taken by oxidation at 300 °C in air atmosphere for 2 hours. The modified AC is prepared from the parent unmodified sample by mixing with nitric acid for oxidation under the ratio of 10g of AC to 250ml of nitric acid. The mixing is under room temperature and lasts for one hour. After washing and drying and amination process in a tube furnace at 800 °C, the modified AC sample is generated as the picture shown below:

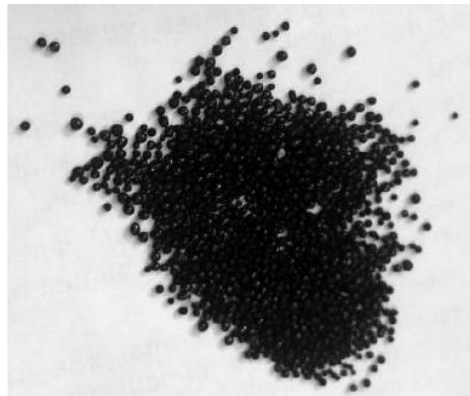


Figure 7.1 Modified AC sample

UoB has built a fixed bed reactor test rig for the activated carbon adsorption process test and PSA implementation. The Schematics of the experiments test rig is shown as Figure 7.2.

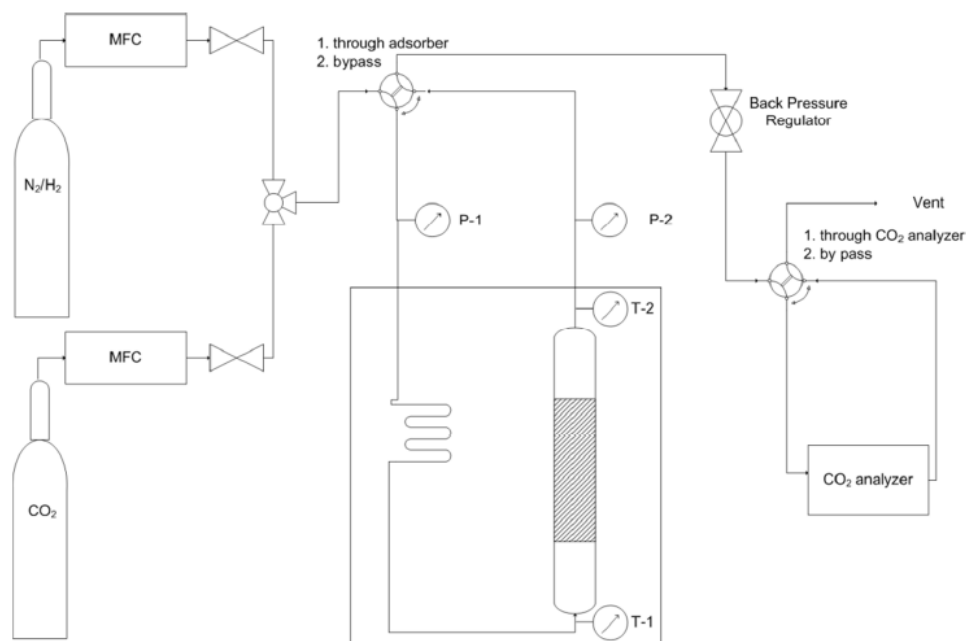


Figure 7.2 Test rig built by UoB (Caldwell, 2015)

The breakthrough experiments were conducted with this test rig. The mixing of pure carbon dioxide and nitrogen allows syngas with different CO<sub>2</sub> mole fractions to be tested. The breakthrough experiments for modified and unmodified samples are both carried out in the test rig. Before taking the breakthrough experiment, the bed is fully regenerated in order to remove all the residual carbon dioxide remaining in the AC sample.

## 7.1.2 Adsorption Isotherms Model for Activated Carbons

### 7.1.2.1 Model Development

Adsorption isotherm model is used to calculate the AC's adsorption capacity for different gases, which is dependent on the system pressure. Hence the pure isotherm model is applied in the work of UoB to predict the material's adsorption capacity  $q_i^*$  (mol/m<sup>3</sup>) which will be used in PSA process simulation.

The simplest model applied is the Langmuir isotherm model shown below in Equation (7.1) (Langmuir, 1918). With Equations (7.2) and (7.3), the Langmuir model can be converted from pressure independent to temperature independent form. The conversion is performed in order to accurately use the isotherm models (Caldwell, 2015).

Langmuir isotherm model

$$q_i^* = \frac{q_{s,i} B_i P_i}{(1 + B_i P_i)} \quad (7.1)$$

$$q_{s,i} = k_{1,i} \times e^{k_{2,i}/RT} \quad (7.2)$$

$$B_i = k_{3,i} \times e^{k_{4,i}/RT} \quad (7.3)$$

where  $q_i^*$  (mol m<sup>-3</sup>) is the component solid phase concentration at equilibrium,  $q_{s,i}$  (mol kg<sup>-1</sup>) is the component solid phase concentration at saturation.  $B_i$  is the Langmuir-Freundlich constant and  $P_i$  (Pa) is the component partial pressure.  $k_{1,i}$ ,  $k_{2,i}$ ,  $k_{3,i}$ ,  $k_{4,i}$  are constant for finding  $q_{s,i}$ .  $R$  is the gas constant and  $T$  is temperature (K). (Caldwell, 2015)

By applying a power law function to pressure term of the Langmuir model, Equation (7.1) can be further derived as Langmuir-Freundlich isotherm model as shown in Equation (7.4) :

$$q_i^* = \frac{q_{s,i} B_i (P_i)^{n_i}}{(1 + B_i (P_i)^{n_i})} \quad (7.4)$$

where  $n_i$  is the exponent in Langmuir-Freundlich isotherm (Caldwell, 2015).

The last implemented isotherm model is the Dual-Site Langmuir (DSL) isotherm model shown in Equation (7.5) With Equation (7.5) to (7.9) , the DSL model can be converted to temperature independent form.

$$q_i^* = \frac{q_{1,s,i} B_{1,i} P_i}{(1 + B_{1,i} P_i)} + \frac{q_{2,s,i} B_{2,i} P_i}{(1 + B_{2,i} P_i)} \quad (7.5)$$

$$q_{1,s,i} = k_{1,1,i} \times e^{k_{1,2,i}/RT} \quad (7.6)$$

$$q_{2,s,i} = k_{2,1,i} \times e^{k_{2,2,i}/RT} \quad (7.7)$$

where  $q_{1,s,i}$  (mol kg<sup>-1</sup>) and  $q_{2,s,i}$  (mol kg<sup>-1</sup>) are components 1 and 2's solid phased concentration at saturation in DSL model.  $k_{1,2,i}$  (-) and  $k_{2,2,i}$  (-) are constants for finding  $q_{1,s,i}$ ;  $k_{2,1,i}$  (-) and  $k_{2,2,i}$  (-) are constants for finding  $q_{2,s,i}$ . (Caldwell, 2015)

$$B_{1,i} = k_{1,3,i} \times e^{k_{1,4,i}/RT} \quad (7.8)$$

$$B_{2,i} = k_{2,3,i} \times e^{k_{2,4,i}/RT} \quad (7.9)$$

where  $B_{1,i}$  (Pa) and  $B_{2,i}$  (Pa) are DSL constant site 1 and 2, respectively.  $k_{1,3,i}$  (-) and  $k_{1,4,i}$  (-) are constants for finding  $B_{1,i}$  in DSL while  $k_{2,3,i}$  (-) and  $k_{2,4,i}$  (-) are constants for finding  $B_{2,i}$  in DSL. (Caldwell, 2015)

In terms of model validation by using experiment data, the sum of the squared relative errors *SSE* is used in the study (García et al., 2013).

$$SSE(\%) = \left( \frac{\sum [(q_{i,\text{exp}}^* - q_{i,\text{mod}}^*) / q_{i,\text{exp}}^*]^2}{N - 1} \right)^{0.5} \times 100 \quad (7.10)$$

where  $q_{i,\text{exp}}^*$  (mol kg<sup>-1</sup>) and  $q_{i,\text{mod}}^*$  (mol kg<sup>-1</sup>) are the component solid phase concentration at equilibrium from experiment and model, respectively.

Since the multicomponent isotherms are difficult to test in experiments, it is necessary to get the original Langmuir-Freundlich equation and Dual site Langmuir equation extended in order to predict the AC's adsorption capacity for gas mixture based on the materials' pure isotherm (Caldwell, 2015). The Multicomponent adsorption isotherm equations are derived as Equation (7.11) and (7.12) (Ruthven, 1984):

Multicomponent Langmuir-Freundlich Isotherm

$$q_i^* = \frac{q_{s,i} B_i (Py_i)^{n_i}}{(1 + \sum_{j=1}^i B_j (Py_j)^{n_j})} \quad (7.11)$$

where  $y_i$  is the component mole fraction.

Multicomponent Dual site Langmuir Isotherm

$$q_i^* = \frac{q_{1,s,i} B_{1,i} Py_i}{(1 + \sum_{j=1}^i B_{1,j} Py_j)} + \frac{q_{2,s,i} B_{2,i} Py_i}{(1 + \sum_{j=1}^i B_{2,j} Py_j)} \quad (7.12)$$

where  $q_{1,s,i}$  (mol kg<sup>-1</sup>) and  $q_{2,s,i}$  (mol kg<sup>-1</sup>) are component  $i$  solid phase concentration upon, dual site 1 and 2 (mol/kg), respectively.  $B_{1,i}$  and  $B_{2,i}$  are LF constant component  $i$ , dual site type 1 and 2, respectively (Pa<sup>-n</sup>).

Besides extended pure component equations detailed in Equations (7.11) and (7.12), the ideal adsorbed solution theory (IAST) can be another solution by using the pure component data to predict multicomponent adsorption capacity (Rouquerol et al., 2013).

Unlike the extended pure component equations, the IAST is based on the assumption that the adsorbed phase thermodynamically ideal, the spreading pressure of each component  $\pi_i^0$  in the syngas are equal (Rouquerol et al., 2013). The IAST base equations are shown as Equations (7.13) to (7.14) ,

$$\frac{\pi_i^0 A}{RT} = \int_0^{p_i^0} \frac{q_i^{pure}}{p_i} dp_i \quad (7.13)$$

where  $\pi_i^0$  (Pa) is the spreading pressure while  $A$  (m<sup>3</sup>) denotes the bed cross sectional area.  $q_i^{pure}$  (mol m<sup>-3</sup>) is the solid phase concentration predicted by pure component isotherm.

$$\frac{1}{q_t} = \sum \frac{x_i}{q_i^{pure}} \quad (7.13)$$

$$q_i = x_i q_t \quad (7.14)$$

where  $q_t$  (mol m<sup>-3</sup>) is the total solid phase concentration while  $q_i$  (mol m<sup>-3</sup>) is the component solid phase concentration,  $x_i$  is the adsorbed phase component fraction. (Caldwell, 2015)

Equation (7.13) establishes the relationship between spreading pressure  $\pi_i^0$  (Pa) and equilibrium pressure which can then be equated for each other (Caldwell, 2015). This can be applied to IAST-LF and IAST-DSL Equations (7.16) and (7.17) respectively:

$$q_{s,1} \ln \left( 1 + B_1 \left( \frac{p_1}{x_1} \right)^{n_1} \right) = q_{s,2} \ln \left( 1 + B_2 \left( \frac{p_2}{1 - x_1} \right)^{n_2} \right) \quad (7.15)$$

$$\begin{aligned}
q_{1,s1} \ln \left( 1 + \frac{B_{1,1} p_1}{x_1} \right) + q_{2,s1} \ln \left( 1 + \frac{B_{2,1} p_1}{x_1} \right) = \\
q_{1,s2} \ln \left( 1 + \frac{B_{1,2} p_2}{1 - x_1} \right) + q_{2,s2} \ln \left( 1 + \frac{B_{2,2} p_2}{1 - x_1} \right)
\end{aligned} \tag{7.16}$$

where  $q_{1,s1}$  (mol kg<sup>-1</sup>) and  $q_{1,s2}$  (mol kg<sup>-1</sup>) are component  $i$  solid phase concentration

The equations can be solved and the results of adsorbed phase component fractions  $x_i$  (-) can be found. Then the results of  $x_i$  can be used in Equations (7.13) and (7.14) and the adsorbent capacity for each component can be found and analysed (Caldwell et al., 2015).

The bed model which is developed as the basic unit for PSA process is based on the adsorption models introduced above, the derivation of bed model is not detailed in this chapter due to the limitation of space, it can be referred to reference (Caldwell, 2015).

### 7.1.2.2 Isotherm Results and Discussion

The simulation results for pure component isotherm based on unmodified activated carbon and modified activated carbon are shown in Figure 7.3 and Figure 7.4, respectively. For the unmodified activated carbon, isotherms are studied at two temperatures (30°C and 45°C) while the isotherms for modified activated carbon are studied at four temperatures (25°C, 30°C, 45°C and 50°C). The results of Figure 7.3 and Figure 7.4 show that the three isotherm models can fit reasonably well with the experiment data for N<sub>2</sub>, which is close to linear. But the CO<sub>2</sub> isotherm is better fitted with LF and DSL models than Langmuir model (Caldwell et al., 2015). Especially in the high pressure range which is applied in pre-combustion capture process, the LF model and DSL model show higher agreement than the Langmuir model. The

pure isotherms model will be used as the base for the multicomponent simulation which is the real working condition in PSA process.

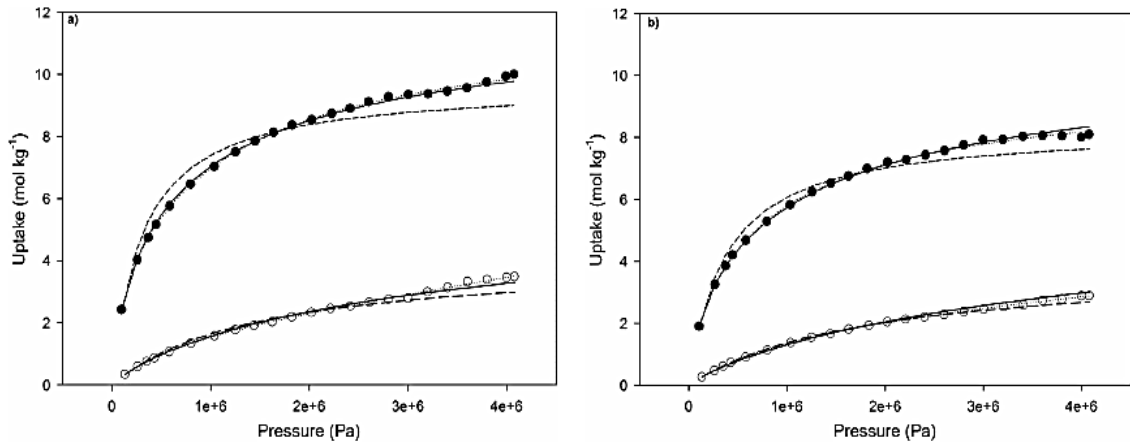


Figure 7.3 Experiment isotherms for unmodified AC for CO<sub>2</sub> (black circles) and N<sub>2</sub> (white circles) at 30 °C (a) and 45 °C (b) and the simulation results of isotherm models: Langmuir model (dashed), LF model (solid) and DSL model (dotted) (Caldwell et al., 2015)

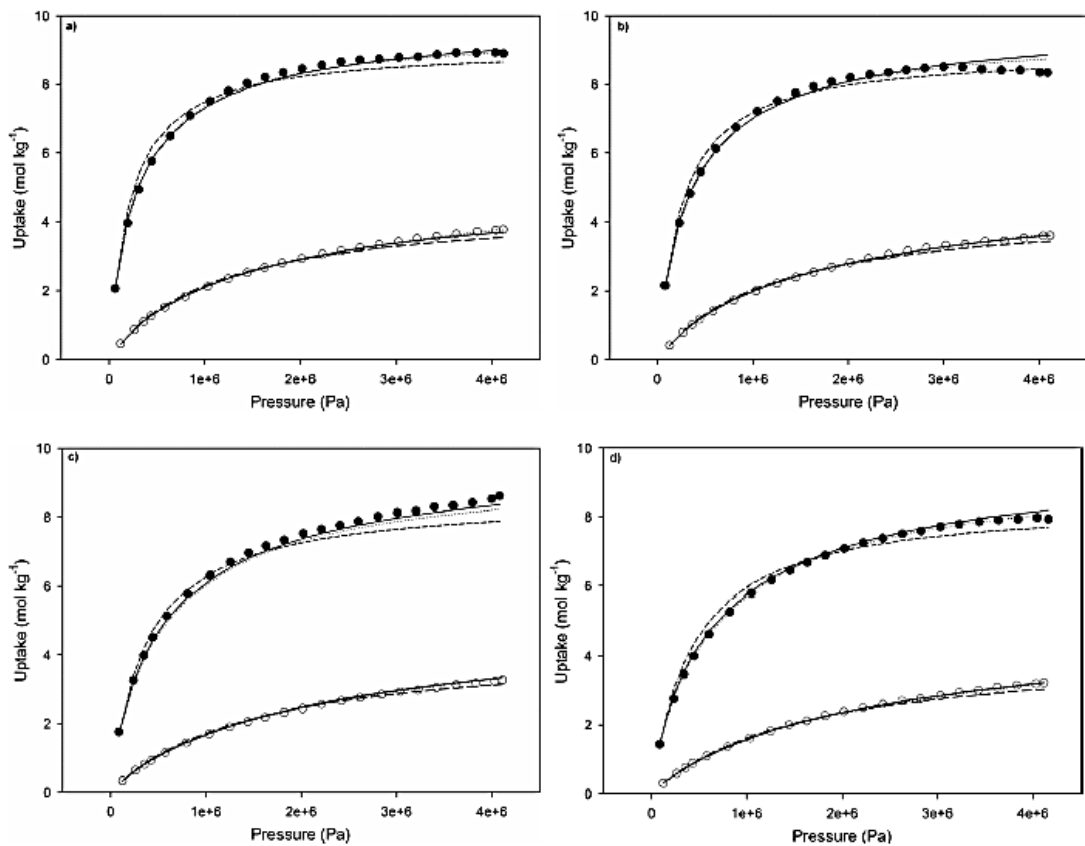


Figure 7.4 Experiment isotherms for unmodified AC for CO<sub>2</sub> (black circles) and N<sub>2</sub> (white circles) at 30 °C (a) and 45 °C (b) and the simulation results of isotherm models: Langmuir model (dashed), LF model (solid) and DSL model (dotted) (Caldwell et al., 2015)



Normally a PSA system will not reach full saturation of the bed, hence the breakthrough capacity of CO<sub>2</sub>/N<sub>2</sub> mixture is more realistic for the prediction of the PSA working unit (Caldwell, 2015). UoB conducted the breakthrough tests for CO<sub>2</sub>/N<sub>2</sub> mixture under different CO<sub>2</sub> feed fraction and provided the average breakthrough capacity over three cycles under 2500kPa and 298K, the details of experiment condition can be found in reference (Caldwell et al., 2015) as well. The experiments results are compared with the predicted capacity for pure isotherms at the equivalent partial pressure with assumption that the N<sub>2</sub> will not interact with CO<sub>2</sub>. Based on the comparison shown in Table 7.1, it is clear that there is large difference spreading degree at low feed fraction (0.1) and the other values difference is almost constant.

Table 7.1 The breakthrough capacities of CO<sub>2</sub>/N<sub>2</sub> mixtures separated using unmodified activated carbon for each experimental run and the predicted capacity for pure components based on the LF and DSL models (Caldwell et al., 2015).

CO <sub>2</sub> feed fraction	Breakthrough capacity	LF Model	DSL Model
(-)	(mol/kg)	(mol/kg)	(mol/kg)
0.1	2.12 ± 0.14	4.38	4.43
0.2	4.05 ± 0.15	5.93	5.94
0.3	5.01 ± 0.08	6.88	6.86
0.4	5.54 ± 0.17	7.55	7.51
0.5	6.09 ± 0.06	8.06	8.02

However, the difference between the isotherm models and experiment data also suggest that the N<sub>2</sub> in mixture will cause significant affect to the CO<sub>2</sub> adsorption hence the more accurate model will be needed to predict the capacity for mixture. As described in the very end of section 7.1.2.1, the models which use pure component data to predict multicomponent adsorption capacities are applied here to complete this mission. As shown in Table 7.2, predicted adsorption capacity for CO<sub>2</sub>/N<sub>2</sub> mixture based on multicomponent LF and

multicomponent DSL models are compared with experiment data. In addition, the Ideal Adsorbed Solution Theory (IAST) is also applied to the corresponding pure component results.

Table 7.2 Breakthrough Predicted multicomponent adsorption capacities based on the multicomponent LF and DSL models and the corresponding IAST models for CO<sub>2</sub>/N<sub>2</sub> mixtures separated using unmodified activated carbon (Caldwell et al., 2015)

CO <sub>2</sub> feed fraction (-)	CO <sub>2</sub> breakthrough capacity (mol/kg)	IASF-LF Model (mol/kg)		LF Model (mol/kg)		IAST-DSL Model (mol/kg)		DSL Model (mol/kg)	
		CO <sub>2</sub>	N <sub>2</sub>	CO <sub>2</sub>	N <sub>2</sub>	CO <sub>2</sub>	N <sub>2</sub>	CO <sub>2</sub>	N <sub>2</sub>
0.1	2.12 ± 0.14	2.8	0.94	2.88	2.04	2.55	1.11	2.95	1.97
0.2	4.05 ± 0.15	4.49	0.60	4.27	1.66	3.88	0.79	4.75	1.43
0.3	5.01 ± 0.08	5.70	0.40	5.30	1.37	4.82	0.60	5.99	1.06
0.4	5.54 ± 0.17	6.60	0.27	6.12	1.13	5.58	0.46	6.91	0.79
0.5	6.09 ± 0.06	7.30	0.18	6.82	0.91	6.21	0.35	7.62	0.59

It is obvious that IAST-LF predicts higher CO<sub>2</sub> capacity and lower N<sub>2</sub> capacity than multicomponent LF model, and the IAST predicts much higher CO<sub>2</sub> selectivity over N<sub>2</sub> than LF model under high CO<sub>2</sub> feed fractions (especially 0.4 and 0.5). IAST-DSL and multicomponent DSL models show opposite conclusion as DSL predicts higher CO<sub>2</sub> and N<sub>2</sub> capacities. The predicted selectivities of CO<sub>2</sub> over N<sub>2</sub> by using unmodified AC are shown in Table 7.3.

Table 7.3 Predicted selectivities of CO<sub>2</sub>/N<sub>2</sub> mixture using unmodified AC based on multicomponent LF and DSL models and the corresponding IAST models (Caldwell, 2015)

CO <sub>2</sub> Feed Fraction	IAST-LF	LF	IAST-DSL	DSL
(-)	(mol <sub>CO2</sub> /mol <sub>N2</sub> )	(mol <sub>CO2</sub> /mol <sub>N2</sub> )	(mol <sub>CO2</sub> /mol <sub>N2</sub> )	(mol <sub>CO2</sub> /mol <sub>N2</sub> )
0.1	26.8	12.7	20.7	13.5
0.2	29.9	10.3	19.6	13.3
0.3	33.3	9.0	18.7	13.2
0.4	36.7	8.1	18.2	13.1
0.5	40.6	7.5	17.7	12.9

It is interesting to compare the selectivity of CO<sub>2</sub> over N<sub>2</sub> predicted by these multicomponent models with pure isotherms shown in Figure 7.3. For multicomponent condition, although there is a reduction on CO<sub>2</sub> capacity comparing with pure form condition, the mixture adsorption capacity of N<sub>2</sub> is significant less than pure component capacity, which makes the selectivity of CO<sub>2</sub> over N<sub>2</sub> for multicomponent is much higher than it is in pure form condition (5.53 under 25bar). Hence it can be concluded that the selectivity results of pure component actually predict a worse separation.

Same routine is repeated for modified activated carbon, the breakthrough capacities of CO<sub>2</sub>/N<sub>2</sub> using modified activated carbon and predicted capacity for pure component capacity based on LF and DSL models are shown in Table 7.4, similar large difference between experiment and prediction happens under low CO<sub>2</sub> feed fraction condition but the difference decreases as the feed fraction rises. This can be attributed to that the AC has not reached equilibrium at breakthrough (Caldwell et al., 2015).

Table 7.4 The breakthrough capacities of CO<sub>2</sub>/N<sub>2</sub> mixtures separated using modified activated carbon for each experimental run and the predicted capacity for pure components based on the LF and DSL models.

CO <sub>2</sub> feed fraction	Breakthrough capacity	LF Model	DSL Model
(-)	(mol/kg)	(mol/kg)	(mol/kg)
0.1	2.61 ± 0.13	4.61	4.53
0.2	4.67 ± 0.04	6.05	6.07
0.3	5.88 ± 0.14	6.83	6.88
0.4	6.84 ± 0.16	7.32	7.39
0.5	7.48 ± 0.09	7.68	7.74

Similar comparison are for the predicted capacities based on multicomponent LF and DSL models and the corresponding IAST models are shown in Table 7.5., with the corresponding selectivity in Table 7.6. As seen for unmodified AC, same trend applies to modified AC. The multicomponent LF and IAST DSL predicts lower CO<sub>2</sub> capacities than IAST LF and DSL, respectively. As shown in Table 7.6, the selectivities of modified AC is even higher than unmodified AC. Compared with the selectivity of CO<sub>2</sub> over N<sub>2</sub> based on pure isotherms shown in Figure 7.4 (4.904 under 2.5bar), it is obvious that the multicomponent models predict much higher selectivity.

Table 7.5 Breakthrough Predicted multicomponent adsorption capacities based on the multicomponent LF and DSL models and the corresponding IAST models for CO<sub>2</sub>/N<sub>2</sub> mixtures separated using modified activated carbon (Caldwell, 2015)

CO <sub>2</sub> feed fraction (-)	CO <sub>2</sub> breakthrough capacity (mol/kg)	IASF-LF Model (mol/kg)		LF Model (mol/kg)		IAST-DSL Model (mol/kg)		DSL Model (mol/kg)	
		CO <sub>2</sub>	N <sub>2</sub>	CO <sub>2</sub>	N <sub>2</sub>	CO <sub>2</sub>	N <sub>2</sub>	CO <sub>2</sub>	N <sub>2</sub>
0.1	2.61 ± 0.13	2.74	1.24	2.58	2.27	2.74	1.21	4.48	0.50
0.2	4.67 ± 0.04	4.46	0.77	3.98	1.76	4.38	0.80	6.02	0.27
0.3	5.88 ± 0.14	5.62	0.49	4.98	1.39	5.45	0.57	6.85	0.17
0.4	6.84 ± 0.16	6.43	0.32	5.77	1.09	6.19	0.41	7.37	0.12
0.5	7.48 ± 0.09	7.01	0.21	6.40	0.85	6.73	0.30	7.72	0.08

Table 7.6 Predicted selectivities of CO<sub>2</sub>/N<sub>2</sub> mixture using unmodified AC based on multicomponent LF and DSL models and the corresponding IAST models (Caldwell, 2015)

CO <sub>2</sub> Feed Fraction (-)	IAST-LF (molCO <sub>2</sub> /molN <sub>2</sub> )	LF (molCO <sub>2</sub> /molN <sub>2</sub> )	IAST-DSL (molCO <sub>2</sub> /molN <sub>2</sub> )	DSL (molCO <sub>2</sub> /molN <sub>2</sub> )
0.1	19.9	10.2	20.4	80.6
0.2	23.2	9.0	21.9	89.2
0.3	26.8	8.4	22.3	94.0
0.4	30.1	7.9	22.6	92.1
0.5	33.4	7.5	22.4	96.5

## 7.2 PSA Model Development and Analysis

The breakthrough models introduced in section 7.1 are further studied and validated with experiment data by UoB and it was found that the multicomponent DSL model gave best fit, hence it was selected to be used in the PSA process simulation using unmodified AC. Detailed information can be found in reference (Caldwell, 2015).

Unlike the traditional studies (Casas et al., 2013, Agarwal et al., 2010, Xiao et al., 2009) which mainly focus on the capture of CO<sub>2</sub> (heavy product) with high purity, the PSA system studied in this work requires the maximum capture rate and purity of both CO<sub>2</sub> (heavy product) and N<sub>2</sub> (light product). The main effect of efficiency loss caused by using PSA system in IGCC will be the loss of light product, hence it is important to minimise the light product loss during the PSA system development. The work of UoB starts from the simplest 4 step Skarstrom cycle to a 10 step cycle which implements pressure equalisation, purge gas recovery and heavy product rinse with detailed information present in reference (Caldwell, 2015).

The working condition for PSA model is under 2.5 MPa and 298K, the feeding steam is mixture of CO<sub>2</sub> (mole fraction 0.4) and N<sub>2</sub> (mole fraction 0.6) with flowrate of  $7.2 \times 10^{-5}$

mol/s. A four step cyclic experiment shown in Figure 7.5 is studied first. This cyclic experiment includes four steps: pressurisation (Press), adsorption (Ad), blowdown (BD) and purge (Pur). The cycle is validated against the experiment data by UoB.

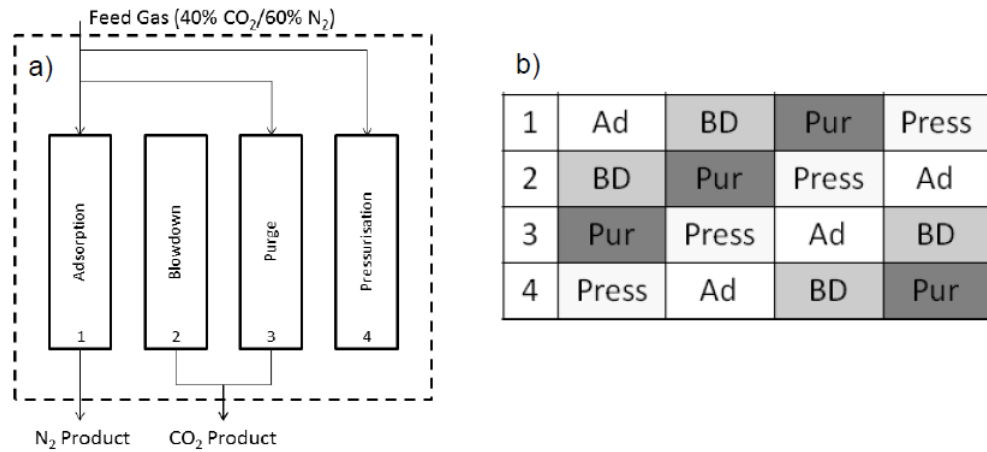


Figure 7.5 The Schematics of four step cycle of PSA process (Caldwell, 2015)

In the industrial process, the feed gas is the sweet syngas at elevated high pressure (5.98 MPa for Texaco based IGCC and 2.69MPa for Shell based IGCC which are introduced in Chapter 5), hence the feed gas can be used to pressurise the bed without additional equipment for pressurisation. For the PSA model, it is therefore reasonable to assume that the pressurisation stream is the same as adsorption feed gas. Moreover, a fraction of the feed gas is also used to for the purge step, the same methodology has been used in Casas and Schell's studies (Casas et al., 2013, Schell et al., 2013). The feed fractions of the feed gas for adsorption purge and pressurisation steps are 0.45, 0.1 and 0.45 respectively. Both co-current and counter-current operation conditions are studied for 4-step PSA process. The cyclic outputs results are shown in Table 7.7.

Table 7.7 Capture rate and purities for CO<sub>2</sub> and N<sub>2</sub> using 4-step Skarstrom PSA process(Caldwell, 2015)

	Co-Current	Counter-current
CO <sub>2</sub> capture rate	84.6%	84.3%
CO <sub>2</sub> purity	59.5%	58.9%
N <sub>2</sub> capture rate	56.5%	56.4%
N <sub>2</sub> purity	88.7%	88.8%

The capture rate of CO<sub>2</sub> is calculated by using the amount of CO<sub>2</sub> captured during blowdown and purge step divided by the total amount of CO<sub>2</sub> input. The capture rate of N<sub>2</sub> is calculated by using the amount of N<sub>2</sub> of adsorption step outlet divided by the total amount of N<sub>2</sub> input. The purities of CO<sub>2</sub> and N<sub>2</sub> are calculated by using the amount of each component divided by the total gas collected in outlets.

In the IGCC system, the PSA is used to separate CO<sub>2</sub>/H<sub>2</sub> mixture, the purity of H<sub>2</sub> is not essential since the advanced gas turbine can operate hydrogen steam with feed fraction more than 90% (Miller, 2011), but the recovery rate of H<sub>2</sub> is essential for the efficiency loss since it dictates the input fuel gas stream input for the gas turbine, in the work presented here, the recovery rate of H<sub>2</sub> is represented by N<sub>2</sub>, the 56.4% of recovery rate is unacceptable for IGCC system. Moreover, in terms of CO<sub>2</sub> captured for sequestration, a typical purity of 95% is applicable (Xiao et al., 2009). With only 84.3% purity of CO<sub>2</sub> product captured by 4-step Skarstrom process, neither light product recovery rate nor purity of heavy product is applicable for IGCC system.

In order to enhance the recovery rate for light product and purity of heavy product, several PSA processes are studied and simulated by UoB, a PSA process with 9 steps and 8 beds co-current cycle using two pressure equalisation step and one recycled purge stream is found to

produce better quality of both heavy and light products without implementing any additional equipment.

The pressure equalisation step can conserve the mechanical energy in pressurisation step and enhance the recovery rate for both products (Yang and Doong, 1985, Yang, 1987), which leads to higher CO<sub>2</sub> purity and N<sub>2</sub> recover rate. The pressure equalisation is achieved by connecting one pressurising beds and a depressurising bed together and allow these beds to reach equilibrium, this process can increase the gas purity by recycling and recapturing the low purity gas (Caldwell, 2015). Multiple pressure equalisation steps can recover more of the low purity gas. As depicted in Figure 7.6, an extra bed is added for the 9 step cycle to achieve additional equalisation step. The idle step is needed for this cycle. This can be implemented by connecting depressurising bed to a bed held in middle pressure and let these two bed equalise. Then the pressurising bed returns to an idle state and will be further pressurised to final bed pressure in the next step. After that, the depressurising bed will be connected with a idle bed, these two bed will equalise in the second equalisation step (Caldwell, 2015).

The introduction of purge gas recycle step is aiming to further improve the CO<sub>2</sub> purity and N<sub>2</sub> capture rate as the purge bed exit stream can be recaptured. The feed stream fractions for adsorption, purge pressurisation are 0.71,0.04 and 0.25 respectively, the CO<sub>2</sub> breakthrough point is set as 0.22 (Caldwell, 2015).

As depicted in Figure 7.6, low purity purge gas is recycled to another purge column to decrease the overall purge stream flowrate by doubling the purge time using two beds. Moreover, the purge gas with high CO<sub>2</sub> purity is captured. These two effects can both rise CO<sub>2</sub> purity and achieve better products qualities.



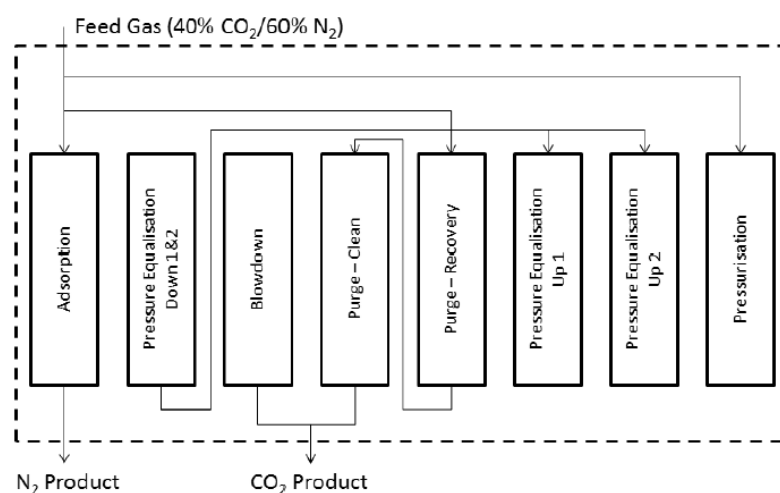


Figure 7.6 Process configuration for 8 beds 9 steps PSA process with two pressure equalisation and one recycled purge stream (Caldwell, 2015).

The cycle output results are shown in Table 7.8. The implementation of two pressure equalisation steps and purge gas recycle step leads to a considerable improvement of CO<sub>2</sub> purity and N<sub>2</sub> capture rate comparing with 4 step PSA process. The CO<sub>2</sub> capture rate rises to 80.89% with purity as high as 82.78%. Meanwhile, the capture rate for N<sub>2</sub> has been improved to 89.13% with 87.33% purity. The results for 9 steps 8 beds cycle is then used in the black box model which is connected with IGCC model for penalty analysis. The capture rate and purity of N<sub>2</sub> are used for H<sub>2</sub> in the analysis.

Table 7.8 CO<sub>2</sub> and N<sub>2</sub> capture rate and purity for 9 steps 8 beds cycle

CO <sub>2</sub> capture rate	80.89%
CO <sub>2</sub> purity	82.78%
N <sub>2</sub> capture rate	89.13%
N <sub>2</sub> purity	87.33%

### 7.3 Penalty Analysis of IGCC with PSA Carbon Capture Process

The sweet syngas of IGCC is used as the input stream for PSA model. As introduced in the beginning of this chapter, the detailed dynamic characteristics for 9 steps PSA model is not modelled, hence the black box model is used to calculate the output syngas properties. The capture ready syngas is then used as fuel gas for the following gas turbine and HRSG modules for power generation.

In order to analyse the penalty caused by carbon capture process, different mole fractions (10%, 50% and 100%) of the syngas stream are separated and pass the black box model, the output capture ready syngas will then mix with the main stream and enter the following gas turbine for combustion, the flue gas then pass the two stage HRSG for further electricity generation. Since the carbon capture process causes light product loss due to the recovery rate is 89.13%, which means only 89.13% of  $H_2$  can be recovered during the PSA process.

The simulation is conducted with the following assumptions that:

- When passing the PSA unit, only the adsorption of  $CO_2$  and  $H_2$  happen, the other contents in syngas will remain as part of the light product ( $H_2$ );
- The PSA bed is capable of capture the  $CO_2$  when 100% of syngas is delivered through the unit;
- Wet air flow rate for gas turbine doesn't change;
- The energy penalty caused by further compression of capture ready syngas is not considered in the simulation.

In order to do the penalty analysis, the combined cycle model introduced and validated in chapter 6 is used and the working condition in the study here is based on full load, which

means the 100% of syngas generated by GEM plant is used in the combined cycle plant for power generation. The HP and LP water feed for HRSG is enlarged as well for the full load working condition while the HP and LP steam generated by GEM will not change.

The amount of the fuel gas amount will reduce in the capture ready working conditions, the parameters of syngas, flue gas, gas turbine net power generation and HRSG net power generation results of Texaco-based IGCC power plant using British coal detailed in chapters 5 and 6 are shown in Table 7.9. The power consumption by GEM plant includes ASU and auxiliary modules is set as 21 MW based on the internal research report (M.Karmarkar, 2005). For each case, the captured CO<sub>2</sub> stream is compressed and heated to 150 bar, 310K (Descamps et al., 2008) and stored as supercritical stream.

Table 7.9 Parameters of Texaco-based IGCC power plant under different carbon capture rates

	Non-capture	Syngas split fraction 10%	Syngas split fraction 50%	Syngas split fraction 100%
CO <sub>2</sub> capture rate (%)	0	8.89	40.45	80.89
GT Net power (MW)	271.02	265.50	250.5	229.8
HRSG power (MW)	128.41	120.0	89.60	88.29
Syngas flowrate (mol/s)	5492.10	5279.58	4484.64	3940.87

Syngas after AGR compositions (mol %)	H <sub>2</sub> :52 CO <sub>2</sub> :37.26 N <sub>2</sub> : 7.6 CO :2.5 Ar :0.6 H <sub>2</sub> O:0.04	H <sub>2</sub> :53.2 CO <sub>2</sub> :35.58 N <sub>2</sub> : 7.9 CO :2.6 Ar :0.68 H <sub>2</sub> O:0.04	H <sub>2</sub> :60.47 CO <sub>2</sub> :27.02 N <sub>2</sub> : 8.94 CO :2.7 Ar :0.70 H <sub>2</sub> O:0.05	H <sub>2</sub> :72.92 CO <sub>2</sub> :10.59 N <sub>2</sub> : 11.93 CO :3.54 Ar :0.9 H <sub>2</sub> O:0.06
Flue gas flowrate (mol/s)	29144.5	28955.6	28216.4	27304.6
Flue gas temperature (°C)	563.4	559.798	556.07	547.358
Flue gas contents concentration (mol %)	H <sub>2</sub> : 0 CO <sub>2</sub> : 7.49 N <sub>2</sub> : 68.33 CO : 0 Ar : 0.82 H <sub>2</sub> O:10.55 O <sub>2</sub> : 12.81	H <sub>2</sub> : 0 CO <sub>2</sub> : 6.90 N <sub>2</sub> : 68.82 CO : 0 Ar : 0.82 H <sub>2</sub> O:10.46 O <sub>2</sub> : 13	H <sub>2</sub> : 0 CO <sub>2</sub> : 4.73 N <sub>2</sub> : 70.60 CO : 0 Ar : 0.82 H <sub>2</sub> O:10.33 O <sub>2</sub> :13.52	H <sub>2</sub> : 0 CO <sub>2</sub> : 1.8 N <sub>2</sub> : 73 CO : 0 Ar : 0.85 H <sub>2</sub> O:10.07 O <sub>2</sub> :14.27
GEM plant consumption (MW)	21	21	21	21
CO <sub>2</sub> compressor power (MW)	0	5.80	27.5	36.5
IGCC power efficiency HHV (%)	35.26	33.43	27.17	24.30

The results shown in Table 7.9 reveal the energy penalty caused by PSA carbon capture process under different capture rates. The power efficiency for non-capture case is 35.26%, which agrees with the reference (M.Karmarkar, 2005). The efficiencies for three carbon capture cases are 33.43%, 27.17 and 24.3%, respectively. The carbon capture process reduces the syngas amount and especially the net hydrogen input, which directly reduce the power generation of gas turbine module, the syngas mole flow rate drop for three cases are 188.9, 928.1 and 1839.9 mol/s, which is the main reason for gas turbine power output reduction. In addition, the amount and temperature of flue gas generated by gas turbine both decrease. The flue gas temperature of carbon capture cases drop from 563.4°C (non-capture case) to 559.8, 556.1 and 547.4°C, respectively. Meanwhile the flue gas flowrate of carbon capture cases drop from 29144.5mol/s (non-capture case) to 28955.6, 28216.4 and 27304.6mol/s, respectively. The decreases of flue gas flowrate and temperature means the flue gas enthalpy that can be recovered by HRSG drop due to the carbon capture processes, this directly cause the HRSG power output drop of 8.41, 38.4 and 40.12 MW for three cases, which lead to a further decrease of net power output of combined cycle plant and power efficiency.

Extra power consumption is caused by compressing the captured CO<sub>2</sub> stream to supercritical state for the further transport and storage target. This compressor power consumption for three cases are 5.8, 27.5 and 36.5 MW, which lead to efficiency drop of 0.54%, 2.56% and 3.40% for three cases. It is obvious the energy penalty increase with the carbon capture rate, the fuel gas loss, flue gas enthalpy loss and CO<sub>2</sub> compressor loss have all contributed to the energy penalty increase.

## **7.4 Discussion of CO<sub>2</sub>/H<sub>2</sub> Based on Experiment Data from UoN**

The work conducted by UoB is based on CO<sub>2</sub>/N<sub>2</sub> mixture, N<sub>2</sub> is used to represent H<sub>2</sub> for PSA simulation. New experiment data for pure isotherm of H<sub>2</sub> adsorption using unmodified and modified ACs are provided by the University of Nottingham, the selectivity of CO<sub>2</sub> over H<sub>2</sub> are much higher than the selectivity of CO<sub>2</sub> over N<sub>2</sub> in the working condition for PSA (Sun et al., 2013). For the unmodified AC, the selectivity of CO<sub>2</sub> over H<sub>2</sub> under 20 bar is 15.9 while the selectivity of CO<sub>2</sub> over N<sub>2</sub> is only 3.01. For the modified AC, the selectivity values under 20 bar is 17.3 (CO<sub>2</sub> over H<sub>2</sub>) versus 2.9 (CO<sub>2</sub> over N<sub>2</sub>). Similar with N<sub>2</sub>, the isotherms for H<sub>2</sub> is close to linear as well. As discussed in section 7.1.2.1, the adsorption selectivity for multicomponent process will be even higher than pure component process, hence it can be concluded the capture rate for H<sub>2</sub> by using same PSA process will be higher than N<sub>2</sub> results. The simulation results of CO<sub>2</sub>/N<sub>2</sub> actually provide a worse prediction than CO<sub>2</sub>/H<sub>2</sub> conditions. Hence the efficiency losses for the real syngas working conditions would be lower than the results based on CO<sub>2</sub>/N<sub>2</sub> mixture.

## **7.5 Summary**

Chapter 7 introduces the experiment work of ACs-based carbon capture conducted by UoB and the subsequent modelling of CO<sub>2</sub>/N<sub>2</sub> PSA separation unit modelled based on theoretical equations derivation and experiment validation. A 9 steps 8 beds PSA model based on unmodified AC is finally adopted for the energy penalty analysis of IGCC power plant, it was found the efficiency loss caused by PSA carbon capture process increase with the rise of carbon capture rate, which is mainly caused by the hydrogen loss by PSA and the subsequent decrease of syngas amount, flue gas enthalpy and CO<sub>2</sub> compression. The results presented are based on CO<sub>2</sub>/N<sub>2</sub> separation, which means N<sub>2</sub> represented H<sub>2</sub> in the modelling in the work. The pure isotherm data for H<sub>2</sub> presented by UoN reveal that the selectivity of CO<sub>2</sub> over H<sub>2</sub> is

much higher than  $N_2$ , which means the actual working condition of separation for  $CO_2/H_2$  will lead to higher recovery rate of  $H_2$ , hence it is reasonable to speculate the actual efficiency loss of IGCC power plant will be lower than the results (1.83%,8.98%,10.96%) presented in this chapter.

## **Chapter 8 Conclusion, Limitations and Future work**

This chapter concludes the research work conducted in this thesis. It summaries the IGCC process simulation and the impact by integration of IGCC and PSA carbon capture process. The limitation of this work is discussed and then the future work based on conclusions and limitations is proposed.

### **8.1 Conclusions**

The study presented in the thesis is aiming to conduct the modelling and simulation study of whole process IGCC power plant and analyse the impact of PSA carbon capture unit to the power plant. The detailed gasifier of Texaco and Shell gasifier models are developed and evaluated, the auxiliary modules in GEM plant built with Thermolib are introduced and analysed. Power generation integrated with GEM based on Texaco gasifier is built, the dynamic performance of gas turbine and HRSG modules are analysed, respectively. A whole process of CHP power plant is presented in Appendix as it is highly relevant to my Ph.D. study. A 9 steps 8 beds PSA model developed by UoB is introduced and integrated with Texaco-based IGCC power plant. Finally the changes of syngas, flue gas and combined cycle power outputs caused by different carbon capture rates are detailed and analysed. The conclusions made from this works are listed as below:

- The zero dimension gasifier model developed based on mass balance, energy balance and chemical equilibrium can reflect the working principles of Texaco and Shell gasifier. The predicted results of syngas contents concentration for different coal feeds are proved to be reliable for the IGCC power plant model. The simulation results reveal that low  $H_2O$ /coal ratio can improve the syngas quality under the studied working condition, the oxygen/coal ratio needs to be well tuned during the gasifier



operation. Oxygen and water input can impact the gasifier operation directly, hence it is important to control this two parameter during gasifier operation.

- The one-dimension Shell slagging gasifier model shows the dynamic performance of gasifier operation. The liquid and solid slag layers thickness will change when the working condition change as this will cause the exiting slag mass flow to change. It is found that oxygen input change cause more rigorous impact to the gasifier operation than the steam blast input. The syngas temperature rise following 1% and 5% of oxygen increase are 20 K and 120 K, respectively. For the 5% oxygen increase condition, the solid slag layers thickness drops about 50% (4mm). The change of 5% oxygen blast leads to a decrease of 1% in cold gas efficiency which is caused by the reduction of  $H_2$  content in the syngas. The 20% steam blast increase leads to a 5K drop of syngas temperature. The solid slag layer increase by 0.3 mm. The steam blast change results the 0.1% rise of  $H_2$  concentration and 0.8% drop of CO concentration but the cold gas efficiency change is negligible.
- The auxiliary modules developed with Thermolib can reflect the working principles and simulate the operation of GEM plant. The Shell gasifier syngas temperature drops to 523K after passing the gas quench and cooling system. The water quench process applied to Texaco gasifier will cool the syngas from 1573 K to 511 K. In addition, the steam concentration after water quench rises from 18.69% to 59.96%, which is enough for the shift reactor use.
- Two stages of WGS integrated with heat exchanger are built for the GEM plant for both of Texaco and Shell gasifier, the module can raise the  $H_2$  and  $CO_2$  concentration in shifted syngas. A dynamic syngas input is used to study the performance of shift reactor model. For Shell gasifier, the  $H_2$  and  $CO_2$  mole concentrations in dry shifted syngas stream are 57.1% and 39.1%, respectively. For Texaco gasifier, the numbers

are 54.7% and 40.6%. The heat released by water gas shift reaction can also be used to raise HP and LP steam for the HRSG, which leads to more power generation. The simplified COS hydrolysis reactor and H<sub>2</sub>S removal unit can remove the minimum sulphides contents in the syngas, the syngas can be further cooled as well.

- The gas turbine and HRSG developed with Thermolib can be used to study the performance of power generation and conduct further efficiency analysis for Texaco-based IGCC power plant. Based on the reference working condition with 17.34% of syngas input, the net power generation by gas turbine is 46.96MW and the thermal efficiency is 31.67%. The dual stage HRSG integrated with GEM shows better performance than single stage HRSG. The dual stage HRSG can generate 50.30 of net power (about 26.5% of power generation from HP cycle), which makes a 97.26 MW net power generation of combined cycle with 65.6% thermal efficiency.
- The PSA model developed by University of Birmingham is connected with the whole IGCC model for the energy penalty analysis for different carbon capture rate. It is found the efficiency losses under 8.89%, 40.45% and 80.89% carbon capture and compression will be 1.83%, 8.09% and 10.96%, respectively. This is caused by the decrease of H<sub>2</sub> content in syngas and the subsequent enthalpy drop in flue gas for HRSG. The compression caused by CO<sub>2</sub> compression will cause extra power consumption and efficiency loss. Although the integration with GEM can generate extra electricity, the power output drop of combined cycle is unavoidable.
- The latest data from UoN reveals the ACs selectivity of CO<sub>2</sub> over H<sub>2</sub> is much higher than N<sub>2</sub>, which means the PSA process for CO<sub>2</sub>/H<sub>2</sub> mixture can lead to higher recovery rate for H<sub>2</sub> than the current recovery rate for N<sub>2</sub>. Hence the real efficiency loss will be lower than the results shown by this work.

## 8.2 Limitations

- Thermolib can't simulate solid phase properties hence the sulphides removal unit is not modelled in details as the product of this unit will be solid phase sulphur. The sulphides content in syngas stream is small hence the simplification will not cause big error for the simulation. The power consumption of the auxiliary modules for GEM plant are not modelled, the value is set based on internal research report.
- The development of models for gas turbine and HRSG unit are based on the internal research report which provides the design data for a Texaco-based IGCC power plant. Hence the power plant is not applicable for Shell gasifier. The main aim of this work is to investigate the operation of whole process IGCC power plant and the impact for its integration with PSA unit. The Texaco-based IGCC power plant model can be used to present the desired results.
- The PSA model developed by University of Birmingham is based on CO<sub>2</sub>/N<sub>2</sub> mixture. Due to the limitation of experiments, the real situation for CO<sub>2</sub>/H<sub>2</sub> separation is not studied hence the H<sub>2</sub> is represented by N<sub>2</sub> in this work. In addition, the PSA model is developed and validated under the simplified working condition (40% CO<sub>2</sub> and 60% N<sub>2</sub> without any other content). Hence assumption has to be made that the other contents in the syngas will not be adsorbed by AC bed and will all exist in the light product stream.
- The PSA model is developed based on experiment work, which is not the same as industrial working condition, especially the syngas stream flowrate. This will need further investigation in the future work.

### 8.3 Future work

- Experiments for ACs-based PSA process for CO<sub>2</sub>/H<sub>2</sub> need to be conducted by following the similar procedure for the CO<sub>2</sub>/N<sub>2</sub> mixture. This work can give detailed information for the capture rate and purity of both CO<sub>2</sub> and H<sub>2</sub> streams. PSA model for CO<sub>2</sub>/H<sub>2</sub> separation can be developed subsequently and provide clear picture for the real working condition in the IGCC power plant. The work can provide more reliable results for the energy penalty analysis.
- As the PSA model is developed based on the experiment condition which is limited by the test rig and environments, larger scale simulation is necessary to give more reliable information of PSA unit integrated with IGCC power plant model. In addition, with the industrial scale PSA model, it is possible to conduct the dynamic performance study for carbon ready IGCC power plant and prepare for the further control strategy study.
- Economic analysis can be made based on the IGCC power plant model with PSA model to investigate the economic cost for the PSA construction and operation. With this information, ACs based PSA can be used to compare with other pre-combustion capture strategies. Suggestions can also be made for difference IGCC power plants for the selection of suitable carbon capture unit.
- Control strategy can be studied in the future to study the IGCC power plant operation and its integration with grid. For example, the introduction of PSA to IGCC power plant will cause reduction in syngas and power generation, controller can be applied with the gas turbine and HRSG unit to tune the gas stream and avoid potential impact for the power plant operation. Meanwhile, controller can also be used to increase feedstock or oxidant input amount in terms of power generation drop.

Combined Heat and Power (CHP) has become one of the most widely used technologies to provide electricity and heat since late twentieth century. Compared with conventional power plants, CHP can recover the waste heat from engine exhaust and the cooling system to deliver electricity and heat simultaneously, which leads to higher system efficiency to achieve fuel saving and emission reduction (Knowles, 2011). In the United States, adoption of CHP technology has resulted in the reduction of fuel consumption by 1.9 quads and 248 million metric tons of carbon dioxide (CO<sub>2</sub>) emissions annually; this is equivalent to removing 45 million cars from road (Anna Shipley 2008). The merits of CHPs are also well recognized and supported in the EU (Bazmi and Zahedi, 2011). In 2005, 9% of electricity generation in the UK is produced by CHP (Odenberger and Johnsson, 2007). To achieve 60% CO<sub>2</sub> reduction within the UK energy system, CHP is now enjoying a number of fiscal incentive programs aiming to promote this economic low carbon energy technology (Toke and Fragaki, 2008, Allen et al., 2008).

One effective way to understand these systems and improve their performance is by using modelling and simulation where the system is described using a set of functions as a relationship between inputs and outputs of the system. In this work, a complete dynamic model is built with Thermolib and Simulink and validated based on a micro-CHP system performance at the University of Warwick (UOW). Seasonal working conditions are analysed while simplified controllers are introduced to ensure stable operation and zero steady-state error. Based on the simulation results, some suggestions are made to optimize the overall plant performance with respect to electrical and thermal demand curves.

## References

- AGARWAL, A., BIEGLER, L. T. & ZITNEY, S. E. 2010. Superstructure-Based Optimal Synthesis of Pressure Swing Adsorption Cycles for Precombustion CO<sub>2</sub> Capture. *Industrial & Engineering Chemistry Research*, 49, 5066-5079.
- ALLEN, S. R., HAMMOND, G. P. & MCMANUS, M. C. 2008. Prospects for and barriers to domestic micro-generation: A United Kingdom perspective. *Applied Energy*, 85, 528-544.
- ANNA SHIPLEY, A. H., BRUCE HEDMAN, PATTI GARLAND, PAUL BAUTISTA 2008. Combined heat and power effective energy solutions for a sustainable future. Oak ridge national laboratory.
- ASFAW, K., OERTEL, H., ERHARD, P., ETLING, D., MULLER, U., RIEDEL, U., SREENIVASAN, K. R. & WARNATZ, J. 2010. *Prandtl-Essentials of Fluid Mechanics*, Springer New York.
- ÅSTRÖM, K. J. & HÄGGLUND, T. 2004. Revisiting the Ziegler–Nichols step response method for PID control. *Journal of Process Control*, 14, 635-650.
- AZUHATA, S., HEDMAN, P. O. & SMOOT, L. D. 1986. Carbon conversion in an atmospheric-pressure entrained coal gasifier. *Fuel*, 65, 212-217.
- BAZMI, A. A. & ZAHEDI, G. 2011. Sustainable energy systems: Role of optimization modeling techniques in power generation and supply—A review. *Renewable and Sustainable Energy Reviews*, 15, 3480-3500.
- BELL, D. A., TOWLER, B. F. & FAN, M. 2010. *Coal Gasification and Its Applications*, Elsevier Science.
- BIRD, R. B., STEWART, W. E. & LIGHTFOOT, E. N. 2001. *Transport Phenomena*, Wiley.
- BREAULT, R. W. 2010. Gasification Processes Old and New: A Basic Review of the Major Technologies. *Energies*, 3, 216.
- BRESCIA, F., ARENTS, J., MEISLICH, H., TURK, A. & WEINER, E. 1975. EXPERIMENT 20 - Thermochemical Equations; Hess's Law. In: BRESCIA, F., ARENTS, J., MEISLICH, H. & WEINER, A. T. (eds.) *Fundamentals of Chemistry: Laboratory Studies (Third Edition)*. Academic Press.
- BROWN, B. W., SMOOT, L. D. & HEDMAN, P. O. 1986. Effect of coal type on entrained gasification. *Fuel*, 65, 673-678.
- BUSKIES, U. 1996. The efficiency of coal-fired combined-cycle powerplants. *Applied Thermal Engineering*, 16, 959-974.
- C. ZHAO, J. C. 2010. Thermal energy storage in Warwick campus main report. University of Warwick.
- CALDWELL, S. J. 2015. *Experimental and computational evaluation of activated carbons for carbon dioxide capture from high pressure gas mixtures*. Ph.D., University of Birmingham.
- CALDWELL, S. J., AL-DURI, B., SUN, N., SUN, C.-G., SNAPE, C. E., LI, K. & WOOD, J. 2015. Carbon Dioxide Separation from Nitrogen/Hydrogen Mixtures over Activated Carbon Beads: Adsorption Isotherms and Breakthrough Studies. *Energy & Fuels*, 29, 3796-3807.
- CASAS, N., SCHELL, J., JOSS, L. & MAZZOTTI, M. 2013. A parametric study of a PSA process for pre-combustion CO<sub>2</sub> capture. *Separation and Purification Technology*, 104, 183-192.
- CASELLA, F. & COLONNA, P. 2012. Dynamic modeling of IGCC power plants. *Applied Thermal Engineering*, 35, 91-111.
- ÇENGEL, Y. A. & BOLES, M. A. 2006. *Thermodynamics: an engineering approach*, McGraw-Hill Higher Education.

- DAN, C. & SEBORG, D. E. Design of decentralized PI control systems based on Nyquist stability analysis. *Control Applications*, 2001. (CCA '01). Proceedings of the 2001 IEEE International Conference on, 2001 2001. 1048-1053.
- DESCAMPS, C., BOUALLOU, C. & KANNICHE, M. 2008. Efficiency of an Integrated Gasification Combined Cycle (IGCC) power plant including CO<sub>2</sub> removal. *Energy*, 33, 874-881.
- DRAGE, T. C., KOZYNCHENKO, O., PEVIDA, C., PLAZA, M. G., RUBIERA, F., PIS, J. J., SNAPE, C. E. & TENNISON, S. 2009. Developing activated carbon adsorbents for pre-combustion CO<sub>2</sub> capture. *Energy Procedia*, 1, 599-605.
- DUAN, Q. 2010. *Thermodynamic analysis for combined cycle power plants*, Beijing, China, Tsinghua University Press.
- EUTECH 2013. User manuscript for Thermolib toolbox, release 5.2.2. Aachen, Germany.
- GARCÍA, S., PIS, J. J., RUBIERA, F. & PEVIDA, C. 2013. Predicting Mixed-Gas Adsorption Equilibria on Activated Carbon for Precombustion CO<sub>2</sub> Capture. *Langmuir*, 29, 6042-6052.
- GASIFICATION, I. 2005. An Overview of Coal based Integrated Gasification Combined Cycle (IGCC) Technology.
- GLASSMAN, I., YETTER, R. A. & GLUMAC, N. G. 2015. Chapter 1 - Chemical thermodynamics and flame temperatures. *In: GLUMAC, I. G. A. Y. G. (ed.) Combustion (Fifth Edition)*. Boston: Academic Press.
- GOVIND, R. & SHAH, J. 1984. Modeling and simulation of an entrained flow coal gasifier. *AIChE Journal*, 30, 79-92.
- HAO XIE, Z. Z., ZHENZHONG LI, YANG WANG 2013. Relations among Main Operating Parameters of Gasifier in IGCC. *Energy and Power Engineering*, 5, 552-556.
- HIGMAN, C. & VAN DER BURGT, M. 2003. Chapter 5 - Gasification Processes. *In: HIGMAN, C. & BURGT, M. V. D. (eds.) Gasification*. Burlington: Gulf Professional Publishing.
- HIGMAN, C. & VAN DER BURGT, M. 2008a. Chapter 1 - Introduction. *In: HIGMAN, C. & BURGT, M. V. D. (eds.) Gasification (Second Edition)*. Burlington: Gulf Professional Publishing.
- HIGMAN, C. & VAN DER BURGT, M. 2008b. Chapter 2 - The Thermodynamics of Gasification. *In: HIGMAN, C. & BURGT, M. V. D. (eds.) Gasification (Second Edition)*. Burlington: Gulf Professional Publishing.
- HIGMAN, C. & VAN DER BURGT, M. 2008c. Chapter 3 - The Kinetics of Gasification and Reactor Theory. *In: HIGMAN, C. & BURGT, M. V. D. (eds.) Gasification (Second Edition)*. Burlington: Gulf Professional Publishing.
- HIGMAN, C. & VAN DER BURGT, M. 2008d. Chapter 5 - Gasification Processes. *In: HIGMAN, C. & BURGT, M. V. D. (eds.) Gasification (Second Edition)*. Burlington: Gulf Professional Publishing.
- IEA 2011. Retrofitting CO<sub>2</sub> capture to existing power plants. IEA Greenhouse Gas R&D Programme.
- J.EURLINGS, D. B. V. 1999a. Process Performance of the SCGP at Buggenum IGCC. *Gasification Technologies Conference* San Fransisco, California.
- J.EURLINGS, J. P. 1999b. Process performance of the SCGP at Buggenum IGCC. *Gasification Technologies Conference*. San Francisco, CA.
- JOHNSON, E. K. 1984. A Non-Newtonian Flow Model for Coal-Ash Slag. *Journal of Engineering for Gas Turbines and Power*, 106, 777-781.
- JONES, D., BHATTACHARYYA, D., TURTON, R. & ZITNEY, S. E. 2011. Optimal design and integration of an air separation unit (ASU) for an integrated gasification combined cycle (IGCC) power plant with CO<sub>2</sub> capture. *Fuel Processing Technology*,

- 92, 1685-1695.
- KNOWLES, J. 2011. 1 - Overview of small and micro combined heat and power (CHP) systems. In: BEITH, R. (ed.) *Small and Micro Combined Heat and Power (CHP) Systems*. Woodhead Publishing.
- KREUTZ, T., MARTELLI, E., CARBO, M., CONSONNI, S. & JANSEN, D. Shell gasifier-based coal IGCC with CO<sub>2</sub> capture: partial water quench vs. novel water-gas shift. ASME Turbo Expo 2010: Power for Land, Sea, and Air, 2010. American Society of Mechanical Engineers, 583-592.
- LANGMUIR, I. 1918. THE ADSORPTION OF GASES ON PLANE SURFACES OF GLASS, MICA AND PLATINUM. *Journal of the American Chemical Society*, 40, 1361-1403.
- LEE, H.-H., LEE, J.-C., JOO, Y.-J., OH, M. & LEE, C.-H. 2014. Dynamic modeling of Shell entrained flow gasifier in an integrated gasification combined cycle process. *Applied Energy*, 131, 425-440.
- LINDEGROUP.LTD. 2015. *CO Shift Conversion* [Online]. Available: [http://www.linde-engineering.com/en/process\\_plants/hydrogen\\_and\\_synthesis\\_gas\\_plants/gas\\_generation/co\\_shift\\_conversion/index.html](http://www.linde-engineering.com/en/process_plants/hydrogen_and_synthesis_gas_plants/gas_generation/co_shift_conversion/index.html) [Accessed 09/03 2015].
- LU, S. & HOGG, B. W. 2000. Dynamic nonlinear modelling of power plant by physical principles and neural networks. *International Journal of Electrical Power & Energy Systems*, 22, 67-78.
- M.KARMARKAR, J. G., R.DELNEY 2005. impact of CO<sub>2</sub> removal on coal gasification based fuel plants. Nottingham, UK: jacob consultancy, Univesity of Nottingham.
- MAE115. 2012. *MAE115 App Thermo* [Online]. Available: <https://www.studyblue.com/notes/n/mae115-app-thermo/deck/4403593> [Accessed 2015-05-01].
- MILLER, B. G. 2005. CHAPTER 2 - Past, Present, and Future Role of Coal. *Coal Energy Systems*. Burlington: Academic Press.
- MILLER, B. G. 2011. 8 - Coal-Fired Emissions and Legislative Action. In: MILLER, B. G. (ed.) *Clean Coal Engineering Technology*. Boston: Butterworth-Heinemann.
- MILLS, K. C. & RHINE, J. M. 1989. The measurement and estimation of the physical properties of slags formed during coal gasification: 2. Properties relevant to heat transfer. *Fuel*, 68, 904-910.
- NETL. 2013. *COMMERCIAL GASIFIERS* [Online]. Available: <http://www.netl.doe.gov/research/Coal/energy-systems/gasification/gasifipedia/fmb> [Accessed 01/02 2015].
- NEWSOME, D. S. 1980. The Water-Gas Shift Reaction. *Catalysis Reviews*, 21, 275-318.
- NI, Q. & WILLIAMS, A. 1995. A simulation study on the performance of an entrained-flow coal gasifier. *Fuel*, 74, 102-110.
- NICHOLS, K. M., HEDMAN, P. O., SMOOT, L. D. & BLACKHAM, A. U. 1989. Fate of coal-sulphur in a laboratory-scale coal gasifier. *Fuel*, 68, 243-248.
- NIST. 2011. *NIST Chemsitry WebBook Standard Reference Database Number 69* [Online]. United States: U.S. Secretary of Commerce on behalf of the United States of America. Available: <http://webbook.nist.gov/chemistry/> 2015].
- ODENBERGER, M. & JOHNSON, F. 2007. Achieving 60% CO<sub>2</sub> reductions within the UK energy system—Implications for the electricity generation sector. *Energy Policy*, 35, 2433-2452.
- PAULEY, C. R., SIMISKEY, P. L. & HAIGH, S. 1984. *Oil Gas J.*, 82, 87.
- RANKINE, W. J. M. 1853. VII.—On the Mechanical Action of Heat, especially in Gases and Vapours. *Earth and Environmental Science Transactions of the Royal Society of Edinburgh*, 20, 147-190.



- RAO, A. B. & RUBIN, E. S. 2002. A technical, economic, and environmental assessment of amine-based CO<sub>2</sub> capture technology for power plant greenhouse gas control. *Environmental Science and Technology*, 36, 4467-4475.
- ROUQUEROL, J., ROUQUEROL, F., LLEWELLYN, P., MAURIN, G. & SING, K. S. W. 2013. *Adsorption by Powders and Porous Solids: Principles, Methodology and Applications*, Elsevier Science.
- RUBIN, E. S., CHEN, C. & RAO, A. B. 2007. Cost and performance of fossil fuel power plants with CO<sub>2</sub> capture and storage. *Energy Policy*, 35, 4444-4454.
- RUPRECHT, P., SCHÄFER, W. & WALLACE, P. 1988. A computer model of entrained coal gasification. *Fuel*, 67, 739-742.
- RUTHVEN, D. M. 1984. *Principles of Adsorption and Adsorption Processes*, Wiley.
- SCHELL, J., CASAS, N., MARX, D. & MAZZOTTI, M. 2013. Precombustion CO<sub>2</sub> Capture by Pressure Swing Adsorption (PSA): Comparison of Laboratory PSA Experiments and Simulations. *Industrial & Engineering Chemistry Research*, 52, 8311-8322.
- SCHOEN, P. 1993. *Dynamic Modelling and Control of Integrated Coal Gasification Combined Cycle Units*. Ph.D., TU Delft
- SEGGIANI, M. 1998. Modelling and simulation of time varying slag flow in a Prenflo entrained-flow gasifier. *Fuel*, 77, 1611-1621.
- SERTH, R. W. & LESTINA, T. G. 2014. 3 - Heat Exchangers. In: SERTH, R. W. & LESTINA, T. G. (eds.) *Process Heat Transfer (Second Edition)*. Boston: Academic Press.
- SIMBECK, D. R., INSTITUTE, E. P. R. & SFA PACIFIC, I. 1993. *Coal Gasification Guidebook: Status, Applications, and Technologies : TR-102034, Research Project 2221-39, Final Report*, Electric Power Research Institute.
- SIVA ARIYAPADI, P. S., MANISH BHARGAVA, DAVID EBBERN 2008. KBR's transport gasifier-an advanced gasification technology for SNG production from low-rank coals. *Twenty-fifth Annual International Pittsburgh Coal Conference*. Pittsburgh, PA.
- SLYCKE, J. T., MITTEMEIJER, E. J. & SOMERS, M. A. J. 2015. 1 - Thermodynamics and kinetics of gas and gas-solid reactions. In: MITTEMEIJER, E. J. & SOMERS, M. A. J. (eds.) *Thermochemical Surface Engineering of Steels*. Oxford: Woodhead Publishing.
- SMITH, P. V., DAVIS B.M, VIMALCHAND,P,LIU,G. AND LONGARBACH,J. Operation of the PDSF transport gasifier. Gasification Technologies Conference, 2002 San Francisco.
- SMITH, R., LOGANATHAN, M. & SHANTHA, M. S. A review of the water gas shift reaction kinetics. *International Journal of Chemical Reactor Engineering*, 8.
- SMITH, R., LOGANATHAN, M. & SHANTHA, M. S. 2010. A review of the water gas shift reaction kinetics. *International Journal of Chemical Reactor Engineering*, 8.
- SUN, B., LIU, Y., CHEN, X., ZHOU, Q. & SU, M. 2011. Dynamic modeling and simulation of shell gasifier in IGCC. *Fuel Processing Technology*, 92, 1418-1425.
- SUN, N., SUN, C., LIU, H., LIU, J., STEVENS, L., DRAGE, T., SNAPE, C. E., LI, K., WEI, W. & SUN, Y. 2013. Synthesis, characterization and evaluation of activated spherical carbon materials for CO<sub>2</sub> capture. *Fuel*, 113, 854-862.
- SUPP, E. 1990. *How to produce methanol from coal*, Springer-Verlag.
- TOKE, D. & FRAGAKI, A. 2008. Do liberalised electricity markets help or hinder CHP and district heating? The case of the UK. *Energy Policy*, 36, 1448-1456.
- UBHAYAKAR, S. K., STICKLER, D. B. & GANNON, R. E. 1977. Modelling of entrained-bed pulverized coal gasifiers. *Fuel*, 56, 281-291.
- V.KRIGMONT, H. 1999. *Integrated Biomass Gasification Combined Cycle Power*

Generation Concept: The Gateway to Cleaner Future.

- VAMVUKA, D., WOODBURN, E. T. & SENIOR, P. R. 1995a. Modelling of an entrained flow coal gasifier. 1. Development of the model and general predictions. *Fuel*, 74, 1452-1460.
- VAMVUKA, D., WOODBURN, E. T. & SENIOR, P. R. 1995b. Modelling of an entrained flow coal gasifier. 2. Effect of operating conditions on reactor performance. *Fuel*, 74, 1461-1465.
- VAN PUTTEN, H. & COLONNA, P. 2007. Dynamic modeling of steam power cycles: Part II – Simulation of a small simple Rankine cycle system. *Applied Thermal Engineering*, 27, 2566-2582.
- WANG, Y., WANG, J., LUO, X., GUO, S., LV, J. & GAO, Q. 2015. Dynamic modelling and simulation of IGCC process with Texaco gasifier using different coal. *Systems Science & Control Engineering*, 3, 198-210.
- WATKINSON, A. P., LUCAS, J. P. & LIM, C. J. 1991. A prediction of performance of commercial coal gasifiers. *Fuel*, 70, 519-527.
- WEN, C. Y. & CHAUNG, T. Z. 1979. Entrainment Coal Gasification Modeling. *Industrial & Engineering Chemistry Process Design and Development*, 18, 684-695.
- XIAO, P., WILSON, S., XIAO, G., SINGH, R. & WEBLEY, P. 2009. Novel adsorption processes for carbon dioxide capture within a IGCC process. *Energy Procedia*, 1, 631-638.
- XU, Y., ZANG, G., CHEN, H., DOU, B. & TAN, C. 2012. Co-production system of hydrogen and electricity based on coal partial gasification with CO<sub>2</sub> capture. *International Journal of Hydrogen Energy*, 37, 11805-11814.
- YANG, R. T. 1987. CHAPTER 8 - Pressure-Swing Adsorption: Models and Experiments. In: YANG, R. T. (ed.) *Gas Separation by Adsorption Processes*. Butterworth-Heinemann.
- YANG, R. T. & DOONG, S. J. 1985. Gas separation by pressure swing adsorption: A pore-diffusion model for bulk separation. *AIChE Journal*, 31, 1829-1842.
- YANG, Z., WANG, Z., WU, Y., WANG, J., LU, J., LI, Z. & NI, W. 2011. Dynamic model for an oxygen-staged slagging entrained flow gasifier. *Energy and Fuels*, 25, 3646-3656.
- YUE, W., JIHONG, W., SHE, G., JUNFU, L. & QIRUI, G. Dynamic modelling and simulation study of Texaco gasifier in an IGCC process. Automation and Computing (ICAC), 2013 19th International Conference on, 13-14 Sept. 2013 2013. 1-6.
- YUE WANG, J. W., SHE GUO, JUNFU LV, QIRUI GAO 2013. Dynamic Modelling and Simulation Study of Texaco Gasifier in an IGCC Process *19th International Conference on Automation & Computing*. Brunel University, London, UK.
- ZHANG, J., ZHOU, Z., MA, L., LI, Z. & NI, W. 2013. Efficiency of wet feed IGCC (integrated gasification combined cycle) systems with coal–water slurry preheating vaporization technology. *Energy*, 51, 137-145.

## Appendix CHP Model Based on UoW Campus Plant with Applied Controllers

### A.1 Introduction of CHP Power Plant Model

During the PhD study period, a project based on the CHP power plant is conducted, as the simulation is highly relevant with power generation simulation, the information about this projected is detailed. The CHP plant at UOW consists of three CHP units, each generating 1.4 MW of electrical power and 1.8 MW of thermal power with a total electrical power generation of 4.2 MW and thermal power production of 5.4 MW (C. Zhao, 2010). The CHP units adopt the reciprocating gas engine system 1370 GQMA provided by Cummins, which is formed with the reciprocating methane gas engine, alternator, generator and control system. The rated voltage is 400V from the CHP and then it is transformed to 11 kV for distribution through the campus ring circuit. The specific information of this CHP power plant is listed in Table.A.1.

Table A.1 Cummins 1370 GQMA CHP unit specification

Fuel	Methane
Excitation	Electric
Cooling	Fluid (water)
Generator	Coolant heater, water circulating pump and thermostat
Nominal Output Power	1370 kW
Power factor	0.8
Frequency	50 Hz
Output Voltage	220/380
Gas Engine	Cummins QSK81G spark ignited lean burn gas combustion engine
Layout	16-cylinder, V form, four cycle, turbo charged
Rotational speed	1500 rpm
Construction	Four valves per cylinder forged steel crankshaft and connecting rods, cast iron block, replaceable wet liners.

The working principle of the CHP unit is shown in Figure A.1. The combustion of methane in the reciprocating gas engine produces the primary driving power to produce mechanical power. The generated mechanical power is then converted to electrical power by alternator and electricity generator. The three-phase synchronous electricity generator converts the mechanical torque to electrical power. The exhaust gas after expansion in the turbine will then pass through economizer and heat exchanger to heat up the flowing water and raise its temperature from 55 °C to around 85 °C. Meanwhile, the exhaust gas temperature consequently drops from 515 °C to 110 °C (C. Zhao, 2010). Totally the system is able to provide 5400 kW of thermal power. The overall power plant efficiency can be raised with the combined heat generation.

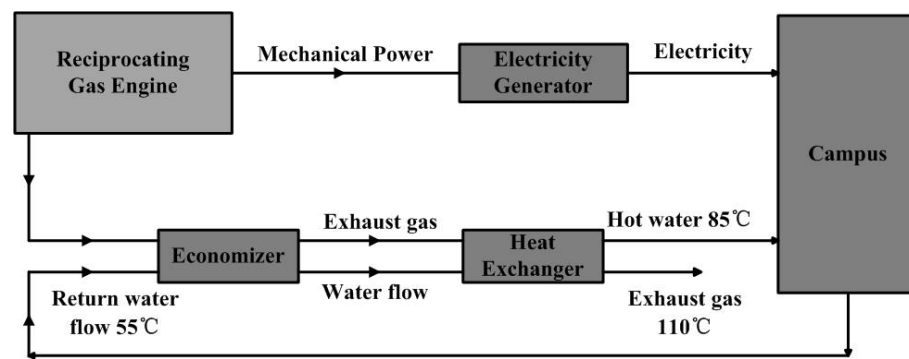


Figure A.1 Layout of micro-CHP of UoW (Serth and Lestina, 2014)

The University CHP plant is operating in the heat following strategy. The engines run in their full capacity only when all the generated heat can be utilized. The usage of both electrical and thermal power on campus fluctuates with hours and seasons. To maintain the generation matching the demand, two auxiliary boilers and two thermal storage tanks are installed for buffering the demand fluctuations and provide extra heat when it is needed.

The auxiliary boiler is a traditional shell and tube water boiler and its structure is shown in Figure A.2. The products of fuel combustion are sent through the shell fitted inside the water tank to reach the reverse chamber. Here, they are diverted to second pass tubes fixed around

the cylinder. Thus, through metallic walls of the shell and tubes the heat is efficiently conducted to the surrounding water. The boilers are capable of generating a maximum of 4850 kW thermal power each (C. Zhao, 2010). The activation of the boiler can successfully support the peak heat power demand especially during the winter period.

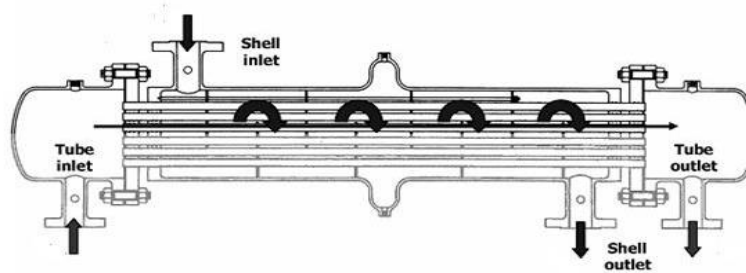


Figure A.2 Shell-tube boiler of UoW (Serth and Lestina, 2014)

Concerning the thermal storage, there are two 10.5 m tall water reservoirs fitted near the Boiler House to store 200 tons of hot water in case of low thermal demand. When demand rises, hot water from the storage is used for circulation on campus. Overall the tanks are able to store a total of 9 MWh thermal energy, which is enough to provide heat to the whole campus for about 5 hours. The installation of the thermal storage system allows extra savings in fuel consumption bills, since firing the boiler became unnecessary during the short periods of high heat demand. In total, the three CHP units along with two boilers who can provide 4.2 MW of electrical power and 15.1 MW of thermal power (C. Zhao, 2010). The overall power production system is shown in Figure A.3.

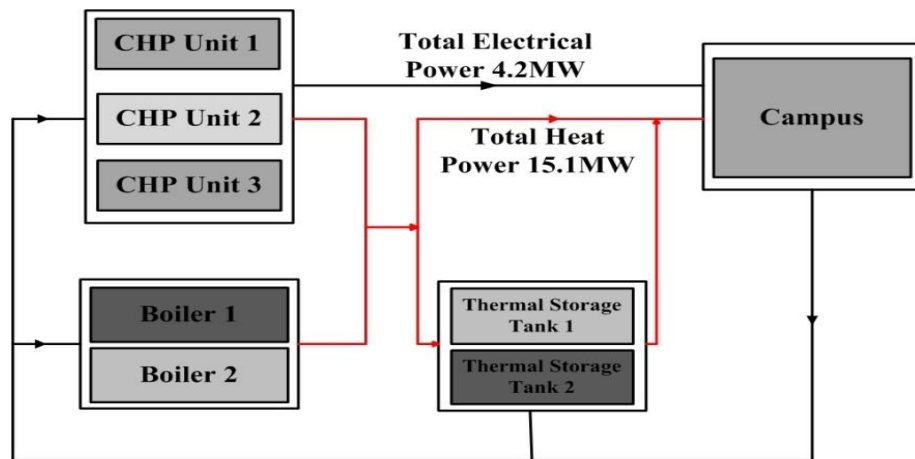


Figure A.3 Power production system Schematics of CHP in UoW

With reference to the layout of the introduced CHP plant, the topology of the model applied with control system is shown in Figure A.4. Subsystems such as gas engine, heat recovery system, feed water, thermal storage and auxiliary boiler are treated as separate blocks. Within these blocks the underlying processes were simulated by applying a particular programming model. This methodology is widely used in the modelling work of power plants (Lu and Hogg, 2000, van Putten and Colonna, 2007). These blocks are then connected graphically to simulate the real physical processes of the CHP power plant. In terms of the model validation, information on hourly gas and water consumption in cubic meters and electricity and heat generation in power units was obtained by meters installed at the CHP plant of the University of Warwick. Records from one full working day of summer (August) and winter (February) are obtained.

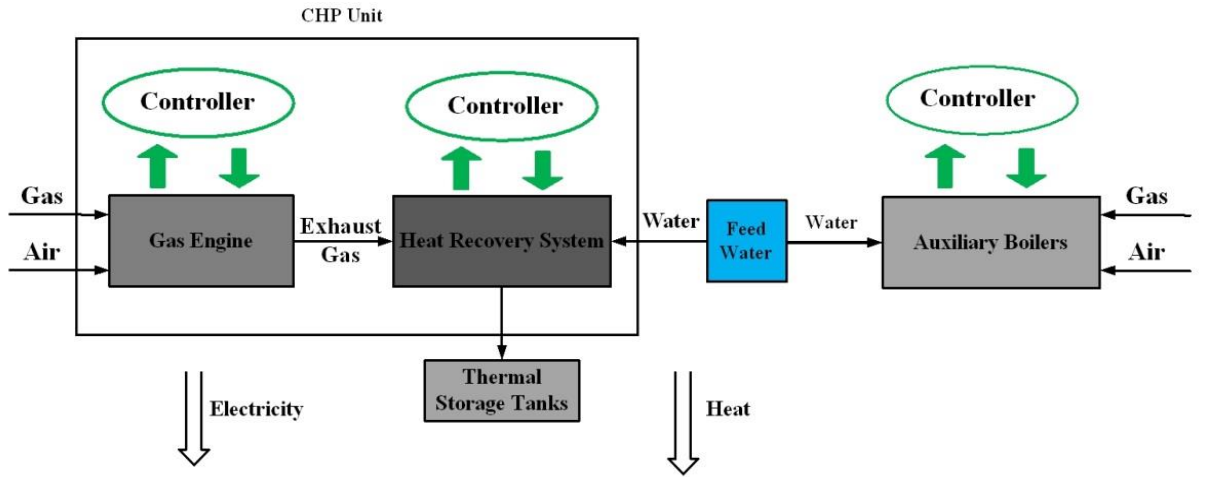


Figure A.4 Power production system Schematics of CHP in UoW

The main subsystems of CHP model are developed with Thermolib blocks: gas engine cycle is similar with gas turbine cycle described in Section 6.1.2. Feed water subsystem is developed with source block and pump blocks. Heat exchanger is developed with heat exchanger block. But for the controller design which will be introduced later, the auxiliary boiler model is built as a lumped model to give back-up support for thermal power supply. The method proposed by Bell and Astrom (Pauley et al., 1984) is adopted in this work. It is viewed as a “single lumped entity” in order to avoid tedious derivation of numerous thermodynamic equations. The model involved two first-order differential equations for the water output temperature and water level in the boiler vessel. The equation was further derived based on mass balance and energy balance equations:

Mass balance:

$$\frac{d(V\rho)}{dt} = \dot{m}_{in} - \dot{m}_{out} \quad (A.1)$$

Where  $V$  ( $\text{m}^3$ ) refers to the media volume and  $\rho$  denotes the density.

Energy balance:

$$\frac{d}{dt}(V\rho h_{out} + k_m A_m T_{out}) = \dot{m}_{in} h_{in} - \dot{m}_{out} h_{out} + \dot{Q}_{com} \quad (A.2)$$

where  $\dot{Q}_{com}$  (kW) denotes the heat transfer rate to the boiler furnace,  $h$  (kW kg<sup>-1</sup>) denotes the working media enthalpy,  $k_m$  (kW m<sup>-2</sup> K<sup>-1</sup>) denotes the steel heat transfer coefficient while  $A_m$  (m<sup>2</sup>) denotes the maximum heat transfer surface between the water and boiler metal walls.

The water output temperature change rate derived based on (A.2) will be:

$$\frac{dT_{out}}{dt} = \frac{\dot{m}_{in} C_p T_{in} - \dot{m}_{out} C_p T_{out} + Q_{com} - A\rho C_p T_{out} \frac{dH}{dt}}{k_m A_m + AH\rho C_p} \quad (A.3)$$

where:

$$\frac{dH}{dt} = \frac{\dot{m}_{in} - \dot{m}_{out}}{A} \quad (A.4)$$

Where  $A$  (m<sup>2</sup>) denotes the boiler bottom area and  $H$  (m) denotes the boiler height.

Equation (A.1) implies the water mass change rate in the boiler vessel equals to the difference between the inlet and outlet water flow rate. Symbols  $\dot{m}_{in}$  and  $\dot{m}_{out}$  represent the water input and output flow rate respectively. Equation (A.2) reveals that the internal energy change is caused by water volumetric change and combustion in the furnace. It can be further developed as Equation (A.3).

To eliminate the unwanted disturbances and possible noise and to provide a valid response, simplified controllers are designed for gas engine and heat recovery sub-systems. In this work, PID control is applied to the gas engine and heat recovery subsystems to ensure the stable output of electrical and thermal power. The gas engine and heat recovery subsystems'



transfer functions are obtained by using the system identification toolbox. Their response to a unit step input was then studied. The mathematical representation of the controlling input is described by (A.5) while the transfer function of the controller is expressed by (A.6):

$$u(t) = K_p[e(t) + \frac{1}{T_i} \int_0^t e(\tau) d\tau + T_d \frac{de(t)}{dt}] \quad (\text{A.5})$$

This equation expresses that based on the error  $e(t)$  between user-defined reference input  $r(t)$  and instant output of the process  $y(t)$ , the feedback controller generates the control variable  $u(t)$ . This control variable is a sum of weighted signals, undertaking proportional, integral and derivative actions on the error.

$$G_c(s) = \frac{U(s)}{E(s)} = K_p + \frac{K_i}{s} + K_d s \quad (\text{A.6})$$

Equation (A.6) is the transfer function of the controller.  $K_p(-)$ ,  $K_i(-)$  and  $K_d(-)$  are the gain parameters of the controllers, each making its own contribution to eliminate the error and ensure the stable output.

Different tuning methods were used for the controllers applied to subsystems. For the PID tuning procedure, Ziegler-Nichols tuning method is adopted (Åström and Hägglund, 2004). While keeping the integral and derivative gains at zero value, proportional gain should be increased to the value at which sustained oscillations appear on the closed loop step response plot. Such critical gain  $K_{cr}$  together with corresponding critical period  $P_{cr}$  is used to obtain parameters for optimal controller.

The gas engine subsystem is treated as a single input and single output (SISO) system. The amount of fuel burnt in the combustion chamber is directly proportional to the electrical

output. Since the heat energy released by fuel combustion is directly converted to mechanical power by a turbine and then to electrical power by a generator, continuous fuel supply must be ensured in order to maintain electricity generation. The design characteristics of gas engine subsystem controller are shown in Table A.2:

Table A.2 Design characteristics of gas engine controller

Critical gain, $K_{cr}$	$2.96e^{-4}$
Critical period, $P_{cr}$ , [s]	$3.7e^{-4}$
Proportional gain, $K_p = 0.45 * K_{cr}$	$1.33e^{-4}$
Subsystem transfer function $G(s)$	$\frac{3552}{1.46s + 1}$
Controller transfer function $G_c(s)$	$(1.33 + \frac{3.09}{s}) \times 10^{-4}$

The heat recovery subsystem is also treated as a SISO system to simplify the modelling procedure. It is assumed there is no feed water loss during the heat transfer. The thermal output power was selected as a controlled variable. The whole loop was built in Simulink with blocks for the transfer function and PI controller. The design characteristics are shown in Table A.3 below.

Table A.3 Design characteristics of heat recovery subsystem controller

Proportional gain, $K_p$	0.00056
Integral gain, $K_i$	0.009
Subsystem transfer function $G(s)$	$\frac{21990}{s + 11.82}$
Controller transfer function $G_c(s)$	$0.00056 + \frac{0.009}{s}$

Again, simplified control strategy by considering single input (water flow) and single output (outlet water temperature) was applied for the auxiliary boiler subsystem. The tuning procedure followed the Biggest Log Modulus tuning (BLT) (Dan and Seborg, 2001) after several tuning methods were compared. With parameters obtained by the Ziegler-Nichols method, the performance of a controller is analysed in a frequency domain on the bode plot. The closed-loop stability of the system can be guaranteed once the biggest log modulus of the response equals to a particular value. This exact value  $L_{\max}$  is introduced here. The expression for  $L_{\max}$  (-) is shown below:

$$L_{\max} = 2 \times N dB \quad (A.6)$$

Where  $N$  is the number of inputs,

The design characteristics of auxiliary boiler subsystem and controller are shown in Table A.4.

Table A.4 Design characteristics of auxiliary boiler subsystem controller

Biggest log modulus, $L_{\max}$	$2dB$
Integral gain, $K_p$	0.0065
Integral gain, $K_I$	0.0002
Subsystem transfer function $G(s)$	$\frac{216.9}{68.4s + 1}$
Controller transfer function $G_c(s)$	$0.00056 + \frac{0.009}{s}$

## A.2 Performance Analysis of CHP Power Plant Model

After the completion of the modelling procedure a series of simulations were carried out to study the validity of the model. Numerical data collected from the University's plant were used for validation of the model, simulation results were generated by the CHP process model. Firstly, steady-state results from each subsystem were compared to hourly measurement data of the CHP plant in summer and winter. Since the auxiliary boiler is not running during summer, the validation data collected is taken during spring and winter operation. For each subsystem, the transient part of response at one particular hour was presented to provide the information of this system's dynamic behaviour.

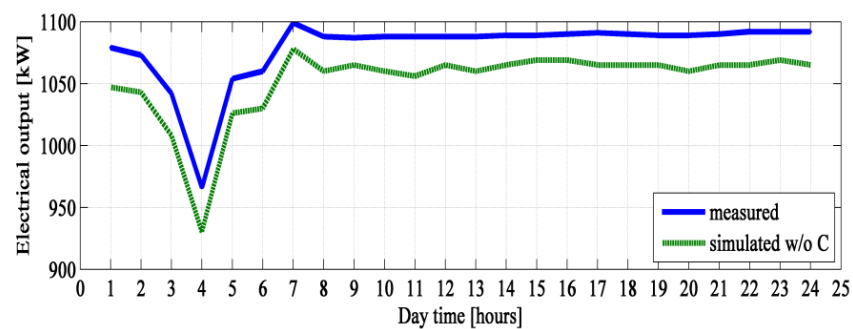


Figure A.5 Comparison of simulated electrical output without controller and operational data in a summer working day

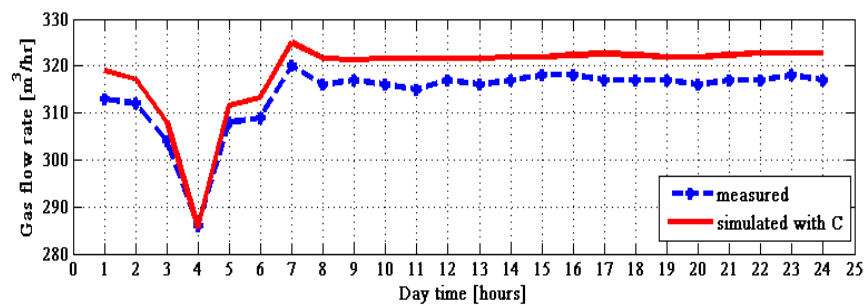


Figure A.6 Comparison of simulated gas flow with feedback control and operational data in a summer working day

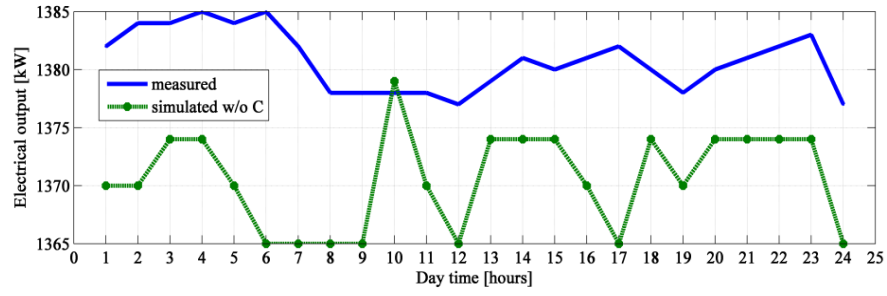


Figure A.7 Comparison of simulated electrical output without controller and operational data in a winter working day

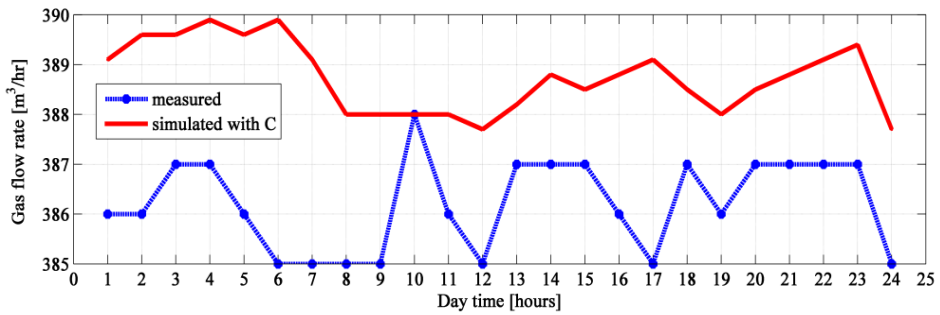


Figure A.8 Comparison of simulated gas flow with feedback control and operational data in a winter working day

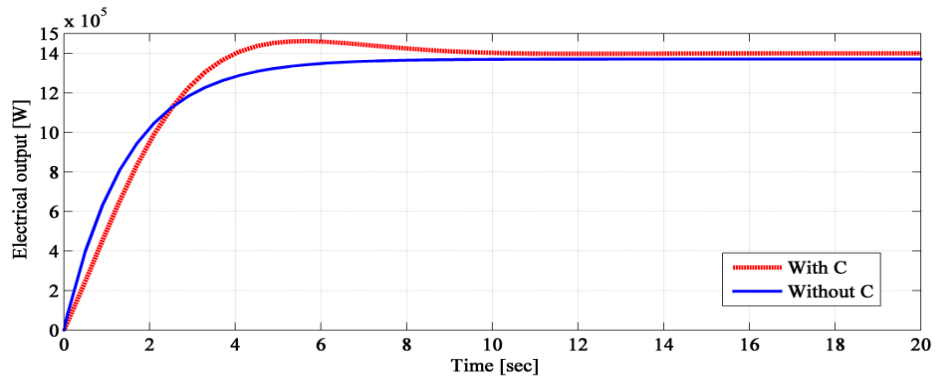


Figure A.9 Dynamic behaviour of electricity generation with/without feedback controller

According to the design data of the power plant, the full power output of 1370 kW is generated when the gas input of engine reaches the reference value of 386 m<sup>3</sup>/h. Results in Figure A.5 and Figure A.6 show that the steady state errors in the gas engine subsystem response with and without controller in summer are 2.46% and 1.55% respectively. The simulation results also show similar trends for the power outputs and gas input volumes. Since there is no large scale air-conditioners running in summer for refrigeration and

electricity for lighting is much less than winter as well, the power load in summer (Figure A.5) is obviously lower than it is in winter (results in Figure A.6). It is clear that the designed controller was efficient in terms of the set point tracking for the summer working day.

Figure A.7 and A.8 show the similar results of the gas engine system simulation and measured data from the CHP plant in a winter working day. Steady-state errors of simulated working condition in winter are 0.75% and 0.66% respectively. A similar conclusion can be made that controller did improve the simulation accuracy. There is fluctuation of the power output result at 10:00 in Figure A.7 for simulation without controller. This is due to the collected input gas volume data jumps to  $388\text{m}^3/\text{h}$  (as shown in Figure A.8) but the collected power output data didn't change. The model faithfully reflected the power output change caused by input gas change. In the simulation with feedback controller for the gas input volume, there is no fluctuation for gas volume as the collected power output didn't change at that time point.

Figure A.8 presents the dynamic output of electrical power with/without control. The gas flow rate reached the reference value of  $386\text{ m}^3/\text{h}$ , with only 11.6% overshoot in 6.34 seconds, the effectiveness of the implemented PI controller is well justified.

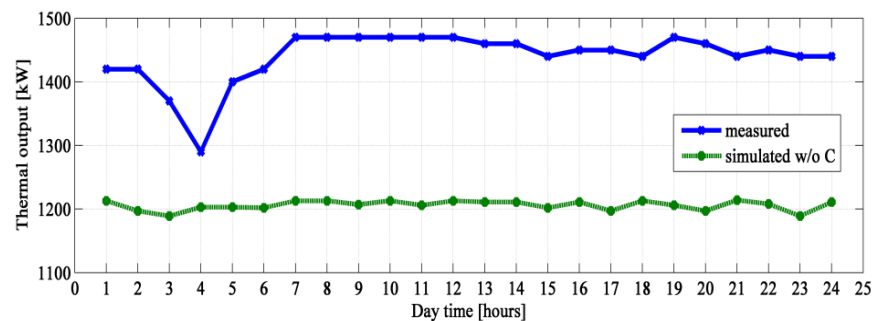


Figure A.10 Comparison of simulated thermal output without control and operational data in a summer working day

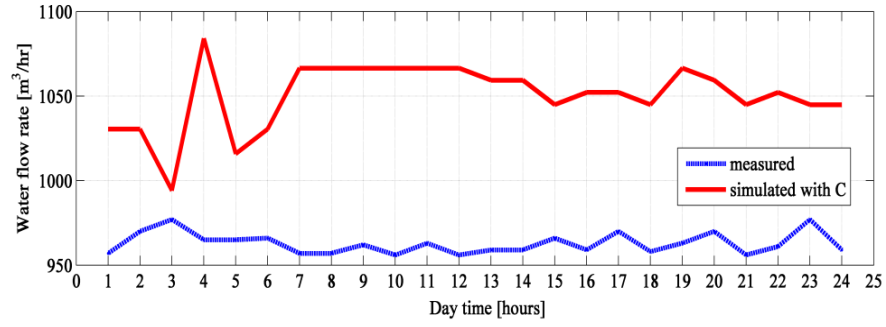


Figure A.11 Comparison of simulated water flow rate with control and operational data in a summer working day

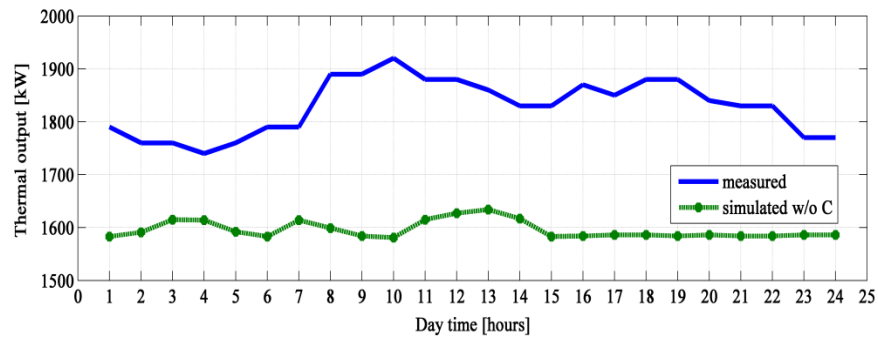


Figure A.12 Comparison of simulated water flow rate without control and operational data in a winter working day

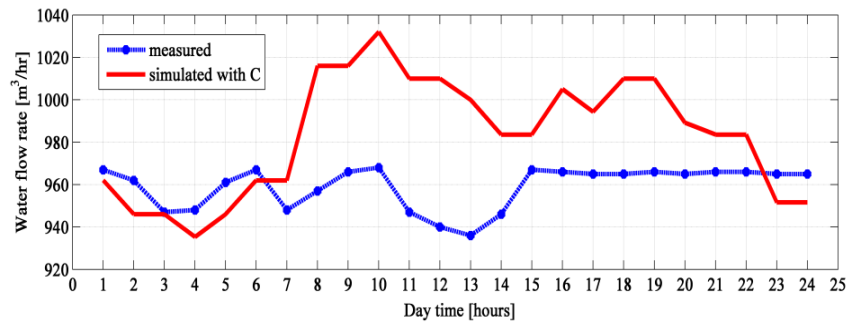


Figure A.13 Comparison of simulated water flow rate with control and operational data in a winter working day

Figures A.10 to A.13 present the simulation data comparison with operational data of the heat recovery subsystems in summer and winter seasons. The model with control shows a smaller error of 9.11% and 3.21% in summer and winter, compared with the model without control error values of 16.14% and 12.67%. Relatively large error appears in this simulation compared with the results of gas engine subsystem. This is mainly caused by the imperfections in the initial design of the heat recovery subsystem. Figure A.14 presents the

dynamic change of thermal power generated by heat exchanger. 1583 kW of thermal power is produced when a water flow rate with the numeric value of  $967 \text{ m}^3/\text{h}$  is inputted to the heat exchanger. The hot water temperature finally reaches  $83^\circ\text{C}$  which can satisfy the demand for campus district heating.

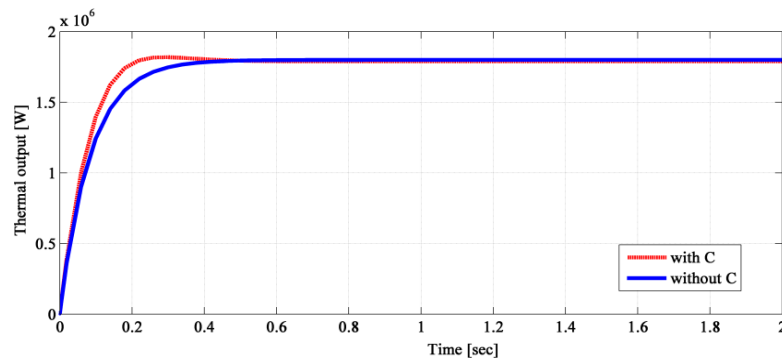


Figure A.14 Dynamic behaviour of heat exchanger thermal output

The auxiliary boiler is mainly used for back-up in cold conditions, thus there were no data on boiler operation in summer days. Figure A.15 shows the simulation results without control for thermal output for one working day in winter while Figure A.16 shows the simulation results with control in a spring working day. Figure A.17 shows that the output temperature is regulated to the required level of  $85^\circ\text{C}$  by the controller in winter.

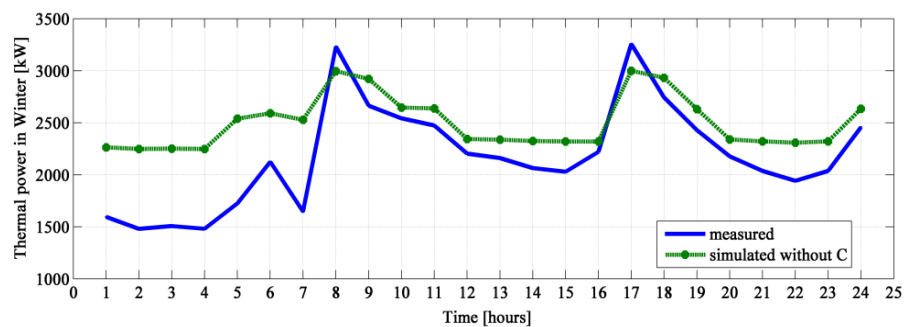


Figure A.15 Comparison of simulated boiler thermal power output without control and operational data in winter working day



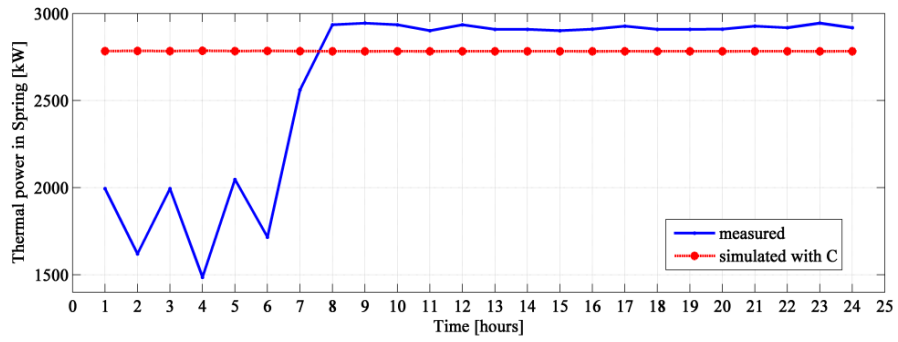


Figure A.16 Comparison of simulated boiler thermal power output with control and operation data in a spring working day

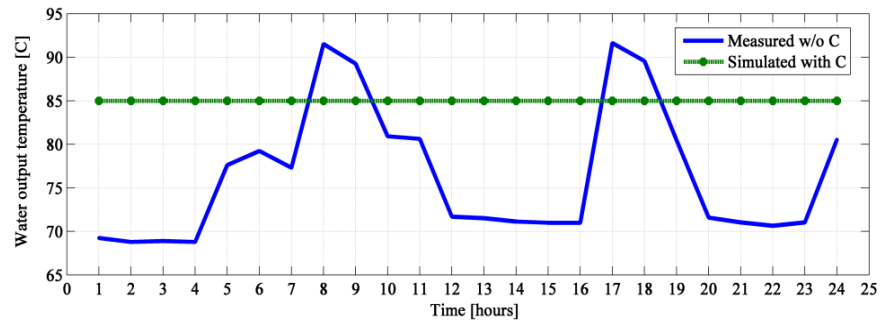


Figure A.17 Comparison of simulated boiler output water temperature with and without control in a winter working day

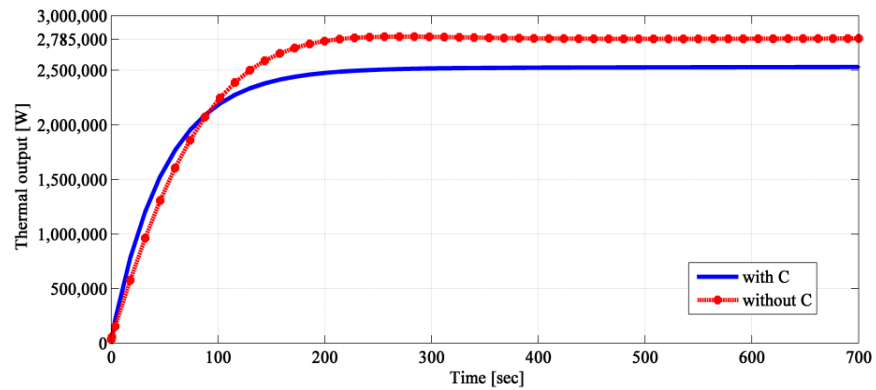


Figure A.18 Dynamic change of boiler thermal power output with/without control

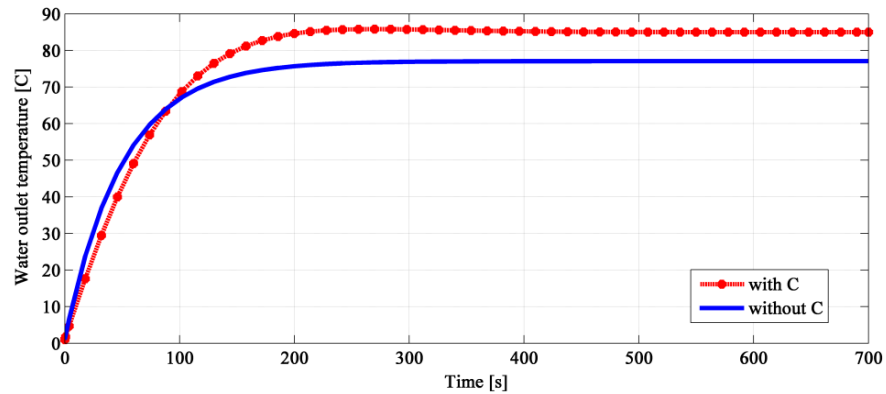


Figure A.19 Dynamic change of boiler water temperature output with/without control

Dynamic change of boiler thermal power output is shown in Figure A.18, with the reference value of 2785 kW, it is clear that a better result of 2792 kW is generated with control. The dynamic change of output temperature is shown in Figure A.19; the result without control is 5 °C less than reference the value 83 °C, the results with control show better accuracy with the value of 85 °C.

### **A.3 Discussion and summary**

In this project, a model is developed to simulate the overall working process of a CHP system based on the configuration of the University of Warwick power plant. The model is derived by applying the engineering principles of combustion reaction, mass balance and energy balance. The simulation results of the gas engine electricity output match well with the collected data from the real plant. Simulation results of the thermal power generation from the heat exchanger and auxiliary boilers are compared with the data collected from the plant. The model can successfully reflect the power plant operation in different seasons. The best overall thermal efficiency of CHP power plant in winter reaches 83%, which is much higher than traditional power plant. CHP is an ideal choice for district energy supply, for example university campuses, in terms of saving energy and reducing carbon emission.

Unlike the traditional modelling method proposed by former researchers (van Putten and Colonna, 2007, Lu and Hogg, 2000, Pauley et al., 1984), the model proposed in this work benefits from the validation data collected from the power plant on campus. The dynamic model developed with Thermolib and Simulink can reflect the dynamic characteristics of CHP process and offer a reliable platform for further control strategy application. A relatively large error happens in the simulation of heat exchanger and auxiliary boiler, which is mainly caused by the limitation of initial process model design.

Different controlling strategies and tuning methods were introduced to optimize the overall performance of the simulated power plant. The comparison of simulated data with and without controller can clearly illustrate that the regulated results with control shows better accuracy with insignificant overshoot and the responses are fast enough to guarantee the system stability.